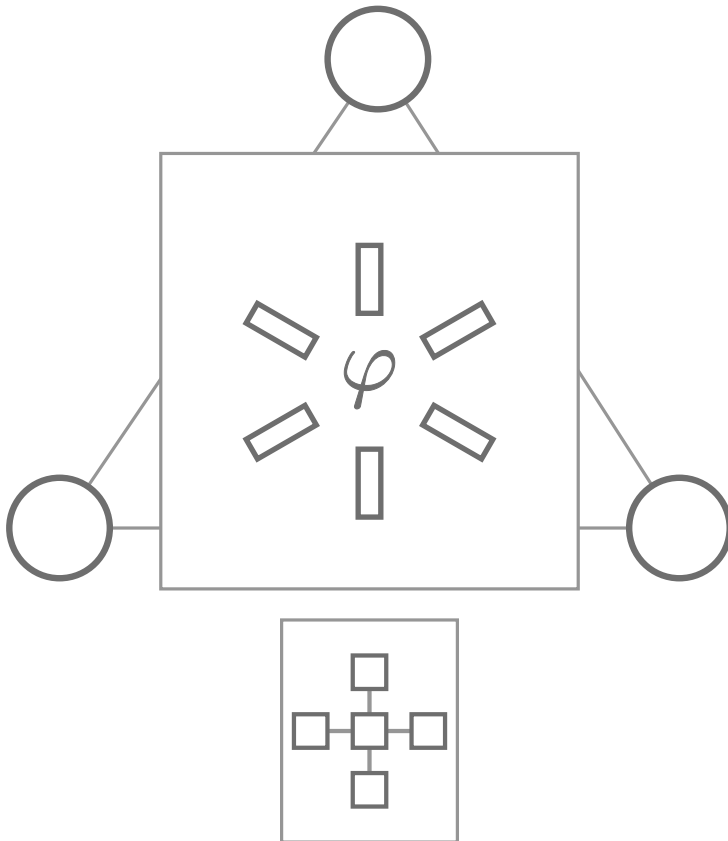


Thomas S. Schwarze

Phase extraction for laser interferometry in space: phase readout schemes and optical testing



Phase extraction for laser interferometry in space: phase readout schemes and optical testing

Von der QUEST-Leibniz-Forschungsschule der
Gottfried Wilhelm Leibniz Universität Hannover
zur Erlangung des akademischen Grades

Doktor der Naturwissenschaften
Dr.rer.nat.

genehmigte Dissertation
von

M.Sc. Thomas S. Schwarze

2018

Referent: Prof. Dr. Karsten Danzmann
Korreferent: apl. Prof. Dr. Gerhard Heinzl
Korreferent: Prof. Dr. Guido Müller
Tag der Promotion: 17.05.2018

Abstract

This thesis was carried out in the area of gravitational physics, specifically in the fields of gravitational wave astronomy and gravimetry. Both fields do or will make use of satellite missions. The planned gravitational wave observatory Laser Interferometer Space Antenna (LISA) aims to detect gravitational waves in the mHz range while missions like the Gravity Field and Steady-State Ocean Circulation Explorer (GOCE) and the Gravity Recovery and Climate Experiment Follow-On (GRACE-FO) measured or will measure, respectively, the Earth's gravity field to obtain valuable information on hydrology and climate dynamics.

The first part of this thesis deals with the heterodyne interferometric readout for LISA and, in particular, its phase extraction system or phasemeter. A summary of the basic principles is followed by a statement of the requirements for the latter. These concern in particular the phase noise contribution, dynamic range and bandwidth. Subsequently, possible testing schemes are being discussed. One experimentally investigated in the scope of this thesis is an optical three-signal test which provides the ability to probe for phasemeter linearity. It utilizes an interferometer of hexagonal footprint, thus called Hexagon, to probe an elegant breadboard model of the LISA phasemeter developed prior to this thesis. An extensive noise hunt was performed to reduce testbed noise. This, in turn, allowed for a measurement in accordance with the single channel LISA requirement extrapolated to three signals ($10.23 \mu\text{rad}/\sqrt{\text{Hz}}$ down to 4 mHz). It was conducted with heterodyne frequencies of 3–5.8 MHz and a dynamic range of six orders of magnitude. A measurement with full LISA-like values for these parameters did meet the targeted performance outside the Fourier frequency range 0.4–20 mHz, inside of which the utilized photoreceivers were limiting.

The second thesis part describes the development and implementation of two phase readout schemes for the interferometry technique Deep Frequency Modulation Interferometry (DFMI). The latter aims to provide high scalability and dynamic range in order to interferometrically track test masses in future gravimetry missions or other applications. Two phase extraction methods were investigated, one based on a spectral analysis followed by a non-linear fit, the other on an extended Kalman filter in conjunction with empiric state space modeling. First tests included proof-of-principle tracking of moving mirrors as well as demonstrated a performance of $4 \mu\text{rad}/\sqrt{\text{Hz}}$ at 0.1–1 Hz.

Keywords: gravitational physics, interferometry, phase extraction

Kurzfassung

Diese Arbeit wurde im Bereich Gravitationsphysik, oder genauer, in den Bereichen Gravitationswellenastronomie und Gravimetrie durchgeführt. Beide Bereiche nutzen oder werden in Zukunft Satellitenmissionen nutzen. Der geplante Gravitationswellendetektor Laser Interferometer Space Antenna (LISA) ist darauf ausgerichtet, Gravitationswellen im mHz Bereich zu messen, während Missionen wie Gravity Field and Steady-State Ocean Circulation Explorer (GOCE) und Gravity Recovery and Climate Experiment Follow-On (GRACE-FO) das Gravitationsfeld der Erde vermessen haben bzw. vermessen werden, um wertvolle Informationen für Hydrologie und Klimaforschung zu gewinnen.

Der erste Teil dieser Arbeit behandelt die interferometrische Auslese in LISA und speziell die zugehörige Phasenextrahierung beziehungsweise das zugehörige Phasenmeter. Nach einer Zusammenfassung der Hauptprinzipien werden die Anforderungen an Letzteres vorgestellt. Diese betreffen in erster Linie den Beitrag von Phasenrauschen, den dynamischen Bereich sowie die Bandbreite. Anschließend werden mögliche Testschemata diskutiert. Eines dieser Schemata, ein optischer Dreisignaltest, wurde in dieser Arbeit durchgeführt. Es ermöglicht die Überprüfung der Linearität des Phasenmeters. Ein Interferometer mit hexagonalem Grundriss, welches daher als Hexagon bezeichnet wird, dient als Hauptbaustein. In dieser Arbeit wird es genutzt, um einen Phasenmeterprototypen für LISA zu testen, welcher im Vorfeld dieser Arbeit entwickelt wurde. Eine ausführliche Suche nach Rauschquellen im Experiment wurde durchgeführt mit dem Ziel, diese zu beheben. Das wiederum ermöglichte eine Messung ($10.23 \mu\text{rad}/\sqrt{\text{Hz}}$ hinunter bis 4 mHz), die Übereinstimmung mit der Anforderung für einen Auslesekanal in LISA zeigte, wenn diese auf die drei Kanäle des Dreisignaltests extrapoliert wird. Die Messung wurde mit Heterodynfrequenzen von 3–5.8 MHz durchgeführt und zeigte einen dynamischen Bereich von sechs Größenordnungen. Eine Messung mit den erwarteten Signalparametern in LISA erfüllte die Anforderung im Messband abgesehen vom Intervall 0.4–20 mHz. Hierbei erwiesen sich die genutzten Photoempfänger als limitierender Faktor.

Der zweite Teil der Arbeit stellt die Entwicklung und Implementierung zweier Phasenausleseschemata für die Interferometriechnik Deep Frequency Modulation Interferometry (DFMI) vor. Diese zielt auf eine hohe Skalierbarkeit und einen hohen dynamischen Bereich bei der interferometrischen Vermessung von Testmassenbewegungen ab. Dieses Verfahren kann für zukünftige Gravimetriemissionen oder in anderen Anwendungen genutzt wer-

den. Zwei Auslesemethoden wurden untersucht. Die Erste baut auf einer Spektralanalyse mit nachfolgendem nichtlinearem Fit auf, während die zweite ein Extended Kalman Filter mit empirischer Zustandsraummodellierung darstellt. Erste Tests lieferten einen Funktionsnachweis in Form der Vermessung der Bewegung eines Spiegels. Des Weiteren wurde eine Genauigkeit von $4 \mu\text{rad}/\sqrt{\text{Hz}}$ zwischen 0.1–1 Hz festgestellt.

Schlüsselwörter: Gravitationsphysik, Interferometrie, Phasenauslese

Contents

Abstract	v
Kurzfassung	vii
Contents	ix
Acronyms	xii
List of figures	xvii
1 Introduction	1
1.1 Laser interferometry and phase extraction	2
1.2 LISA	3
1.3 Tracking of multiple test masses in future gravimetry missions	5
I Investigating heterodyne phase extraction for LISA	7
2 Heterodyne interferometry in LISA and other applications	9
2.1 Heterodyne interferometry	9
2.2 LISA	13
2.2.1 Free-falling test masses	13
2.2.2 Interferometric readout	14
2.2.3 Laser frequency noise and TDI	17
2.2.4 Clock noise in LISA	22
2.2.5 Optical bench motion and local laser frequency noise .	23
2.2.6 Clock synchronization and arm-length determination .	23
2.2.7 Prerequisites for TDI	25
2.2.8 Phase extraction and metrology requirements	26
2.3 Phase extraction with a LISA phasemeter	29
2.3.1 EBB phasemeter overview	29

Contents

2.3.2	Heterodyne phase extraction core	29
2.3.3	Clock and pilot tone generation	34
2.3.4	Digital servo for laser locking	34
2.3.5	PRN generation and recovery	35
2.3.6	Clock tone readout	35
2.4	Noise sources for the phase extraction	36
2.4.1	Additive noise	36
2.4.2	Tracking errors and cycle slips	38
2.4.3	Direct phase noise	39
2.4.4	Direct phase noise due to small vector noise	40
2.5	Other applications and alternative extraction techniques	42
2.5.1	LPF	42
2.5.2	GRACE-FO	43
2.5.3	Other applications	44
2.5.4	Alternative extraction methods for LISA	44
3	Investigating heterodyne phase extraction performance	47
3.1	Formalism	47
3.2	Absolute test	48
3.3	Split-signal test	50
3.4	Three-signal test	52
3.5	Optical three-signal test	53
3.6	LIME	57
4	Implementing an optical three-signal test	59
4.1	Initial experimental setup	59
4.1.1	Laser preparation	59
4.1.2	Auxiliary phasemeter and frequency lock	61
4.1.3	Vacuum chamber	62
4.1.4	Optical bench and auxiliary optics	62
4.1.5	Main phasemeter	63
4.2	Noise hunting and evolution of the experimental setup	64
4.2.1	Initial measurements	64
4.2.2	Influence of air in the interferometers	68
4.2.3	Amplitude coupling	68
4.2.4	Measurements with synchronized clocks and lock to Iodine reference	77
4.2.5	A low-frequency amplitude stabilization scheme via digital heterodyne amplitude decoupling	81

4.2.6	A low-frequency temperature stabilization scheme via cyclic control of single laser powers	83
4.2.7	Probing for temperature coupling into photoreceiver performance	85
4.2.8	Probing for temperature coupling via fibers	85
4.2.9	Temperature coupling via fibers: mechanism and compensation	86
4.2.10	Parasitic signals at microradian levels	91
4.2.11	Photoreceiver noise at higher heterodyne frequencies .	107
4.3	Final performance and discussion	112
4.3.1	Final performance for moderate input conditions . . .	112
4.3.2	Final performance with LISA-like input conditions . .	115
4.3.3	Final performance with LISA-like input conditions and Doppler-like frequency drift	118
4.4	Measurements of RIN coupling	120
4.4.1	Method	120
4.4.2	Measurements	121
5	Outlook	127
5.1	Performance and stability improvements	127
5.2	Expansion to more testing schemes	128
II	Development and implementation of phase extraction schemes for Deep Frequency Modulation Interferometry	131
6	Deep Frequency Modulation Interferometry	133
6.1	Key principles	133
6.2	Experimental setup	135
6.3	Comparison to other interferometry techniques	137
7	Phase extraction schemes for DFMI	139
7.1	Spectral analysis and non-linear fit	139
7.2	Kalman filter	140
7.2.1	Basic Kalman filter	141
7.2.2	Adaption for DFMI	143
8	Testing phase extraction schemes for DFMI	147
8.1	Implementation on an SoC	147
8.2	Performance tests	149

Contents

8.3 Comparison	153
8.4 Future developments and outlook	154
9 Conclusions	157
III Appendix	161
A LIME setup	163
B Heterodyne frequency catalog	165
C Additional measurements	169
D Temperature maps of lasers utilized in the experiments	177
E Kalman filter properties in programmable logic derived using a high level synthesis tool (Vivado HLS)	179
F Monitored powers for RIN coupling measurements	181
Bibliography	183
Acknowledgments	191
Curriculum Vitae	193
Publications	195

Acronyms

I ²	cascaded integral
LISA	Laser Interferometer Space Antenna
AC	air conditioning
ADC	analog-to-digital-converter
ADPLL	all-digital phase-locked loop
AEI	Albert Einstein Institute
AM	amplitude modulation
AM-PM	amplitude-modulation-to-phase-modulation
ASD	amplitude spectral density
BNC	Bayonet Neill-Concelman
CAD	computer-aided design
CIC	cascaded integrator comb
CMM	coordinate measurement machine
CPSD	cross power spectral density
CPU	central processing unit
D-Sub	D-Subminiature
DAC	digital-to-analog-converter
DAQ	data acquisition
DFACS	drag-free attitude control system
DFMI	Deep Frequency Modulation Interferometry
DFT	discrete Fourier transform
DLL	delay-locked loop
DPMI	Deep Phase Modulation Interferometry
DSN	Deep Space Network
DSP	digital signal processing

Acronyms

DSS	digital signal generator
DWS	differential wavefront sensing
EBB	elegant breadboard
EOAM	electro-optical amplitude modulator
EOM	electro-optical modulator
ESA	European Space Agency
FDS	frequency distribution system
FFT	fast Fourier transform
FIOS	fiber injector optical subassembly
FIR	finite impulse response
FMC	FPGA mezzanine card
FPGA	field programmable gate array
GBWP	gain bandwidth product
GOCE	Gravity Field and Steady-State Ocean Circulation Explorer
GRACE-FO	Gravity Recovery and Climate Experiment Follow-On
GRS	gravitational reference sensor
GW	gravitational wave
HLS	high-level synthesis
I	integral
IP	intellectual property
JPL	Jet Propulsion Laboratory
LED	light emitting diode
LIGO	Laser Interferometer Gravitational-Wave Observatory
LIME	LISA metrology chain experiment
LPF	LISA Pathfinder
LRI	Laser Ranging Interferometer
LUT	look-up table
NASA	The National Aeronautics and Space Administration

NCO	numerically controlled oscillator
NGGM	Next Generation Gravity Mission
NPRO	non-planar ring oscillator
NSF	noise shape function
OH	optical head
OOL	out-of-loop
OP	operational amplifier
p-pol	parallel polarization
PA	phase accumulator
PBS	polarizing beam splitter
PCB	printed circuit board
PCI	peripheral component interconnect
PI	proportional-integral
PIR	phase increment register
PL	programmable logic
PM	phase modulation
PRN	pseudo random number
PS	processing system
QPR	quadrant photoreceiver
RIN	relative intensity noise
RMS	root-mean-square
s-pol	“senkrecht” polarization
SBFT	single bin Fourier transform
SFP	scanning Fabry-Pérot
SMA	SubMiniature version A
SoC	system-on-a-chip
TDI	Time-Delay Interferometry
TIA	transimpedance amplifier
TM	test mass
USB	universal serial bus
VOA	variable optical attenuator

List of Figures

1.1	Homodyne interferometer	2
1.2	LISA constellation	4
1.3	LISA strain sensitivity	5
1.4	Upscaling of interferometric readout	6
2.1	Heterodyne interferometer	10
2.2	Master-transponder scheme	15
2.3	LISA optical bench	17
2.4	Geometric interpretation of TDI	21
2.5	Laser frequency noise coupling and dynamic range	27
2.6	LISA phasemeter EBB	30
2.7	ADPLL	31
2.8	Small vector noise	40
2.9	I-Q demodulation	43
3.1	Absolute phasemeter test	49
3.2	Split-signal phasemeter test	51
3.3	Stray light coupling	52
3.4	Three-signal phasemeter test	54
3.5	Hexagon interferometer	55
4.1	Laser preparation	60
4.2	Hexagon setup	63
4.3	Initial electrical measurement	65
4.4	Initial optical three-signal measurement	66
4.5	Measurement without pilot tone interference	66
4.6	Impact of different setup changes	67
4.7	Application of different vacuum levels and polarization control.	69
4.8	Coupling of single laser amplitude modulation	70
4.9	Electrical amplitude-coupling tests	71

List of Figures

4.10	Digital absolute ADPLL test scheme	72
4.11	Digital amplitude coupling tests	73
4.12	Amplitude noise projection	74
4.13	Optimized laser operation points	75
4.14	Frequency modulation with master laser piezo	77
4.15	Effect of different clocks	78
4.16	Measurements with clock synchronization	78
4.17	Measurements with Iodine reference and switched laser operation point	79
4.18	Composition of photoreceiver temperature fluctuations	80
4.19	Laser amplitude stabilization via digital decoupling of heterodyne amplitudes	82
4.20	Photoreceiver temperature fluctuation suppression due to amplitude stabilization	83
4.21	Photoreceiver temperature stabilization via laser power modulation	84
4.22	Coupling of temperature modulations via OP and photodiode	86
4.23	Coupling of temperature modulations via fiber	87
4.24	Polarization-maintaining fiber and Poincaré sphere	87
4.25	Fiber bench assembly picture	90
4.26	Suppression of temperature coupling with fiber bench	90
4.27	π measurements with and without fiber benches	92
4.28	Impact of laser power attenuation	93
4.29	Impact of temperature modulation on fiber behind fiber bench	94
4.30	Fiber temperature modulation into beam jitter coupling	95
4.31	More precise adjustment of photoreceiver polarizers and improved polarization stability in the fibers	97
4.32	Measurements with stabilized polarization in fibers and adjusted polarization in front of photoreceivers	98
4.33	Optical setup for simultaneous optical split and π measurements	100
4.34	Comparison of π and optical split measurement	100
4.35	Intentionally mismatched polarizers between optical split measurement photoreceivers	101
4.36	Intentionally mismatched polarizers between complementary output ports	102
4.37	Impact of polarization alignment behind FIOSs with and without subsequent readjustment of folding mirrors	103
4.38	Three simultaneous π measurements	105
4.39	Three-signal measurement with post-FIOS polarizers	106

4.40	Measurements with higher heterodyne frequencies	106
4.41	Reduced power in one laser path	108
4.42	Setup to probe photoreceivers	109
4.43	Photoreceiver tests at 2.1 MHz	109
4.44	Photoreceiver tests at 19.1 MHz	110
4.45	Three-signal measurements with low input signal dynamics and low heterodyne frequencies	113
4.46	Temperatures during measurements in Figure 4.45	113
4.47	Three-signal measurements with high heterodyne frequencies	115
4.48	Three-signal measurements with high input signal dynamics	117
4.49	Three-signal measurements with full LISA input conditions	119
4.50	Measurements with f -RIN coupling	123
4.51	Measurements with $2f$ -RIN coupling	124
4.52	Measurements with DC baseband RIN	125
6.1	Unequal arm lengths Michelson interferometer with deep fre- quency modulation	134
6.2	Experimental DFMI setup	136
8.1	Full DFMI phasemeter assembly	149
8.2	Testbed for an electrical split test with optical signals	150
8.3	Phase tracking with non-linear fit	151
8.4	Phase tracking with Kalman filter	151
8.5	Comparison of non-linear fit and Kalman filter	152
8.6	Optimized non-linear fit measurement	153
A.1	LIME setup	164
C.1	Coupling of single laser amplitude modulation with high fre- quency lock gains	170
C.2	Measurements with amplitude stabilization	170
C.3	Electrical split measurement with two ADC cards	171
C.4	Measurement with slightly mismatched Glan-Laser polarizers	171
C.5	Electrical split measurement performed with the signal of one π measurement channel	172
C.6	π measurements with high heterodyne frequencies	172
C.7	Photoreceiver test with changed components	173
C.8	Correlation between phase and relative amplitude	174
C.9	Rearranged plot of Figure 4.48	174
C.10	Probing of dynamic range	175
C.11	Reference measurement without RIN	176

1

Introduction

Laser interferometry benefits from the stability of the laser wavelength and uses it as a ruler to precisely measure optical path length changes. Possible applications for this method are manifold. One of them is the tracking of free-falling test masses (TMs) in the context of gravitational wave (GW) astronomy and gravimetry. In the field of GW astronomy, the ground-based interferometers of the Laser Interferometer Gravitational-Wave Observatory (LIGO) already achieved to track the distance changes between mirrors due to the impact of GWs [1] and hence opened the door to a new era of astronomy. While the ground-based observatories are limited at lower frequencies by seismic and gravity gradient noise, the planned space-borne detector Laser Interferometer Space Antenna (LISA) [2, 3] aims to explore these frequency ranges with free-falling test masses tracked by intra- and inter-spacecraft interferometers. While the former was successfully tested with LISA Pathfinder (LPF) [4, 5], an implementation of the latter is deployed as a technology demonstrator on the satellites of the gravimetry and geodesy mission Gravity Recovery and Climate Experiment Follow-On (GRACE-FO). Future missions in the fields of gravimetry and geodesy plan to increase the experimental complexity by means of multiple local TMs in one satellite, thus resembling an improved version of the mission Gravity Field and Steady-State Ocean Circulation Explorer (GOCE), ideally with optical readout.

Three of the named missions have in common the interferometric readout. Its basic idea is to measure the motion of TMs, or in GRACE-FO of satellites, by tracking the associated optical path lengths in an interferometer. Changes of these path lengths are directly associated to variations in the interferometer phase. Consequently, a method to accurately extract this phase information is required. In this thesis, the phase extractions for two interferometry techniques are investigated. The first is heterodyne interferometry and is in particular important for LISA while the second is Deep

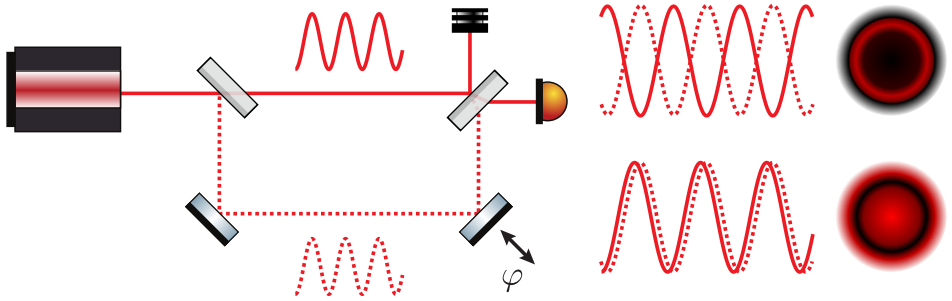


Figure 1.1: Sketch illustrating the basic principle of a homodyne interferometer. In this example, the phase change induced by a moving mirror is tracked. The phase change leads to constructive or destructive interference detected by a photoreceiver.

Frequency Modulation Interferometry (DFMI) and primary aims to increase the scalability of the interferometric tracking of TMs for future multi-TM gravimetry missions. The following sections will provide more details about the basic principles of laser interferometry and its phase readout, as well as a brief summary of the two aforementioned applications.

1.1 Laser interferometry and phase extraction

This section illustrates the basic principles of laser interferometry. The name interferometry is related to the term interference, which in this case means the coherent superposition of two mono-frequency electro-magnetic waves or laser beams. Coherence implies that instead of the two beam powers, their amplitudes are combined. Dependent on the phase relation between the beams, the superposition can lead either to the addition or the extinction of the two amplitudes. This dependency is exploited to estimate the phase relation by measuring the power of the super-imposed beams. This concept is illustrated in Figure 1.1 for the example of a homodyne Mach-Zehnder interferometer. A homodyne interferometer operates with the same frequencies in both interferometer arms. Here a phase change induced by a moving mirror leads to constructive or destructive interference detected by a photoreceiver. The phase itself is often the mediator of another primary measurand that changes the optical path length and thus the phase. Besides the mirror movement or TM movement, a further example is given by changes in diffractive indices. The presented homodyne Mach-Zehnder interferometer exhibits a sinusoidal phase-power relationship. A different technique, heterodyne interferometry, combines two beams with different

frequencies, which leads to a continuously time-dependent output power. The latter is sinusoidal and is called a beat note. Ideally, the interferometer phase is encoded solely in the beat note phase. Finally, the aforementioned technique DFMI, which is under investigation in the second part of this thesis, encodes the interferometer phase in several harmonics of a deep frequency modulation. The two latter techniques will be explained in more details in the respective thesis parts.

Each of these techniques comes with different advantages and disadvantages. Among others, criteria to be considered are accuracy, setup complexity and dynamic range. Furthermore, as described, the phase is encoded in distinct ways in the photoreceiver signals of the different techniques. Hence the phase extraction schemes need to be tailored for the specific case. Like the interferometry itself, the schemes are described in the respective thesis parts.

1.2 LISA

As already stated, LISA is a planned space-based GW observatory aiming to complement existing ground-based detectors in the lower frequency band around mHz. At first sight, their working principles are similar. They are designed to measure the ripples in space-time, which are GWs, by their impact on the displacement between test mirrors or TMs. Described in simplified terms, the displacement increases when space-time between the test mirrors is stretched, and decreases when it is compressed. However, even for highly-energetic sources, the amplitude of the emitted gravitational wave and thus the associated displacement is extremely small. This leads to the demand for high-precision metrology of the TM displacement on the one hand as well as their sufficient isolation from external forces on the other. The LIGO detectors aim to achieve this task within the frequency band of 20–1000 Hz. Impressive proofs of its success were given by the detection of multiple GWs from different sources. Several black hole mergers were detected [1, 6], in particular one coincidental with Virgo, a GW detector in Italy [7]. Additionally, a binary neutron star inspiral could be observed [8]. The latter not only marked the first GW detection of such a source, but also the first multi-messenger detection coincidental with electro-magnetic observations [9]. These results further motivate the extension of the observable frequency band to lower frequencies, namely the mHz band. This would not only allow the detection of sources emitting GWs solely in that frequency range, but also for the multi-band detection of sources changing

1 Introduction

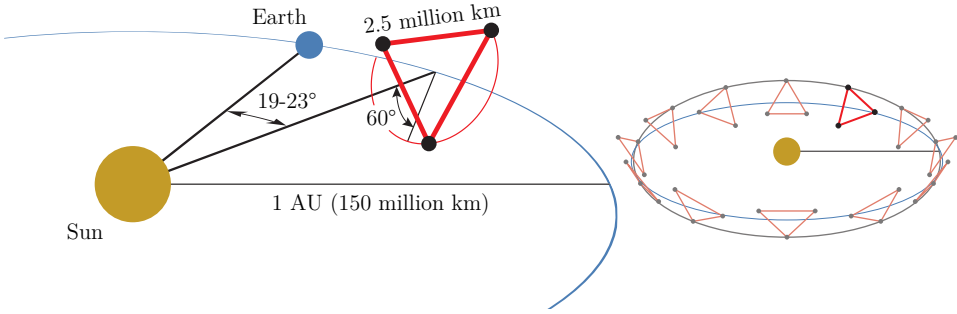


Figure 1.2: Sketch of the planned LISA constellation. The left side shows a snapshot with numbers for different orbit parameters while the right side illustrates the orbit evolution in the time frame of a year. Source: [3].

frequency over time [10]. However, in the mHz band, gravity gradient and seismic noise spoil the LIGO instrument sensitivity. An approach to solve this problem is pursued with the design of LISA. Here, a brief introduction will be given, while the technical details important for this thesis will be given in Section 2.2. The key principle of LISA is to put the test mirrors or TMs into space where seismic and gravity gradient noise are negligible. They will be hosted in spacecraft or satellites trailing the Earth on its orbit around the sun. Figure 1.2 shows a sketch of simulated LISA orbits and planned constellation parameters. Figure 1.3 presents a plot of the estimated detector strain sensitivity together with exemplary sources. The strain amplitude h of a GW determines its impact on a length L by means of the relative change ΔL , and is written as $h = \Delta L/L$.

In order to serve as GW probes, the LISA TMs have to be free-falling. That means they need to follow their geodesic motion only, without any influence of external forces. Only this way displacement can be traced back to incoming GWs. For this purpose the spacecraft will host the TMs and will follow their movement while simultaneously serving as shields against external forces, like for example solar radiation. Additionally, they carry the necessary electrical and optical devices to perform intra- and inter-spacecraft laser interferometry for the determination of the TM displacement. The final constellation will consist of three spacecraft or satellites forming a more or less equilateral triangle with arm lengths of about 2.5 million km. Due to orbit dynamics, the difference between the three arms can reach up to 50.000 km. These unequal arm lengths lead to the coupling of laser frequency noise. For mitigation, a post-processing technique called Time-Delay Interferometry (TDI) has been developed. It uses sub-measurements of the single

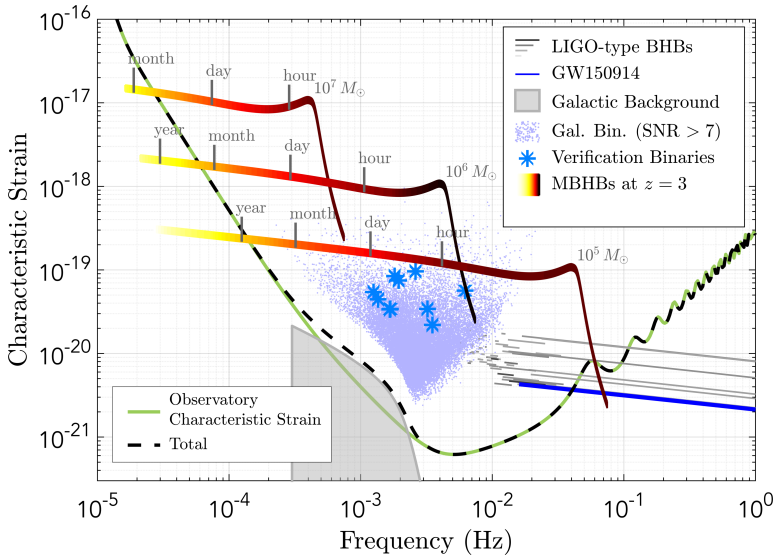


Figure 1.3: LISA strain sensitivity curve with exemplary GW sources. Source: [3].

LISA arms and shifts them in time to synthesize an equal-arm-length interferometer [11, 12]. Another consequence of the orbit dynamics is the occurrence of Doppler shifts in the inter-spacecraft interferometers. Hence the arm measurements in LISA are heterodyne interferometers with varying heterodyne beat note frequency. This shows in turn why a heterodyne phase extraction is required for LISA. In the respective part of this thesis, its requirements will be derived by a more detailed analysis of the LISA key principles. Subsequently, the efforts and the results of an experimental optical test of the phase extraction system or phasemeter will be presented.

1.3 Tracking of multiple test masses in future gravimetry missions

After the introduction to LISA in the last section, another space mission cannot remain unmentioned: LPF [4] was launched on December 3rd 2015 and started its operation phase at the Earth-Sun Lagrange point L1 on March 1st 2016. Its goal was to verify the feasibility of core technology for LISA by the interferometric tracking of two TMs. This goal was reached spectacularly by surpassing the requirements by orders of magnitude. While this lays a corner stone for the development of LISA, also the field of gravime-

1 Introduction

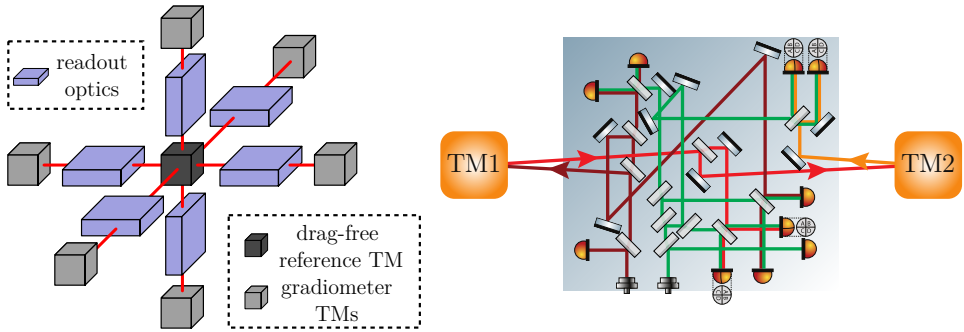


Figure 1.4: Sketches illustrating the challenge of scaling a LPF-like interferometric readout to a NGGM mission concept. The latter on the left requires the readout of up to nine TM. The LPF bench on the right comprises the readout of two. An upscaling of the concept is thus not straight-forward. Image credit right: K.-S. Isleif.

try may profit from the successful technology demonstration, as proposals for future missions called Next Generation Gravity Missions (NGGMs) are built upon the technology of optical TM readout. Their conceptual design is based on the aforementioned mission GOCE. The GOCE satellite was launched on March 17th 2009 and until November 11th 2013 mapped the static Earth gravity field with a gravity gradiometer consisting of three pairs of accelerometers. The latter were read out by means of capacitive sensing. The utilization of an optical interferometric gradiometer promises a boost in the achievable sensitivity and the extension to measurements of dynamic changes in the Earth gravity field. However, the deployment and tracking of multiple TMs by means of laser interferometry poses another technological challenge. While LPF proved the precision of its interferometer strikingly, it is not easily scalable to more TMs. Figure 1.4 shows a schematic of the LPF optical bench in direct comparison with a sketch of a possible NGGM concept. The latter comprises the utilization of seven TMs as a local gradiometer (which could be optionally linked to another satellite in GRACE-FO fashion). The LPF bench was designed for the readout of two TMs only and already exhibits the shown optical complexity. Thus alternative approaches are pursued. A promising candidate is the aforementioned interferometry technique DFMI. Its interferometric concept and its phase extraction schemes are described in the second part of this thesis. The latter also covers the efforts carried out to develop and implement two of these schemes together with proof-of-principle and sensitivity measurements.

Part I
**Investigating heterodyne phase
extraction for LISA**

Heterodyne interferometry in LISA and other applications

As mentioned in the introduction of this thesis, heterodyning is a special case of interferometry. In this chapter, it is described in more details with a focus on its phase extraction. Furthermore, its specific role in LISA is presented. To clarify the context, a summary of the key principles of LISA is given as well. Additionally, other missions and applications are discussed.

2.1 Heterodyne interferometry

A main difference between the conceptually more basic homodyne interferometry and heterodyning is the ability of the latter to track phase changes over several wavelengths or equivalently the interferometer fringes. A heterodyne interferometer can have different topologies. Here, a Mach-Zehnder setup is chosen. Figure 2.1 shows a simple generic setup. Two lasers running at different frequencies serve as light sources. In this example, frequency fluctuations are assumed to be zero. The laser beams are combined with a beam splitter and captured by photoreceivers [13]. Photoreceivers transform optical power into photocurrent which is in turn transformed into a voltage. The resulting interferometric signal or interferogram is available as an electric signal. One of the two beam paths may include a subsystem contributing to its optical path length and thus resulting in a relative phase between the two beams. Changes in the subsystem can then be tracked by extracting the phase from the interferogram. A possible quantity of the subsystem particularly important for this thesis is the displacement of TMs.

In order to understand the phase extraction schemes introduced later, it is helpful to take a look at the analytical expression of the interferogram. In order to calculate it, the laser beams will be modeled as plane waves with

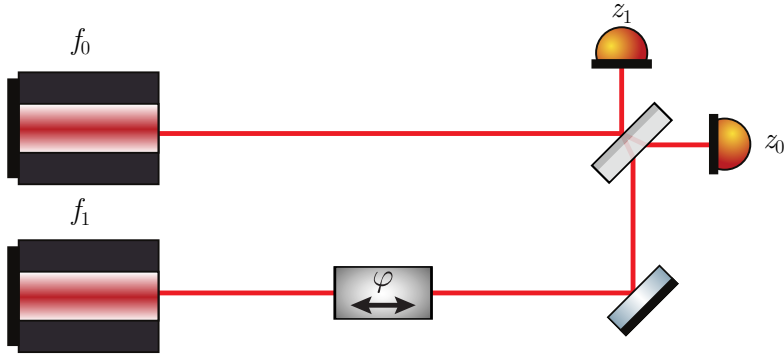


Figure 2.1: Sketch of a heterodyne interferometer measuring a generic quantity via relative phase changes. Two lasers running at slightly different frequencies are used as light sources.

nominal wavelength λ . Furthermore, a formalism is used that describes the electric field of the laser beams as the real part of a complex number. The electric fields E_0 and E_1 of the beams emitted by laser 0 and 1, respectively, at the point of detection z_0 can be written as

$$\begin{aligned} E_0(t) &= \sqrt{\tau} a_0 e^{i\omega_0 t} + \text{c.c.} \\ E_1(t) &= \sqrt{r} a_1 e^{i\omega_1 t + i\varphi} + \text{c.c.} \end{aligned} \quad (2.1)$$

where ω is the angular laser frequency, related to the laser frequency f and the laser wavelength λ via: $\lambda = c/f = 2\pi c/\omega$, with c being the speed of light. Furthermore, a_1 and a_2 represent the initial laser amplitudes. They are scaled by transmissivity τ and reflectivity r of the beam splitter. A change in the optical path length of the second beam is modeled by the phase shift φ . The beam splitter model used here is a plate beam splitter. On one of his sides it has a dielectric surface coating with refractive index lower than its bulk material but higher than air. The other side typically has an anti-reflective coating. A balanced splitting with $\sqrt{r} = \sqrt{\tau} = 0.5$ is assumed in the following.

If placed at z_0 , a photoreceiver captures the total power $P(t)$ of the beams impinging on its active surface (in the following formula described as PR). It can be computed as the integral over the combined beam intensity I , which is proportional to the squared sum of the individual electric field amplitudes. It is given by the formula

$$P(t) = \frac{cn\epsilon_0}{2} \int_{\text{PR}} |(E_0 + E_1)|^2 dA \quad (2.2)$$

where n is the refractive index of the medium and ϵ_0 is the vacuum permittivity. For a plain wave, its electric field is independent of the position on the photoreceiver and the resulting integral is a scaling factor dependent of the total size of the active area. It is normalized to 1 here for convenience. This is consistent with the practical case of a photoreceiver area exceeding the beam size. To get the power, the sum of the electric fields needs to be evaluated:

$$\begin{aligned}
 |(E_0 + E_1)|^2 &= \frac{1}{2}((a_0 e^{i\omega_0 t} + a_1 e^{i\omega_1 t + i\varphi}) + \text{c.c.})^2 \\
 &= a_0^2 + a_1^2 + a_0^2 \cos(2\omega_0 t) + a_1^2 \cos(2\omega_1 t + 2\varphi) \\
 &\quad + 2a_0 a_1 \cos(\omega_0 t + \omega_1 t + \varphi) + 2a_0 a_1 \cos(\Delta\omega t - \varphi)
 \end{aligned} \tag{2.3}$$

where $\Delta\omega = \omega_0 - \omega_1$ is called the heterodyne frequency. At this point, it is further assumed that the photoreceiver has a limited bandwidth and cannot capture signals beyond THz. Thus all terms except the time independent ones and the one including the heterodyne frequency are discarded. This leads to a power of

$$\begin{aligned}
 P(t) &= \frac{cn\epsilon_0}{2}(a_0^2 + a_1^2 + 2a_0 a_1 \cos(\Delta\omega t - \varphi)) \\
 &= \frac{P_0 + P_1}{2} + \sqrt{P_0 P_1} \cos(\Delta\omega t - \varphi) .
 \end{aligned} \tag{2.4}$$

In the last step, the single beam power was computed in analogy to the combined beams above. The final beam power on the photoreceiver now consists of the single beam power and a time dependent interference term oscillating with the heterodyne frequency. From hereon this will be referred to as the heterodyne beat note. The main measurand φ acts as phase modulation to the latter. In actual experiments, the interference term depends on the coherence of the two beams. The coherence is determined by the geometric overlap of the two beams and the matching of their beam parameters and polarizations, which are beam attributes neglected in the formalism so far. As a measure of this overlap and matching, a factor called heterodyne efficiency η_h is introduced. Finally, the total power on the photoreceiver is translated to a photocurrent i_{PR} by the receiver, and scaled with a factor called responsivity R . Furthermore, it has to be taken into account that the photocurrent is transformed into a voltage by a transimpedance amplifier (TIA). For simplicity, its transfer function is assumed to be flat with a gain

2 Heterodyne interferometry in LISA and other applications

G_A . Thus the voltage of the photoreceiver output v_{PR} can be written as

$$\begin{aligned} v_{PR} &= G_A \cdot i_{PR} = G_A R \cdot \left(\frac{P_0 + P_1}{2} + \sqrt{\eta_h P_0 P_1} \cos(\Delta\omega t - \varphi) \right) \\ &= G_A R \cdot \left(\frac{P_0 + P_1}{2} \right) \cdot (1 + C \cdot \cos(\Delta\omega t - \varphi)). \quad (2.5) \\ &= A \cdot (1 + C \cdot \cos(\Delta\omega t - \varphi)). \end{aligned}$$

The power scaling factor A is introduced alongside the commonly used interferometer property called the contrast C . The latter is closely related to η_h and is particularly useful in practical applications. It can be determined empirically via

$$C = \frac{v_{\max} - v_{\min}}{v_{\max} + v_{\min}}, \quad (2.6)$$

where v_{\max} and v_{\min} are the maximum and minimum measured voltages, respectively. A is utilized in the following to split the receiver's output signal into a static (v_{DC}) and a time-dependent (v_{AC}) part. This is written as

$$v_{PR} = v_{DC} + v_{AC} = A + \underbrace{AC}_{k_{\text{het}}} \cdot \cos(\Delta\omega t - \varphi) \quad (2.7)$$

with k_{het} denoting the heterodyne amplitude. As seen in this formula, a phasemeter for heterodyne interferometry must be able to extract the phase φ from the heterodyne beat note. It should be mentioned here, that the signal at the second beam splitter output of a photoreceiver placed at z_1 looks slightly different. The beam being reflected at a medium with higher refractive index picks up an additional constant phase shift by π [14]. This directly traverses into the receiver signal and makes the two different photoreceiver outputs complementary to each other. The signal of such a complementary photoreceiver reads

$$\bar{v}_{PR} = A + AC \cdot \cos(\Delta\omega t - \varphi - \pi). \quad (2.8)$$

Additionally, it should be kept in mind that while laser frequency noise was neglected here to explain the basic principles, it must be considered in the application of inter-spacecraft interferometry. Differential frequency and phase noise between the lasers will directly couple into the measurement. Yet even when assuming that both lasers' frequency noise is common, the individual laser frequency fluctuations can couple via unequal arm lengths, as explained later in Section 2.2.3.

This concludes the derivation of the heterodyne signals. Before going into details of the phase extraction, the next sections will discuss where, why and how heterodyning is applied in the context of this thesis.

2.2 LISA

The application of heterodyne interferometry in this work primarily aims at LISA. This section will give a description of the key LISA principles. This description is divided into several conceptual sub-parts. For details and as main reference for this, the author would like to point out the mission proposal [3]. Alternatively, [15] can be consulted. Among other things, it describes how the various aspects of the mission design influence its sensitivity estimation.

2.2.1 Free-falling test masses

As mentioned before, the goal of LISA is to measure GWs in the low frequency band (from 0.1 mHz to 0.1 Hz and above), complementary to the high-frequency band of ground-based detectors. Yet, just like the ground-based detectors, LISA aims to detect GWs by measuring their influence on the space-time geometry using test mirrors or TMs. The curvature of space-time due to GWs can be measured by tracking the tiny spatial displacement between the TMs. GWs have two polarizations, thus it is useful to measure the changes in space-time curvature along several axes. This is done by a triangular constellation formed by three spacecraft, where the displacements are measured along each side. These sides are referred to as the LISA arms from hereon. They are planned to be 2.5 million km long and the whole constellation will trail the earth on its own orbit around the sun. Furthermore, it will rotate around its center of gravity, thus it will be sensitive to different incoming polarizations at different times.

Each spacecraft contains two TMs, both with a laser link to one of the remote spacecraft. The TMs serve as geodesic references. That means they are supposed to solely follow their local geodesic curvature in free fall, without any external disturbances acting on them within the measurement band. The measured displacement between any two remote TMs can then be traced back to incoming GWs. Celestial dynamics in the solar system which change space-time curvature act significantly slower and thus do not spoil the detection.

The TMs themselves are cubes with 46 mm side length. They are made of 2 kg Au/Pt and are Au-coated, with the purpose to achieve low magnetic susceptibility and high electrostatic homogeneity on the surface. They are located in and are part of the so-called gravitational reference sensors (GRSs). One task of these systems is to directly limit disturbances. For example the residual gas motion around the TMs is reduced by a vacuum

chamber. It is designed with a high thermal conductivity assuring small thermal gradients, while special LEDs discharge the TMs to reduce electrostatic forces.

Another task of the GRS is to measure the TM position with respect to the spacecraft. This is done with an electrode housing of the TM which performs capacitive sensing. The drag-free attitude control system (DFACS) uses these measurements together with micro-newton thrusters to maneuver the spacecraft to follow the TM motion. In this way the spacecraft effectively shields the latter from external forces like for example solar radiation. The task becomes more complicated due to the fact that one spacecraft has to follow two TMs. Yet it is feasible as only the free fall along the sensitive axes and thus the line of sights between the spacecraft have to be ensured [16].

Additionally, the spacecraft itself has to be designed carefully to avoid disturbances. For example, the total mass distribution has to be balanced in order to minimize gravity gradients. The same applies to a thermal balance to avoid thermal gradients. Furthermore, sources of electro-magnetic fields should be kept sufficiently weak or should be shielded properly. All of the above-mentioned constraints are included in a requirement for the single TM residual acceleration $S_a^{(1/2)}$ with exemplary values of

$$\begin{aligned} S_a^{(1/2)} &\leq 3 \text{ fm/s}^2/\sqrt{\text{Hz}} && \text{for } f = 1 \text{ mHz} \\ S_a^{(1/2)} &\leq 12 \text{ fm/s}^2/\sqrt{\text{Hz}} && \text{for } f = 0.1 \text{ mHz} . \end{aligned} \tag{2.9}$$

The feasibility of this requirement was successfully shown by LPF [4, 5]. In order to accurately measure the TMs residual movement and their relative displacement due to GWs, LISA utilizes a heterodyne interferometric readout. It is the topic of the next section.

2.2.2 Interferometric readout

The first step for the readout of the TM motion is to break its measurement into single arm measurements. These single arm TM-TM measurements are further split into another subset of measurements. One is realized between the local TM and the spacecraft or equivalently the optical bench. Another is the long arm spacecraft to spacecraft measurement and finally a third is done between the remote spacecraft and the remote TM.

The concept for the single arm inter-spacecraft measurement with laser interferometry is called the LISA arm metrology. One important variation of it is the master-transponder scheme, which is shown in Figure 2.2. The key

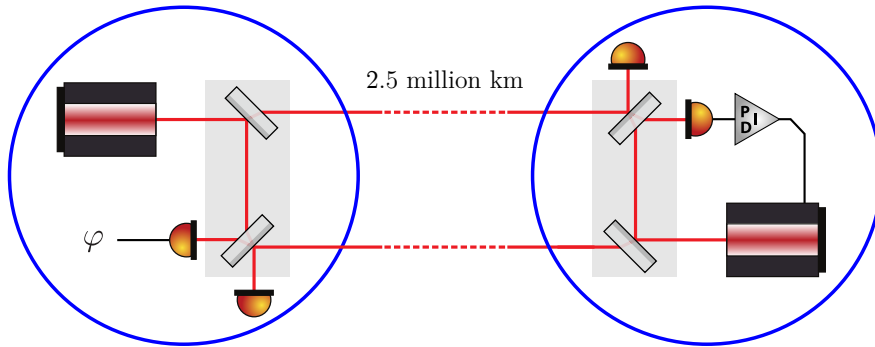


Figure 2.2: Sketch of the master-transponder scheme used for a LISA arm. A phase copy of the laser beam sent by a first (master) spacecraft is created on a second (transponder) spacecraft. Subsequently a high-power version is transmitted back to the first for the interferometric measurement.

idea is to transmit one laser beam, carrying the first spacecraft's motion in its phase, through space to the second spacecraft, where it is interfered with another laser. Similar to the example in Section 2.1, this interference already yields the desired spacecraft-spacecraft motion. Yet if left like this, it would be dominated by the differential laser frequency noise. The differential noise could be avoided by sending back a reflection of the incoming beam to the initial spacecraft and interfering it with the initial laser. However, due to the huge distances between the spacecraft and the beam's divergence, and even with the utilization of telescopes, only a small fraction of the initial power actually reaches the second spacecraft. Numbers in [3] set initial laser power to 2 W and received power to 700 pW. Reflecting back the 700 pW once more would not leave sufficient power at the master spacecraft. Thus, instead of using a direct reflection, the interference performed on the second spacecraft is used as an error signal to phase lock the local laser to the incoming beam. Hence the local laser can generate a high-power version of the incoming beam. It is sent back to the first spacecraft where it is interfered with the initial laser to obtain the desired phase information, without noise due to *differential* frequency fluctuations of the two involved lasers. Yet the single laser frequency noise has to be taken into account as well and will be discussed later in this chapter.

Contrary to the sketch in Figure 2.2, both spacecraft at either end of the LISA arms are actually identical and thus the two links back and forth are symmetric in hardware. More importantly, the measurement between the optical benches can be broken down once more into the individual measure-

2 Heterodyne interferometry in LISA and other applications

ments of those two links, and they are done by the independent photoreceivers on the different spacecraft.

It has to be considered that, while following their orbits, the involved spacecraft move towards and away from each other during the beam's propagation through space. This leads to variable Doppler shifts with alternating sign. Thus the described master-transponder interferometers will detect a heterodyne signal. At certain points the heterodyne frequency would cross a value of zero. This becomes an issue when the heterodyne beat note is readout with the associated phase extraction scheme. Both scheme and issue will be explained later in Section 2.3. To avoid it, the mentioned laser phase lock is operated with a frequency offset.

Consequentially, the Doppler shifts and the associated spacecraft orbits directly influence the required bandwidth for the beat note detection. The frequency shift is stated as ± 5 MHz. In the example above however, the beat note measured at the master spacecraft will have twice this shift. Additionally, the choice of the frequency lock offset influences the absolute required bandwidth. These will be adapted during mission time according to so-called frequency plans, as described in [15]. Nevertheless, the requirement for the phase extraction bandwidth range is fixed roughly to 5–25 MHz.

As stated earlier, it is desirable to have a GW detector with three arms for GW polarization sensitivity. In order to move from the single arm measurements to the triangular detector, it must be taken into account that the two line of sights between one spacecraft and its remote counterparts varies by $\pm 1^\circ$ according to their simulated orbits. Hence the two emitted beams from the spacecraft must be steered independently. The current mission concepts handle this so-called “breathing” by deploying two identical telescopes for independent beam steering. Additionally, two identical optical benches, each rigidly connected to one single telescope and hence also moving, are required per spacecraft. This in turn leads to the need for an optical reference between the two moving sub-systems. Referred to as the backlink, the optical reference can be transmitted from one bench to the other by fiber or free beam [17, 18]. Another approach called in-field pointing operates with one single bench only, using active steering mirrors before the telescopes to guide the beams [19]. In the following, only the proposed solution with two moving optical benches and telescopes, also called telescope pointing, will be considered. This includes the deployment of an independent laser source for each individual bench.

Finally, the total interferometric system on one of those benches comprises the reference measurement between itself and the second local bench, itself and a remote spacecraft's bench, and finally between the local TM and the

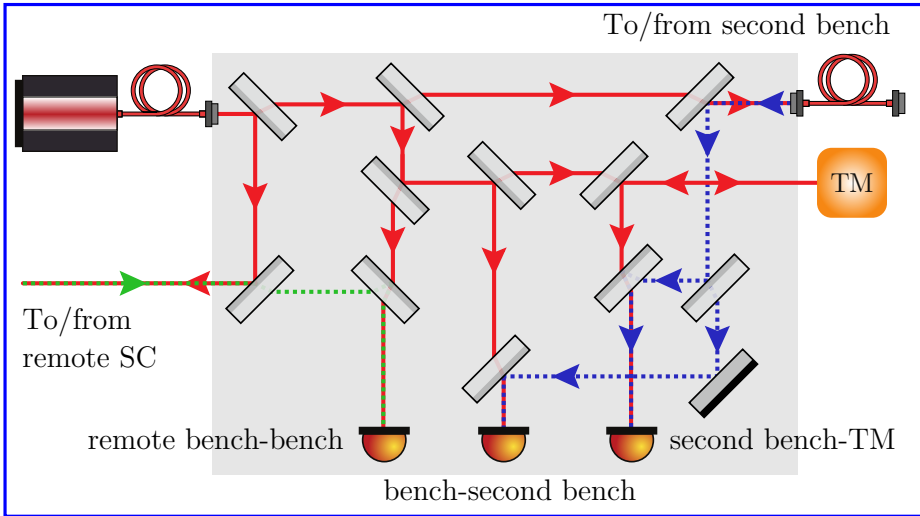


Figure 2.3: Sketch of the different interferometers on one LISA optical bench. This includes the displacement measurement between local bench and remote spacecraft bench, the reference measurement between bench and second local bench and the measurement between second local bench and local TM. The beam splitter output behavior is simplified for convenience.

second local bench. It should be noted that also the two local interferometer measurements are heterodyne, as the lasers providing light for the individual benches are controlled to exhibit different frequencies.

This design can track all relative TM displacements via combinations of the sub-measurements. A schematic of the interferometry on a single spacecraft bench is shown in Figure 2.3. The sensitivity requirement for a single TM-TM optical readout is fixed at $10 \text{ pm}/\sqrt{\text{Hz}}$ with a relaxation to lower frequencies where residual acceleration noise dominates the overall sensitivity. A maximum noise contribution of $1 \text{ pm}/\sqrt{\text{Hz}}$ is allocated to the phase extraction. With a laser wavelength of $\lambda = 1064 \text{ nm}$ used in LISA, it corresponds to a phase noise of $\approx 6 \text{ } \mu\text{rad}/\sqrt{\text{Hz}}$.

Unfortunately, a major limitation has to be taken into account caused by the aforementioned individual laser frequency noise. The next section is dedicated to this issue.

2.2.3 Laser frequency noise and TDI

The essence of the problem is that, in any interferometer, laser frequency noise couples into interferometric displacement measurements if the inter-

2 Heterodyne interferometry in LISA and other applications

ferometer arms are unequal. In LISA, two cases have to be considered where this issue of laser frequency coupling occurs.

The first is the interferometer in the master-transponder scheme. One interferometer arm is situated locally on the master spacecraft, while the second arm comprises twice the distance between the spacecraft, resulting in an arm length mismatch of the same size. Thus laser frequency noise will couple strongly into these measurements. This is in particular important for the phase readout, as explained later.

The second case takes into account a second LISA arm. The interferometry in this scenario can be considered to be a Michelson-like interferometer, with one master-transponder spacecraft pair representing one Michelson interferometer arm. Assuming equal distances between the spacecraft, the laser frequency noise measured in the two single arm measurements would cancel out once combined. However, due to the celestial dynamics affecting the motion of the spacecraft, the assumption of equal arm length does not hold. Simulations predict a changes in spacecraft distances of ± 25.000 km and hence an arm length mismatch in the Michelson-like configuration of up to 50.000 km. This leads to a coupling of the laser frequency noise into the scientific measurements.

To assess this issue more quantitatively, it will be investigated in an example. For this purpose, the beam splitter in the master spacecraft depicted in Figure 2.2 is analyzed. Instead of the local and the remote electric fields emerging on its two input ports, only their phase noises will be considered. The phase noises are denoted as $\delta\varphi_L(f)$ and $\delta\varphi_R(f)$ in the Fourier domain. Only frequency noise is assumed in this example. It translates to the phase noise via an integration or, equivalently, via a division by the Fourier frequency. For phases in units of radian, it can be written as:

$$\begin{aligned}\delta\varphi_L(f) &= \frac{\delta f(f)}{if} \\ \delta\varphi_R(f) &= \frac{\delta f(f)}{if} \cdot e^{-i2\pi f\tau} .\end{aligned}\tag{2.10}$$

In the expression of $\delta\varphi_R(f)$, the delay τ experienced in the long interferometer is modeled with the appropriate delay operator. It translates to an arm length mismatch Δl via $\tau = \Delta l/c$. Consequently the phase difference

denoted as $\delta\varphi_1$ is calculated as

$$\begin{aligned}\delta\varphi_1(f) &= \frac{\delta f(f)}{if} - \frac{\delta f(f)}{if} \cdot e^{-i2\pi f\Delta l/c} \\ &= \frac{\delta f(f)}{if} \left(1 - e^{-i2\pi f\Delta l/c}\right).\end{aligned}\quad (2.11)$$

The expression can be rewritten in terms of the displacement noise

$$\delta x(f) = \frac{c}{2\pi f_0} \frac{\delta f(f)}{if} \left(1 - e^{-i2\pi f\Delta l/c}\right) \quad (2.12)$$

where f_0 is the average laser frequency. For equal arms or $\Delta l = 0$ the frequency noise would cancel. For $\Delta l \ll 1$, the expression can be linearized. This leads to a formula commonly used in laboratory experiments:

$$\delta x(f) = \frac{\Delta l}{f_0} \delta f(f). \quad (2.13)$$

However as mentioned, the master transponder scheme exhibits an arm length mismatch of twice the distance between the spacecraft, hence $\Delta l = 5 \times 10^9$ m.

The same calculation can be applied in analogy to the Michelson-like interferometer described above with $\Delta l = 50 \times 10^6$ m. The Fourier frequencies of the associated delays $f = c/\Delta l$ are in the LISA measurement band. That means that within the LISA band, the factor in brackets in Equation (2.12) varies between total mitigation and doubling of the laser frequency noise. Using it to compute an upper limit, laser sources would need to exhibit laser frequency stabilities of $\delta f_{\text{req}} < 3 \times 10^{-6} \text{ Hz}/\sqrt{\text{Hz}}$ at 1 Hz in order not to limit the readout budget. This value is far from what space-qualified state-of-the-art lasers can provide. Hence another solution was pursued.

The efforts resulted in the development of the post-processing technique called TDI [20, 21]. It takes advantage of the fact that multiple phase measurements are taken simultaneously throughout the LISA constellation. The method applies individual time delays in post-processing to the different phase measurements in order to cancel laser frequency noise while preserving scientific signals. A simple example based on [21] will illustrate the basic idea. It utilizes the unequal-arm-length-Michelson-like interferometer like in the LISA arms. The spacecraft at the mutual node serves as the master to the two transponder spacecraft. Hence two phase difference measurements φ_1 and φ_2 can be conducted on the master spacecraft. The concept of TDI can be intuitively shown in the time domain. Assuming the two laser sources

2 Heterodyne interferometry in LISA and other applications

for both arms are locked and assuming an individual frequency noise δf for the master laser, the two phase measurements can be written as

$$\begin{aligned}\varphi_1(t) &= \int (\delta f(t - 2\tau_{L1}) - \delta f(t)) dt + h_1(t) \\ \varphi_2(t) &= \int (\delta f(t - 2\tau_{L2}) - \delta f(t)) dt + h_2(t).\end{aligned}\tag{2.14}$$

Here, h_1 and h_2 model signals due to a passing GW and should be preserved. τ_{L1} and τ_{L2} denote the one way delays to the transponder spacecraft 1 and 2, respectively. Combining both measurements for the Michelson-like interferometric combination yields:

$$\varphi_1(t) - \varphi_2(t) = \int (\delta f(t - 2\tau_{L1}) - \delta f(t - 2\tau_{L2})) dt + h_1(t) - h_2(t).\tag{2.15}$$

Obviously the expression is still dominated by laser frequency noise. In the TDI post-processing technique, time delays are applied to the two different measurement streams. The basic idea is to shift each single arm measurement with the delay of the other and subsequently calculate a second interferometric combination. This is later recombined with the initial combination. Putting the first step in formula leads to

$$\begin{aligned}\varphi_1(t - 2\tau_2) - \varphi_2(t - 2\tau_1) &= \int (\delta f(t - 2\tau_{L1} - 2\tau_{L2}) - \delta f(t - 2\tau_{L2})) dt \\ &\quad - \int (\delta f(t - 2\tau_{L2} - 2\tau_{L1}) - \delta f(t - 2\tau_{L1})) dt \\ &\quad + h_1(t - 2\tau_2) - h_2(t - 2\tau_1) \\ &= \int (\delta f(t - 2\tau_{L1}) - \delta f(t - 2\tau_{L2})) dt \\ &\quad + h_1(t - 2\tau_2) - h_2(t - 2\tau_1).\end{aligned}\tag{2.16}$$

As the cross terms cancel out, the frequency noise appears like it does in the initial combination. Consequentially subtracting Equation (2.15) and Equation (2.16) leads to:

$$\begin{aligned}(\varphi_1(t) - \varphi_2(t)) - (\varphi_1(t - 2\tau_2) - \varphi_2(t - 2\tau_1)) \\ = h_1(t) - h_2(t) - h_1(t - 2\tau_2) + h_2(t - 2\tau_1).\end{aligned}\tag{2.17}$$

The last expression is free of laser frequency noise and still contains the GW signals, yet with an effective transfer function.

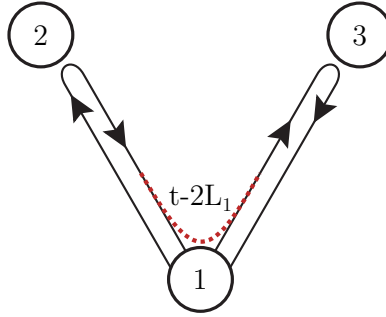


Figure 2.4: Illustration of a geometric interpretation for TDI. Adding a delayed version of the 1-3 arm measurements extends the 1-2 arm measurement to a round trip. Based on [22].

A more geometric interpretation of the method is given in [22] and illustrated in Figure 2.4. Subtracting the time delayed single arm measurement of arm 2 from the undelayed version of arm 1 can be interpreted as extending the initial beam path of the latter along arm 2, creating a round trip. The same can be done the other way around. The expression can be taken literally for the resulting second round trip. This reinterpretation of (2.17) is also called a zero-area Sagnac interferometer. In this form it is easy to see that both beams experience the same delay in their respective round trip. Thus effectively an equal-arm-length interferometer was synthesized.

It should be noted that this example only gives the principle idea of TDI. For the actual application in LISA, an advanced algebra has been developed and is still in development. In particular the modeling of moving spacecraft poses a mathematical challenge. For further studies the author refers to [12, 21, 22]. Nevertheless another aspect of TDI should be emphasized at this point. With the availability of all six separate single link measurements (two for each arm) and the possibility to combine them differently but simultaneously in post-processing, LISA can be thought of as an entire array of gravitational wave detectors. For example, [21] shows how the sensitivity for a certain GW source can be improved by “picking” the optimal synthesized detector. Additionally, a Sagnac combination with round trips along the three sides of the LISA triangle can permanently serve as a tool to characterize the instrument noise as it is mostly insensitive to GWs. This way, TDI can be regarded not just as a necessity to get rid of laser frequency noise, but also as an enrichment.

Finally it should be emphasized that independent of TDI, laser frequency noise will still occur in the single arm measurements and needs to be handled

by the phase extraction.

In addition to the laser frequency noise, yet another limiting noise source needs mitigation, namely clock noise or clock jitter. The next section will discuss this topic.

2.2.4 Clock noise in LISA

In the last section, $\varphi(t)$ described data streams of phase measurement with a continuous time dependency. In practice, these streams are given in discrete samples. The initial samples being processed later are generated by analog-to-digital-converters (ADCs) connected to the photoreceivers. ADCs require a trigger signal, here given by a clock. Real clocks come with an uncertainty concerning their stability, leading to ADC samples not taken in equidistant time steps. For a timing offset Δt with respect to an ideal clock, a measured beat note as derived in Equation (2.7) can be written as

$$\begin{aligned} v_{AC} &= k_{\text{het}} \cos(\Delta\omega(t + \Delta t) - \varphi) \\ &= k_{\text{het}} \cos(\Delta\omega t + \underbrace{\Delta\omega\Delta t}_{\varphi_{\text{err}}} - \varphi). \end{aligned} \quad (2.18)$$

The expression shows that a direct phase error φ_{err} occurs which scales with the heterodyne frequency $f_{\text{het}} = \Delta\omega/2\pi$. Clock noise, given as \tilde{q} with units of $\text{s}/\sqrt{\text{Hz}}$ and with the tilde denoting the amplitude spectral density (ASD), can likewise be directly translated into the ASD of φ_{err} as

$$\tilde{\varphi}_{\text{err}} = 2\pi\tilde{q}f_{\text{het}}. \quad (2.19)$$

For a 25 MHz beat note, the clock noise would need to be below $40 \text{ fs}/\sqrt{\text{Hz}}$ in order not to exceed its budgeted contribution to the required readout sensitivity given in Section 2.2.2. At the time this thesis was written, no space-qualified clocks were available that would meet these specifications.

An approach to correct for the phase errors induced by clock noise is to measure it first and subtract it in post-processing. Yet, following the description in [23], this can be thought of as a pre-processing step for the laser frequency noise removal by TDI¹. The measurement itself is performed by imprinting an amplified version of the local clock noise onto a local laser's sidebands. Those are transmitted to the remote spacecraft, where they are interfered with the remote laser's sidebands. On each one of the remote

¹Other approaches exist that apply the clock noise correction *after* the laser frequency noise removal.

spacecraft, the resulting signal yields the noise of both involved clocks in a differential measurement. This system is again planned to be symmetric in terms of hardware for the whole constellation. Details of the implementation will be given in Section 2.2.7. During post-processing, the separate clock noise measurements can be used to remove the aforesaid clock noise from the phase measurements. One way to do so is shown in [12, 23, 24]. There, one of the clocks is set as an ideal, noiseless reference or master clock. Consequently the two differential sideband measurements performed with the reference clock can be treated as direct measures of the respective clock noise of the non-ideal clocks. Finally this information can be used to generate clock-noise-free data streams applicable for the mentioned TDI algebra.

Besides the clock noise removal, yet two additional pre-processing steps involving the sub-measurements will be shown in the next section for completeness.

2.2.5 Optical bench motion and local laser frequency noise

Before the removal of laser frequency noise and clock noise can take place, two more processing steps have to be performed. One is the reduction from two to one laser frequency noise source per spacecraft, sometimes referred to as the removal of “primed” laser noise [23, 24]. The other is the cancellation of optical bench movement.

Both steps can be understood in an intuitive way. The first utilizes the difference between the reference interferometers on both benches per spacecraft. After all they serve for the purpose of having an optical reference between the spacecraft benches. The second uses the difference between reference and test mass interferometers on each spacecraft. This way the test mass motion can be isolated and the optical bench motion is bypassed.

While all previously described processing steps involved combining the different data streams, it is also necessary to know “when” and “where” those were sampled. This is the topic of the next section.

2.2.6 Clock synchronization and arm-length determination

In order to be able to apply the correct delays in TDI as described in Section 2.2.3, the absolute distance between the spacecraft has to be known up to a certain accuracy. The same applies to the timestamps of the raw phase measurements, or to be more precise, the relative mismatch of timestamps on different spacecraft. Such a mismatch is caused by clock offsets or biases and translates directly into an error in the absolute distance esti-

2 Heterodyne interferometry in LISA and other applications

mation. Likewise, the correct estimation of clock noise from the sideband measurements is disturbed.

At this point, the differentiation between clock noise or clock jitter on one side and clock offset or clock bias on the other should be clarified. While the first couples directly into the phase measurements as shown in Equation (2.19), the latter limits the performance of the post-processing due to uncertainties in the mentioned timestamps or unsynchronized clocks. While for the first, effective stabilities of $40 \text{ fs}/\sqrt{\text{Hz}}$ within the LISA band would be required, the clock offset needs to be known with an accuracy of some dozens of nanoseconds.

To avoid the errors due to aforesaid distance and timestamp uncertainty, a measure of the absolute spacecraft distances as well as for the clock offsets is required. The first is implemented by a ranging technique measuring the time of flight of pseudo random number (PRN) codes modulated on the laser sidebands. It is described in more detail in Section 2.2.7. Besides the absolute distances, this measurement also includes information about the clock offset, as the PRN codes need to be re-sampled by the receiving spacecraft's clocks. A late sample can be interpreted as an increased distance and vice versa. However, this means both measures cannot be distinguished easily. In order to decouple them, a Kalman-like filter has been developed [25]. A brief description of the functionality of a Kalman filter is given within a different context in Section 7.2. The filter here uses simulations of orbits to model the behavior of the state variables position, velocity, clock jitter and clock frequency jitter on each spacecraft. For improved estimations, predictions of those are combined with multiple measurements in a Kalman-like fashion. The latter include the ranging measurements, the optical bench to remote optical bench displacement measurements as well as the differential sideband-sideband measurements for each spacecraft. Rough initial values are given by the Deep Space Network (DSN) with uncertainties of $\approx 20 \text{ km}$. It has been shown in simulations, that with state of the art ranging accuracies, the filter itself can provide sufficient clock synchronization and distance estimations.

While for better comprehensibility, the removal of laser frequency noise was described first in this thesis, it is not the first step of the post-processing. In fact, the succession of processing steps is opposite to the order in which it was presented here². Furthermore it should be added, that after TDI is applied to synthesize virtual interferometers, similar data analysis techniques

²Alternatively, the sequence of clock noise removal and laser frequency noise removal is switched, see above.

as in ground-based detectors can be utilized to search for GWs in the data streams of the different TDI combinations.

To be able to perform all the post-processing steps properly, some technical prerequisites, like for example a sufficiently accurate ranging scheme, have to be met. They will be discussed in the next section.

2.2.7 Prerequisites for TDI

As mentioned earlier, a measurement of the absolute spacecraft distance needs to be implemented. This is done in LISA by a ranging scheme based on PRN codes. The working principle is explained exemplary for one link only in the following. A local PRN code is imprinted on the laser beam as a phase modulation via an electro-optical modulator (EOM). It is transmitted to the remote spacecraft and is demodulated. The recovered PRN is subsequently compared with a delayed version of the remote PRN code for correlation. Only a correct delay applied to the latter will result in correlation. The applied delay gives a measure of the time of flight and hence the inter-spacecraft distance. This process is performed in a closed feedback loop for automatic delay estimation which is called a delay-locked loop (DLL). Different experimental proofs of the principle have been performed [24, 26, 27].

Besides the PRN codes, also the clock noise is supposed to be imprinted on the laser for distribution to the remote spacecraft. For this purpose, the tone of an oscillator serving as clock tone and running at 2.4 GHz is combined with the PRN code prior to the phase modulation via the EOM. Locally, the clock tone is downsampled to 80 MHz to generate the ADCs sampling clock. While Section 2.2.4 stated that an amplified version of the clock noise is sent to the remote spacecraft, technically the situation is different. The clock noise is actually transmitted directly while the divided version for the local ADCs is effectively attenuated by the frequency division. The attenuation can be explained by the fact that timing jitter is preserved even when the clock frequency is divided. Nevertheless, the basic idea of transmitting an amplified version of the local clock noise remains valid.

Connected to this topic is the removal of ADC jitter. Like unstable clocks, real ADCs introduce a sampling jitter coupling into the phase measurements of individual phasemeter channels. Thus even if assuming perfect clocks, the ADC jitter would lead to sampling jitter. To mitigate the coupling, a common reference signal called the pilot tone is added to the wanted signals. The differential phase errors of these references, measured between channels of one phasemeter, are then primarily caused by the ADC jitter. They can

thus be measured and subtracted from the wanted signals. This correction can be done in real-time and hence is already included in the raw data streams. In LISA, the pilot tone is derived from the 2.4 GHz clock tone with high phase fidelity [15]. This way it relieves the local clock generation of the requirement of high phase fidelity, as the pilot tone reference measurements include and correct for the errors occurring in the downconversion. Together with the clock tone transfer, it hence serves as an inter-spacecraft pilot tone.

Another prerequisite for TDI follows from the first case considered in Section 2.2.3 for the laser frequency noise acting in LISA. As shown, the data stream of a single arm measurement will exhibit fluctuations up to two times the laser frequency noise. A phase extraction or readout device needs to be able to conserve the scientific phase measurement despite these high signal dynamics. Only then can the scientific phase be recovered in post-processing. The associated characteristic of the readout is what is commonly called dynamic range. Here it describes the ratio between the maximum phase signal dynamics and the readout's precision. Figure 2.5 shows a plot of an exemplary laser frequency noise curve used as target of the measurements performed in this thesis. It is plotted together with its associated phase noise coupling (according to Equation (2.12)) and the phase extraction requirement, revealing a required dynamic range of 8–10 orders of magnitude. To accommodate for the aforementioned relaxation due to residual TM acceleration noise, the following noise shape function (NSF) is applied to the phase extraction requirement:

$$\text{NSF}(f) = \sqrt{1 + \left(\frac{2.8 \text{ mHz}}{f}\right)^4}. \quad (2.20)$$

Being a keystone for a working TDI and also the focus of this thesis, the phase extraction for the LISA metrology system will be discussed in the next section.

2.2.8 Phase extraction and metrology requirements

While the last section described the key principles of LISA, this section will summarize the resulting requirements for the phase extraction and metrology. In the context of this thesis, the expression phase extraction refers to the pure determination of the phase in a signal like Equation (2.18). A device which implements this method is consequently called phasemeter. In LISA, the phase extraction is embedded in the overall metrology system, which will cover also auxiliary functions, for example for ranging and

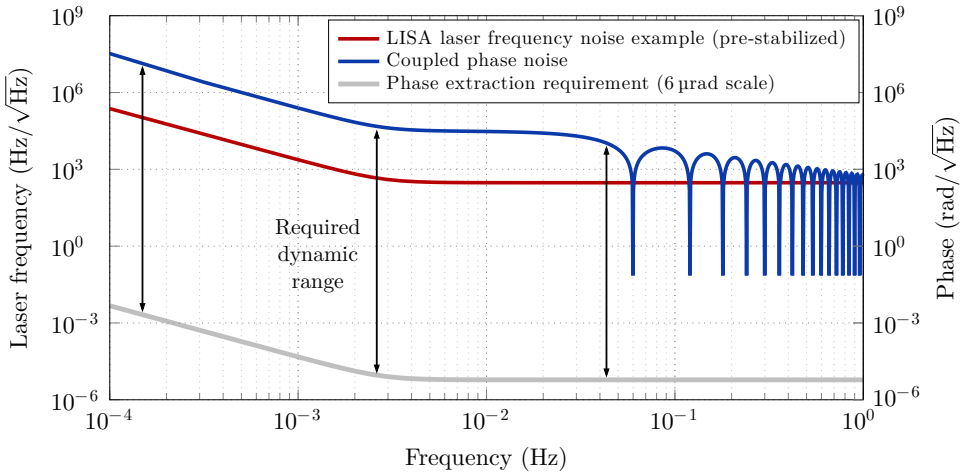


Figure 2.5: Plot of laser frequency noise coupling into phase. It allows the estimation of the required dynamic range for the phase extraction.

clock noise transfer. The device which comprises all these functionalities is referred to as LISA phasemeter in the following.

A list will serve as summary for the main requirements for the LISA phasemeter. It should be noted that some of them refer to requirements of the whole metrology system, which includes other components, like EOMs, as well. As done in prior sections, the actual values are taken from [3] and are likely to change in the future.

- **Phase noise contribution:** the phase noise contribution of a single LISA phasemeter channel to the overall displacement readout noise needs to be less than $1 \text{ pm}/\sqrt{\text{Hz}}$ or correspondingly $\approx 6 \text{ } \mu\text{rad}/\sqrt{\text{Hz}}$. The NSF stated in Equation (2.20) applies.
- **Pilot tone:** the ADC jitter has to be removed from the phase measurements by applying a pilot tone. It furthermore serves as a reference for the local clock generation. Therefore it has to be derived with high phase fidelity from the 2.4 GHz clock tone and must be added to the wanted signals without a differential error. Its performance requirement is directly woven into the phase extraction requirement above.
- **Dynamic range:** for a working TDI, the LISA phasemeter needs to be able to deliver performance even with high input signal dynamics.

2 Heterodyne interferometry in LISA and other applications

Different models of expected laser frequency noise lead to a requirement for dynamic range of roughly 8–10 orders of magnitude within the LISA band.

- **Bandwidth:** the operating bandwidth of the LISA phasemeter is determined by the expected Doppler shifts due to spacecraft orbits as well as the planned frequency offsets. It is fixed to the range of 5–25 MHz.
- **Auxiliary functions for ranging:** in order to obtain the absolute spacecraft distances, the LISA phasemeter will implement necessary functions. This comprises the generation of PRN codes as well as the determination of the time of flight delays. The overall ranging resolution needs to be below 1 m.
- **Auxiliary functions for data transfer:** a feature neglected so far is data communication between the spacecraft. For this purpose, data bits are combined with the PRN codes before transmission. The LISA phasemeter provides de- and encoding of these bits. Desired data rates are 15 kbit s^{-1} bidirectionally.
- **Auxiliary functions for clock tone transfer:** the 2.4 GHz oscillator is transmitted directly to the remote spacecraft, while the LISA phasemeter runs at 80 MHz. Thus it needs the capability to divide the GHz signal. Like for ADC jitter suppression, requirements for the clock jitter suppression are woven into the phase extraction requirement.
- **Auxiliary functions for laser locking:** the laser locks for creating a local phase copy of the remote laser require a sensor, a servo and an actuator. Those are to be implemented partially by the LISA phasemeter.

In the scope of this thesis, the focus lies on the main functions directly connected to the phase extraction. These are phase extraction performance, dynamic range and bandwidth.

The next section will present a prototype that aims for the achievement of the requirements summarized in the table. It will be used as a concrete example of heterodyne phase extraction, while its concepts can be generalized.

2.3 Phase extraction with a LISA phasemeter

The key concepts for heterodyne phase extraction will be discussed here in the context of the LISA phasemeter. An elegant breadboard (EBB) model was implemented within a technology development activity initialized by the European Space Agency (ESA). The efforts and results were published under the activity name “LISA Metrology System” [28]. Contributors included the National Space Institute of the Danish Technical University (DTU Space), the Danish industry partner Axcon Aps. and the Albert Einstein Institute (AEI). Besides the cited publication, [29] comprises many of the conducted measurements as well as a detailed description of concepts and hardware utilized in this thesis. Consequently, only a summary of those will be given here.

2.3.1 EBB phasemeter overview

To literally get a picture of the device, Figure 2.6 shows an image of the EBB of the LISA phasemeter. It is set up in a modular fashion and consists of a mainboard connected to several daughterboards. The main board itself is populated with power supplies, a field programmable gate array (FPGA) called bridge which bundles traffic from the daughterboards, an FPGA with dedicated processing power for fast Fourier transforms (FFTs), a central processing unit (CPU) for additional data filtering and the interfacing with an external client computer. Furthermore, there are six slots for ADC and digital-to-analog-converter (DAC) cards plus one for a clock module. The ADC cards come with an analog front end, the ADCs and an FPGA for signal processing. The DAC cards, in turn, cover an FPGA for signal generation, the DACs themselves and an analog back-end. Finally, the clock module is equipped with divider and filter electronics for clock and pilot tone distribution.

In the following, the functionality will be explained ignoring the structural separation in terms of hardware.

2.3.2 Heterodyne phase extraction core

The core of the LISA phasemeter is an all-digital phase-locked loop (ADPLL). It was selected over other methods as the baseline in LISA. For the sake of completeness, the alternatives will be briefly discussed in Section 2.5.4. As suggested by its name, an ADPLL is a feedback loop operating in the digital domain [30]. Yet its working principle is similar to its analog

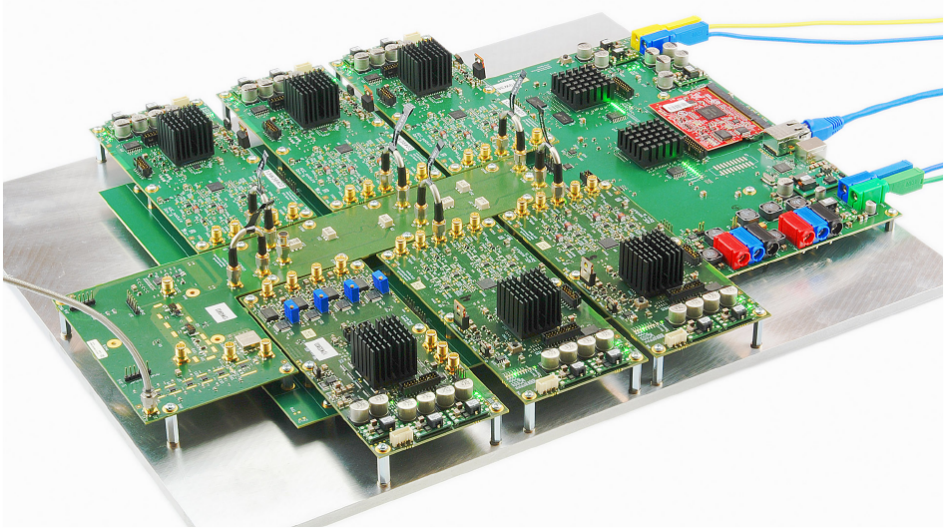


Figure 2.6: Photograph of the LISA phasemeter EBB. In this specific configuration, the mainboard is connected to five ADC cards and one DAC card.

counterpart. Conceptually, it phase-locks a local oscillator to an incoming external signal, effectively creating a local copy. The frequency and phase values used to generate the local copy are digitally accessible and can thus be read out. Figure 2.7 shows an overview of the conceptual design. It can be split into the following components: phase detector, servo and numerically controlled oscillator (NCO). Additionally, an amplitude detector can be implemented, which is done for the LISA phasemeter. The description starts with the NCO. It serves as the local oscillator and consists of a phase increment register (PIR), a phase accumulator (PA) and a look-up table (LUT). The PIR register determines the frequency, which is the increment of the phase. The second register accumulates or integrates the PIR value to obtain the phase. The phase is finally used as input for the LUT. A LUT in general stores arbitrary function values $y(x)$ that can be addressed by using the input x . In the application at hand, the function $y(x)$ is a sinusoid.

The phase detector compares the external and the local signal and calculates a phase difference. This is achieved by mixing both. For a mathematical model, the incoming signal is assumed to be similar to the AC part of the photoreceiver signal derived in Equation (2.7). The local NCO is set to an amplitude of 1 and a frequency ω_{lo} defined by the PIR. Furthermore, the functions are modeled as continuous in time and amplitude for simplicity.

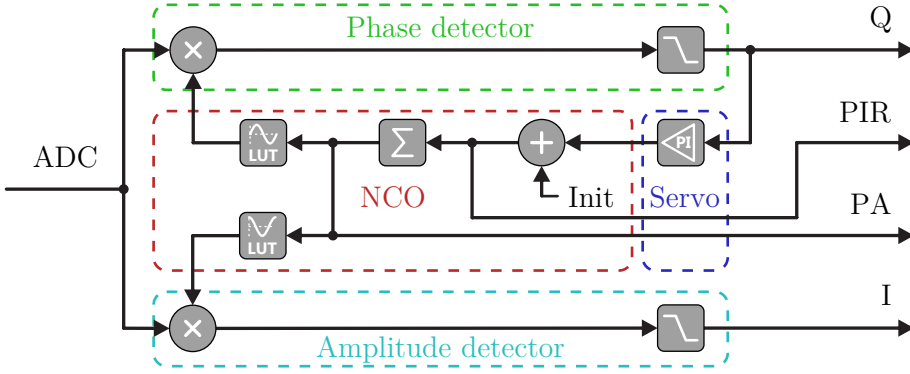


Figure 2.7: Schematic of an ADPLL. A feedback loop is implemented via a phase detector, a servo and a NCO. Not essential for the phase extraction is an optional amplitude detector.

Finally, the process can be written as

$$\begin{aligned}
 Q &= k_{\text{het}} \cos(\omega_{\text{het}}t - \varphi) \cdot \sin(\omega_{10}t) \\
 &= \frac{k_{\text{het}}}{2} \{ \sin(\omega_{10}t - (\omega_{\text{het}}t - \varphi)) + \sin(\omega_{10}t + (\omega_{\text{het}}t - \varphi)) \} .
 \end{aligned} \tag{2.21}$$

The mixing product is labeled Q , which stands for “quadrature”. As the two mixed trigonometric functions exhibit a $\pi/2$ phase relationship in an ideal case, their two complex phasors can be thought of as spanning a square which has a “quadratic” shape. At this point, it is assumed that the NCO is already adjusted to the incoming frequency. This means phase differences are small. In order to achieve this, proper initialization values within the NCO have to be set. With $\sin(x) \approx x$ for $x \ll 1$ the expression becomes

$$Q \approx \frac{k_{\text{het}}}{2} \{ \varphi + \sin(2\omega_{\text{het}}t - \varphi) \} . \tag{2.22}$$

The next assumption is to neglect the second harmonic. This is attributed to a filter following the mixer, which is designed to suppress the second harmonic. Nevertheless, it should be noted that the system can also work without the dedicated filter, as the closed loop features a low-pass-like transfer function [29]. Yet, the lower the heterodyne frequency gets, the more stringent the requirement to the suppression becomes, ultimately down to an inoperable loop at DC. This is the issue for LISA mentioned in Section 2.2.2.

Finally, neglecting the second harmonic, the phase detector output can be written as

$$Q = \frac{k_{\text{het}}}{2} \varphi . \tag{2.23}$$

With a constant amplitude in a first order approximation, a measure of the phase difference of incoming signal and NCO is obtained. In the formalism here, it coincides also with the optical phase difference. Nevertheless, it can be generalized to describe the phase difference between the local oscillator and an arbitrary harmonic input. Thus it is referred to as loop phase error. The same generalization applies to the amplitude of the signal. The latter was treated as constant as its absolute fluctuations are small compared to the phase which fluctuates around zero in locked state.

The phase detector output is subsequently used as servo input. The specific servo for the LISA phasemeter is implemented as a proportional-integral (PI) servo. Its parameters can be adjusted during runtime. The servo output serves as the actuator signal of the loop and drives the frequency of the NCO or local oscillator. Its output is transmitted to the phase detector, effectively closing the loop. An important loop quantity is the overall open-loop gain $G(f)$, which is determined by its individual components and in particular the servo. Additionally, Equation (2.23) shows that it is also proportional to the amplitude. The open-loop transfer function or gain $G(f)$ affects the two functions called closed-loop transfer function $H(f)$ and loop error function $E(f)$. These are commonly used in control theory and can be written as

$$\begin{aligned} H(f) &= \frac{G(f)}{1 + G(f)} \\ E(f) &= 1 - H(f) = \frac{1}{1 + G(f)}. \end{aligned} \tag{2.24}$$

Loosely speaking, the first gives a measure or factor of how noise added inside the loop to the error signal is suppressed. The second describes the ability of the loop to track the incoming phase and gives a factor of how the phase error between input signal and NCO is suppressed.

While this description summarizes the basics of phase extraction via the ADPLL, the devil is in the detail. A more comprehensive model of the loop is presented in [29, 31].

With a locked loop, the value of the PIR serves as the central measurand of the ADPLL³ and is sent to a client PC after prior downsampling. The downsampling is implemented by a cascaded integrator comb (CIC) filter as first stage in the FPGA and a finite impulse response (FIR) filter as second stage in the CPU. In the example above, integration of the PIR data yields the desired optical phase.

³It should be noted here specifically that the ADPLL tracks the *instantaneous* frequency and the *instantaneous* phase of the input signal in the PIR and the PA register, respectively.

Other outputs of the ADPLL are the PA values, Q and I . The first is not sent directly to the client PC, as it exhibits overflowing numbers. Yet it can be used to calculate differential phases between ADPLLs sampling similar signals. This is utilized in the technique differential wavefront sensing (DWS), which will be introduced later in this section. While Q provides a diagnostic value in terms of the loop phase error, I is the output of the amplitude detector. It can be calculated similarly to Q . A copy of the NCO output is shifted by $\pi/2$ and fed to a second mixer.

$$\begin{aligned}
 I &= k_{\text{het}} \cos(\omega_{\text{het}}t - \varphi) \cdot \cos(\omega_{\text{lo}}t) \\
 &= \frac{k_{\text{het}}}{2} \{ \cos(\omega_{\text{lo}}t - (\omega_{\text{het}}t - \varphi)) + \sin(\omega_{\text{lo}}t + (\omega_{\text{het}}t - \varphi)) \} \quad (2.25) \\
 &= \frac{k_{\text{het}}}{2} \cos(\varphi) \stackrel{\varphi \ll 1}{\approx} \frac{k_{\text{het}}}{2}.
 \end{aligned}$$

As two phasors with ideally identical phase are mixed here, the quantity is called I like “in-phase”.

This concludes the conceptual description of the ADPLL. Its actual implementation for the LISA phasemeter is conducted with FPGAs. These are preferred over a software solution due to the expected heterodyne frequencies in the MHz regime and the need for parallel multi-channel processing.

Besides the main ADPLL, another copy is implemented for a single phasemeter channel to track the pilot tone which is required to mitigate ADC or timing jitter. Ideally, the pilot tone frequency is chosen higher than the desired signal in order to amplify the phase error induced by timing jitter. For example, many measurements presented in this thesis were conducted with a 38 MHz pilot tone. It should be noted that this value may be higher than the system’s Nyquist frequency as the phase error is not affected by aliasing. The phase measured with the pilot tone ADPLL φ_{pt} can then be subtracted from the uncorrected main signal φ_{m} to obtain a signal $\varphi_{\text{m,cd}}$ free of ADC jitter. This can be described as

$$\varphi_{\text{m,cd}} = \varphi_{\text{m}} - \varphi_{\text{pt}} \frac{f_{\text{m}}}{f_{\text{pt}}} \quad (2.26)$$

where f_{m} and f_{pt} are the base frequencies of the main signal and the pilot tone, respectively. A higher phase noise is measured with a higher pilot tone frequency. Thus it needs to be rescaled in the formula⁴. In the experiment

⁴For differential measurements between two phasemeter channels with the pilot tone correction performed in post-processing, it turned out that it is more practical to compute the differential pilot tone correction first and subtract it from the difference of the main signals subsequently.

2 Heterodyne interferometry in LISA and other applications

presented in this thesis, the pilot tone computations were performed on the client PC. In LISA, it could be beneficial to do the computations on-spacecraft in order to save precious bandwidth for the communication to Earth.

Prior to the phase extraction via the described scheme, the input signal needs to be converted from the analog to the digital domain. This conversion is done by ADS6445 ADCs from Texas Instruments. They are embedded in analog circuitry which also provide signal conditioning and the pilot tone addition. In the current version, four phasemeter channels are implemented on one ADC card using one four-channel ADC chip and one FPGA. A single analog channel consists of a gain and a buffer stage and a differential amplifier. The latter not only generates a differential signal necessary for the ADCs but is also used to add the pilot tone. As a final note, the four channels of one ADC card are expected to sample the four segments of a quadrant photoreceiver (QPR) in order to implement a technique called DWS [32]. It allows the determination of a differential wavefront mismatch between two beams using the phase differences between the signals from QPR segments. This presents an ideal application for the aforementioned PA output, as all four channels are driven by the same optical heterodyne signal.

2.3.3 Clock and pilot tone generation

As explained in Section 2.2.7, the phasemeter/ADC clock and the pilot tone need to be generated from the spacecraft's 2.4 GHz oscillator, where the latter generation has to be performed with high phase fidelity. The clock module serves for that purpose. It takes the oscillator signal as input and uses two divider chains to generate an 80 MHz clock as well as an 75 MHz pilot tone. The latter is subsequently low-pass-filtered to isolate the fundamental harmonic from the formerly rectangular signal⁵.

2.3.4 Digital servo for laser locking

To obtain an error signal for the locking of the lasers in LISA, a copy of the PIR signal is transferred to the FPGA on the DAC card. In the current implementation, PI servos are implemented to generate two actuator signals.

⁵Most of the measurements in this thesis utilizing the EBB were conducted without the clock module but with an on-board 80 MHz clock and a pilot tone generated by an external signal generator. This offered more flexibility for the pilot tone and kept the setup simpler while using a single phasemeter.

A single PI servo is used for a fast control loop, while a second one is connected to a copy of the output of the first servo for a slow one. This scheme was developed to control the non-planar ring oscillator (NPRO) lasers from the company Coherent and is explained later in Section 4.1.2 in more detail.

2.3.5 PRN generation and recovery

The generation of PRN codes takes place in the FPGA on the DAC card. Likewise, the data for inter-spacecraft transmission is woven into the codes here. The combined signal is fed to the DACs. In order to compute the delay of the received remote codes, the FPGAs on the ADC cards contain additional digital logic. Assuming the detection of a single beat note with all four channels of the card by using a QPR, the phase error Q of all channels can be summed up to recover the PRN codes. The Q values contain the codes as the sharp phase modulation cannot be compensated fast enough by the ADPLLs. The sum is subsequently fed into two DLLs. Two are required, as each beat note contains two codes, one for each single laser beam. It should be noted that the codes for the six different lasers throughout the LISA constellation are designed specifically not to influence each other [33]. For the spacecraft-to-spacecraft interferometer beat note, one of the single laser beams originates from the local spacecraft while the other is received from the remote spacecraft. Hence the two DLLs compute the delays of the local and the remote code, with the latter yielding the important ranging information.

2.3.6 Clock tone readout

The clock tones for the determination of the differential clock noise are tracked in the FPGAs on the ADC cards as well. Additional sideband ADPLLs are implemented for this purpose. They are fed by the sum of all four sampled time series. In comparison to the main phase extraction, the sideband ADPLLs have to cope with the weaker signal amplitude of the sidebands. Nevertheless, their required bandwidth can be reduced by utilizing the frequency measurements of all main ADPLLs. Taking into account the known frequency offset, which is typically set to 1 MHz, the sum of the main ADPLLs can be used as a feed forward signal for the PIRs of the sideband ADPLLs. This relieves them from tracking the laser frequency noise. The sideband phases are cleaned from ADC jitter and its data is decimated and transmitted to the client computer in a similarly

fashion as done for the main phases and data.

After describing the conceptual parts of the phasemeter which are important for the LISA metrology chain, a step back is taken to examine the phase extraction and noise sources that can limit the measurements.

2.4 Noise sources for the phase extraction

This section gives an overview of some known noise sources that can influence and limit the phase extraction performance [29, 31, 34]. The techniques to detect and quantify them are discussed later in Chapter 3. The many noise sources leading to phase noise can be categorized in different ways. One example would be to classify them in terms of their physical source, like temperature fluctuations or amplitude noise. A second possibility is to sort them according to the point of coupling, and yet another to classify them by the coupling mechanism. While for the testing schemes described later it appears useful to categorize them in terms of the point of coupling, here the approach of sorting the noise sources by the coupling mechanism is chosen.

2.4.1 Additive noise

Additive noise refers to the amplitude noise the beat note is embedded in, or to be more precise, the uncorrelated amplitude noise at the Fourier frequency of the beat note. The coupling into the phase noise, denoted as $\tilde{\varphi}$, can be described as follows.

$$\tilde{\varphi} = \frac{\tilde{k}}{k_{\text{het,RMS}}} = \frac{\tilde{k}\sqrt{2}}{k_{\text{het}}} \quad (2.27)$$

where $k_{\text{het,RMS}}$ is the root-mean-square of the beat note amplitude in units of V and \tilde{k} is the ASD of the additive noise at the beat note frequency in $\text{V}/\sqrt{\text{Hz}}$. This can also be written in terms of the quantity carrier-to-noise density C/N_0 , which is given in units of dBHz:

$$C/N_0 = 20 \log \left(\frac{1}{\tilde{\varphi}} \right). \quad (2.28)$$

While these formulas are valid in general for the downconversion of a signal to baseband, they will be derived from the extraction principle of the AD-PLL and in particular from the downconversion of the beat note by mixing. As shown in Equation (2.23), the output of the mixer contains the phase

error of the loop. The additive noise is assumed to be white at the heterodyne frequency and according to its name is added to the beat note. Hence the phasemeter input sees

$$v_{\text{PM}} = \tilde{k} + k_{\text{het}} \cdot \cos(\Delta\omega t - \varphi). \quad (2.29)$$

The mixing process, including the earlier made assumptions, acts on both summands independently. The white additive noise is converted up and down by the heterodyne frequency. The upper part is filtered out, while the content of the bin formerly at the heterodyne frequency is shifted to the DC baseband. Formerly lower frequencies are shifted to negative frequencies and are wrapped around DC. The wrapped noise will add incoherently with the positive frequencies. Hence a factor of $\sqrt{2}$ is applied to the baseband noise. As the beat note is converted like described in Equation (2.23), the phase detector output can be written as

$$Q = \left(\frac{\tilde{k}(f_{\text{het}})\sqrt{2}}{2} \right) + \left(\frac{k_{\text{het}}}{2} \varphi \right) = \left(\frac{\tilde{k}(f_{\text{het}})}{k_{\text{het}}} \sqrt{2} + \varphi \right) \frac{k_{\text{het}}}{2}. \quad (2.30)$$

The formula shows that the additive noise is added to the phase error *inside* the ADPLL loop and cannot be distinguished from the desired phase signal. The additional noise is scaled with the closed-loop transfer function $H(f)$ before coupling as phase extraction noise [29]. In the LISA band, $H(f)$ should be close to 1, hence this in-loop phase noise is directly translated into the overall phase extraction noise of the phasemeter.

It should be noted that, within the model of this mechanism, additive noise around DC in the LISA band does not couple into phase extraction noise, as it is upconverted to the MHz regime during mixing. Section 4.4.2 will put this model to the test.

The most important additive noise in LISA is shot noise. Other sources are relative intensity noise (RIN) of the local laser and voltage fluctuations in the photoreceivers. The latter is usually referred to as electronic noise. Yet those sources are not intrinsic to the phasemeter. $H(f)$ is the only set screw for the phasemeter to influence this kind of noise. However, it is assumed to be 1 within the LISA band, where $G(f)$ is supposed to be high for a locked ADPLL. For these reasons, the aforesaid noise sources are treated separately from the phase extraction contribution in the overall LISA readout budget.

Nevertheless, sources of additive noise can also occur directly in the phasemeter. One example is the electronic noise of the analog front end. Furthermore, ADC quantization noise has to be taken into account. It translates

to white additive noise as

$$\tilde{k} = \frac{2^{-N}}{\sqrt{6 \cdot f_s}} \quad (2.31)$$

where N denotes the ADC bitwidth and f_s the sampling frequency.

2.4.2 Tracking errors and cycle slips

In the last section, it was shown how additive noise is converted into phase noise by the phase detector in the ADPLL. Another property of the ADPLL that needs to be examined is its ability to track the incoming phase with sufficient fidelity.

A figure of merit for this tracking fidelity is given by the variance $\sigma_{\text{trk,err}}^2$ of the loop phase tracking error $\varphi_{\text{trk,err}}$ between an input signal and the NCO. This phase tracking error directly couples into phase extraction noise. It is primarily determined by the loop gain $G(f)$, which also defines the loop error function $E(f)$ and its loop bandwidth. This bandwidth describes the Fourier frequency range in which the loop can actually achieve tracking and can suppress the phase tracking error. Typical values for the ADPLL presented here are in the kHz range. It should be emphasized that even though tracking errors in the LISA band directly translate to phase extraction noise, the tracking error in the kHz range does not affect the phase extraction noise for the LISA band directly. In particular, it is attenuated during the downsampling and averaging from the fast loop sampling rate to the output sampling rate. Nevertheless, they contribute to the total value of $\sigma_{\text{trk,err}}^2$. High values of $\sigma_{\text{trk,err}}^2$ should be avoided, as they can drive the phase detector out of its linear range. This can lead to an effect called cycle slipping, which would cause distortions in the LISA band. If too many samples with a phase tracking error beyond $\pi/2$ occur, the loop will operate with the wrong sign and drive the NCO to the adjacent zero crossing. This introduces a phase shift of 2π and effectively causes red noise in the LISA band. With R representing the slip rate in units of Hz, the noise can be written as

$$\tilde{\varphi}(f) = \frac{\sqrt{2}\sqrt{R}}{f} . \quad (2.32)$$

This can be understood when taking into account that a step in the time domain is translated into Brownian noise in Fourier space.

In the following, three major contributors to $\sigma_{\text{trk,err}}^2$ are listed. The first is defined by the input signal phase dynamics $\tilde{\varphi}_{\text{in}}(f)$. In simple terms, the faster the input changes, the harder it is for the loop to follow. To improve

tracking, the loop gain $G(f)$ can be increased. Mathematically, the relation can be written as

$$\sigma_{\text{trk,err,in}}^2 = \int E(f)^2 \cdot \tilde{\varphi}_{\text{in}}(f)^2 df. \quad (2.33)$$

The second contribution is from noise intrinsic to the loop. While the formalism was conducted here with continuous signals so far, at this point it has to be taken into account that the loop is implemented in digital. In particular are the digital signals represented with a limited amount of bits. In order to keep those numbers limited, the digital signals need to be truncated at some point in the loop. To avoid harmonic distortion, the truncation is followed by artificial whitening or so-called dither. The introduced phase tracking error can be summarized as

$$\sigma_{\text{trk,err,trunc}}^2 = \int E(f)^2 \cdot G'(f)^2 \cdot \tilde{\varphi}_{\text{trunc}}(f)^2 df \quad (2.34)$$

where $G'(f)$ describes the reduced open-loop transfer function, shortened by the loop elements in front of the entering point of the truncation noise.

The third contributor was already introduced in Section 2.4.1 as additive noise translated to in-loop phase noise. It scales with $H(f)$ and can be written as

$$\sigma_{\text{trk,err,add}}^2 = \int H(f)^2 \cdot \tilde{\varphi}_{\text{add}}(f)^2 df. \quad (2.35)$$

The influence of the open-loop gain G via H and E shown here allows an optimization to minimize $\sigma_{\text{trk,err}}^2(G)$ for specific values of additive noise and input dynamics [29, 31].

Another contribution to $\sigma_{\text{trk,err}}^2(G)$ neglected for the optimization can occur due to residual second harmonics generated in the mixer. It was estimated in [29] to exhibit a maximum value of $\tilde{\varphi}_{\text{trk,err}} = |G(2f_{\text{het}})|$.

$E(f)$ typically exhibits low values at low frequencies. Thus the contribution of $\tilde{\varphi}_{\text{in}}(f)$ to the tracking error at low frequencies is suppressed strongly. Yet for very high values of $\tilde{\varphi}_{\text{in}}(f)$, this suppression can still be insufficient and can lead to residual phase extraction errors directly visible in the LISA band. However, the outputs Q and I can be used jointly to compute this residual phase error and correct for it in post-processing. This technique works similar to the phase readout in LPF, which is described in Section 2.5.1.

2.4.3 Direct phase noise

Even with a perfectly tracking ADPLL, naturally phase distortions that couple prior cannot be corrected. One example is the formerly mentioned ADC

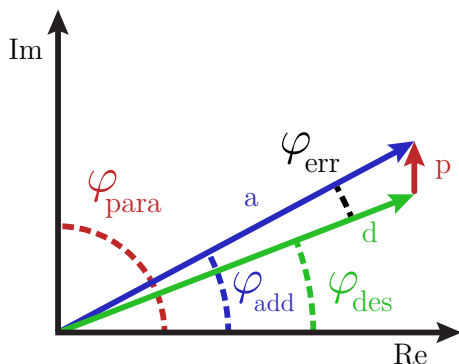


Figure 2.8: Phasor picture of a parasitic tone being added to the desired signal as a small vector. The associated phase angles are sketched as well. a , d and p denote the signal amplitudes.

jitter. More sources can be found in the analog front end. Some are linked to the transfer function of the whole chain between input and ADCs. The individual electronic components and their electronic properties define the transfer function. These properties are temperature dependent and thus also the transfer function is. Consequently, temperature fluctuations can cause phase delays and slow amplitude fluctuations. While the amplitude fluctuations can be discarded in first order according to the mechanism described in Section 2.4.1, the phase delays couple directly into the measurement performance. Another coupling related to the transfer function is associated to the slope of the absolute phase response of the transfer function. For a given slope, large changes in the phase or in the heterodyne frequency change the frequency-specific phase response of the transfer function. This is referred to as “finite phase response” in the sense that a system with a finite response must exhibit a slope in order to reach a zero response at a certain frequency.

While it was stated that slow amplitude noise does not spoil the measurement via the additive noise coupling, [35] states that a non-linear mechanism in analog amplifiers might upconvert DC-flicker into phase noise of the beat note, which will also appear as phase extraction noise.

2.4.4 Direct phase noise due to small vector noise

Direct phase noise can also be induced by parasitic tones. This process can be modeled in the phasor picture as depicted in Figure 2.8. To obtain the induced phase extraction error, the phasors of the desired signal and

the parasitic tone need to be added first. Then, the phase of the resulting phasor can be subtracted from the phase of the phasor of the desired signal, which yields the induced phase error. Usually, the parasitic signal is rather small compared to the desired signal. Thus the associated noise is called small vector noise. Additionally, parasitic signals with substantially different carrier frequency can be regarded as not critical due to the ADPLL acting as a bandpass filter. The scenario with equal or similar carrier frequencies can be broken down into special cases. The first occurs when the phase relation of both phasors is fixed. If the reference frame is assumed to be rotating with the desired signal's frequency, the picture in Figure 2.8 is static and accordingly only a static phase offset is added. The situation is different if the small phasor is moving with respect to the desired phasor due to different phase dynamics. Assuming a static desired phasor and a parasitic phasor rotating around its tip, the induced phase error can be written as

$$\varphi_{\text{err}} = \frac{p}{d} \sin(\Delta\varphi) \quad (2.36)$$

where $\Delta\varphi = \varphi_{\text{des}} - \varphi_{\text{para}}$ is the phase difference between the desired and parasitic signals. Their amplitudes are written as d and p , respectively. This formula can be derived by applying the sine rule of trigonometry and the mentioned assumption of a small parasitic vector. It shows that in general this coupling is non-linear.

Physical coupling mechanisms of the parasitic tones are for example crosstalk and reflections. In the phasemeter itself, crosstalk can occur between the different channels via electro-magnetic induction or galvanic coupling. In the concrete case of the LISA phasemeter EBB, the common pilot tone distribution was identified as a reason for crosstalk. Reflections can occur due to impedance mismatch, for example between cable impedance and analog front end input impedance. While one interface with impedance mismatch generates one reflection and thus would not cause issues, a second spot that generates a back reflection leads to a parasitic tone influencing the phasemeter. The parasitic tone in this scenario is the delayed copy of the initial signal. For a short delay and low phase dynamics in the initial signal, the coupling can manifest as a static offset. However, if the delay is big enough and/or the signal dynamics are rather high, the signal phase of the delayed signal can change significantly during its back and forth propagation. Then, it shows different phase dynamics compared to the desired signal and the case described in Equation (2.36) applies.

A parasitic coupling that can occur inside the ADPLL is caused by residuals of the second harmonics generated in the mixer. They can propagate

through the loop and act as a small parasitic tone. In [31] the model of small vector coupling is used to derive the phase distortion as

$$\tilde{\varphi}_{\text{err}}(f) \approx \frac{|G(2f_{\text{het}})|}{4} \tilde{\omega}_{\text{in}}(f) \tau_g. \quad (2.37)$$

Here τ_g is the total loop delay and $\tilde{\omega}_{\text{in}}(f)/f = \tilde{\varphi}_{\text{in}}(f)$ the instantaneous input frequency.

2.5 Other applications and alternative extraction techniques

This section starts with the presentation of two space missions, LPF and GRACE-FO, that used or will use heterodyne laser interferometry. Afterwards, other ground-based applications will be mentioned. The section concludes with a short summary of alternative phase extraction methods for LISA.

2.5.1 LPF

The LPF mission was launched in 2015 and served as a technology demonstrator for LISA. Its main components were two TMs, each inside one GRS, and four heterodyne laser interferometers.

One main goal was to demonstrate the drag-free control for the TMs and to achieve a reduction of residual differential acceleration noise down to approximately $30 \text{ fm/s}^2/\sqrt{\text{Hz}}$ in the LISA measurement band. In LISA, this performance is necessary to assure that the motion of the TMs is close to free-fall and along geodesics. For LPF, verifying the drag-free control by optical measurements of the TM displacement is linked to its second goal, which is the demonstration of the readout of moving TMs by heterodyne interferometry with sufficient precision. Those two goals were reached, surpassing the targeted performance by orders of magnitude. Besides these performance goals, LPF showed the reliability of all components involved and offered the possibility to characterize them in detail.

The laser interferometers were operated at a heterodyne frequency of several kHz. The used phase extraction scheme can be regarded as the primary stage of its counterpart in LISA [36]. It is based on an I-Q demodulation or single bin Fourier transform (SBFT). A schematic of the LPF extraction scheme is shown on the left side of Figure 2.9. It can be interpreted as an ADPLL in open-loop operation. As the heterodyne frequency is not

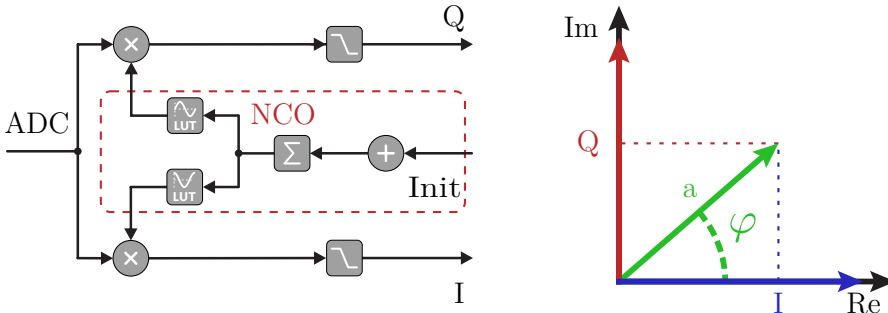


Figure 2.9: Illustration of the LPF I-Q demodulation. The schematic on the left shows the processing pipeline. The right side illustrates the scheme with a phasor picture. The signal phasor is projected onto the two phasors of the local oscillators which operate in quadrature. This provides the real and imaginary part of the phasor in the frame of the local oscillator.

affected by Doppler shifts, a closed-loop tracking is not necessary. However, this means that the NCO frequency or phase cannot serve as a phase readout, as it is not a copy of the input. Instead, the Q and I values are utilized to extract the phase and amplitude in post-processing in the following fashion:

$$\varphi = \arctan \left(\frac{Q}{I} \right) \tag{2.38}$$

$$k_{\text{het}} = \sqrt{Q^2 + I^2} .$$

This process can be visualized in the phasor picture, see right side of Figure 2.9. The reference frame is assumed to be rotating with the heterodyne frequency. The input signal is then a vector exhibiting a random orientation with respect to the reference frame axes. Here, those coincide with the two phasors symbolizing the two NCO outputs. By mixing the signal phasor with the individual axes, it is projected onto them and thus amplitude and phase can be computed with the simple vector arithmetic above.

2.5.2 GRACE-FO

Another spacecraft or satellite mission that is going to be equipped with heterodyne interferometry is GRACE-FO. Its goal is to measure the dynamics of the Earth’s gravity field. For example, the gained gravimetric information can be used in climate science to track the loss of ice mass at the poles. The measurements are conducted with two satellites orbiting the



2 Heterodyne interferometry in LISA and other applications

Earth as probes. Inhomogeneities in the gravity field will cause differential acceleration between the satellites. In comparison to LPF, the satellites acting as TMs are not drag-free due to friction in the atmosphere. Therefore, accelerometers are installed at the satellites' centers of gravity to measure and cancel out the drag in post-processing. The differential motion of the satellites will be primarily tracked by a microwave ranging instrument. The laser interferometer, also referred to as Laser Ranging Interferometer (LRI), is mainly a technology demonstrator for inter-spacecraft laser interferometry in particular for future gravimetry missions [32]. Nevertheless, its data can be used to complement the microwave measurements in post-processing.

In contrast to LPF, which carried the first laser interferometer in space, the LRI will be the first inter-spacecraft laser interferometer in space. Similar to the LISA interferometers, it features a master-transponder scheme and will experience Doppler shifts due to differential spacecraft motion. For that reason, the phase extraction scheme chosen was an ADPLL. For the phasemeter and the metrology system in general, the main differences with respect to LISA are less stringent requirements. This is due to the more relaxed overall noise budget (in the range of $80 \text{ nm}/\sqrt{\text{Hz}}$), and other mission parameters, like the arm length of 220 km. Due to these values, clock noise and laser frequency noise can be neglected if the latter is stabilized with a cavity.

2.5.3 Other applications

Besides the deployment of heterodyne interferometers in space, they can also be found in ground-based applications. Displacement measurements with high precision provided by heterodyne interferometry are for example beneficial in photo lithography [37]. Furthermore, the interferometric phase measurement can also be linked to other quantities, like acoustic pressure in water [38].

2.5.4 Alternative extraction methods for LISA

The ADPLL as the phase extraction for LISA was not selected right from the start and other schemes were also investigated. One that was considered an alternative was the zero-crossing technique [28, 39]. This technique is based on measuring the timing of the intervals between zero-crossings of an AC-coupled heterodyne signal by counting pulses with a fast reference clock. The deviation from equal time intervals between the crossings gives a measure for phase fluctuations. Studies conducted in Glasgow [39]

showed feasibility in terms of pure phase extraction performance with kHz frequencies. Nevertheless, downsides were the necessity of high reference clock frequencies for tracking LISA heterodyne frequencies as well as the lack of a straight forward multi-tone tracking capability. In particular the latter is indispensable for LISA due to the sideband modulations.

A similar approach was taken by another group [40]. Here, a slower reference clock is used and the zero-crossings are counted in between clock ticks. Furthermore, prior downconversion was conducted to convert the LISA-like MHz signal into an intermediate frequency for the phasemeter. The downconversion introduces additional aliased noise that gets wrapped around DC, resulting in an increase of technical noise and in particular shot noise by a factor of $\sqrt{2}$. The mechanism is the same as the one explained in Section 2.4.1. However, in comparison to the ADPLL, it occurs here twice, as the aforesaid intermediate signal still needs to be mixed down to the LISA baseband.

The same applies to another approach which included a prior downconversion and the utilization of the LPF phasemeter [28].

Finally, the investigations converged into the choice of the ADPLL as the phase extraction core. In particular, the digital implementation of the phase locked-loop was chosen to avoid temperature coupling into an analog mixer.

Investigating heterodyne phase extraction performance

This chapter is dedicated to the presentation and description of the methods to characterize phase extraction schemes and phasemeters in terms of their phase noise, linearity and stability as well as in terms of auxiliary functionalities. This is done in the context of LISA. In the first section, a short description of the utilized formalism is given. Afterwards the different test methods together with their potentials and shortcomings will be described. These comprise absolute, split and three-signal tests. Finally, the last section shows a possible extension towards a testbed with the capability to test all aspects required for the LISA metrology chain, including clock tone transfer, ranging and data communication.

3.1 Formalism

Throughout this chapter, the written explanations of the different test methods will be supplemented by mathematical formulations. While some of the tests presented in the following were conducted with signals of electric origin, the terminology inherited from the optical signals in LISA is utilized. Furthermore, as it was done in Section 2.1, the instantaneous phase of the heterodyne beat note or carrier will be modeled as constant average frequency \bar{f}_{het} with an additional phase term φ . Hence the AC part v_{AC} of the voltage as detected by the phasemeter looks like

$$v_{\text{AC}} = k_{\text{het}} \cdot \cos(2\pi\bar{f}_{\text{het}}t - \varphi(t)). \quad (3.1)$$

This will be rewritten and reduced to the pure phase signal $\varphi_{k_{\text{het}}, \bar{f}_{\text{het}}}(t)$ with average heterodyne frequency \bar{f}_{het} and amplitude k_{het} given as parameters. Additional parameters can be added for a refined model. A measure of the

3 Investigating heterodyne phase extraction performance

signal dynamics is given by an integration of the instantaneous frequency dynamics in the LISA band $\sigma_{f_{\text{het}}}^2 = \int \tilde{f}_{\text{het}}^2(f) df$. Furthermore, the additive noise $\tilde{k}(\bar{f}_{\text{het}})$ around the heterodyne frequency can be taken into account as well. Finally, all parameters are collected in $\mathbf{p} = (k_{\text{het}}, \tilde{k}(\bar{f}_{\text{het}}), \bar{f}_{\text{het}}, \sigma_{f_{\text{het}}}^2)$. Thus the phase signal in the time domain is written as $\varphi_{\mathbf{p}}(t)$. More parameters like sidebands tones could be added but will be disregarded in this description. From hereon, the explicit time dependence will be dropped for convenience.

The phasemeter or phase extraction is described as an operator $\mathcal{E}_{\mathbf{p},n}(\varphi)$ acting on the phase signal and is parameterized with the signal parameters and the phasemeter channel number n . Ideally, it should be

$$\mathcal{E}_{\mathbf{p},n}(\varphi) = \varphi + \mathcal{O}(\mathbf{p}) \quad (3.2)$$

which is an identity operator with vanishing influence of the signal parameters. Yet it can be generalized to a linear form

$$\mathcal{E}_{\mathbf{p},n}(\varphi) = g \cdot \varphi + \text{const.} + \mathcal{O}(\mathbf{p}) \quad (3.3)$$

which is still acceptable for most applications and in particular for LISA. The constant offset can be ignored as in LISA only phase changes are measured¹. Furthermore, a generic linearity factor g (not to be confused with the loop gain G introduced earlier) which is common to all channels is also tolerable to certain degrees, as it would increase input phase noise and scientific signal equally.

As the set of parameters could be adapted to describe for example signals occurring in other interferometry techniques, the following formulas can be generalized and can be used also for other phase readout applications. However, the schematics of exemplary implementations shown in this chapter are specific for the case of heterodyne interferometry.

3.2 Absolute test

In terms of concepts, the most straight forward way to test a phasemeter for LISA is an electrical absolute test. This means a signal with a well-known reference phase is fed to a phasemeter and the extracted phase is compared

¹The DWS technique introduced in Section 2.3.2 actually compares the absolute phases of four QPR segment signals. Nevertheless, unwanted offsets can be calibrated.

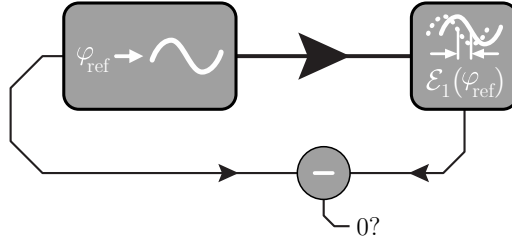


Figure 3.1: Schematic of an implemented absolute phasemeter test. A signal generated with a well-known reference phase is fed to a phasemeter. The extracted phase is subsequently compared to the reference.

with the reference subsequently. A mathematical description is given by

$$\mathcal{E}_{\mathbf{p},1}(\varphi_{\mathbf{p},\text{ref}}) - \varphi_{\mathbf{p},\text{ref}} \stackrel{?}{=} 0 \quad (3.4)$$

$$\mathcal{E}_{\mathbf{p},1}(\varphi_{\mathbf{p},\text{ref}}) - g \cdot \varphi_{\mathbf{p},\text{ref}} \stackrel{?}{=} \text{const.} \quad (3.5)$$

where Equation (3.4) describes an absolute identity test while Equation (3.5) presents a test for linearity with g denoting the linearity factor. It is easy to see that, with this scheme, the phasemeter operator could be probed for any deviation from its wanted form by checking with all desired values of \mathbf{p} in the parameter space. A schematic of an implementation is shown in Figure 3.1. However, implementing this scheme is cumbersome due to the fact that any distortions between the signal generation and the phasemeter channel will be indistinguishable from actual phasemeter noise. Yet it yields the possibility to test all critical aspects of the readout. For this reason, efforts were carried out at the AEI to develop a signal generator that minimizes the distortions between reference and phasemeter [29]. The basic concept is a digital signal synthesis driving a DAC while particular effort is put into the mitigation of DAC jitter. The digital phase reference could then be conveniently compared to the likewise digital output of the LISA phasemeter. The jitter correction was designed similar to the ADC jitter correction of the phasemeter itself, namely using a pilot tone as reference. However, it turned out in a pre-test, which used the signal generator itself as the readout device, that additional noise limited the measurements severely. Assuming thermal fluctuations coupling into the converter electronics, the project was halted in favor for the other test schemes presented later. Nevertheless, an absolute test of the digital core in a purely digital testbed, thus bypassing converter electronics, was conducted. It was implemented on a single FPGA with an NCO and an ADPLL developed for the EBB

of the LISA phasemeter [29]. A similar test was developed and utilized in this thesis in order to analyze amplitude coupling. The results are shown in Section 4.2.3.

3.3 Split-signal test

A testing scheme easier to implement compared to the absolute test is called split-signal test and is performed by means of a differential measurement. As suggested by the name, a signal is split and the two ideally identical copies are fed into two phasemeter channels. The extracted phases can be compared subsequently². The results should ideally be zero throughout the LISA band. Hence the technique is also designated zero or null measurement. In first order, all noise sources that couple beyond the split point and that are not common in the two channels will show up in the phase difference. The mathematical description offers a similar perspective:

$$\mathcal{E}_{\mathbf{p},1}(\varphi_{\mathbf{p},\text{ref}}) - \mathcal{E}_{\mathbf{p},2}(\varphi_{\mathbf{p},\text{ref}}) \stackrel{?}{=} \text{const.} \quad . \quad (3.6)$$

Here it is assumed that the channels do not show different linearity factors while different offsets are likely to occur. The formula shows that a zero or constant test signal can be obtained even if $\mathcal{E}_{\mathbf{p},1}$ and $\mathcal{E}_{\mathbf{p},2}$ deviate from a linear form if done so commonly. This reveals the flaw of the split technique. The test cannot probe for the phasemeter's linearity completely. The same applies to common noise sources or its dependency on the parameters \mathbf{p} . Basically any noise source or dependency common in both channels will show up in the test in attenuated form or even not at all. Thus they cannot be properly tested for.

Despite these issues, the technique is easy to implement and hence usually serves as a first stage for phasemeter testing. A schematic of an implementation is depicted in Figure 3.2. For the LISA phasemeter, the scheme can be implemented by a multi-way passive-resistive split of a sinusoidal MHz output of a signal generator. Alternatively, in order to test the EBB for LISA-like signal dynamics, a digital signal generator (DSS) was developed at the AEI by Iouri Bykov. It mimics realistic signals occurring in LISA which are subsequently split. The conducted measurements with this scheme and the EBB showed a phase extraction performance of $\approx 6 \mu\text{rad}/\sqrt{\text{Hz}}$ [29, 34]. These measurements included the successful utilization of a pilot tone

²For the LISA phasemeter, the comparison is usually carried out by a subtraction using the PIR values in post-processing or alternatively directly on-chip using the PA registers.

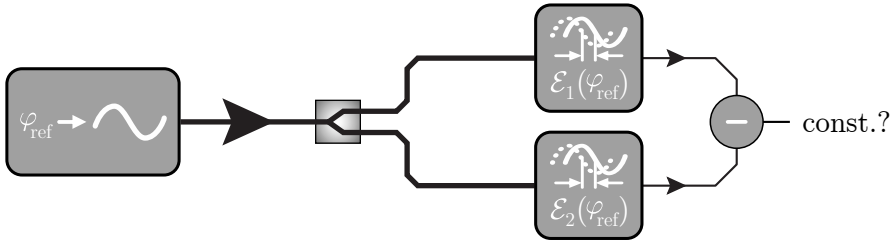


Figure 3.2: Schematic of an implemented split-signal test. A signal carrying a phase is generated, split and fed to two phasemeter channels. The extracted phases are subsequently compared.

correction. The performance was primarily limited by thermal fluctuations coupling via the analog electronics in the front end. This coupling is introduced by unequal temperature coefficients in the different channels and/or gradients of the temperature across the same.

Besides these measurements, the split method was also used by other groups to test different phasemeter versions [41].

When used with an optical signal captured by a photoreceiver and split electrically, the technique can be referred to as a split measurement with optical signals. Furthermore, the scheme can be extended and the split point can be moved to the optical domain, for example by using a beam splitter to divide the already combined beam in front of two photoreceivers. This is consequently referred to as an optical split measurement. As the splitting point is shifted compared to Figure 3.2, the photoreceivers are also included in the test and need to provide a proper phase fidelity in order to isolate the effects of the phasemeter. Additionally, if low powers are applied to the photoreceivers, shot noise will show up in the test as additive noise. As it is uncorrelated on both photoreceivers, it will couple into the measurement.

The optical split should not be confused with the measurement between two photoreceivers at complementary ports of an interferometer recombining beam splitter. Here, the heterodyne beat notes exhibit a phase shift of π compared to each other, see Section 2.1. Due to the π phase shift, the technique is called π measurement. In comparison to an optical split test, it shows a different behavior concerning some types of parasitic tones. One example is stray light captured by both photoreceivers but not being interfered at the beam splitter which is used for the π measurement. Figure 3.3 visualizes this behavior in the phasor picture. The beams interfered at the π measurement beam splitter exhibit the 180° phase shift, while the parasitic beam couples with equal sign. Independent from the split test, this fact can

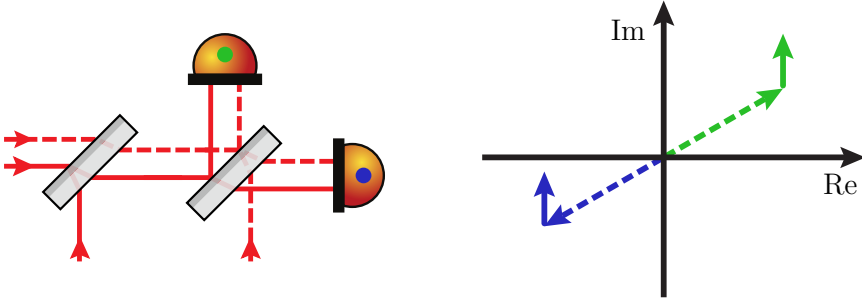


Figure 3.3: Example of stray light coupling in a π measurement. The parasitic light interfered before the π measurement beam splitter couples with equal signs, while the main beams exhibit a 180° phase shift.

be used to cancel the parasitic tone. The associated technique is called balanced detection and uses the difference of the two complementary receivers, thus effectively subtracting the parasitic tones but adding the wanted signals. This technique can also be applied to cancel direct amplitude noise, which is detected with identical sign on both receivers. Section 4.4.2 presents its utilization in that context.

To conclude, the optical versions of the split measurement can be used to extend the test to more components of the LISA metrology chain and can serve as intermediate steps to more advanced testing schemes like those described in the next section.

3.4 Three-signal test

As shown in the last section, the split-signal measurement lacks the capability to probe the full phasemeter behavior. A three-signal test represents a more elaborate test method. As suggested by the name, three instead of two signals are utilized and are supposed to cancel out after readout. To the author's knowledge, the first mention of this technique can be found in [42]. Three initial phase signals $\varphi_a, \varphi_b, \varphi_c$ are combined pairwise. The resulting three intermediate signals $\varphi_1, \varphi_2, \varphi_3$ are then processed by the phasemeter channels. The extracted phases can subsequently be added and subtracted. In formula this is expressed as:

$$\begin{aligned} \text{const.} &\stackrel{?}{=} \mathcal{E}_{\mathbf{p}1,1}(\varphi_{\mathbf{p}1,1}) + \mathcal{E}_{\mathbf{p}2,2}(\varphi_{\mathbf{p}2,2}) + \mathcal{E}_{\mathbf{p}3,3}(\varphi_{\mathbf{p}3,3}) \\ &= \mathcal{E}_{\mathbf{p}1,1}(\varphi_{\mathbf{p}a,a} - \varphi_{\mathbf{p}b,b}) + \mathcal{E}_{\mathbf{p}2,2}(\varphi_{\mathbf{p}b,b} - \varphi_{\mathbf{p}c,c}) + \mathcal{E}_{\mathbf{p}3,3}(\varphi_{\mathbf{p}c,c} - \varphi_{\mathbf{p}a,a}) . \end{aligned} \quad (3.7)$$

The equations show that, in contrast to the split-signal test, the involved channels are probed with different phases and signal parameters, thus dependencies of the latter can be revealed. Furthermore, the equation can in general only be valid, or practically speaking a cancellation of the individual phase outputs can be achieved, if the phasemeter operations are equal except a phase offset and, most importantly, comprise additivity and therefore linearity³. Then Equation (3.7) becomes:

$$\begin{aligned} \text{const.} &\stackrel{?}{=} (\varphi_{\mathbf{p}_{a,a}} - \varphi_{\mathbf{p}_{b,b}}) + (\varphi_{\mathbf{p}_{b,b}} - \varphi_{\mathbf{p}_{c,c}}) + (\varphi_{\mathbf{p}_{c,c}} - \varphi_{\mathbf{p}_{a,a}}) \\ &= \varphi_{\mathbf{p}_{a,a}} - \varphi_{\mathbf{p}_{a,a}} + \varphi_{\mathbf{p}_{b,b}} - \varphi_{\mathbf{p}_{b,b}} + \varphi_{\mathbf{p}_{c,c}} - \varphi_{\mathbf{p}_{c,c}} . \end{aligned} \quad (3.8)$$

This represents a more thorough test than the split-signal method. Compared to the latter, also noise sources common and uniform in the channels should show up in the combined output signal due to the uneven number of channels utilized. Yet it should be noted that noise contributions that dependent solely linearly on one of the signal parameters \mathbf{p} cannot be revealed within this testing scheme either.

Different forms of the three-signal test have been implemented so far using different phasemeters. A general schematic for an implementation is presented in Figure 3.4. The combination is realized by mixers as the phase is imprinted on initial carrier signals. Those can be generated by lasers or high-frequency signal generators. Purely digital tests were conducted in order to test the functionality of the ADPLL core presented in this thesis [31, 42]. In order to include the analog front end in the test, an electrical version was assembled as well [29]. Three signal generators with different GHz output frequencies were combined to create intermediate signals at MHz using analog mixers. The latter were identified as testbed noise source spoiling the test measurement via excess phase noise. This can be avoided when shifting the mixing process into the optical domain by means of assembling an optical three-signal test. This will be discussed in the next section.

3.5 Optical three-signal test

Different approaches were pursued to implement an optical three-signal test. The National Aeronautics and Space Administration (NASA) Jet Propulsion Laboratory (JPL) incorporated the scheme into their TDI testbed [43]. At the AEI, an optical bench was developed specifically for this purpose.

³The validity of this implication can be shown for functions $f : R \mapsto R$ if continuity for the mathematical phasemeter operation is assumed.

3 Investigating heterodyne phase extraction performance

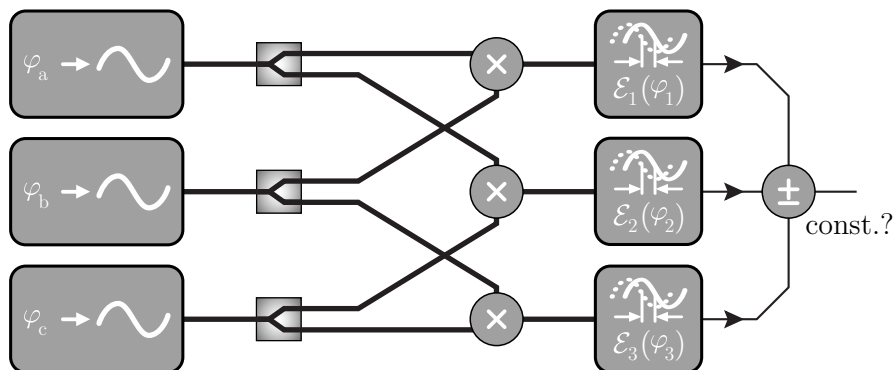


Figure 3.4: Schematic of an implemented three-signal test. Three initial phase signals are imprinted on carriers generated for example by lasers or high-frequency signal generators. Those are split and mixed pairwise. The resulting beat notes are fed to three phasemeter channels. Finally the outputs are recombined.

The core elements are six beam splitters and three fiber injector optical sub-assemblies (FIOs) for the beam injection of three independent lasers. The former are positioned in a hexagonal shape. Three serve for beam splitting and three for recombination. Due to their arrangement, the optical bench is also referred to as “Hexagon”. Figure 3.5 shows a photograph and a sketch of it. Taking into account the notation introduced in Section 3.4, the injected beams carry the initial phases $\varphi_a, \varphi_b, \varphi_c$. They are first split and subsequently recombined pairwise. The interferometer or recombination beam splitter outputs represent the intermediate phases $\varphi_1, \varphi_2, \varphi_3$. Each output also features a complementary port. Those beams are captured with photoreceivers aside of the optical bench. After conversion to a voltage, the signals are subsequently fed to the phasemeter. All together this implements the three-signal testing scheme described in Equation (3.7).

For a precise phasemeter test, it is essential that no additional phase noise is introduced after the splitting. In the optical assembly, critical parameters are thus the stability of the displacement between each dividing beam splitter and its subsequent recombining beam splitters. In particular can non-common fluctuations of the two displacements between two recombining beam splitters and their mutual splitting counterpart couple directly into the phase. If these fluctuations occur in the LISA band, they introduce optical path length noise and hence phase noise in the LISA phasemeter measurement and cannot be distinguished from phasemeter noise. Besides, a static mismatch in the displacements creates an unequal-arm-length interferometer and accordingly leads to the coupling of the individual laser

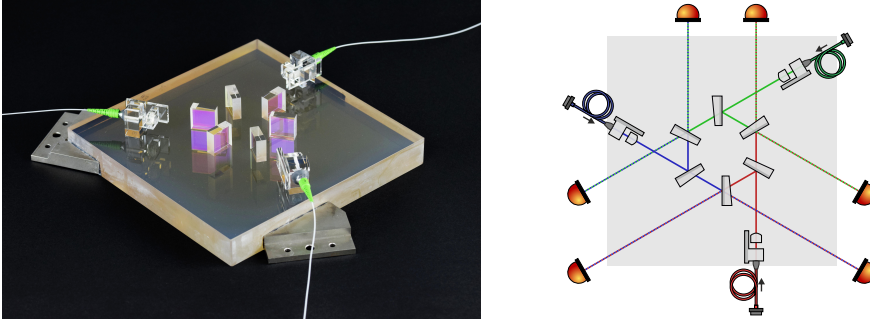


Figure 3.5: The Hexagon interferometer. The left side shows a photograph (image credit: D. Penkert), on the right a simplified sketch is depicted. The Hexagon implements a three-signal test by combining the individual beams which are injected with the FIOSs. The combined signals are then captured by photoreceivers.

frequency noise, see Section 2.2.3. The latter should not be confused with the differential laser frequency noise between two lasers, which serves as a signal parameter of the intermediate signals introduced in the formalism of Section 3.4.

Optical path length noise beyond the recombination beam splitters can be neglected in first order as it translates to phase noise with the beat note's heterodyne frequency only. Yet, other noise couplings past the aforesaid point can be critical, as will be shown in Section 4.2.

To attenuate the impact of the interferometric noise sources, the interferometer footprint was setup in the mentioned hexagonal shape. Theoretically, this allows the matching of the static displacement between all beam splitters. Furthermore, it allows a compact implementation which attenuates the influence of thermally induced length changes. To mitigate those further, the optical bench is built with Fused Silica components on a bulk baseplate made of ZERODUR®. While the splitting beam splitters were bonded [44], the in terms of interferometer contrast more critical recombination counterparts were fixed with the reversible method of optical contacting.

The component placement was assisted by a coordinate measurement machine (CMM)⁴ to minimize the displacement mismatch. The assembly of the bench was performed by Marina Dehne [46]. The mentioned FIOSs were individually built from glued Fused Silica components and were op-

⁴The exact CMM assembly can be looked up in [45]. Its maximum error is given by the formula $\Delta l = 1.5 \mu\text{m} + \frac{L}{333000}$ for a measurement of a displacement between two points with rough distance L in m.

3 Investigating heterodyne phase extraction performance

tically contacted onto the bench by Daniel Penkert and Dennis Schmelzer during their diploma thesis [45] and master's thesis [47], respectively. The former was supervised as part of this PhD thesis.

The FIOSs were added to reduce angular beam jitter compared to commercial fiber couplers. The angular beam jitter translates into optical path length jitter via the beam splitters which have a wedge angle. The latter was implemented to avoid the generation of parallel ghost beams. The fibers glued to the FIOSs are polarization-maintaining and their slow axes were adjusted manually to the bench surface normal.

Two of the three lasers used as light sources are loosely locked onto the third master laser in order to assure beat notes with heterodyne frequencies within the phasemeter operation bandwidth. Adding artificial noise at the error points of the frequency offset phase locks allows a convenient tuning of the phase signal dynamics. This in turn is important to probe the dynamic range of the phasemeter.

As described before, since the splitting point of the three-signal test was moved to the optical domain, photoreceivers are also in the phase sensitive path. While they somewhat complicate the evaluation of the phasemeter performance, they actually have to be tested for LISA in any case. Thus the testbed can be regarded as a photoreceiver testbed as well. In particular interesting is the case of low applied laser power. Low in this case refers to some dozens of pW and a few mW for two lasers generating a beat note, respectively. This represents the interferometry case for the spacecraft-spacecraft measurement in LISA, where a local laser is interfered with the weak incoming beam. The test requirements can then be relaxed with the budgeted contribution of shot noise and additive electronic noise. While the first is determined by the laser power and the quantized nature of light and current, the latter is dependent on the actual photoreceiver design. Thus the low power case allows the testing of generic photoreceivers' LISA-compatibility.

The whole experiment set up for this thesis with the Hexagon as its core will be described in more details in Chapter 4. Furthermore, the measurements conducted with the Hexagon including an extensive noise hunting for the testbed noise sources is presented there.

Besides the test of phase extraction and photoreceivers, a testbed based on the Hexagon offers the possibility to be extended further to cover more aspects of the LISA metrology chain. This is described in the next section.

3.6 LISA metrology chain experiment (LIME)

The basic idea of the Hexagon's testbed extension towards a LIME is the utilization of three separate LISA phasemeters with three independent clocks [48]. One phasemeter and one clock can be combined with an EOM and one of the lasers providing light for the Hexagon. The joint parts of such an assembly can then be regarded as the metrology elements of one of the LISA spacecraft. Three of those complete the picture. Each is supposed to read out one complementary photoreceiver pair. A sketch of the proposed experimental setup can be looked up in Appendix A.1. Due to the independent clocks, clock tone transfer and ranging mechanism are required to achieve phase extraction performances similar to the single clock and single phasemeter setup.

The clock tones themselves are implemented by signal generators running at 2.4 GHz. They drive the EOMs and imprint the clock tone onto the laser beam. Naturally, the clock tone is also connected to the LISA phasemeter, which derives its system clock and the pilot tone from it. Like in LISA, if all three oscillators imprint the same frequency of 2.4 GHz as sidebands, the associated sideband beat notes would mix into the same frequency bin like the main beat notes. To avoid this, two of the phasemeters are supplemented with an additional signal generator each. These generate 2.401 GHz and 2.402 GHz, respectively, and drive the associated EOMs. This leads to sideband beat notes exhibiting offsets of 1 MHz and 2 MHz with respect to the main beat note. In order to cancel the differential clock noise between the two signal generators supplementing a single phasemeter, their signals are combined electronically and read out by the phasemeter as well. Together with the sideband-sideband measurements, this phase information can be used to test clock noise removal algorithms applied in post-processing.

Additionally to the clock tone, also the PRN codes and data bits generated by the LISA phasemeter can be added to the signal driving the EOM and being transmitted to the other phasemeters. This allows the testing of ranging and data transfer via the optical links. At some stage, also the signal generators and the phasemeter clock module are supposed to be replaced with a LISA frequency distribution system (FDS). The latter accepts a clock tone at 10 MHz and upconverts it to 2.4 GHz and for example 2.401 GHz. The first tone then is used to generate the pilot tone (with high phase fidelity) and the phasemeter clock.

To put it in a nutshell, the LIME can test all contributions of the LISA phasemeter to the metrology chain. Additionally, some components important for the metrology chain apart from the phasemeter can be tested.

3 Investigating heterodyne phase extraction performance

Besides the photoreceivers, this includes the EOMs. The latter allow the implementation of the auxiliary functions clock tone transfer, ranging and data communications. This in turn provides the data for the application of the post-processing steps clock synchronization and clock noise removal. Only the last step in the metrology chain, which is the removal of the LISA master laser frequency noise by TDI, cannot be fully tested under realistic conditions. This is primarily due to the difficulties of emulating an optical delay in the order of magnitude required for LISA (≈ 10 s).

Representing the first step towards the LIME, the next chapter describes the implementation of an optical three-signal test with the Hexagon.

Implementing an optical three-signal test

In this chapter, the efforts to set up an optical three-signal test are documented. This comprises the description of the noise hunting process to reduce the testbed noise sources. In the beginning, the general description of the experimental setup given in Section 3.5 is continued in more technical details. Afterwards, the most important steps of the noise hunting process are summarized. Subsequently, the results of these efforts in terms of benchmark performances are presented together with a discussion of probable reasons for their limitations. Furthermore, the application of the setup to measure RIN coupling is described. At the end, an outlook on planned steps to overcome the aforementioned limitations and to expand the experiment to advanced testing schemes is given.

4.1 Initial experimental setup

The basic experimental setup can be divided into five major parts, the laser preparation, the auxiliary phasemeter controlling the latter, the vacuum chamber, its content in form of the Hexagon and auxiliary optics and finally the EBB of the LISA phasemeter or main phasemeter.

4.1.1 Laser preparation

After the task of the laser preparation was stated briefly in the last chapter, here the actual setup will be described in more detail. The order of explanation follows the light travel path in the experiment. Figure 4.1 accompanies the description schematically. Three NPRO 500 mW lasers by Innolight/Coherent serve as independent light sources. The emitted beams are collimated and are cleaned in terms of polarization with pairs of $\lambda/4$

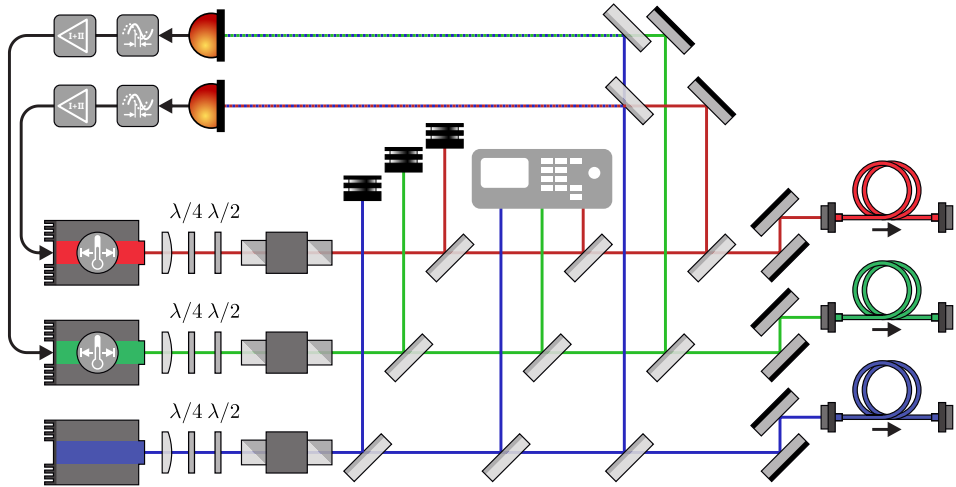


Figure 4.1: Schematic of the laser preparation. Its main task is to lock two lasers onto one master laser. Furthermore, their light is coupled into fibers connected to the main experiment.

and $\lambda/2$ wave plates and Faraday isolators. The latter act as optical diodes protecting the laser from back reflections. All beams are subsequently split once for power attenuation by 10:90 beam splitters and a second time with 50:50 beam splitters to create low-power diagnostics channels. For example, those can be used to couple light into scanning Fabry-Pérot (SFP) interferometers. A third split is performed to inject the reflected beams into an assembly of beam splitters that serve the purpose of combining the three laser beams pairwise. This results in three beat notes, of which two are detected by a set of photoreceivers. They are used to generate error signals to lock two of the laser as slaves onto one master laser. For the locks, a second, auxiliary phasemeter is utilized. It is described in Section 4.1.2 and its task is to keep the frequency offset between the lasers within the bandwidth of the LISA phasemeter. To achieve this, the piezo as well as the temperature actuators of the NPROs are used. Additionally, it can control the differential frequency noise by adapting the loop gains or add artificial noise at the loop error point.

The beams that are transmitted in the third split are coupled into polarization-maintaining fibers via fiber couplers. Margin was left for additional wave plates which can be utilized to control the polarization in front of the couplers more precisely. Ideally, the orientation of the linear polarization should be matched to the fiber's slow axis, as will be discussed in detail in

Section 4.2.9.

Initially, fiber-coupled EOMs were connected to the couplers in order to be able to imprint the clock tone and PRN codes at a later stage. Using a fiber mating sleeve for fiber-to-fiber coupling, the EOMs in turn were connected to feedthrough fibers of the vacuum chamber.

4.1.2 Auxiliary phasemeter and frequency lock

As mentioned, the task of the auxiliary phasemeter is to lock the laser frequency of each of the two slave lasers onto the master laser. To achieve this, it needs to act as a frequency sensor measuring the actual differential frequency values. Furthermore, it needs to individually compare these to desired values and subsequently needs to generate actuator signals which drive the laser frequencies and hence close the feedback loops. These functionalities are implemented in the digital domain in an FPGA which is connected via ADCs and DACs to the analog domain. The digital design was assembled by the author, partially using existing building blocks. For example, the essential frequency sensor is once again a ADPLL designed by Oliver Gerberding based on the ones developed for the LISA phasemeter. It requires the operation with a non-zero differential frequency, hence the loop is operated with an adjustable offset. The feedback loop controller is an $I+I^2$ servo. After downsampling to 2.5 MHz, the actuator signal is put out to the laser piezo modulator controlling the frequency. With a limited tuning range of ± 65 MHz for the piezo, the loop alone cannot compensate for slow thermally induced drifts. Hence a second feedback loop additionally controls the temperature actuator. It utilizes the digital actuator signal of the fast piezo loop as error signal, processes it in a PI servo and generates an actuator signal for the laser. The loop unity gain frequencies were measured to be in the range of several kHz for the piezo loops and around a few hundreds of mHz for the temperature loops.

Besides the main locks, the auxiliary phasemeter is also used to implement DC readout channels as well as additional servo loops for amplitude stabilization schemes, for example for one that will be introduced in Section 4.2.5. The actual hardware components are mostly commercial and off-the-shelf. The FPGA board is the model ML605 by Xilinx. The ADC card is the FPGA mezzanine card (FMC) 107 by 4DSP. Finally the DAC card is a custom-made printed circuit board (PCB) designed by Oliver Gerberding and Iouri Bykov based on the DAC8801 by Texas Instruments. The clock distribution is performed on the ADC card with a dedicated clock chip which in turn is sourced by a clock on the FPGA board. Optionally, the

4 Implementing an optical three-signal test

source clock can be replaced with an external clock.

4.1.3 Vacuum chamber

The vacuum chamber is cubical with dimensions of 75 mm \times 75 mm \times 75 mm. It is equipped with the feedthroughs for 3 fibers and more feedthroughs for electric connectors like D-Sub and SMA-to-BNC. The latter is used to transmit the essential signals from the photoreceivers. The chamber is placed on a table with passive vibration isolation. A turbopump is connected via a gate valve. It is in turn coupled to a piston pump and a socket which can be hooked up with the in-house vacuum facility of the AEI.

4.1.4 Optical bench and auxiliary optics

The heart of the experiment is the ultra-stable optical bench. As mentioned in Section 3.5, it consists of two stages of beam splitters arranged in a hexagonal shape and is thus referred to as Hexagon. It effectively implements the optical three-signal test, while custom-made FIOSs provide for beam injection with low angular jitter. The bench is placed on a steel baseplate via Macor® feet and is fixed in position with metal tips to minimize thermal conductivity. The baseplate is equipped with auxiliary optics and is itself surrounded by an aluminum thermal shield. The whole assembly is placed in the vacuum chamber. Inside the chamber, the fiber feedthroughs were connected initially with fiber savers which in turn were connected via fiber mating sleeves to the fibers glued to the FIOSs. On the outside, the feedthrough fibers can be connected directly to the fiber couplers of the laser preparation bench or via fiber mating sleeves to fiber-coupled components like the initially added EOMs. The steel plate that hosts the Hexagon was initially equipped with optics to read out five of the three times two interferometer output ports. For each port, a mirror folds the combined beams towards a lens which in turn focuses the beams onto a photoreceiver. The photoreceivers with small single element InGaAs photodiodes (0.5 mm in diameter) were designed by Germán Fernández Barranco and are based on a TIA using a single operational amplifier (OP), namely the model LMH6624 by Texas Instruments. The AC and the DC channels are coupled. The small diodes were chosen over larger ones due to their low junction capacity of about 8 pF, which is beneficial when low laser powers are applied (see Section 3.5). Yet, the power levels the photoreceivers had to handle within the work of this thesis were roughly in the sub-mW regime. Four of the photoreceivers were used in the beginning, one at each of the three indepen-

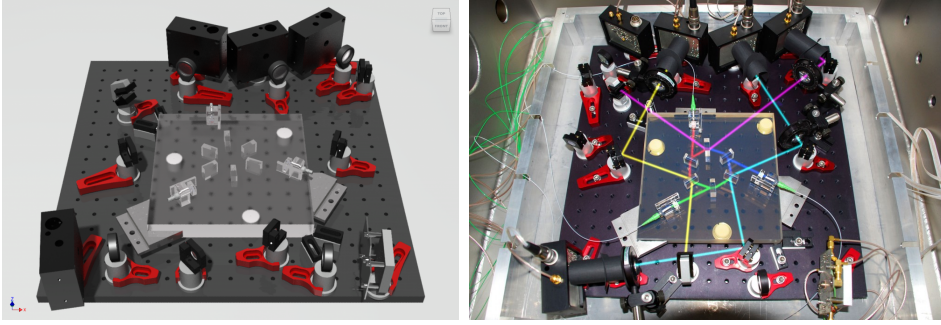


Figure 4.2: CAD model and photograph of the Hexagon and the auxiliary optics. The CAD model on the left shows the initial configuration, while the photograph on the right was taken at a later stage. Image credit: D. Penkert.

dent output ports with the fourth added to one of them for complementary detection. In the measurements shown in this chapter, they are numerated accordingly. The aforementioned lenses are necessary to focus the beam on the small diodes. A second complementary output port was equipped with a QPR for diagnostic purposes. The sixth output port was blocked. Additional space was left in front of the receivers for the optional placement of thin-film polarizers in rotational mounts. Figure 4.2 shows a CAD model of the initial setup and a photograph taken at a later stage of the experiments.

4.1.5 Main phasemeter

As the LISA phasemeter was already presented in Section 2.3, this section will be brief. An EBB of the aforesaid LISA phasemeter was composed as the main unit-under-test. As initial setup, one ADC card was installed along with the clock module. For the purpose of an active temperature control, the phasemeter was put into a housing constructed with double-sided aluminum walls and covers. The temperature control is performed by a thermo-electric assembly (AA-200-24-22 by Laird Technologies) which utilizes Peltier elements for the heat exchange between the housing's inside and its outside. Ventilators provide a better thermal coupling via air circulation on both sides. More details are given in [29].

After all the five major components were set up as just presented, first measurements were taken and the process of noise hunting was started.

4.2 Noise hunting and evolution of the experimental setup

The following section will describe the various measurements and steps performed during the process of finding and eliminating the testbed noise sources. The description follows mostly a chronological order while at some points priority is given to a proper succession with regard to content. Naturally, the section starts with the first measurements performed after the assembly of the experiment. While the main focus is put onto the continuous enhancement of the testbed performance, additional effort was put into describing methods that did not yield much direct improvement but are regarded as useful and interesting by themselves. At the end of the section, the performances considered final in the scope of the experimental work of this thesis are shown and the residual limitations are discussed.

It should be noted that the performance references given in the following plots are derived from the phase noise contribution requirement in LISA (Section 2.2.8). However, it is relaxed by a factor of $\sqrt{2}$ for split and π measurements and by a factor of $\sqrt{3}$ for three-signal measurements. This takes into account the root-mean-square (RMS) noise addition of the multiple channels.

Furthermore, the use of the pilot tone correction is indicated by the suffix PT in the first measurements. From Figure 4.34 on it is always applied.

4.2.1 Initial measurements

Before the optical testbed was put to work, electrical split measurements were performed to verify a correctly operating LISA phasemeter. It was conducted by splitting a 6 MHz signal from a signal generator with a 4-way resistive splitter. The clock module was driven with a 2.4 GHz clock tone put out by a separate signal generator. Finally, the pilot tone was provided by a third signal generator. It was used instead of the pilot tone derived on the clock module in order to stay flexible with its frequency. The latter two generators were locked via a 10 MHz reference signal. For the first tests the pilot tone was set to 37.5 MHz. Figure 4.3 shows the results of the test. In contrast to the plots in [29, 34] which compared the single channels to the their average, here all differential split measurements between the channels are shown. The results show that the required performance is reached. A deterioration towards lower frequency can be observed. In the next step, the optical setup was connected. The initial measurement was performed in air and is shown in Figure 4.4. Heterodyne frequencies were chosen to be around

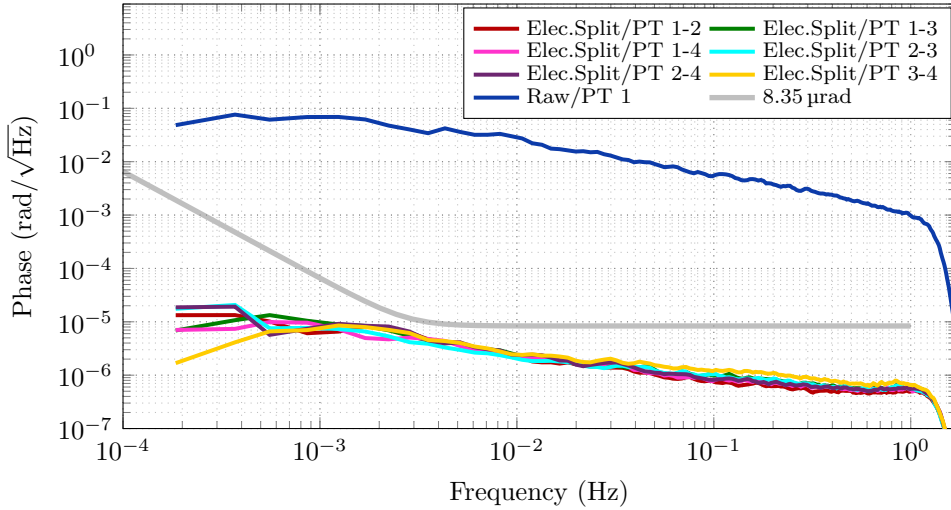


Figure 4.3: Initial electrical measurement. All differential measurements showed the required performance. The raw single channel noise is given as reference.

13 MHz, 8 MHz and 5 MHz and signal dynamics to be moderate with levels equivalent to frequency noise of $1 \text{ Hz}/\sqrt{\text{Hz}}$ at 1 Hz. The π measurement was performed with the 5 MHz beat note.

The frequencies and signal dynamics were changed from time to time in the following measurements, it is pointed out when an effect due to it was assumed to be dominating. Additionally, all heterodyne frequencies can be looked up in Appendix B.

As confirmed later in Section 4.2.2, here the three-signal measurement was limited due to the air between the Hexagon beam splitters, or to be more precise, by the fluctuations of its refractive index, which ultimately leads to phase fluctuations in the phase sensitive part of the testbed. The refractive index is, among other quantities, influenced by pressure fluctuations and temperature fluctuations [49]. A reduction of the absolute pressure can decrease both, the first directly and the latter by damped convection. Before doing so by evacuating the chamber, focus was laid on the π measurement. The excess white noise limiting it was identified to be caused by the pilot tone. Its second harmonic was at 75 MHz and thus was aliased down to 5 MHz. Consequently, the pilot tone interfered with the main carrier at 5 MHz. For verification, a measurement was conducted with a beat note of 9 MHz. It is shown in Figure 4.5. The excess white noise vanished.

After these tests, the EBB broke down due to exposure to excess supply

4 Implementing an optical three-signal test

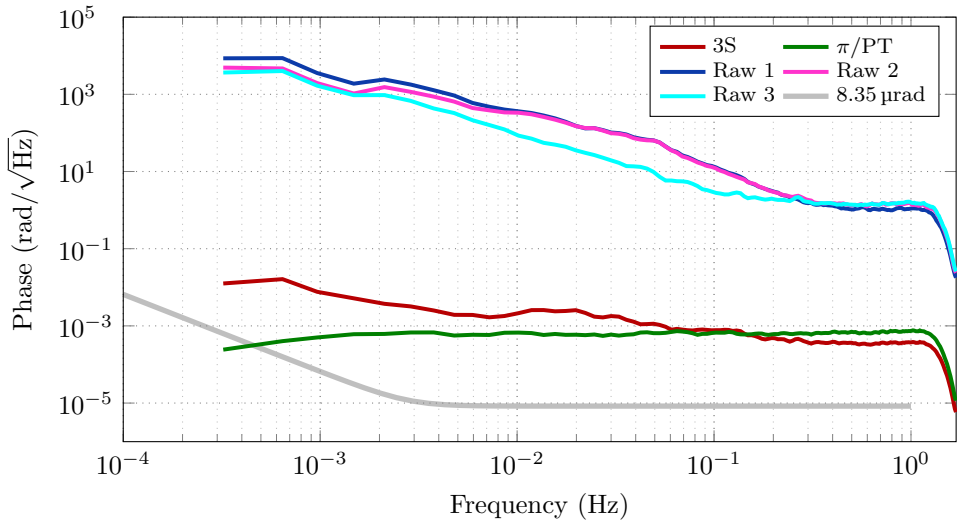


Figure 4.4: Initial optical three-signal and π measurement. The first is limited by phase fluctuation due to air between the beam splitters, while the latter is distorted by pilot tone interference.

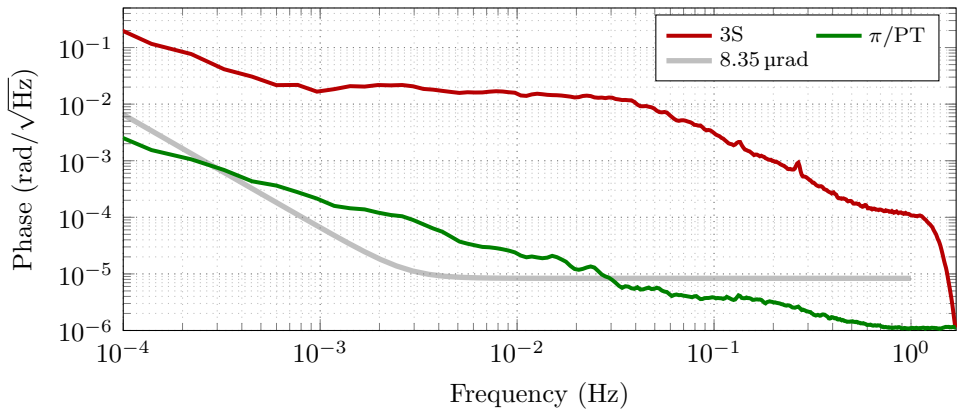


Figure 4.5: Measurement with changed heterodyne frequency in the π measurement. The white noise due to pilot tone interference was removed.

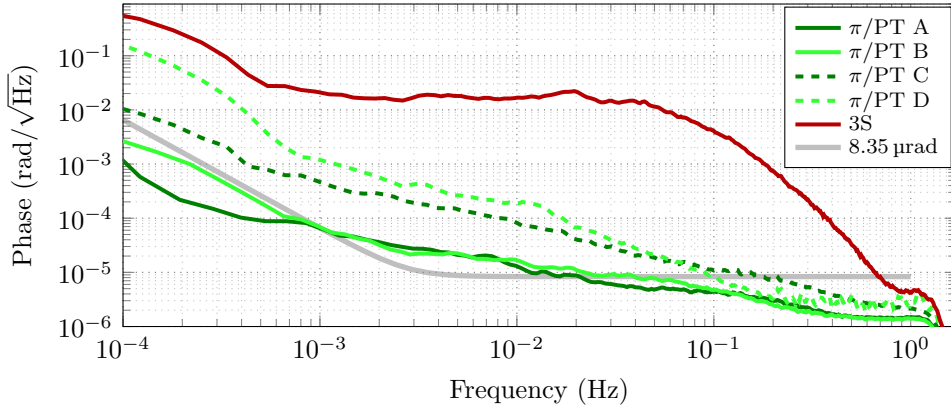


Figure 4.6: Impact of different setup changes. The first π measurement (π /PT A) is taken with a new set of phasemeter hardware, the second (π /PT B) with improved cable isolation and baffles, the third (π /PT C) with thin-film polarizers in front of the photoreceivers and the fourth (π /PT D) with removed EOMs. For the latter also a three-signal measurement is shown.

voltage. Therefore it was replaced by a spare piece. Due to the lack of a clock module, the 80 MHz on-board clock was utilized as digital clock from that point on. Electrical split measurements were conducted to verify the phase extraction performance of the new hardware.

After this was done successfully, a set of measurements was conducted with certain changes to the setup, aiming to improve the π measurement. Figure 4.6 summarizes the impact. To start with, the new hardware was used for the first time jointly with the Hexagon. In the second, the cables from chamber to phasemeter with a length of about 2 m were thermally isolated with bubble wrap. Additionally, cardboard baffles were put in front of the photoreceivers to block potential off-axis stray light. In the third measurement it was tried to improve the polarization control by adding thin-film polarizers in front of the photoreceivers. They were coarsely adjusted manually to the Hexagon “senkrecht” polarization (s-pol) axis. In the fourth measurement, the EOMs were removed from the setup to exclude any noise contribution. For this case also the three-signal measurement is shown as reference. Significant changes occurred when the pre-photoreceiver polarizers were inserted. An $1/f$ noise dominated the π measurement. Furthermore a low frequency oscillation appeared. As will be shown later in Section 4.2.10, polarization mismatches between the beams impinging on the photoreceivers have a limiting effect in this experiment. They in particular increase the coupling of temperature fluctuations, drifts or oscillations into the measure-

4 Implementing an optical three-signal test

ments. At this point, due to the lack of the later acquired knowledge, the polarizers were removed because of their apparently limiting effect. The same applies to the cardboard baffles, which were not stable enough for the process of evacuating which was performed subsequently.

4.2.2 Influence of air in the interferometers

The chamber was evacuated with the goal of probing for the effect of the refractive index influencing the three-signal measurement. Additionally, it was assumed that an increased thermal stability would have a positive effect on the π measurement as well.

In a first trial stage, only the piston pump was used shortly to get to pressure levels close to 10 mbar. Afterwards the chamber was sealed using the gate valve and a measurement was taken. In a second stage, the turbopump was used to pump down to below 1×10^{-4} mbar before the chamber was sealed again and another measurement was taken. Finally, it was tried to decrease the coupling of laboratory temperature fluctuation into polarization via the fibers of the chamber feedthrough fibers. For this purpose, $\lambda/2$ wave plates and polarizers were added in front of the fiber couplers of the laser preparation to adjust the polarization to the fiber slow axis. The set of measurements is presented in Figure 4.7. Both the three-signal and π measurement showed improvement due to the evacuation. The three-signal noise dropped significantly in the upper mHz band and was dominated by an $1/f$ -like noise shape. The π measurements supposedly benefited from the removal of the photoreceiver polarizers. While the further decreased pressure improved the latter, the three-signal measurement actually deteriorated. The work on the temperature-polarization coupling yielded some improvement. It should be stated that measurements were typically taken after a thermalization time which varied between one and several hours or could even be several days for high vacuum.

Until now, the signal amplitudes and laser amplitudes have not been considered at all. Thus in the next step their coupling into the phase measurement was investigated.

4.2.3 Amplitude coupling

As a straight forward option, the amplitude of one slave laser was modulated via the pump current with a sinusoidal signal, see Figure 4.8. The I values of the LISA phasemeter normalized by their respective mean value are plotted as the measure for the relative heterodyne amplitude fluctuations. As

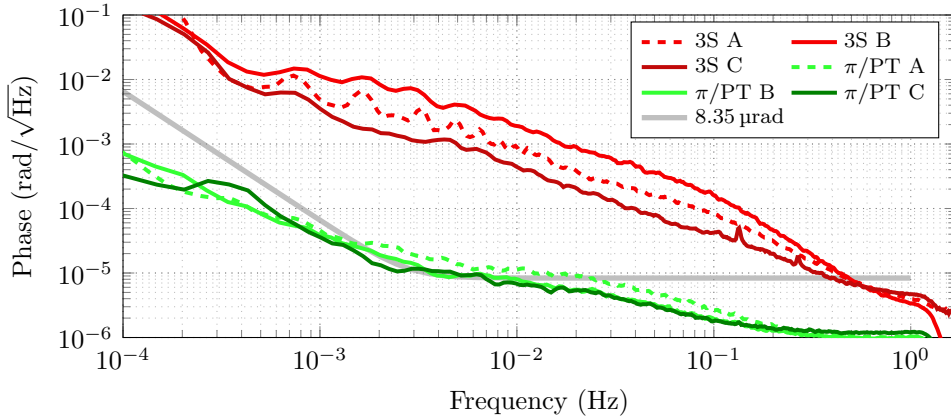


Figure 4.7: Application of different vacuum levels and polarization control. The dashed lines are π and three-signal measurement with around 10 mbar, light lines with 1×10^{-4} mbar and dark lines with additional polarizers in front of the feed-through fibers.

it turned out, this modulation coupled into the frequency of the laser. Thus it was desirable to be able to differentiate between effects of the amplitude and effects of the laser frequency coupling via possible dynamic range limitations. Consequently, a measurement with tighter frequency locks by means of higher gain and therefore higher suppression of the frequency distortion was conducted for comparison. It can be looked up in Appendix C.1 and verifies that the observable effect is independent of the gain and thus not caused by dynamic range limitations.

Several things should be noted here. Firstly, a non-linear transfer of the sinusoidal modulation into the heterodyne amplitude measured with the phasemeter is visible. In particular it can be seen that even the signal in which the modulated laser is not involved directly is affected. Reasons are not clear. Secondly, a coupling into the three-signal measurement and π measurement, which also shows contributions at higher harmonics, occurred. However, a direct linear relation between the two graphs cannot be made, as for example the second harmonic is dominating in the relative heterodyne amplitudes but not in the phase measurements. All in all it is not entirely clear how the signal inserted as pump current modulation is finally transferred to phase noise in the measurements. In order to be able to characterize the noise as either testbed or phasemeter noise, an electric testbed for the phasemeter was assembled.

4 Implementing an optical three-signal test

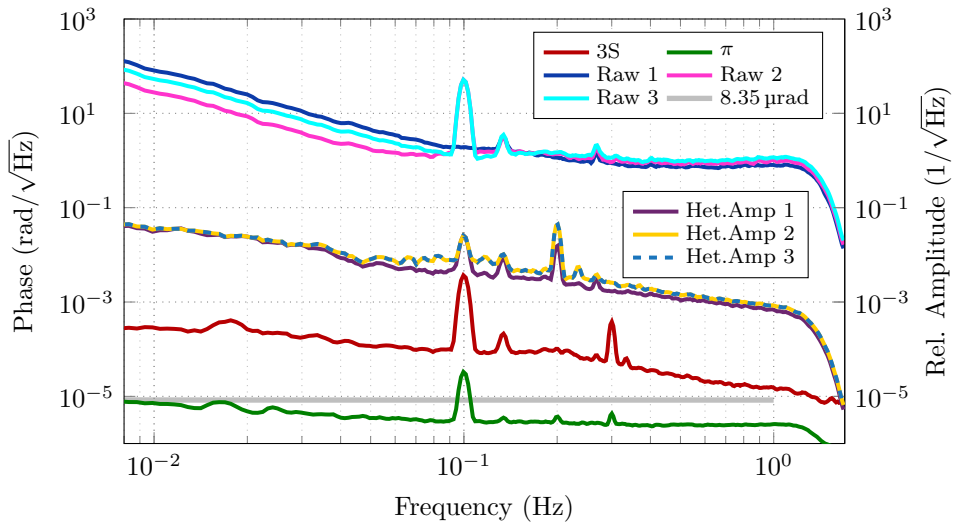


Figure 4.8: Coupling of single laser amplitude modulation. The modulation couples non-linearly into the different heterodyne amplitudes and also affects the differential frequencies. Most importantly, a coupling into the three-signal measurement and π measurement is visible.

Electrical and digital tests of amplitude coupling

The phasemeter’s electrical testbed to characterize the amplitude coupling is a slight deviation of the earlier described split measurement. Two signal generators interlocked via a 10 MHz reference and set to the same output frequency serve as equal signal sources for two phasemeter channels. It was not expected that the setup could provide sufficiently low testbed noise around $6 \mu\text{rad}/\sqrt{\text{Hz}}$. However, it allowed for the generation of a differential amplitude modulation in the two channels. This is realized by a third generator driving one of the amplitude modulator inputs. The frequency dependence of the coupling was probed with independent measurements at different modulation frequencies. The measurement was conducted without applying a pilot tone as it is not needed for coupling measurements. Plots of spectra of the relative heterodyne amplitude as well as the associated split measurements in the same color are shown in Figure 4.9. The matching colors indicate the relative amplitude spectra and absolute phase difference spectra of a single measurements. They were computed with a flat top window (HFT90D) [50] for proper peak detection. A frequency independent coupling coefficient of approximately 0.01 rad/1 was derived from the mea-

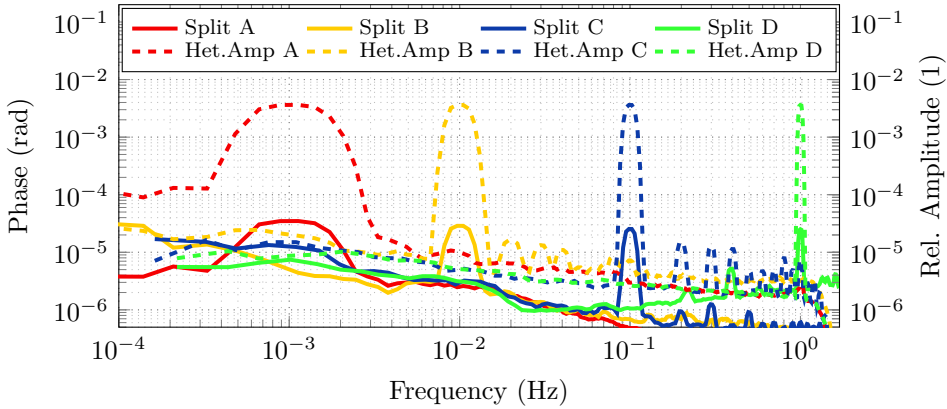


Figure 4.9: Electrical coupling tests for differential amplitude modulations. Four measurements at different frequencies reveal a coupling factor of 0.01 rad/1.

measurements. A repetition with a DC heterodyne amplitude twice as high yielded no changes, indicating that no saturation effects are present. The coupling coefficient measured here does not fit when applied to the optical setup, neither for the three-signal measurement nor for the π measurement. The three-signal measurement shows a higher coupling of about an order of magnitude. However, it should be kept in mind that as discussed before the relation between the laser amplitude modulation via the pump current and the three-signal phase is non-linear and might not even be direct. The π measurement in contrast shows lower coupling by an order of magnitude compared to the electrical test. It could be explained by the fact that the amplitude modulation is common mode in the π measurement and thus might cancel out partially. Likewise, similar investigations with an earlier prototype of the phasemeter came to the conclusion that in particular the differential amplitude modulation is critical [51]. Also it cannot be excluded that the amplitude modulation within one of the signal generators creates phase noise. It would be indistinguishable from phasemeter noise. Therefore the estimated coupling coefficient should be regarded as an upper bound.

In order to verify that the coupling is not a principle issue of the ADPLL phasemeter core, a purely digital testbed was developed. The testbed was designed as an absolute tests similar to the one described in Section 3.2. An independent NCO acts as a source and generates a sinusoidal signal which is captured by one of the ADPLLs. The NCO consists of a PIR, a PA register and a LUT, as it does in the ADPLL. This allows for a direct comparison of the phases by subtracting the PA registers. A sketch of the design is

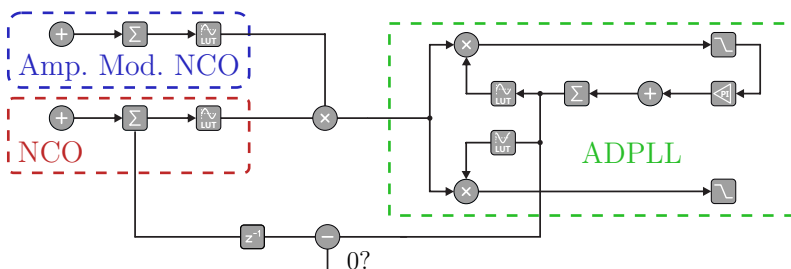


Figure 4.10: Schematic of a digital absolute ADPLL test. The reference phase is generated with an NCO identical to the one in the ADPLL. Hence the PA registers can be compared directly. A second NCO provides an amplitude modulation.

shown in Figure 4.10. To avoid a comb filter-like behavior due to different delays, the source PA register is delayed by the same amount of digital taps that the signal needs to traverse in the ADPLL. Finally, a second NCO creates a low frequency sinusoidal signal which it utilized to modulate the source's output. The measurement conducted with the setup is presented in Figure 4.11. It was done with the ADPLL design used throughout this thesis. A high source frequency noise of $1 \text{ kHz}/\sqrt{\text{Hz}}$ at 1 Hz and a $1/f$ shape dominating from 10 mHz down to lower frequencies was applied. Again, the single tone amplitude modulation was carried out at different frequencies in several runs. The associated absolute phase errors are indicated by matching colors. It seem that there is no significant frequency dependence and the coupling factor can be estimated to about $1 \times 10^{-5} \text{ rad/1}$. An additional test using a third order filter for second harmonic suppression showed a even further decreased coupling factor of $1 \times 10^{-7} \text{ rad/1}$. This is assumed to be related to the mechanism explained in Equation (2.37). There, a higher filter order effectively reduces the absolute fluctuations of the loop gain G that occur due to the amplitude changes and that can influence the coupling.

In summary, the tests show that the digital design provides quite high suppression of relative heterodyne amplitude noise. Thus the digital phase-meter core can be neglected as possible noise coupling mechanism. In a next analysis step, the measured coupling was converted into a noise projection.

Amplitude noise projection

As the laser amplitude modulation did not yield the possibility to estimate a linear coupling coefficient, the one obtained from the electrical testbed was used to generate a noise projection of amplitude to phase. For this

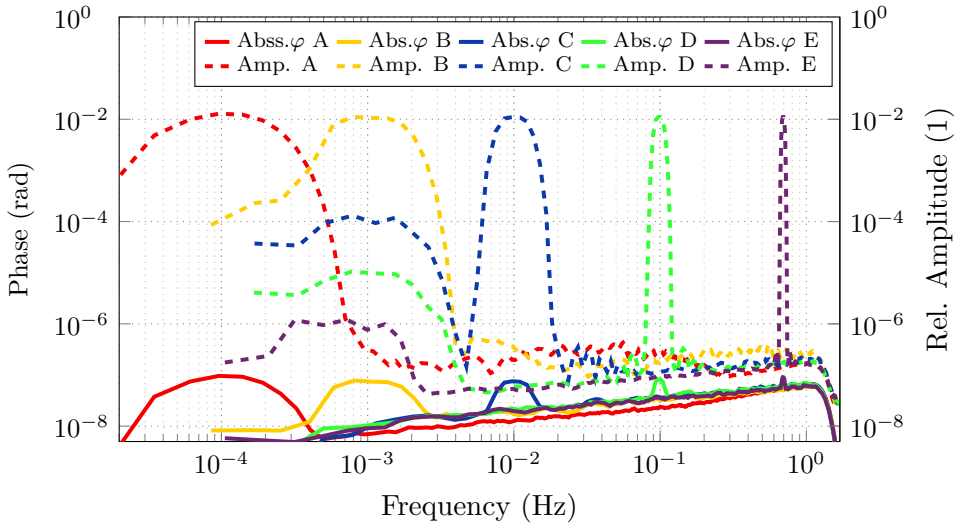


Figure 4.11: Digital coupling tests for absolute amplitude modulations. Five measurements at different frequencies reveal a coupling factor of 1×10^{-5} rad/1.

purpose, the data of the last three-signal measurement in Figure 4.7 was utilized again. Figure 4.12 shows the result (top). The projected curve is the RMS sum of the three involved heterodyne amplitudes multiplied by the estimated coupling factor. The noise was overestimated and is above the measurements. As already discussed, this might be due to the insufficient estimation of the coupling coefficient in the electrical testbed. Nevertheless, the noise shape looks fitting and thus it was decided to investigate the coupling further. A look at the time series (Figure 4.12, bottom) of the heterodyne amplitudes reveals rather rough jumps. During the setting of the frequency operation points of the lasers in terms of primarily crystal temperature but also pump current, the main goal so far was to get settings with which a beat note could be found for all three laser combinations, without taking into account mode hop regions. A mode hop means the laser power is split between different laser modes that both exhibit enough gain to oscillate in the crystal resonator. Pushing the temperature further away from this point leads to less gain for one mode and more gain for the other, until only the latter keeps oscillating. While the laser is in the mode hop range, temperature fluctuations in the laboratory can couple strongly via this mechanism. Consequently, it was tried in a next step to find operating points that can provide three beat notes without mode hops.

4 Implementing an optical three-signal test

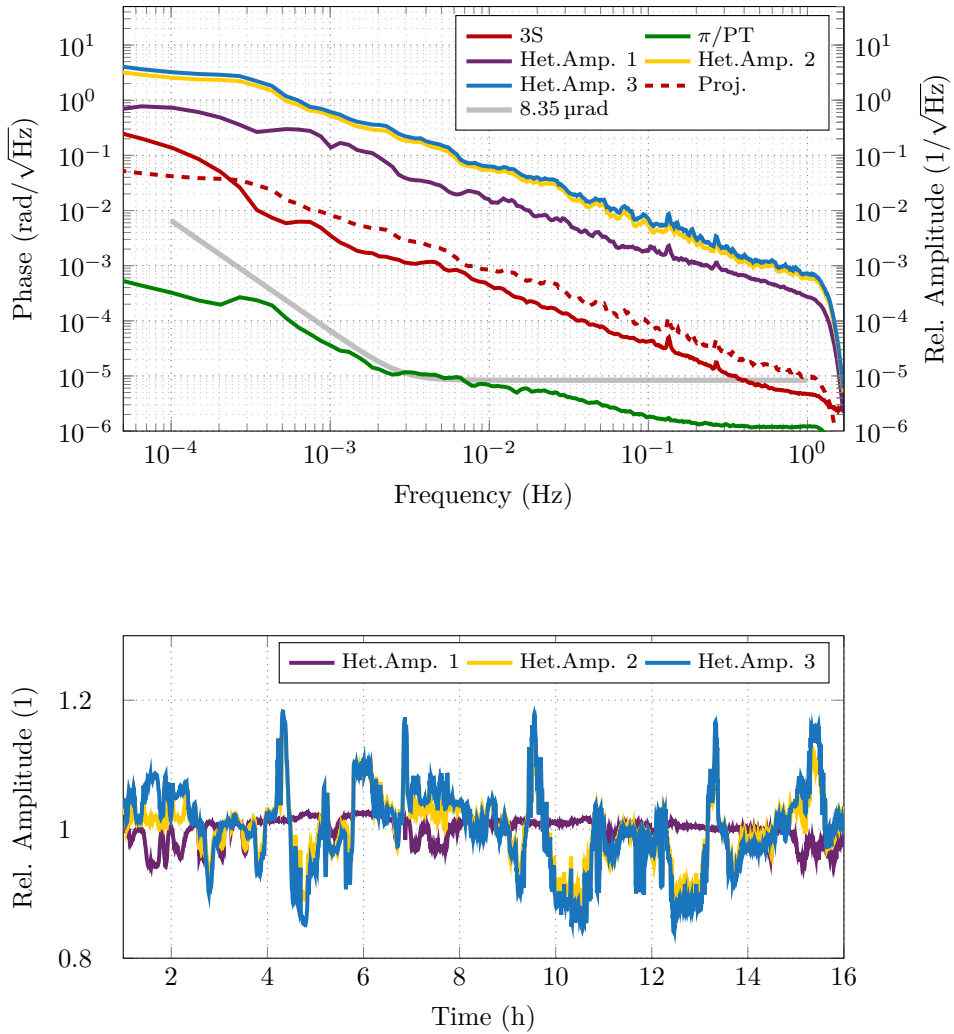


Figure 4.12: Amplitude noise projected to phase noise and its representation in a time series. The noise projection on the top shows an overestimation of the coupling factor. The time series of the relative heterodyne amplitudes on the bottom reveal prominent jumps.

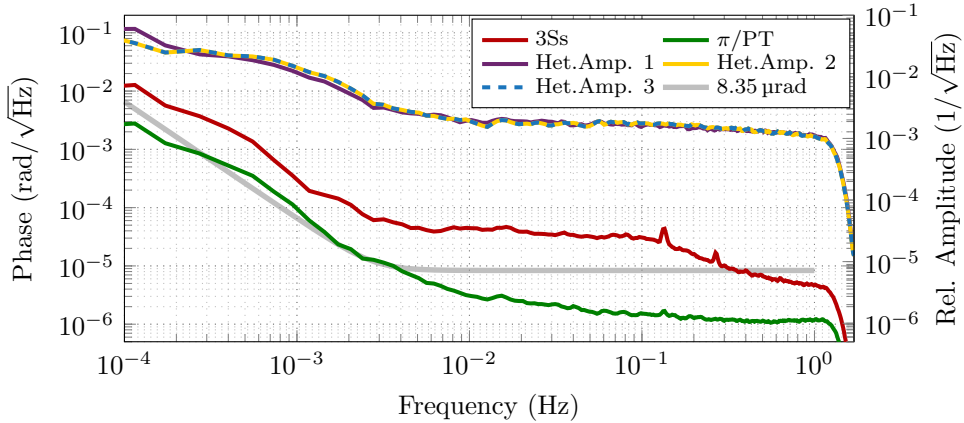


Figure 4.13: Measurement with optimized laser operation points. A reduction of the amplitude fluctuations as well as the phase noise was achieved.

Adjusting laser operation points

The tool of choice for the task at hand is a SFP interferometer. It can be utilized to probe a laser beam for multi-mode operation. It was applied to all three lasers individually via split beams on the preparation bench. Thus it was possible to recreate a more precise temperature map of the mode hop ranges. It can be looked up in Appendix D.1. Subsequently, the temperatures of the three lasers were changed within the mode-hop-free regions until three beat notes were found. This was constrained by the requirement for the beat notes to exhibit values between 5–25 MHz, according to the LISA requirements. It was further complicated by the fact that one of the lasers was a newer model with a different temperature profile. Figure 4.13 shows a measurement with the new operation points. The first thing to recognize is the improvement of the three-signal measurement, which loses its former $1/f$ behavior. In correlation to it also the heterodyne amplitude spectral densities experience a similar effect. It should however be noted, that despite the correlation, the causality was not entirely clear up to this point. Instead of a coupling via the amplitudes, the phase measurements might as well have been limited by phase distortions directly caused by the mode hops. Nonetheless, in order to explore whether the three-signal performance could be improved further by reducing amplitude noise, a laser amplitude stabilization scheme was implemented. It used the split beams on the laser preparation bench. Single element photodiodes were used to capture the fractions of the laser power. These were fed to an analog servo built by

Germán Fernández Barranco. The generated actuator signal was used to modulate the laser pump current. However, it turned out that the stabilization performance was heavily dominated by thermally induced noise in the sensor path. This becomes clear when considering that the band for the desired stabilization is in the mHz regime. Here, temperature fluctuations are dominant as their spectral power typically exhibits an $1/f$ shape. Observable coupling points were reflectivity and transmissivity of optics in the beam path which change with drifting temperature. Further issues could be beam pointing and sensor noise in the electronic path. Former studies dealt with these issues and could only solve them with greater efforts [52].

Therefore, it was tried to follow another observation from the latest performance measurement. The noise shoulder visible in the upper mHz regime of the three-signal measurement accompanied with the two small peaks in Figure 4.13 could be found likewise in the digital actuator signals of the laser piezo frequency locks. A subsequent assumption was that a coupling via the single channel phase noise was occurring. The latter in turn is influenced by the locks. For example, an apparent coupling would be via dynamic range limitations. In order to probe for this, an electrical sinusoidal signal was applied to the unused piezo modulation input of the master laser. The associated plots are shown in Figure 4.14. Besides a visible coupling, a severe deterioration of the π measurement towards lower frequencies was observable. It was discovered only later that the reason was a flawed fiber connector. The issue is explained in detail in Section 4.2.9.

As a slight coupling was visible, further investigations were conducted in order to reduce coupling or at least the single laser phase noise. The latter was tried by increasing the frequency lock suppression. However, the single channel noise observable with the main phasemeter hit a limit that could not be surpassed by further raising the lock gains, while an out-of-loop (OOL) sensor on the laser preparation bench still showed improvement. The out-of-loop sensor tracked the complementary port of one recombination beam splitter on the optical table of the laser preparation. A first assumption was that the discrepancy was caused by phase noise added by the long feed-through fibers. In a next step, the signals from the chamber were split with a resistive splitter and fed to the LISA phasemeter as well as to the auxiliary phasemeter. Additionally, the OOL sensor on the preparation bench was monitored with both phasemeters. The discrepancies are illustrated in Figure 4.15 when comparing the blue and cyan lines. In particular the auxiliary phasemeter shows less noise in the measurements than the LISA phasemeter. Finally, this was traced back to the clock noise between the two phasemeters. Consequently, a clock synchronization was established by

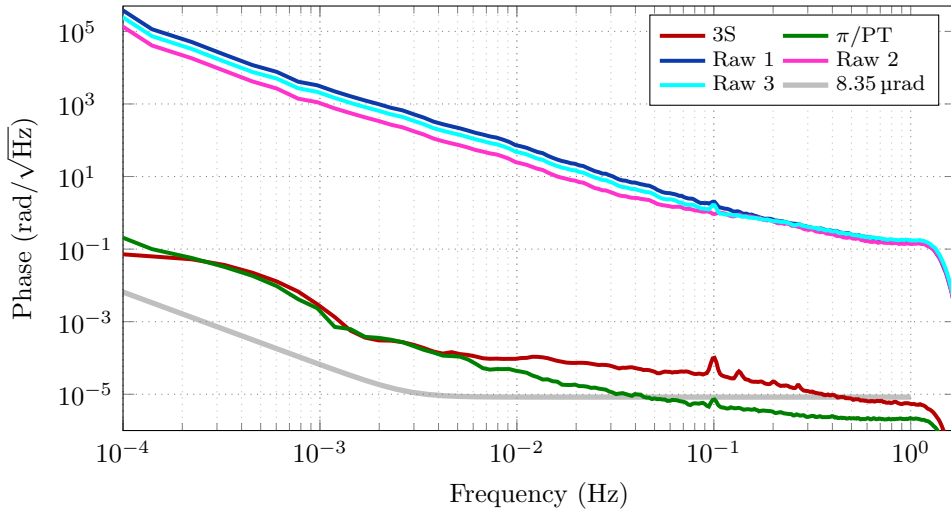


Figure 4.14: Frequency modulation with master laser piezo. A coupling into the phase measurements is visible.

routing out the 80 MHz digital clock of the main phasemeter via a DAC card. It was then used as external clock for the auxiliary phasemeter with a re-configured clock tree. This led to aligned noise levels (pink in Figure 4.15), which shows that the initial difference was mostly based on the differential clock noise. The residual discrepancy between the OOL measurements towards sub-mHz frequencies is not entirely clear.

4.2.4 Measurements with synchronized clocks and lock to Iodine reference

With the clock synchronization it was possible to push the single channel phase noise applied to the LISA phasemeter further down. A measurement conducted under these conditions is presented in Figure 4.16. No significant impact can be observed in the upper mHz regime of the phase measurements.

While the investigation took into account solely *differential* laser frequency noise so far, it was extended to probe for an improvement using a more stable master laser frequency. As mentioned in Section 3.5, one possible coupling can occur via unequal arms in the Hexagon. An Iodine stabilized NPRO laser (Prometheus by Innolight/Coherent) was used as the absolute reference. As it was located in an adjacent laboratory, its light was transmitted via an optical fiber to the laboratory hosting the Hexagon

4 Implementing an optical three-signal test

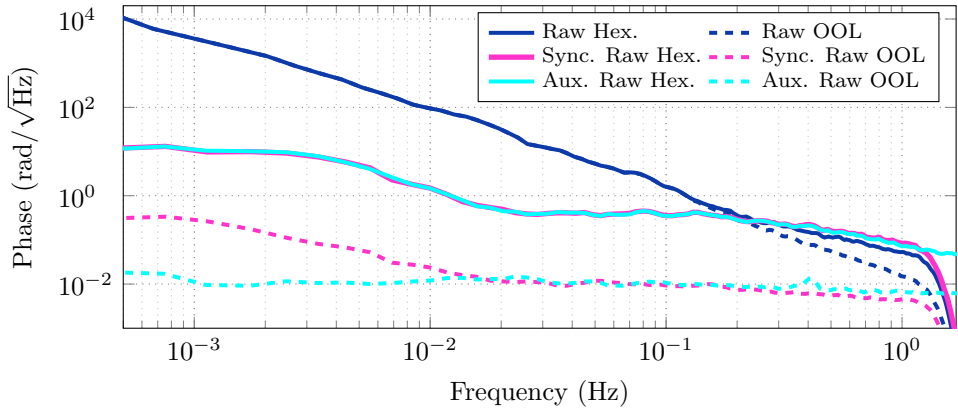


Figure 4.15: Comparison between single channel raw phases measured with main and auxiliary phasemeter. Two sensors measuring the same beat note were tracked. One was in the chamber while the other one was located in the laser preparation as an OOL sensor to the frequency lock. The measurement was done with and without the clocks being synchronized. The result shows that the initial difference is mostly based on differential clock noise.

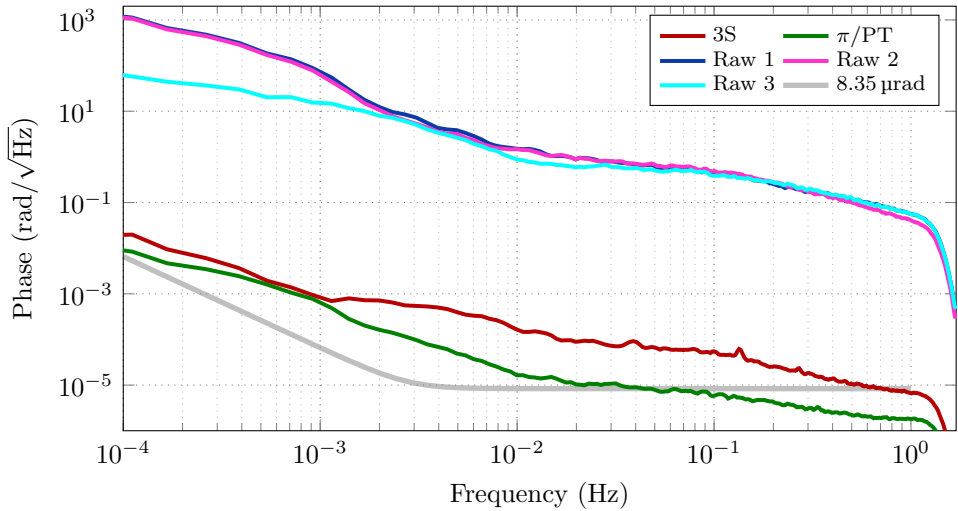


Figure 4.16: Performance measurement with low single channel raw phase noise due to clock synchronization. While the raw phase noise could be reduced successfully, the differential phase measurements showed no improvement.

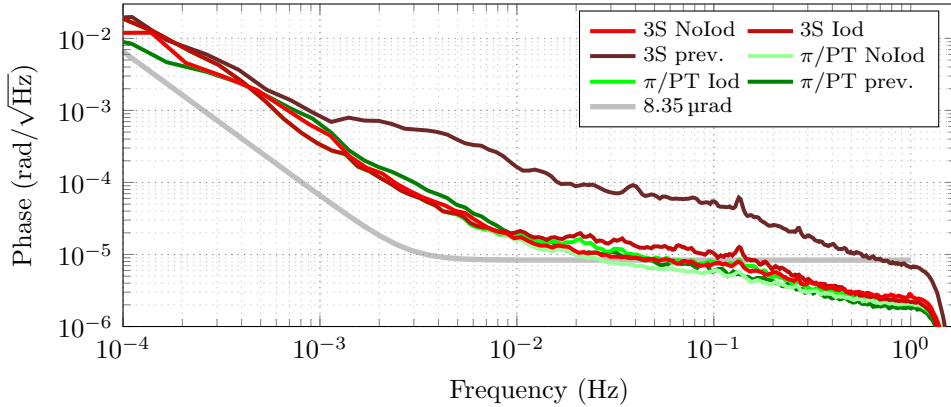


Figure 4.17: Changes in laser operation points to accommodate for lock to Iodine reference. The measurements with and without the applied lock as well as the previous measurement as reference are shown. The major effect visible in the three-signal measurement is assumed to be due to the changes of the operation points rather than the Iodine reference.

and the preparation table. Here it was coupled out and interfered with a split beam of the master laser. The created beat note was tracked by a photoreceiver connected to the auxiliary phasemeter, which could then establish another offset frequency lock. Like with the beat notes between the preparation lasers, the master laser needed to be set in a temperature range in which a beat note was created within the bandwidth of the photoreceivers and the auxiliary phasemeter. This is basically a more complicated version of the scenario with three lasers only. Nevertheless, new operating points could be found and all locks were set up. While a first measurement seemed to reveal an improvement due to the absolute reference, an even slightly better performance could be achieved when the lock to the Iodine laser was switched off again, see Figure 4.17. It is not entirely clear what mechanism is responsible for the improvement. A possible reason could be again the changed operation points. However, this time effects due to the mode-hop-free regions can be excluded.

While the test performance dropped below the LISA reference in the upper measurement band, the lower frequencies still exhibited the severe rise in noise mentioned previously. Thus efforts were focused on finding the reasons of this low frequency behavior.

A likely candidate were the photoreceivers, or more specifically their temperature dependence. During the earlier investigation, the four photoreceivers were equipped with temperature sensors. To be more precise, the

4 Implementing an optical three-signal test

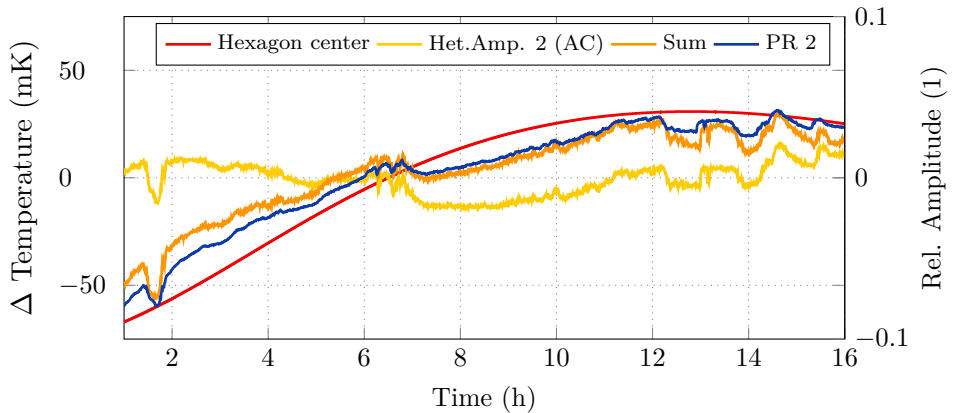


Figure 4.18: Composition of photoreceiver temperature fluctuations from environment and impinging laser power in terms of the heterodyne amplitude. Only the AC part of the latter is considered and is summed up with the reference temperature at the Hexagon center.

sensors were taped onto the OPs of the TIAs. Additional sensors were installed on the top and the bottom of the chamber as well as in the center of the Hexagon. One was left free-floating.

The sensors themselves are based on a design by Gerhard Heinzl. Here, a PT10000 is used within a Wheatstone bridge which is read out using four-terminal sensing with switching voltages. The switching circuitry is hosted within an analog front end on a PCB which can read out up to 8 sensors. ADCs digitize the signals and an FPGA collects the data and interfaces with a client PC.

A direct temperature control of the whole photoreceiver seemed cumbersome. However, a correlation between photoreceiver temperature and the heterodyne amplitudes was observed in the time series. It is assumed that this was either due to the beam power itself heating the device or the changing power consumption of the OP for different signal amplitudes. In fact, the temperature can be expressed as a combination of the environmental temperatures and the aforementioned influence of the amplitude. This can be shown with the time series of an exemplary measurement like in Figure 4.18. In an attempt to utilize this relation, it was tried to stabilize the laser amplitudes and thus with it the photoreceiver temperatures.

In contrast to the earlier described efforts towards an amplitude stabilization, which used the pump currents of the lasers, now fiber-based variable optical attenuators (VOAs) (reflective style) by OZ optics were used as ac-

tuators behind the fiber couplers of the laser preparation.

The VOA are based on two parallel fibers. A micro mirror is responsible for the coupling of the light between the two. It can be steered with an applied voltage, thus changing the coupled power. The voltage-attenuation relation is exponential. Therefore they were usually used with offset voltages setting the desired operation point. Small actuator signals can then assure an approximately linear operation.

Within the progress of the experimental part of this thesis, different choices for sensors and servos used in the amplitude stabilization were made. One is described in more detail in the following section.

4.2.5 A low-frequency amplitude stabilization scheme via digital heterodyne amplitude decoupling

The experimental setup at this point exhibited the technical issue that no power pickups were available in the chamber to capture the laser powers separately. All the photoreceivers at the Hexagon output ports capture the power of two lasers. Thus no single beam laser power error signal can be obtained easily during nominal operation. An approach to bypass this issue is to use the three different Hexagon outputs in a system of equations with the three laser powers being the unknown variables. In particular are the AC parts, in terms of the heterodyne amplitudes, used here. As the I values of the ADPLLs provide a measure of the latter, the system for the decoupling of the amplitudes was implemented in the digital domain. The same applies to the servo. In order to describe the system of equations, the ADPLL I values are denoted as I_j and are defined in terms of single laser powers P_i :

$$I_1 = g_{ab} \cdot \sqrt{P_a P_b} \quad I_2 = g_{bc} \cdot \sqrt{P_b P_c} \quad I_3 = g_{ac} \cdot \sqrt{P_a P_c} \quad (4.1)$$

where g_{kl} are proportionality factors including the heterodyne efficiency between the two lasers k and l . The system can be solved for the single laser powers and combined proportionality factors g_j as follows

$$P_a = g_a \cdot \frac{I_1 \cdot I_3}{I_2} \quad P_b = g_b \cdot \frac{I_1 \cdot I_2}{I_3} \quad P_c = g_c \cdot \frac{I_2 \cdot I_3}{I_1} \quad . \quad (4.2)$$

While written down easily in formula, the actual implementation of the system in electronics and in particular in the digital fixed point arithmetics of an FPGA is not straight forward. The primary issue here is the division. In the implementation for this thesis, pre-tailored intellectual property (IP) blocks from Xilinx were utilized for the division. To analyze and adapt the

4 Implementing an optical three-signal test

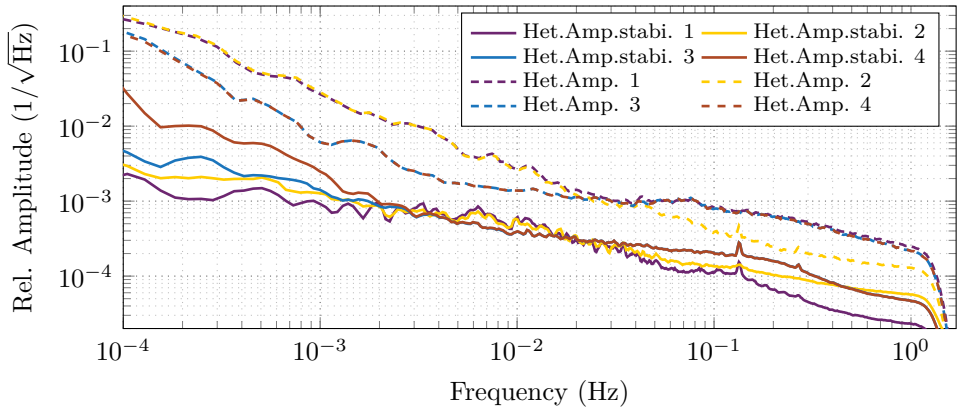


Figure 4.19: Laser amplitude stabilization via digital decoupling of heterodyne amplitudes. A noise suppression is observable when comparing the test to a similar measurement without stabilization. A lower suppression is detected with the complementary photoreceiver which is OOL (brown line).

required amount of bits in the divisor block the obtained error signal was transmitted to the client PC where it was compared with the same values computed in software. It should be noted that in principle the whole digital part could have been implemented in software. However, the transmission delay between FPGA and PC proved to be insufficient for a unity gain frequency that would provide suppression in the LISA band. Instead, the obtained error signals are subsequently fed into a PI controller on the same FPGA and are then transformed to the analog domain with the assembly's DAC card. For the actual optical setup, the output signals are conditioned by attenuators and low passes and finally applied to the VOAs.

The scheme was initially implemented in a phasemeter with the same specifications as the auxiliary one and was tested in an electrical three-signal setup, similar to the one presented in [29]. Afterwards the digital design was integrated into the auxiliary phasemeter. Three additional ADC channels are used to track the beat note signals that are split with resistive splitters from the signals captured by the main phasemeter. A result is shown in Figure 4.19 along with the comparison to a measurement with a similar setup but without stabilization. The signals of the photoreceivers tracked with the main phasemeter are shown. They exhibit a noise suppression for the heterodyne amplitude, in particular towards low frequencies. Nevertheless, the first three signals can be considered as quasi-in-loop, as they are electrically split from the in-loop signal behind the critical temperature dependent

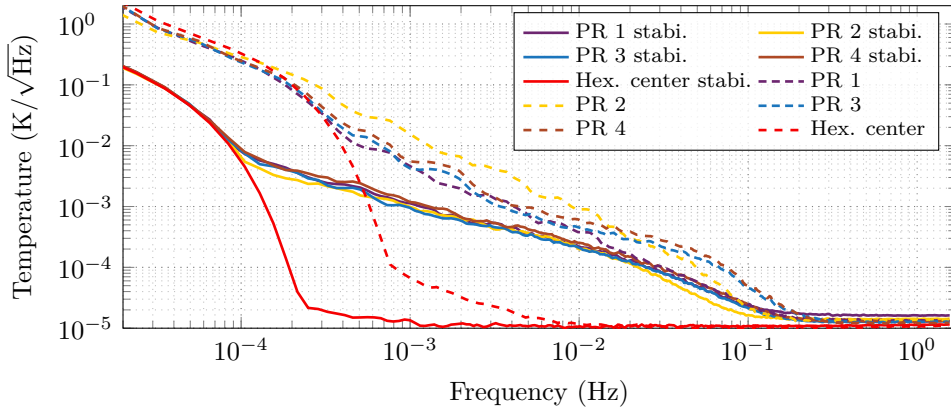


Figure 4.20: Photoreceiver temperature fluctuation suppression due to amplitude stabilization.

noise sources. The signal of the photoreceiver not directly involved in the loop exhibits a prominent rise to lower frequencies. Assumptions are that those are caused by temperature effects outside the loop, like for example mirror movement. In order to check the effect of the amplitude stabilization on the temperatures at the photoreceiver OPs, the latter were compared as well to the case without the stabilization. The comparison is presented in Figure 4.20. In the mHz regime, the temperature noise could be suppressed successfully. Presumably this applies also to lower frequencies, however it is dominated here by the environmental fluctuations. Unfortunately, no improvement could be observed in the phase measurements, as can be looked up in Appendix C.2.

4.2.6 A low-frequency temperature stabilization scheme via cyclic control of single laser powers

Additionally to the amplitude and temperature stabilization just described, another, more direct variation was tested. It utilized the temperatures on the photoreceivers themselves as error signals. As they were available digitally on a client PC, the required servo was implemented in software. The actuator signal for the VOAs was subsequently generated with a USB DAC box (model USB-3105) by Data Translation. The loop bandwidth was consequently limited by the temperature sensor readout box's sampling rate of around 3.125 Hz. Nevertheless the system was utilized for a proof of principle measurement. Similar analog attenuation and filtering as used before

4 Implementing an optical three-signal test

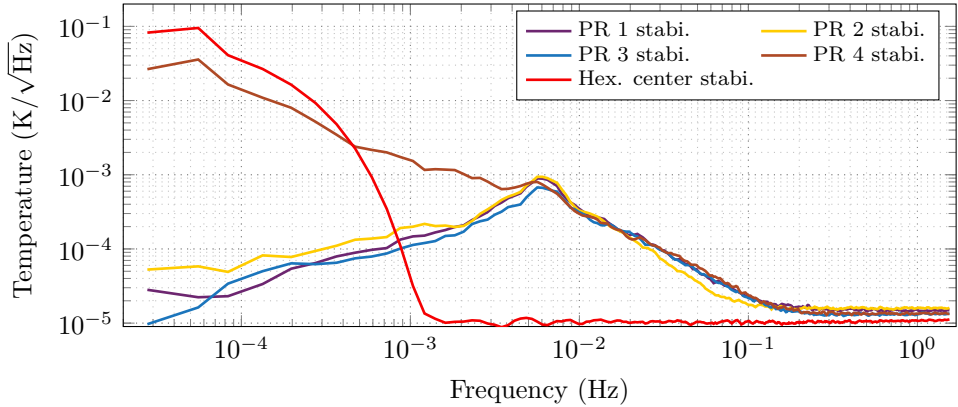


Figure 4.21: Photoreceiver temperature stabilization via laser power modulation. Noise suppression can be observed in the in-loop signals as well as slightly in the OOL one (brown line).

with the VOAs served as an analog back-end. The issue of two lasers impinging on a single receiver remained. In this scenario, a cyclic approach for the decoupling of the single laser powers was chosen where one laser power only controls the temperature of one photoreceiver. Consequently, it has to compensate for the actuation of the second laser impinging on the same receiver. The second laser in turn controls another receiver with the third laser simultaneously illuminating it. The third laser finally controls the last photoreceiver, with the first laser as second power source.

Taking into account a short relaxation oscillation, the scheme worked for a certain amount of time. This time was limited by the insufficient actuation ranges that could be achieved with the laser power in the current configuration. Eventually, the power became too low for the ADPLLs to maintain their locks. Additionally, the phase measurements could not be improved with the scheme. In any case, Figure 4.21 shows the plot of one trial measurement. The temperature itself shows suppression in the in-loop signal and slightly in the OOL signal, which is represented by the brown line.

The tested stabilization schemes did not yield a satisfying answer for the issue of amplitude and photoreceiver temperature coupling into phase. Thus a more direct approach was chosen, which is the direct temperature modulation close to the photoreceivers. The method is described in the next section.

4.2.7 Probing for temperature coupling into photoreceiver performance

To perform the noise hunting for the temperature coupling into the photoreceivers, the chamber was vented and two heating resistors were installed on a single photoreceiver, one close to the photodiode and one close to the OP. They were successively driven by modulation signals from the DAC box. The signals had to be amplified by a dedicated current amplifier. Furthermore, an additional temperature sensor was installed close to the photodiode to be able to differentiate between the effect on diode and OP. Figure 4.22 shows both measurements which were performed with slightly different modulation frequencies. As the chamber was vented, in particular the three-signal measurement deteriorated and is not shown. Also the π measurement showed additional noise in comparison to former measurements in air. The additional noise was ignored in the following, as the goal was to measure coupling coefficients. Here the coupling measurement was performed with the π measurement. The coupling seems to be quite weak in general. The most consistent interpretation of the plot is that the coupling is stronger in the OP than in the photodiode, as the bumps in the phase mostly follow the strength of the OP temperature peaks. The coupling coefficient can be estimated to be around 1×10^{-4} rad/K. As it turned out later, the temperature sensor on the photoreceiver had partially lost contact with the OP. Thus the actual temperature fluctuations might be higher than the measured one meaning the coupling coefficient would be even lower. In any case, the coupling was considered negligible. Nevertheless, the method of temperature modulation itself was carried on and was applied to other components like the fibers in the chamber.

4.2.8 Probing for temperature coupling via fibers

To implement the temperature modulation test of the fibers, a Peltier element was glued to the bottom of the thermal shield which then served as thermal body. One of the feedthrough fibers was subsequently taped on the top side of the element together with a temperature sensor. The purpose of the latter was to verify the applied temperature modulation. Again, only the π measurement was considered for the test. Figure 4.23 shows the results. The coupling is more severe than the one observed in the photoreceivers. It has to be taken into account that here only a small piece of the fiber is heated, thus the scenario cannot be directly compared quantitatively to the coupling via the photoreceivers. Apart from that, coupling via the fiber was

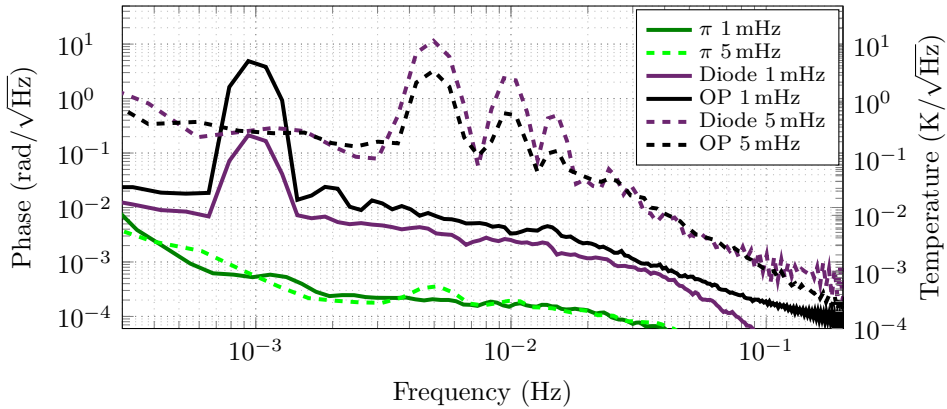


Figure 4.22: Coupling of temperature modulations near OP and photodiode at different frequencies. The coupling is rather weak and seems to happen mostly at the OPs, as the bumps at 1 mHz and 5 mHz show a similar ratio as the OP modulations.

still considered as a critical noise source and was thus the subject of further investigation. This investigation comprised the modeling of the coupling mechanism and the development of a compensation.

4.2.9 Temperature coupling via fibers: mechanism and compensation

In order to be able to understand the coupling at hand, it is useful to recapitulate the basic concepts of optical fibers, in particular of the polarization-maintaining fibers utilized here. The left side of Figure 4.24 shows the lateral cut through one for illustration of the following explanations. The right side shows a mathematical tool, namely a Poincaré sphere, used later to describe the polarization in the fiber. Light is transmitted through the inner core via total reflection on the boundary surface between the core itself and the cladding exhibiting a different refractive index. For the panda-style fiber shown here, two stress elements cause a break of radial symmetry in the fiber. This effectively creates two main axes with slightly different refractive indices making the fiber birefringent. It is thus desirable to match the polarization of incoming light with one of these two axes in order to maintain the light's polarization. For the further discussion, focus is put on some aspects of the fiber and its usage which are in particular important for the three-signal testbed. Firstly, the total reflection in a fiber is naturally not total in the sense of the word. Instead, the fiber exhibits a certain loss

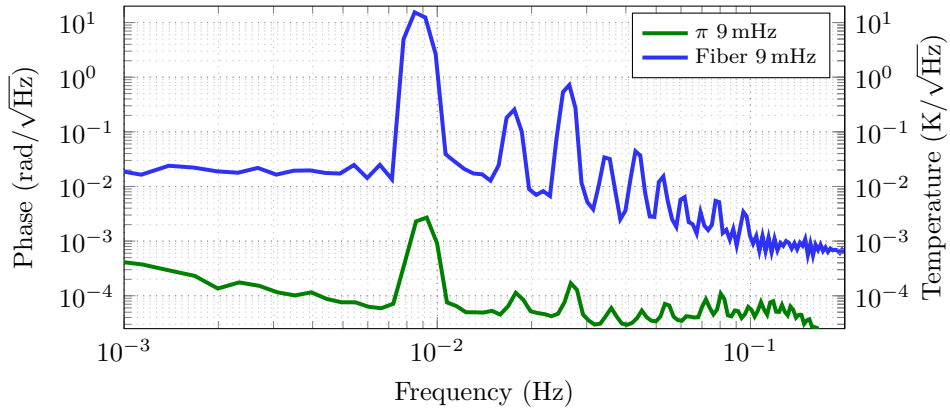


Figure 4.23: Coupling of temperature modulations applied to feedthrough fiber. A significant linear relation can be observed together with weaker non-linear components.

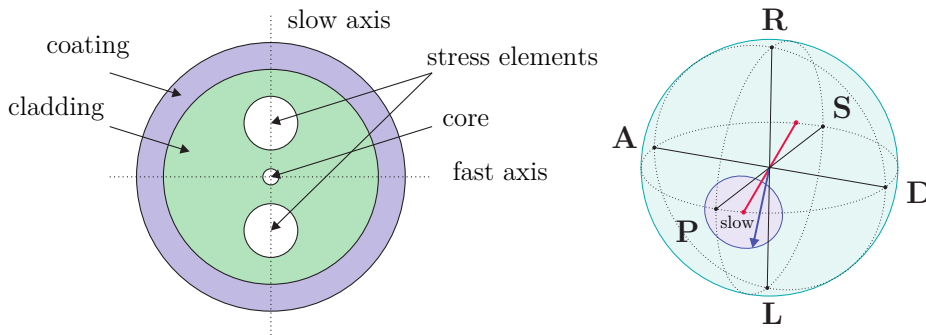


Figure 4.24: Sketch of a lateral cut through a polarization-maintaining fiber on the left and the tool to describe its polarization, a Poincaré sphere, on the right. Image credit: D. Penkert.

4 Implementing an optical three-signal test

of power which increases with fiber length.

Secondly, the light coupled into one of the two axes will undergo a phase shift if the fiber is distorted mechanically or stretched or compressed by temperature fluctuations. In the application of the three-signal testbed, this is not critical, as the induced phase noise will occur as common-mode at the input of the interferometer. It can be observed via comparison measurements between the auxiliary phasemeter and the main phasemeter like in Figure 4.15 and appears to be sufficiently low in terms of coupling via dynamic range limitation. It should be noted that the described effect of phase shifting is stronger in the fast axis than in the slow axis.

Thirdly, even for perfectly matched polarization at the fiber input with respect to one axis, a leakage into the other occurs. Hence the effective polarization measurable at the output depends on the fiber length and the effective wavelength in the two axes. Ideally, the parasitic polarization can vanish if the fiber length matches certain values and the leakages summed up over the whole fiber cancel each other out.

Fourthly, and most important at this point of the noise hunting, is the effect of the fiber as a birefringent optical component when the input polarization is not well matched to one of the axes. In that case, the incoming polarization can be formally decomposed into two components along the two fiber axes. After traversing the fiber experiencing different refractive indices, they can be recombined afterwards. Consequentially, the result depends on the refractive indices and more importantly on the fiber length. As mentioned earlier, the latter is prone to temperature fluctuations or mechanical distortions. When describing the state of the output polarization using a Poincaré sphere, the effect of the mentioned distortions can be visualized as a cyclic movement of the polarization state vector on the sphere's surface. The radius then depends on the mismatch at the fiber input.

Applying in particular the latter to the three-signal testbed, it seems likely that the temperature modulation and the environmental temperature fluctuations lead to polarization fluctuations in the Hexagon via the fiber. This leaves the question how those polarization fluctuations finally couple into phase noise. The question was left unanswered at that point. Instead, it was tried to improve the stability of the polarization. Apparently, the utilization of solely polarization filters in front of the photoreceivers was not sufficient. Thus an alternative solution was the filtering in front of the interferometer right after the FIOSs. As this would have involved putting components onto the ZERODUR® base plate possibly leading to distortion of the beam geometry and to additional ghost beams, the option was deferred at that time. The next most feasible alternative then appeared to be

the control of the polarization of the light within the fibers.

As stated earlier, the laser preparation bench was already equipped with wave plates and polarizers to ensure a proper polarization matching. Nevertheless, the whole experiment requires at least one fiber mating sleeve in between the couplers of the laser preparation and the Hexagon FIOSs. Mating sleeves match the slow axes of two fibers by mechanically matching their keys. These keys are metal noses indicating the slow axis of the fiber. Due to mechanical tolerances, the mating sleeves typically cause a slight orientation mismatch of the two involved fibers' slow axes. Hence even with a perfectly aligned polarization in the input fiber, it will be mismatched with respect to the slow axis of the second fiber. This effect can be avoided by replacing the final fiber mating sleeve with more sophisticated mechanics and optics. These replacements essential need to clean the polarization and match it to the final fiber.

As an implementation, FiberBenches by the company Thorlabs were chosen. In the following they will be referred to as fiber benches in general. They offer the possibility to put arbitrary optics between two fiber couplers, all attached to a short optical bench breadboard. The breadboard FT-38X100 with length 10 cm was chosen together with PAF-X-5-C fiber couplers. The initial design of the optics included a polarizer behind the input coupler for polarization cleaning. Then a 10:90 beam splitter served as a power pickup together with a slow silicon photodiode. It was added as a sensor for a future single laser amplitude stabilization. At the back end, a $\lambda/2$ wave plate and another polarizer were supposed to match the polarization to the output fiber in the output coupler. A picture of the assembly can be seen in Figure 4.25. As a proof of principle, one of the benches was installed as replacement of one mating sleeve between a fiber feedthrough and a fiber saver. The feedthrough fiber was subsequently modulated in the same fashion as in the previous measurement. As Figure 4.26 shows, the phase distortion associated with the temperature modulation was successfully suppressed.

To improve the overall performance of the π measurement, which utilizes two laser and two fiber paths, a second fiber bench was installed. Additional changes were conducted. One was based on the finding that one of the feedthrough fiber connectors exhibited a flaw. A screw, which serves for the fixation of fiber key and slow axis, was found to be loose. In particular when using a fiber mating sleeve, a random relation between slow axis and key leads to a mismatched polarization. As a first quick fix, the alignment between key and axis was renewed manually and was tightened again. Nevertheless, this technical issue can be considered as probable reason for the

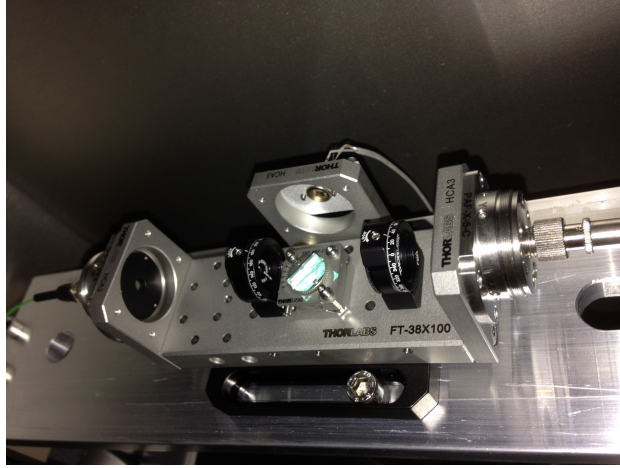


Figure 4.25: Photograph of a fiber bench assembly. The coupled light from the left is filtered by a polarizer in front of a power pickup via a 10:90 beam splitter. Behind it, a $\lambda/2$ wave plate serves for matching the beam polarization to the output fiber on the right.

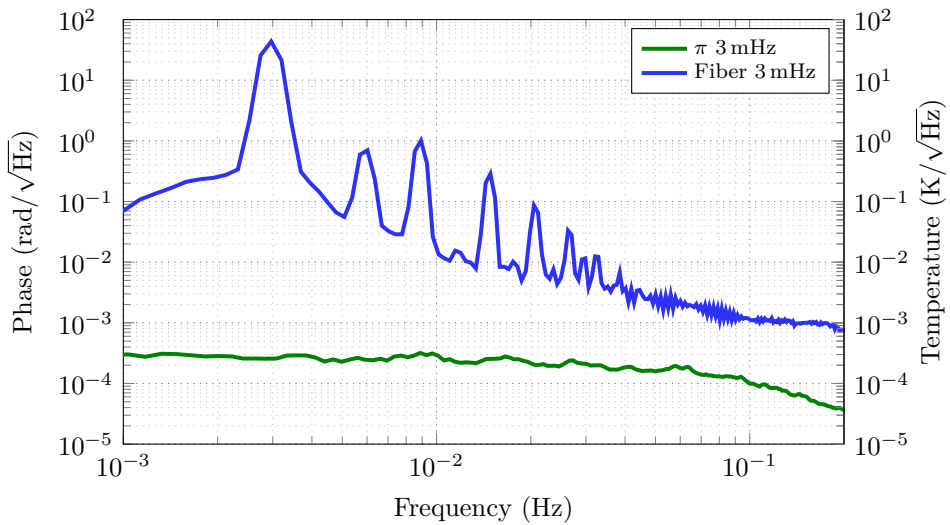


Figure 4.26: Temperature coupling via feedthrough fiber with subsequent polarization cleaning by a fiber bench. The coupling vanishes within the sensitivity of the current testbed.

deterioration of particularly the π measurements since the test shown in Figure 4.14.

Furthermore, the polarization filters in front of the photoreceivers were readjusted with the goal of matching their transmission axis to the surface normal of the Hexagon ground plate as reference. The alignment was done using polarizing beam splitters (PBSs). These split the light according to its polarization. The parallel polarization (p-pol) with respect to the optical bench is transmitted while the s-pol is reflected. The suppression factor of pure s-pol light leaking into in the transmitted light is called extinction ratio, similar as for the polarizers. A PBS was put carefully onto the bench in one of the π measurement interferometer output ports and was illuminated by a single laser only. Then ideally solely p-pol reaches the photoreceivers. Subsequently, the polarizers were aligned for minimal power. This should simultaneously adjust their transmission axis to s-pol. The method was performed on the same output port and with the same PBS for both filters which were involved in the π measurement. Thus one had to be moved after adjustment, with the assumption that the rotational adjustment was maintained. It should be noted that the finding that light was transmitted through the PBS hints to the fact that light is not injected into the interferometer with s-pol only. This point will be picked up later in Section 4.2.10.

Besides the described treatment of the polarization, stray light was taken into account. To limit the possible sources, cardboard baffles were put back in front of the photoreceivers and the laser not involved in the π measurement was blocked.

In order to be able to observe the experiments behavior past the relaxation time of temperatures subsequent to changes in the chamber, a long-term measurement was conducted. A time interval of it is used in Figure 4.27. It shows an improved long-term stability compared to a measurement done before the changes. However, doing this comparison also reveals a deterioration at the mHz range, presumably due to parasitic signals. This will be the topic of the next section.

4.2.10 Parasitic signals at microradian levels

In the measurement just presented, the limiting noise exhibits a relation reciprocal to the square root of the Fourier frequency. Yet it appears as a noise shoulder under less calm thermal conditions. With that being the case in many following measurements, this part of the noise floor will be referred to as “shoulder” in the following. The shape is typical for parasitic

4 Implementing an optical three-signal test

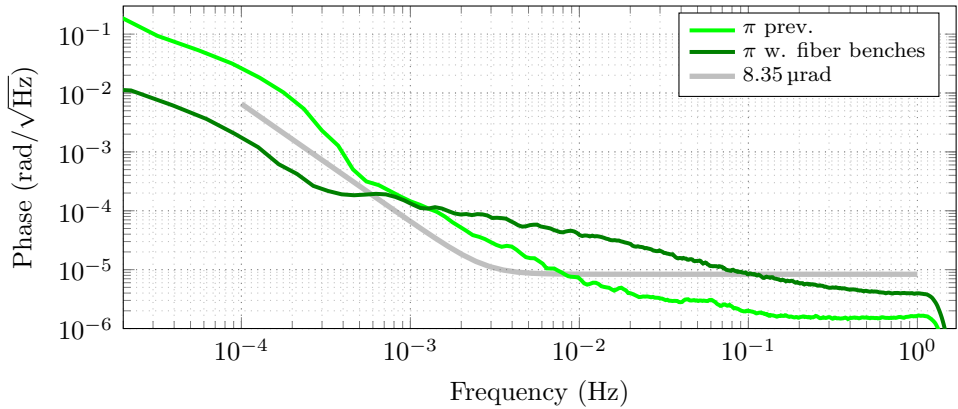


Figure 4.27: Comparison of π measurements with and without fiber benches, a fixed fiber connector, adjusted photoreceiver polarizers and baffles. The long-term stability could be improved while the mHz range exhibits a deterioration.

signals which are added to the desired signal as a small vector. During the progress of the experimental work conducted in this thesis, it later became clear the shoulder is a composition of different noise sources. A set of tests were conducted to investigate the origin of the parasitic signal. Assumptions were that it was most likely optical, possibly stray light, including parasitic polarizations.

After different fruitless tests, a significant effect was achieved due to an increase in power from the laser preparation. The power gain was obtained when the earlier mentioned flawed fiber was replaced and at the same time the associated beam path on the optical table was reworked. This minimized losses due to misalignment. To verify the effect of the power change, a gray filter was put in front of the fiber coupler of the reworked beam path to reverse the rise in power. The two corresponding measurements are shown in Figure 4.28. The gray filter has a fractional transmittance of about 0.29, which corresponds to a factor for the heterodyne amplitude of $\sqrt{0.29} = 0.54$. This factor was verified with the monitored I values. In the noise shoulder, the level ratios for the single measurements corresponds to the ratio of the heterodyne amplitudes as well. Thus it seems likely that the stray light source limiting at that point must have had its source on the beam path behind the gray filter. For a brief theoretical explanation, it is helpful to look at Equation (2.36). If assuming that the change in heterodyne amplitude only attenuates the desired signal, it is clear that it also effectively changes the ratio between desired and parasitic signal with the same factor. As a

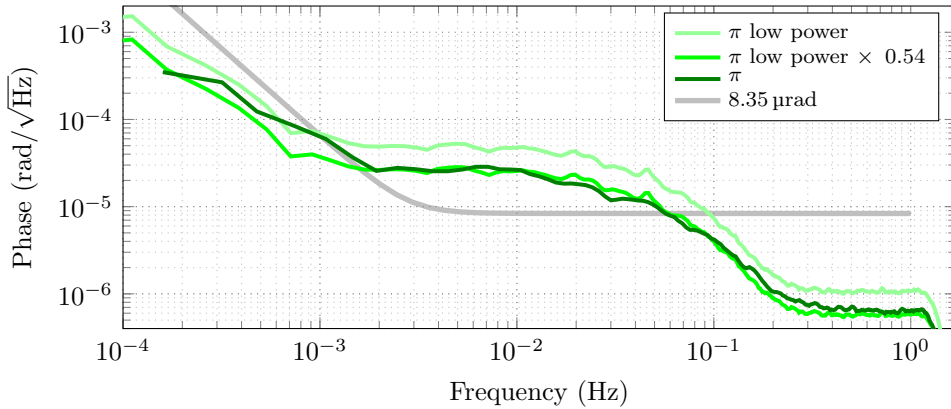


Figure 4.28: Impact of laser power attenuation with gray filter in front of single fiber coupler. The limiting noise sources could be amplified by the same factor that the heterodyne amplitude was reduced by.

brute force measure, the power could be increased more until the parasitic contribution vanishes. However, it would be more desirable to eliminate the source of the parasitic signal, thus decreasing the numerator in the aforementioned formula.

As a side note, in the frame of tests with different powers, another attempt for an amplitude stabilization was conducted. This time, the photodiodes on the fiber benches were used as sensors. The formerly used analog servo completed the all-analog control loop together with the VOAs as actuators. While the single laser powers could be stabilized to a certain degree, the stability of the heterodyne amplitude could not be significantly improved. Thus the loop was deactivated and the stabilization was not pursued further at that point.

Instead, in an attempt to learn more about the nature of the parasitic signal, the fibers in the chamber were once more equipped with Peltier elements and a temperature modulation was applied, see Figure 4.29. In contrast to the former modulation tests that showed an almost linear coupling, the temperature oscillation is translated into a broadening of the shoulder. Here, the modulation is applied to one of the involved FIOS fibers (therefore behind the fiber bench). The effect can be interpreted as an acceleration of the temperature-driven small parasitic vector's rotation, thus changing the signal dynamics in the argument of the sinusoid in Equation (2.36). This is a highly non-linear process. These observations led back to the question how the temperature fluctuations actually couple into the phase measure-

4 Implementing an optical three-signal test

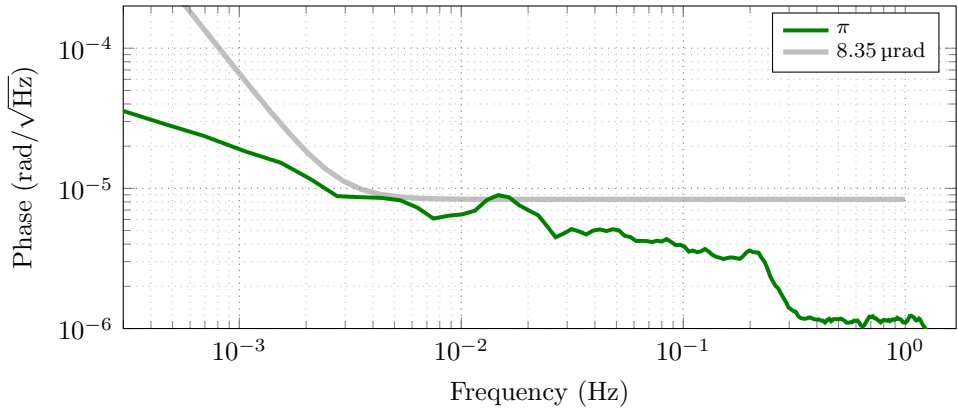


Figure 4.29: Non-linear impact of temperature modulation on fiber behind fiber bench. A broadening of the spectrum is visible. Presumably, the temperature modulation acts as driving source of a parasitic signal.

ments. As described above, temperature fluctuations changing fiber length can lead to polarization changes within the fiber. This naturally effects the polarization behind the fiber. Additionally, experiments carried out at the University of Glasgow suggested that the polarization changes within the fiber also influence the pointing at the fiber output and can thus induce angular pointing jitter. The latter might also occur directly by the mechanical distortions of the FIOSs due to temperature changes. To investigate the described mechanisms of direct polarization coupling and jitter, two test were conducted.

In the first, PBSs were carefully put directly behind the FIOSs in order to filter the distortions of the polarization before they can reach the interferometer. The PBSs were turned by 90° to allow the s-pol to propagate. A side effect was a loss in coherence of the single beams at the photoreceivers due to the slightly changed beam geometry and possible wavefront distortions. Accordingly, the heterodyne amplitude slightly decreased. In total, no significant effect on the noise shoulder could be observed. Also it should be stated that with the PBS behind the FIOSs only the π measurement was performable, as beams for the other output ports were blocked. As an alternative, more compact thin-film polarizers similar to the ones used in front of the photoreceivers were used as replacement. They also come with a higher extinction ratio between their transmissive and absorptive axes. The loss in heterodyne efficiency was even more severe though. Thus this option was dropped for the time being. It was later picked up again, as described

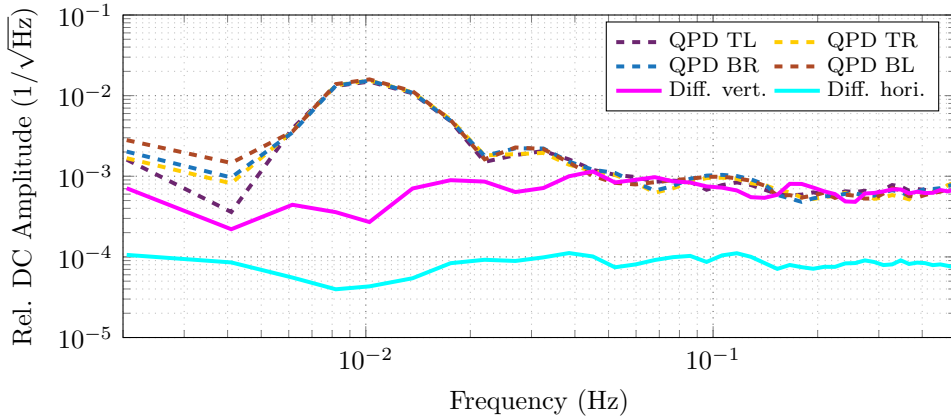


Figure 4.30: Test for coupling of fiber temperature modulation into beam jitter. A possible pointing should be visible in the differential measurements between the horizontal and vertical segments or the left and right segments. Within the sensitivities of this test, no such coupling could be observed.

in Section 4.2.10.

A second test was designated to check for beam pointing due to the temperature modulation. For this purpose, a QPR was installed in one of the open ports of the Hexagon. The port was illuminated by a single laser of the two involved in the π measurement only. The DC components of the four QPR segments were tracked with a data logger. Beam centering of the single laser beam was achieved via balancing the four DC values by adjusting the mirror between interferometer output and receiver. Subsequently, the attached fiber's temperature was driven in the usual fashion. The result is shown in Figure 4.30. The power on all four segments was oscillating in phase with the modulation frequency. This linear coupling into amplitude was already visible in the heterodyne amplitude of the earlier measurements. More importantly, the differential signal between the sum of the top segments and the sum of the bottom segments did not show the oscillation. The same was true for the differential signal between the sum of the left segments and the sum of the right segments. Thus no changes in the beam pointing could be detected within the sensitivity of this method.

Besides these tests, an important finding was made when experimenting with the polarization control in front of the fiber. Throughout the experiment, the mentioned pairs of $\lambda/2$ wave plate and polarizer were utilized for the polarization matching. The established assumption was that a polarizer with a high extinction ratio is sufficient to match the incoming free

laser beam's polarization to the slow axis of a fiber. The $\lambda/2$ wave plate was added to save beam power and to increase the effect of the polarizer by providing it with light polarized along the transmission axis. However, replacing the polarizer with a $\lambda/4$ wave plate yielded much higher stabilities for the polarization within the fiber. This was verified with direct polarimeter measurements which showed a significant reduction of the cycle radii on the Poincaré sphere behind the fiber. It should be stated that the combination of a $\lambda/2$ and a $\lambda/4$ wave plate is already commonly used for the polarization adjustments in front of fibers. However, it was not clear that the combination of $\lambda/2$ wave plate and polarizer cannot compete with it. A possible explanation for this discovery could be birefringent behavior of the lenses used in fiber couplers and non-uniform stresses in the fiber ends. In particular the addition of circular components cannot be averted by the linear polarizer in front of the coupler. The $\lambda/4$ wave plate instead could counteract this effect preventively.

As a consequence of these findings, the fiber bench optics were adapted and equipped with a pair of $\lambda/4$ and $\lambda/2$ wave plates. A polarizer still served for the initial cleaning of polarization. The beam splitters for the power pickup were removed since it was not intended to use the amplitude stabilization.

Additionally, it was tried to improve the polarization control at the Hexagon output. For this purpose, Glan-Laser polarizers were used. These were chosen due to their high extinction ratio and their availability in a rotational mount within a plane stand not exceeding the Hexagon beam height. Once more, the goal was to adjust all output polarizations to the Hexagon surface normal. It was done in two steps with the following method. First, the Glan-Laser polarizers are adjusted to the surface normal. For that purpose, the output behind the Glan-Laser polarizers are monitored with the polarimeter once. Then they are turned by 180° around the surface normal. The two measured polarizations can only be the same if the polarizer transmission axis matches the surface normal. For any other case, the polarizer is turned to the intermediate point between the two measurements and the process is repeated until both measurements give the same result. In a second step, the thin-film polarizers in front of the photoreceivers are aligned to the Glan-Laser transmission axis and thus the Hexagon surface normal. For that purpose, the polarization is measured with and without the thin film polarizers and the latter are turned until a match is achieved.

The changes of the wave plates and the polarizer adjustment were applied in series. Figure 4.31 shows the associated measurements. The interpretation of the results is, on one hand, that the more stable polarization in the

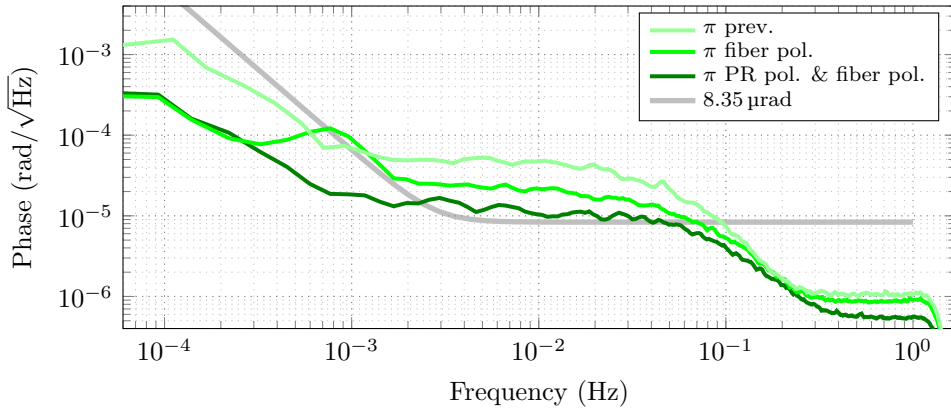


Figure 4.31: More precise adjustment of photoreceiver polarizers and improved polarization stability in the fibers through wave plate pairs. A previous measurement is shown for comparison. The more stable fiber polarization seemed to have improved the long term stability while the polarizers mitigated the parasitic signal shoulder.

fibers improve the long-term trend and, on the other hand, that the interferometer output control suppresses the mHz noise shoulder a bit further.

At this point, the findings during the analysis of the π measurement were applied to get an intermediate three-signal measurement. Hence a third fiber bench was installed and the polarizers in front of the photoreceivers were readjusted following the earlier described method. However, a slight adaption had to be done for the paths that could not fit a polarimeter between thin-film polarizers and photoreceivers. Instead, the adjustment to the Glan-Laser transmission axis was done by a maximization of DC power. Afterwards, the chamber was evacuated to below 10 mbar and a three-signal measurement was performed. It is presented in Figure 4.32. Unlike in earlier plots, two three-signal measurements, each using one of the complementary photoreceivers, are shown. Different observations can be made. Compared to earlier three-signal tests like in Figure 4.17, the long term drift could be attenuated, presumably by the polarization control in the fibers. The whole measurement is however dominated by a drift with approximately a $1/f$ dependency. The π measurement is clearly not yet free of parasitic signals. However, its behavior changed in the different thermal environment of the vacuum and the energy is more concentrated in the lower Fourier frequencies. A significant difference in the two three-signal measurements with the different complementary photoreceivers is visible at the same Fourier fre-

4 Implementing an optical three-signal test

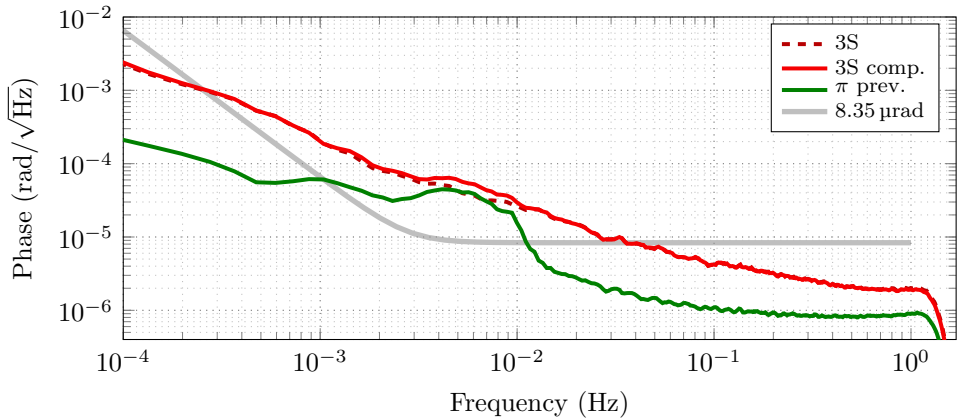


Figure 4.32: Three-signal measurements with stabilized polarization in fibers and adjusted polarization in front of photoreceivers. The long-term drift improved compared to earlier measurements. Additionally, similar limitations as in the π measurement are visible.

frequencies as the ones of the shoulder in the π measurement. This apparent limitation of the three-signal measurement by the π measurement was the motivation for the next noise hunting step.

Its goal was the implementation of the remaining two π measurements in order to get a better diagnostic tool for the three-signal test as well as an all-balanced detection. However, for the readout of at least six channels, another ADC card had to be installed on the LISA phasemeter which was initially equipped with only one. A performance verification was performed with an 8-way resistive splitter. It can be found in Appendix C. The inter-card measurement made the utilization of the pilot tone correction essential. It was generated by an external signal generator whose reference clock was locked on the LISA phasemeter clock. The tone is split with a commercial resistive 2-way splitter (ZX10R-14-S+ by Mini-Circuits) for synchronous use on the two ADC cards. As stated before, in the following measurements all signals are corrected with the pilot tone if not stated otherwise.

Before the new card was utilized in the application with three π measurements, a few more attempts to get a hold on the already limiting parasitic signal in the existing one were conducted. Most turned out to be inconclusive, but are listed here for completeness.

In order to achieve a similar effect as in Figure 4.28 and to change the ratio between desired signal and parasitic one, gray filter were inserted at different position in the beam paths and measurement performances were

compared.

Furthermore, the output of one photoreceiver was monitored with a spectrum analyzer while one of the associated laser beams was blocked right in front of the recombining beam splitter. The intention was to check for a residual beat note from stray light that might reach the photoreceiver offside the original beam axis.

Subsequently, it was tried to examine a single laser beam for selfinterference. A laser with the capability of high frequency modulation (the same as presented in Section 6.2, was utilized for this purpose and was injected in one of the fibers outside the chamber. The other lasers were blocked. The general idea is to reveal a interferometer formed by delayed stray light combined with the original beam. A strong frequency modulation should then be visible in the output due to the unequal arm length of the interferometer. The related math can be looked up in Section 6.1. While an interference pattern was actually visible, it was traced back to the amplitude modulation that comes along with the frequency modulation of this particular laser model. Consequently, an amplitude stabilization was applied, its noise suppression was however not sufficient to distinguish between amplitude modulation residuals and a possible interferometer pattern.

Finally, the π measurement was performed by using one channel of each of the two ADC cards as a check for possible influence of crosstalk.

As said, none of these methods gave new insights, in contrast to the one described in the next section.

Optical split measurements

A method that appeared fruitful is an optical split measurement. As described earlier in Section 3.3, instead of measuring both the two complementary outputs of a recombination beam splitter, one of them is split again and is captured by two photoreceivers. Here, the scheme was implemented by inserting an additional beam splitter behind one of the folding mirrors involved in the π measurement. Figure 4.33 shows the schematic of this simple setup. It allows the simultaneous operation of two π measurements and one optical split measurement. The latter was conducted using two channels on different ADC cards. Consequentially, there was one intra- and one inter-card π measurement.

In the initial constellation of the optics, the output ports of the recombining beam splitter were filtered by a pair of aligned Glan-Laser and thin-film polarizers. The results are shown in Figure 4.34. A significant difference between optical split and π measurement can be observed. The prominent

4 Implementing an optical three-signal test

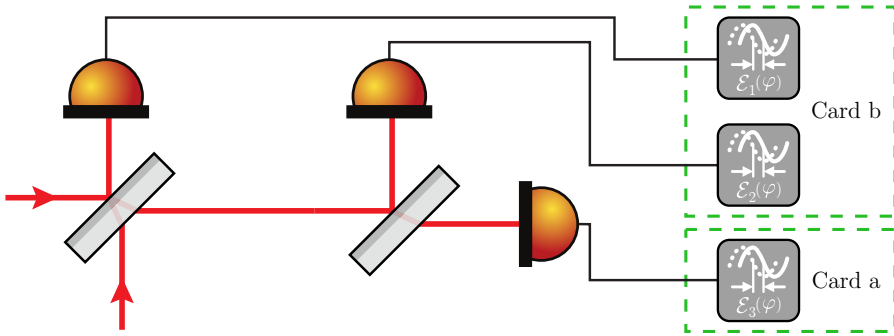


Figure 4.33: Optical setup of simultaneous optical split and π measurements. The measurements are distributed on two ADC cards.

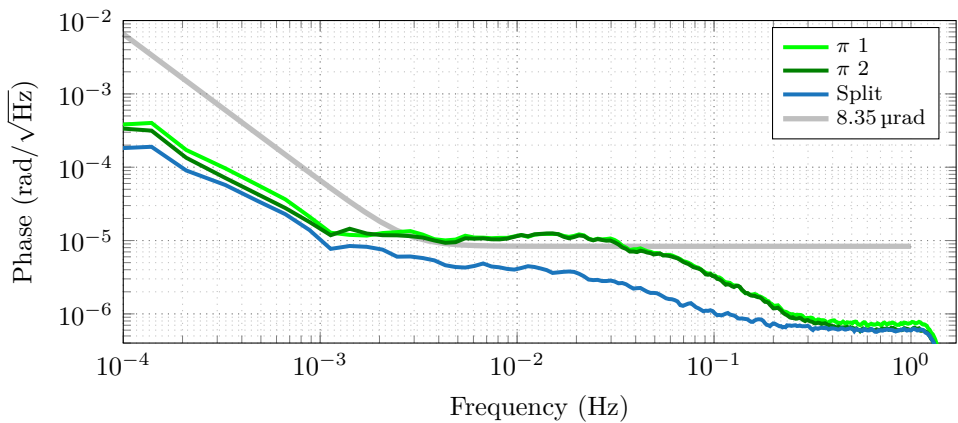


Figure 4.34: Comparison of π and optical split measurement. The prominent shoulder is suppressed significantly in the latter.

shoulder is suppressed in the former, but still visible. For the purpose of the investigation on the influence of polarization alignment, the different polarizer adjustments were varied in several scenarios. In one of them, the polarizers in the common path of the split measurement were removed and instead two individual thin-film polarizers were placed behind the splitting point. One was adjusted in the earlier described manner to the Hexagon surface normal while the second was intentionally misaligned. The effect in terms of deterioration can be seen in Figure 4.35. The same scenario with a Glan-Laser polarizer back in the common path reproduced the initial scenario rather than the latter. Finally, a setting with two Glan-Laser polarizers, each at one output of the recombination beam splitter, was put

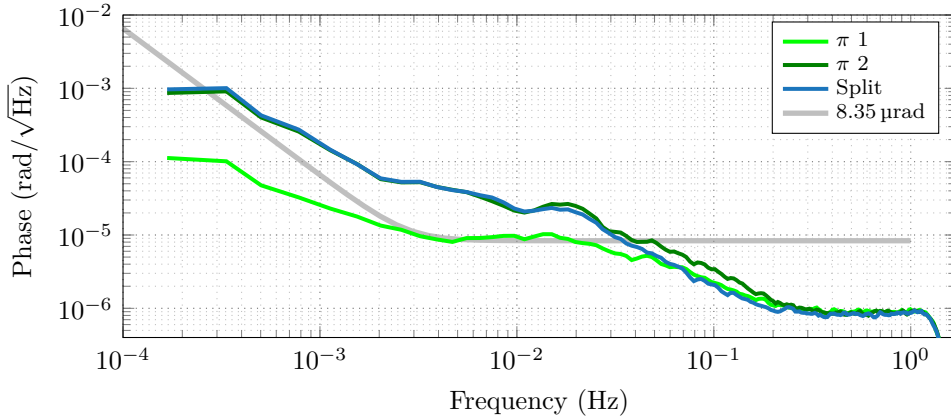


Figure 4.35: Intentionally mismatched polarizers between the optical split measurement photoreceivers. The performance is decreased significantly. The mismatch likewise affected the π measurement which involves the path with the turned polarizer.

together. The one in the common path of the split measurement was misaligned severely by dozens of angular degrees. Again, the performance between the mismatched paths deteriorated, as visible in Figure 4.36. Despite the misalignment with respect to the Hexagon surface normal, the split measurement still goes below the requirement reference. Interestingly, the situation did not change when the misaligned Glan-Laser polarizer was roughly turned closer to the point of perfect alignment. The corresponding measurement can be found in Appendix C.4.

Summing up the results of the different scenarios, it seems that the very exact matching of the polarization between the different photoreceivers is decisive in order to suppress the parasitic effects of interacting polarization components and to achieve $6 \mu\text{rad}/\sqrt{\text{Hz}}$ performance. In the presented tests, the alignment could only be accomplished in measurements with a common beam path behind the polarizer. Besides, the scaling of this noise source is not entirely clear as stated above. Additionally, it should be noted that while the surface normal of the Hexagon was used as a reference, the measurement in Figure 4.36 shows that the mismatch between beam polarizations and aforesaid surface normal seems to be of little influence. Yet it should not be completely discarded and might still be hiding in the composition of noise sources manifested as the noise shoulder.

As the polarization alignment appeared only sufficient when a polarizer was placed in the common beam path of a differential measurement, the

4 Implementing an optical three-signal test

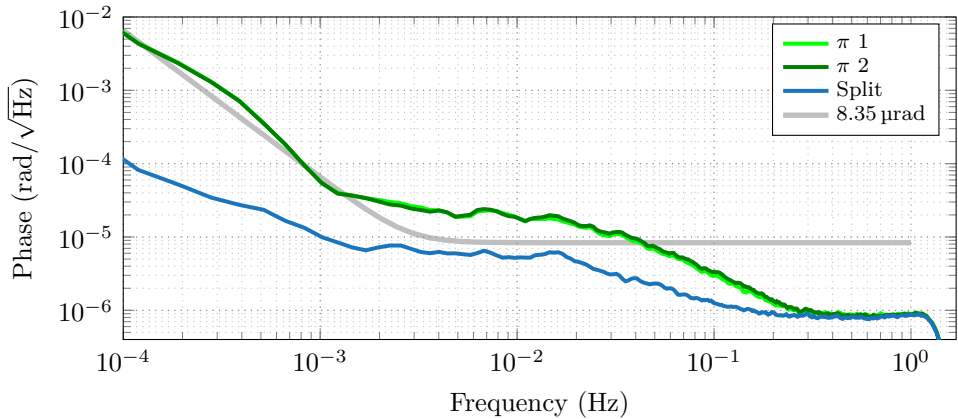


Figure 4.36: Intentionally mismatched polarizers between the complementary output ports. The performance of the π measurement deteriorated while the split measurement is below the requirement.

next method aims for doing exactly that. It picks up the earlier idea of filtering right behind the FIOSs, thus putting the polarizers in the common path of the beams. The approach is described in the following section.

Hexagon polarization alignment

So far, PBSs and thin-film polarizers were utilized to filter the polarization of the light injected by the FIOSs. While the first did not match the spatial requirements regarding the beam paths, the latter led to a loss of coherence at the photoreceivers. Avoiding the two downsides, a laminated version of the thin-film polarizers (colorPol®VISIR CW02, laminated, by CODIXX) was put to the test. As stated in the product specifications, the laminated component provides a wavefront distortion of less than $\lambda/4$ at 633 nm and a beam distortion of less than $1'$. The non-laminated version in comparison exhibits values of less than 3λ and less than $20'$, respectively. The utilized laminated filters came with a square aspect ratio and 10 mm edge length. They were mounted provisionally with holders printed in a 3D printer. In a second revision, the holder were manufactured from Invar for use in vacuum and to attain a low coupling of temperature into polarization alignment. It was fabricated with particular focus on achieving parallelism between the polarizer edge and the Hexagon ground plate. The intention was to use the ground plate again as common reference, as the lack of the rotational degree of freedom made fine adjustment to arbitrary angles impossible.

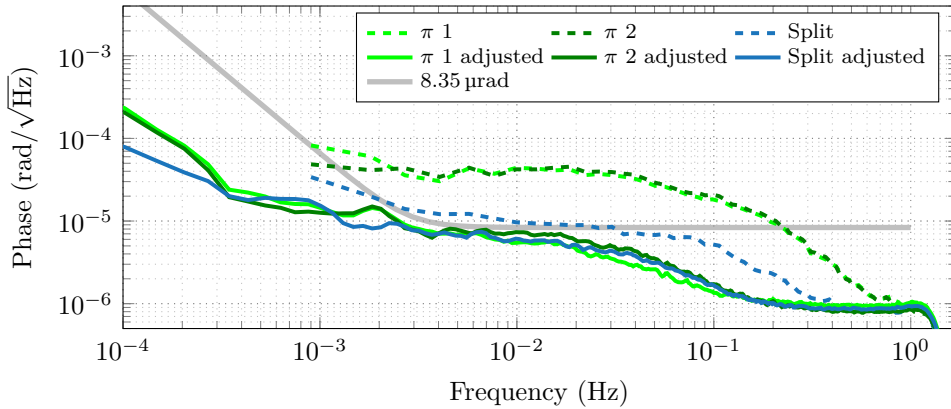


Figure 4.37: Impact of polarization alignment behind FIOSs with and without subsequent readjustment of folding mirrors. The common path polarization alignment enables performances below the LISA requirement reference if the folding mirrors are readjusted after the polarizer placement.

An initial test showed no noteworthy degradation in coherence and thus heterodyne amplitude, hence qualifying the polarizers for the utilization in the experiment. Subsequently, different placing scenarios for the manifold of polarizers were tested within the configuration of two π and one split measurement.

In summary, the best result was achieved with solely the filters behind the FIOSs. Besides, another finding was made. In the initial setup with post-FIOS filters only, the performance deteriorated significantly. Later it was discovered within another scenario iteration that additional care has to be taken after the placement of the polarizer to readjust the folding mirrors for maximum power on the photoreceivers. These corrections were assumed to be necessary to compensate for the slight beam pointing changes caused by the additional optical components in the beam geometry. The two measurements with and without mirror readjustment are plotted in Figure 4.37. They show, on one hand, a π measurement performance comparable to the one of the split measurement below the LISA requirement reference and, on the other hand, the effect of misaligned folding mirrors. The latter is associated with the aforesaid beam pointing and will be discussed later.

To pick up the former goal to implement three π measurements, two additional photoreceivers were installed in the auxiliary optics. As proper performance could not be achieved right away, multiple iterations of adjustments were necessary. During that process several changes were made that

4 Implementing an optical three-signal test

are listed here for the sake of completeness.

In order to counteract probable pointing issues, lenses with shorter focal length and smaller focus beam waist were installed on a trial basis. Additionally, two broken photodiodes were replaced. One was substituted with the same model, the other tentatively with a larger model with a 1 mm diameter. Hopes were that the larger diode would mitigate influence of pointing. However, no significant improvement by the two provisions could be observed.

For additional diagnostics, one of the photoreceiver signals was divided with a resistive splitter to perform an electrical split measurement. In particular was one of the paths extended with a long cable in order to create a π phase delay, thus reproducing the scenario of the optical π measurement without the influence of two receivers. The measurements can be looked up in Appendix C.5.

Eventually, as a measure to exclude more possible sources of parasitic signals in terms of stray light, the fiber bench optics were removed. Concerns were that reflections on the bench's optical components with incident angles close to 0° could occur. Those could then couple back into the original beam path. Furthermore, the polarizers used on the bench were found to have potentially insufficient apertures. According calculations led to an expected beam waist failing slightly the commonly used rule of thumb to exceed the beam waist by a factor of three. Possible consequences are diffraction and clipping.

With the fiber bench optics removed and more adjustment of post-FIOS polarizers and folding mirrors, the performance shown in Figure 4.38 was achieved for the three π measurements. While they did not entirely fall below the requirement, expectations were that the thermally calmer environment in vacuum would flatten out the curves more. Consequentially, a three-signal test in moderate vacuum (below 10 mbar) was conducted. It should be noted that with the two additional photoreceivers, now a total of eight different combinations plus an all-balanced detection are possible. The latter is the pairwise constructive combination of the complementary receiver signals explained in Section 3.3. Figure 4.39 shows all three π measurements and their incoherent sum, two out of the eight possible combinations for the three-signal measurement and the balanced detection. The performance of the six other combinations were almost equal to the plotted pair. It was picked as it used the two complementary receivers of the π measurements showing a bump. Interestingly, the noise contribution seems to be distributed among the two involved channels, as non of the two three-signal combinations is completely limited by it. Furthermore, it can be canceled by

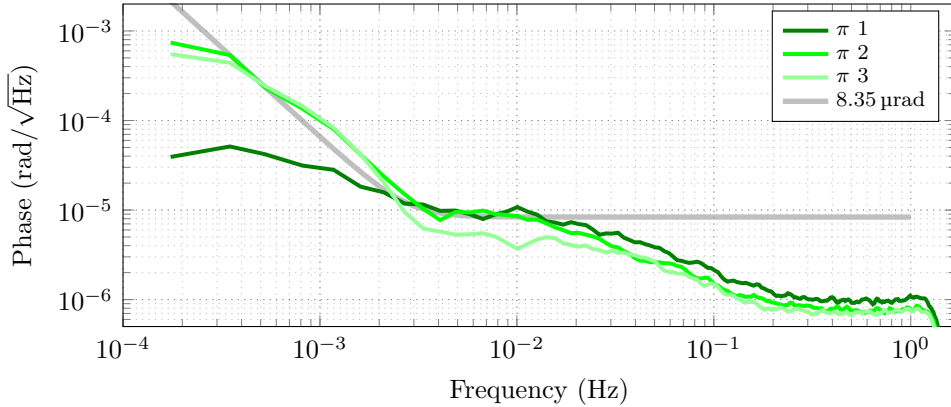


Figure 4.38: First measurement with three π photoreceiver pairs. The fiber benches were removed during the noise hunting.

the balanced detection. The other two π measurements show the expected effect of the thermally calmer environment. In summary, the overall performance in the mHz regime improved in comparison to the last three-signal measurement in Figure 4.32, yet the long-term behavior got worse.

After this test, another was run with higher heterodyne frequencies (23.9 MHz, 18.1 MHz, 5.8 MHz). The result is plotted in Figure 4.40. The performance of some of the combinations deteriorated compared to the measurement with lower frequencies. When analyzing the different three-signal combinations, it can be deduced that in particular two channels exhibit high noise. For the sake of this analysis, the channels are numbered in the scheme x-y-z, denoting which of the two complementary ports 1 or 2 of the three Hexagon outputs x, y and z was used. It is observable that the complementary ports at output z contribute no noise. This finding is consistent with the corresponding π measurement, which can be looked up in Appendix C.6. Instead, the major noise contributors are port 2 at output x and port 1 at output y. Nevertheless, also the optimal combinations exceed the noise level of the tests with lower frequencies. Subsequent analysis suggested the photoreceivers to be the sources of the excess noise.

This was confirmed with a modified testbed, which was used in succession to the measurements just shown. It utilizes an electro-optical amplitude modulator (EOAM) to generate MHz signals with a single laser. The tests are described in detail in Section 4.2.11. For the purpose of consistency with regard to content, the chronology is halted here. Instead of the photoreceiver analysis, first the next step in polarization control is described.

4 Implementing an optical three-signal test

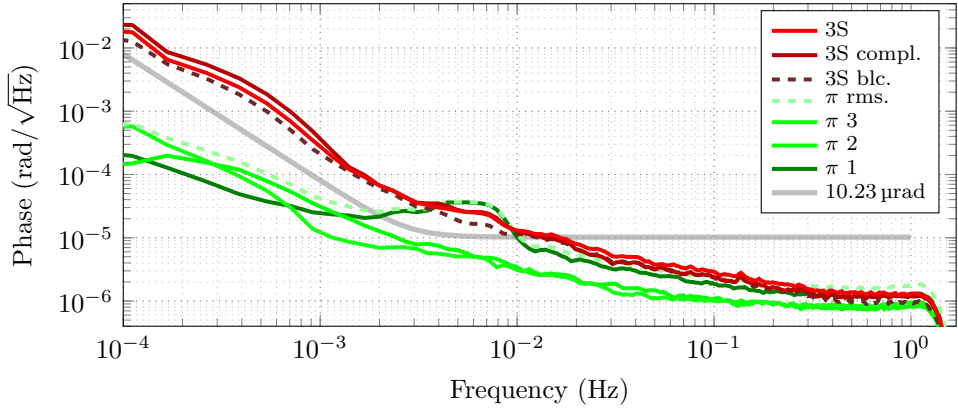


Figure 4.39: Three-signal test with post-FIOS polarizers. The residual parasitic noise in one π measurement is canceled by balanced detection.

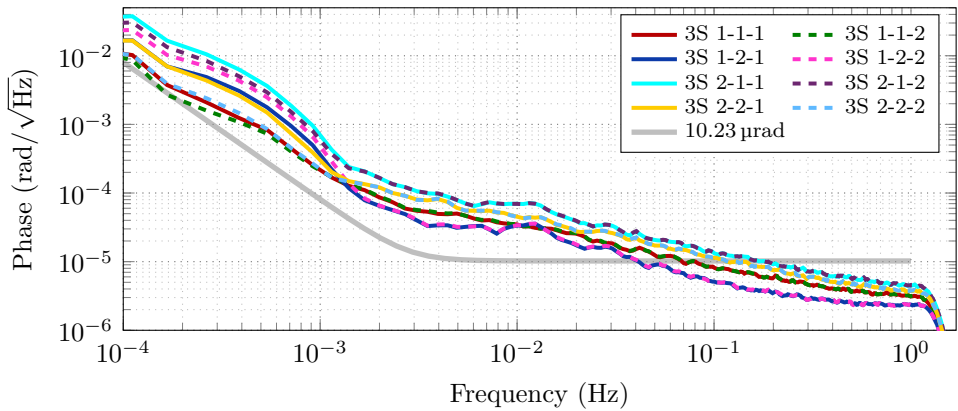


Figure 4.40: Measurement with higher heterodyne frequencies (23.9 MHz, 18.1 MHz, 5.8 MHz). The three-signal combinations are described following the scheme x - y - z , denoting which of the two complementary ports 1 or 2 of the three Hexagon outputs x , y and z was used. Limitations are visible with major noise contributions from two specific channels (2-1- \times).

As the low frequency or long-term trend degraded in the last three-signal measurement compared to earlier tests, it was planned to put the fiber bench optics back in place. In order to do so without creating parasitic signals by stray light or the like, the optics were put in step-by-step with subsequent short π test measurements in air. Moreover, the formerly used fiber bench polarizers were replaced with similar thin-film polarizers and mounts as are used behind the FIOSs. This measure was meant to avoid clipping and diffraction. The adjustment with a non-zero angle of incident assured further that no reflection could couple back into the light-injecting fibers.

While two π measurements could be kept close to the requirement reference, one exhibited a more prominent shoulder. After another noise hunt, a suppression of the shoulder was achieved by an attenuation of power via an VOA in one of the laser paths providing light for the involved π measurement. The two measurements are shown for comparison in Figure 4.41. On first sight, this stands in contrast to the findings in Figure 4.28. Nevertheless, it should be considered that the power is primarily a parameter for other noise sources like stray light and does not affect the phase performance directly in the current sensitivity and parameter regions. Yet it is not entirely clear which noise sources were influenced here with the decrease in power. It should be noted that in particular the heterodyne amplitude of the beat note affected by the parasitic signal in the recent measurement exhibited a high value. This was due to the intentional increment of laser power coupled in one of the involved fibers on the optical table, which was in turn done to provide sufficient power for the EOAM utilized in the photoreceiver tests. This adds thermal issues as well as saturation effects to the range of possible mechanisms that were reversed by the power attenuation.

In any case, the setup was used in the given state for the final three-signal measurements in this thesis. They are presented in Section 4.3, while at first the mentioned photoreceiver tests will be described.

4.2.11 Photoreceiver noise at higher heterodyne frequencies

This section presents the analysis of the photoreceiver noise occurring at higher heterodyne frequencies. For this purpose, a fiber-based EOAM was placed in the path of one laser. It was used to alter the beam with MHz amplitude modulations according to LISA phasemeter bandwidth requirements. With the other two lasers being blocked, a heterodyne signal could be simulated effectively excluding interferometric effects from the noise hunting. A schematic of the setup is shown in Figure 4.42. Four receivers can

4 Implementing an optical three-signal test

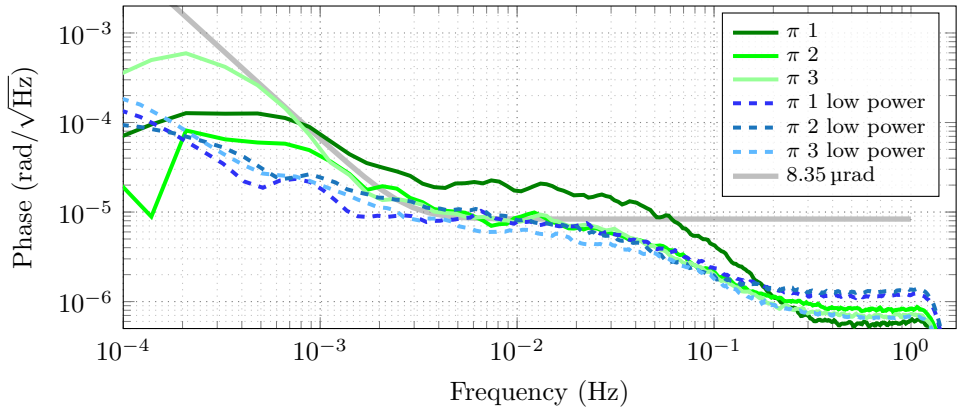


Figure 4.41: Measurement with reduced power in one laser path. The noise shoulder of $\pi 1$ could be attenuated.

be analyzed at once and hence six differential measurements can be taken.

With the testbed, the former diagnosis of the particular high noise contribution of two channels could be extended to the finding that the two photoreceivers with exchanged diodes were the reason for the more severe distortions. For the time being, they were put together as one complementary pair at one of the Hexagon outputs with the intention of using them to track a low frequency beat note in the three-signal test. With the new photoreceiver permutation and the EOAM, the following measurements were taken.

Figure 4.43 presents the combined plots of two verification tests with low carrier frequencies of 2.1 MHz. Compared to each other, they were conducted with the single laser light being coupled into two different FIOSs. This way, all receivers could be tested at least once. The nomenclature of the differential measurements follows the scheme in Figure 4.40. However, the designation of the channels is reinterpreted as a designation of the used photoreceivers. Thus, the aforementioned placement permutations can be ignored when comparing the following measurements to Figure 4.40.

The test shows a low noise contribution. It should be noted that the measurements were conducted in rather quick succession to changes in the chamber and were hence performed within the relaxation time of chamber temperatures. For the purpose of compensating for the associated drift, the data was detrended linearly before the spectral densities were computed.

In the next test, the receivers were probed with higher carrier frequencies of 19.1 MHz. Figure 4.44 shows two of those measurements, again with

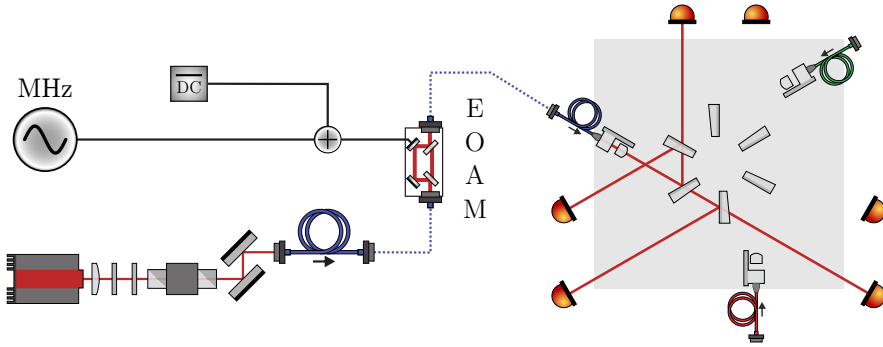


Figure 4.42: Setup to probe the photoreceivers in the MHz range without interferometric signals. An EOAM provides an amplitude modulation in the aforesaid bandwidth.

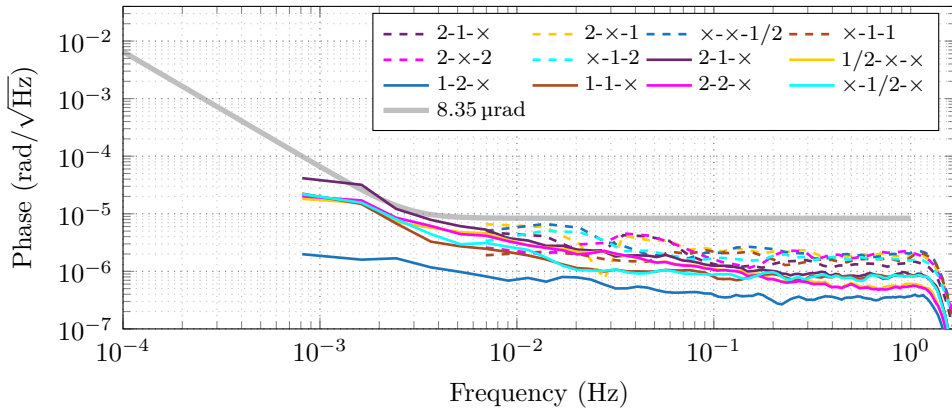


Figure 4.43: Photoreceiver tests with amplitude modulated single laser at 2.1 MHz. Differential measurements between two receivers each are shown. The nomenclature follows the scheme x-y-z, denoting which of the two complementary receivers 1 or 2 of the three Hexagon outputs x,y and z were used in the full interferometric configuration.

4 Implementing an optical three-signal test

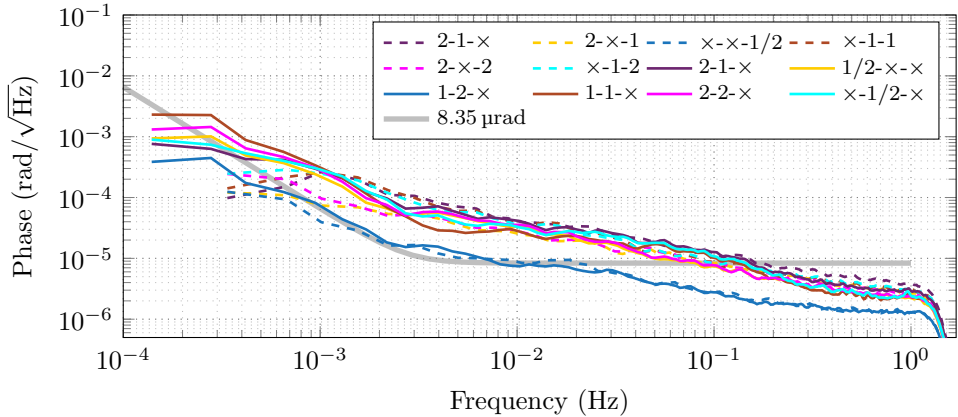


Figure 4.44: Photoreceiver tests with amplitude modulated single laser at 19.1 MHz. Differential measurements between two receivers each are shown. The nomenclature follows the scheme x-y-z, denoting which of the two complementary receivers 1 or 2 of the three Hexagon outputs x,y and z were used in the full interferometric configuration.

switched input FIOSs. The two flawed receivers were utilized in both tests. It can be noted that all differential measurements involving these are worse. Nevertheless, as already suggested earlier in the discussion of the three-signal measurement, the four other detectors are likewise dominated by noise related to the higher carrier frequencies. It exhibits a $1/\sqrt{f}$ pink noise shape and it is assumed to increase with higher carrier frequencies. According tests were spoiled by the occurrence of distortions when driving the EOAM with higher frequencies.

The findings will briefly be discussed in the following. Firstly, the focus is put on the photoreceivers with the particular bad performances and changed diodes. The most apparent difference of one of them to the four others is the larger diode which comes with a higher junction capacitance. This influences the corner frequency f_c of the TIA. As stated in [13], the relation can be described using

$$f_c = \sqrt{\frac{\text{GBWP}}{2\pi R_f C_j}} \quad (4.3)$$

with the gain bandwidth product (GBWP), the feedback resistor R_f and the junction capacitance C_j . The stated values of the latter are 8 pF for the smaller 0.5 mm diode and 40 pF for the larger 1 mm diode. Thus the substitution leads to a decrease in corner frequency by a factor of ≈ 2 . This leads to a possible explanation for the worse behavior of this specific

receiver in terms of a finite phase response (see Section 2.4.3), as a lower corner frequency increases the coupling of temperature fluctuations due to a higher transfer function slope. In order to counteract the change in corner frequency partially, as a first step the feedback resistor was reduced by a factor of ≈ 2 and thus f_c was increased by a factor of ≈ 4 . In a second additional step, the utilized OP was swapped with a model exhibiting a higher GBWP: the model LMH6624 with a GBWP of 1.5 GHz was replaced with the model OPA847 (both by Texas Instruments) with a GBWP of 3.9 GHz. The two steps were tested in two quick measurements which can be looked up in Appendix C.7. Only the first yielded some improvement according to the expectations, thus making the finite phase response as a sole explanation unsatisfying. In addition it leaves the question open why the modified receiver using the 0.5 mm diode with less capacitance exhibits a comparably bad performance as the receiver with the larger one. Also, it is not clear if this explanation can be extrapolated and used for the photoreceivers with the initial components.

Another hint is given by a correlation between heterodyne amplitude and phase measurement between the initial photoreceivers. An exemplary comparison of according time series can be looked up in Appendix C.8. While the possible causalities cannot be evaluated yet, a possible mechanism for the noise coupling could be what is usually referred to in the literature as AM-PM conversion in the receiver TIA [35, 53, 54]. Temperature modulations caused by the changed amplitude is another possible mechanism. Quick tests with Peltier elements on the photoreceiver boards were conducted. However, they showed no significant coupling. Nevertheless, due to the provisional execution of the negative tests, the mechanism should not be discarded right away.

More thorough tests on the receivers are planned for the future. A testbed will be set up to be operated independently of the measurements in the chamber while using the same working principle as the tests with the EOAM just presented.

For the next three-signal measurements, the configuration with the two most limiting photoreceivers in one Hexagon output was used. Those were then driven with the lowest of the occurring heterodyne frequencies. The aforementioned replaced OP was re-substituted for the initial model while the feedback resistor with lower value remained in place.

4.3 Final performance and discussion

In this section, the final performances achieved during the experimental work for this thesis are presented jointly with a discussion of possible limitations. While at the end a test with LISA-like signal parameters is shown, the section is divided into several measurements approaching these conditions in several steps. This simplifies the differentiation between the relevant noise sources.

4.3.1 Final performance for moderate input conditions

The following benchmark three-signal measurement was conducted using heterodyne frequencies of 2.79 MHz, 5.8 MHz and 3.01 MHz and input dynamics at low levels ($0.25 \text{ rad}/\sqrt{\text{Hz}}$ at 1 Hz). This measurement is shown in Figure 4.45. Additional to the best three-signal combination of the eight phase measurements, the all-balanced detection, the π measurements and their RMS, it shows a noise projection of in-band amplitude noise. The latter was computed by the RMS of the heterodyne amplitudes times a coupling coefficient estimated by several single measurements with an amplitude modulation via a VOA. Furthermore, a plot of temperatures of four sensors is shown in Figure 4.46. They were placed in the center of the Hexagon, the inside chamber wall, on the steel plate hosting the Hexagon and on the OP of one photoreceiver. The vacuum chamber was evacuated to approximately 3 mbar, then the chamber was sealed and the pumps deactivated.

Before the discussion of the results, it should be stated that the duration of this data is an interval of roughly three hours taken from a long time measurement. While the same performance cannot be guaranteed for every arbitrary window taken from the long time series, the one shown here serve as a proof-of-principle. Additionally, a long-term measurement over several days with comparable performance is presented later in Section 4.3.3.

In the measurements presented in Figure 4.45, the LISA requirement reference is reached. The dynamic range constitutes six orders of magnitude. The phase performance is not yet limited by the phasemeter noise measured in the electrical split measurements, see Figure 4.3 for a comparison. The difference is caused either by excess phasemeter noise only revealed in the three-signal test, or by residual testbed noise. Here it is assumed that the latter is the case, as the three-signal measurement seems to be mostly limited by the π measurements, which in turn are split measurements. The limitation by the π measurements furthermore suggest that the testbed noise is not limited by the Hexagon stability at least down to mHz. At 1 mHz, the

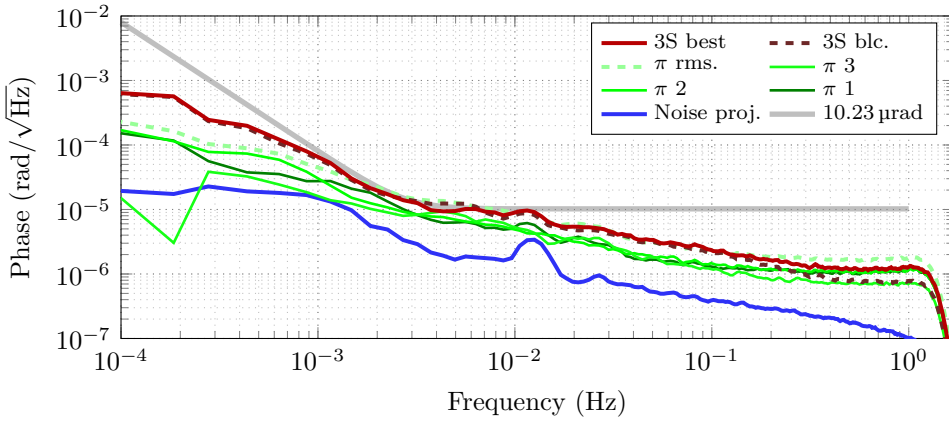


Figure 4.45: Three-signal and π measurements in the final setup with low input signal dynamics and low heterodyne frequencies. The LISA requirement reference could be reached. The RMS of the π measurements coincides with the best three-signal measurement down to mHz. A limitation due to in-band amplitude fluctuation is unlikely, as its noise projection shows.

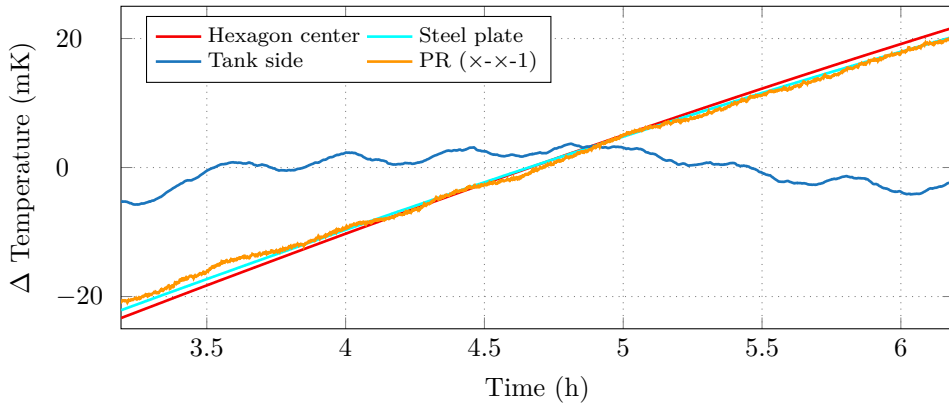


Figure 4.46: Temperatures during the measurement with low input signal dynamics and low heterodyne frequencies. A linear drift is observable for the temperatures of the steel plate sensor and of one photoreceiver sensor with a change of ≈ 50 mK during 3 hours.

4 Implementing an optical three-signal test

π and three-signal measurements diverge slightly. While the explanations could be manifold, a connection to the chamber temperature seems likely. In any case, when taking into account the temperature drift of almost 50 mK inside the thermal shield during the measurement interval, it can be stated that a proper decoupling of temperature drift could be reached. Naturally, the drift could be further improved by better thermal stability. This might be achieved by better passive isolation or active control schemes like a flow box around the chamber.

Interestingly, it was found that a more or less constant temperature drift improved the noise behavior of the residual parasitic signal shoulders visible in the π measurements. A likely explanation is a re-distribution of the shoulder's spectral energy to lower frequencies. Nevertheless, additional effort should be put into the further search for parasitic signals and their attenuation for a lower overall noise level. Based on the various performed measurements, several suggestions for their sources can be made. One are residual polarization mismatches in the Hexagon, with the small parasitic vector being driven by temperature. Improvements might be achieved by replacing the static, square post-FIOS polarizer with round, rotatable ones which allow a more controllable adjustment. Another issue could be clipping of the beams on the small photodiodes. There, temperature could couple in particular via the folding mirror into pointing- and clipping-induced phase noise. For mitigation, it is planned to revise the design of the auxiliary optics in the future. This would include the placement of the photoreceivers in line to the interferometer outputs, effectively getting rid of the folding mirrors. Fine alignment could be done with adjustable lens mounts. Larger photodiodes for all ports together with a new photoreceiver design could be an option as well. This would require the diodes' junction capacitance to be sufficient so that no excess noise must be expected if the experiment is conducted with low light powers to simulate LISA conditions.

Lower priority will be given to the noise sources apparently not limiting at the current state. This includes low-frequency laser amplitude fluctuations. The noise projection shown in Figure 4.45 suggests no imminent or direct coupling. That being said, it might still be beneficial to reactivate and rework the laser amplitude stabilization using the power pickups on the fiber benches for the sake of thermal stability on the Hexagon and in the photoreceivers. Although the latter were tested to be sufficiently insensitive to temperature fluctuations, the same might not be valid for future revisions that would thus benefit from more stable amplitudes.

With the formerly described limitation of the three-signal measurement visible in the π measurement, it should be possible to analyze most of the

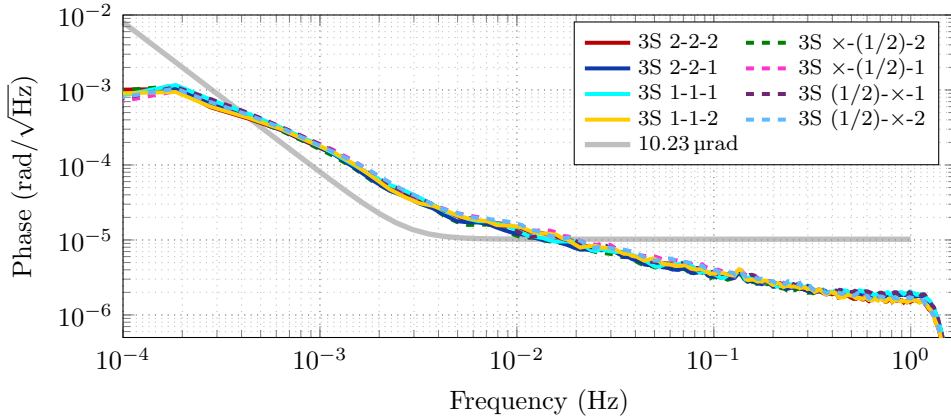


Figure 4.47: Three-signal measurement with high heterodyne frequencies in the final setup. The nomenclature describes which of the photoreceivers defined in the reference measurement in Figure 4.40 were utilized. The excess noise due to the photoreceivers could be reduced by permutations of the same. It exceeds the requirement reference solely at 0.4–20 mHz.

corresponding noise sources with the latter, making the noise hunting much more practical for future improvements.

4.3.2 Final performance with LISA-like input conditions

In order to get closer to the actual LISA conditions, in a first step the heterodyne frequencies were increased to 24.9 MHz, 6.8 MHz and 18.1 MHz. The measurement is presented in Figure 4.47. Once again the earlier assignment of channels via the utilized photoreceivers defined in Figure 4.40 are chosen. The measurement shows the limitation anticipated due to the designated test with the EOAM. The associated discussion was already given in Section 4.2.11. Yet, the operation of both the two flawed receivers in the Hexagon output with the lowest heterodyne frequency improved the involved performances. They exceed the requirement reference solely at 0.4–20 mHz.

Subsequently, the input phase dynamics were increased via injection of artificial noise at the laser lock error points to simulate LISA master laser frequency noise coupling. It was modeled with white noise resulting in $\approx 450 \text{ Hz}/\sqrt{\text{Hz}}$ at 1 Hz Fourier frequency and $1/f$ noise dominating from Fourier frequencies of 10 mHz downwards. The model was chosen in order to surpass current LISA requirements. The noise is depicted in Figure 4.48

together with the phase performance measurements. Here, for reasons explained in the following, the latter are described in terms of the ADC cards utilized for their capturing. The color assignment of the different three-signal combinations was switched back to be in accordance with the channels but not the photoreceivers of Figure 4.40. A plot with a color consistency in terms of the used receivers can be found in Appendix C.9. Also, scaled versions of the input frequency fluctuations of four single channels are added to the π measurements in Figure 4.48. Several aspects can be discussed here. For the performance evaluation, the best intra-card three-signal measurement is considered. It presents a similar noise level as the previous tests even with the higher input dynamics applied here. The dynamic range yields 8 orders of magnitude at 1 Hz and up to 11 orders of magnitude at 0.1 mHz. Measurements in an earlier stage of the experimental development showed a limit of 9 and 12 orders of magnitude, respectively, with a non-linear coupling, as can be looked up in Appendix C.10. Reasons for the discrepancy are to be found.

In the last measurement, not all channels perform equally well. As said, the best performance is achieved with all channels on one single ADC card. The second best utilizes only channels of the other ADC card, though being significantly worse. Finally, the different inter-card measurements rank in performance consistently with the π measurements. The reason for this is not entirely clear. The noise source seems inherent to the worse ADC card. Furthermore, its shape perfectly resembles the one of the single channel frequency noise. A possible explanation is the coupling via the earlier described second harmonic coupling in the ADPLL, see Equation (2.37).

In order to make the best of the limitations on the single ADC card, its particular sensitivity could be used to investigate the coupling of input frequency and phase noise more easily. The same coupling could occur likewise but attenuated in the well-performing card and might be a limiting factor at higher frequency and phase noise levels. In any case, the card should be revised for flaws in the analog front end, including the pilot tone distribution, as well as in the digital part, where for example an incorrectly configured ADPLL low pass filter order could lead to frequency noise coupling via the aforementioned second harmonic. Apart from that, the issue is considered non-critical since a proof-of-principle measurement could be achieved with the other card. Additionally, formerly conducted electrical multi-card tests with high dynamic range [29] showed sufficient performance as well.

To conclude the investigation, a provisional measurement with a 16 m cable between one of the photoreceivers and the phasemeter was conducted to check for the effect of absolute delays in combination with high signal

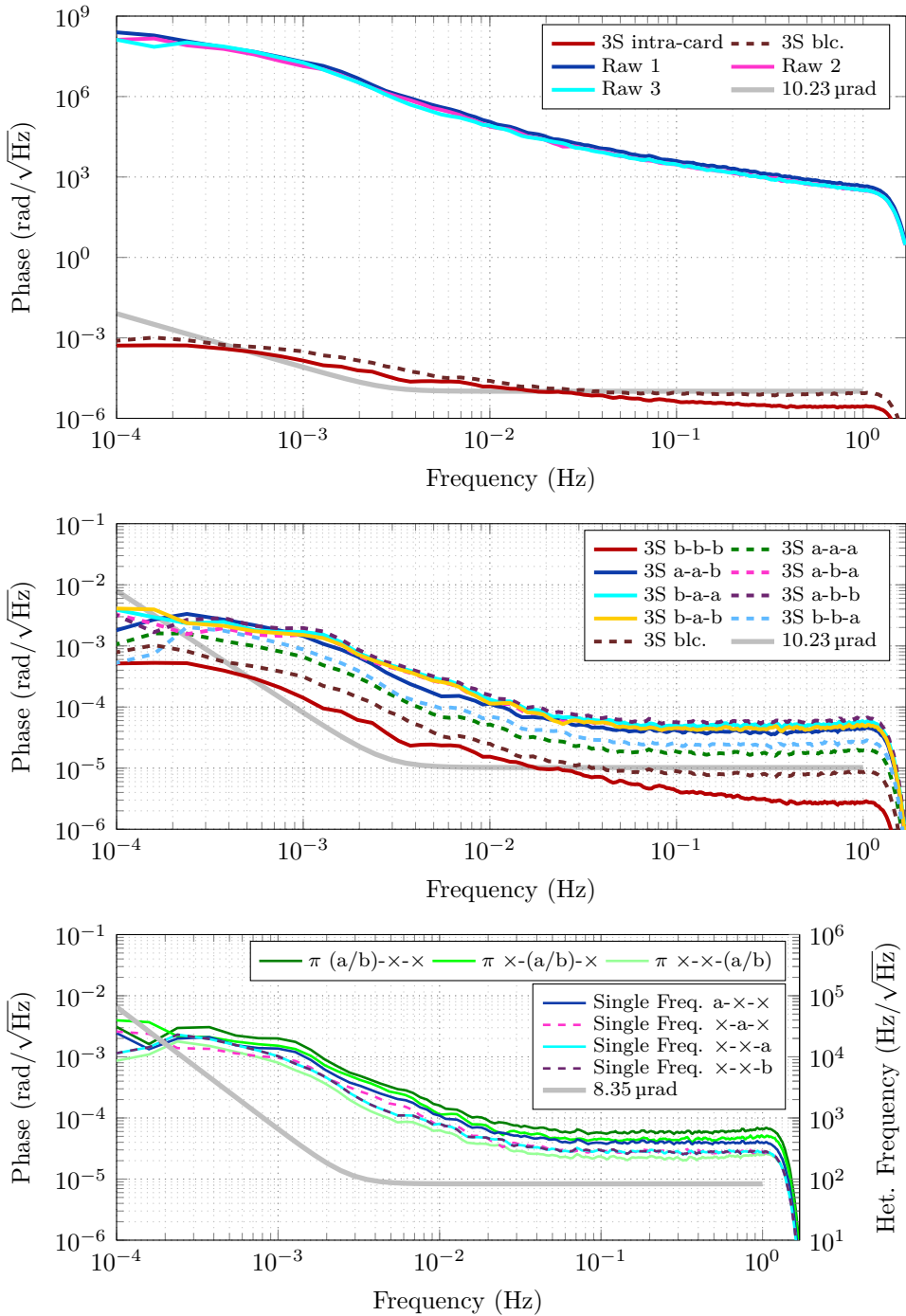


Figure 4.48: Three-signal measurements with high input phase dynamics in the final setup. A dynamic range between 8 and 11 orders of magnitude can be observed in the top plot. The center and bottom plots denote the channels by listing the utilized ADC cards. It shows limitations in all channels involving inter-card measurements, while one intra-card measurement showed performance similar to tests with low input dynamics. The shape is similar to the single channel frequency noise shape.

dynamics. No significant change could be observed.

Afterwards, the final step towards LISA input conditions was conducted by a sweep of the heterodyne frequencies to simulate the LISA Doppler shifts.

4.3.3 Final performance with LISA-like input conditions and Doppler-like frequency drift

While the sweep of the heterodyne frequencies should resemble the LISA scenario as good as possible, it had to be adapted for pragmatic reasons. A measurement using the drift rates defined by the estimated LISA orbits to cover the whole bandwidth of 5 MHz to 25 MHz would take weeks. Thus the drift rates were increased for the experimental test with the Hexagon. This however moves its impact on the input phase noise into the LISA measurement band and limits the performance estimation by exceeding the dynamic range. To avoid this issue (which will not occur in LISA) the sweep was performed linearly. This allowed the simple removal of its limiting effect via detrending in post-processing. Despite the change of the drift rate, the test still serves the purpose to show uniformity of the phasemeter performance over the required bandwidth. The measurements utilizing this procedure are presented in Figure 4.49. The single channel phase noise was generated with the same method and the same values as in the previously described test.

The result shows similar performances as achieved in former measurements. It exceeds the reference only at 0.4–20 mHz. Also, it is computed from data of a time span of several days. This can be considered as evidence of reliability of the measurements shown before.

The time series of the best three-signal measurement is given to reveal possible weak points of the phasemeter within the LISA bandwidth. Potential spots with increased noise appeared at different frequencies in a repetition of the measurement, which leads to the assumption that they were caused by temporary external distortions.

This test concludes the noise hunt for testbed and phasemeter noise. Current limits with LISA input conditions are assumed to be due to the photoreceivers. For more relaxed conditions, the limit in the mHz regime is supposedly given by residual parasitic signals. The Hexagon's fundamental path length stability does not appear to be a constraint yet. For lower frequencies, temperature fluctuations are rather strong, thus the performance at that range might benefit from a more stable thermal environment.

In the next section, the utilization of the testbed for the investigation of

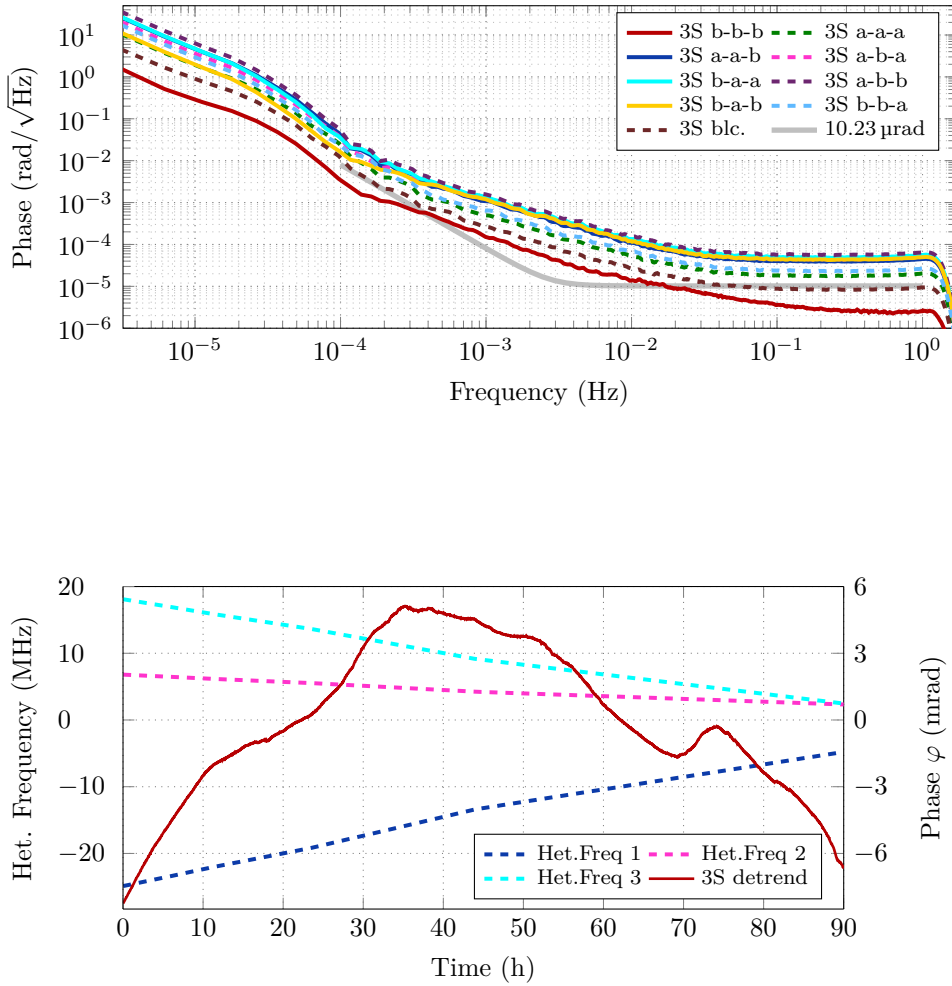


Figure 4.49: Three-signal measurements with full LISA input conditions. A linear sweep is applied over several days and is shown in the bottom plot. The measurements presented in the top plot are limited by the dynamic range for inter-card measurements or by the photoreceivers (3S b-b-b).

another noise source important for LISA, namely relative intensity noise, is described.

4.4 Measurements of RIN coupling

As emphasized, the three-signal testbed and later on the LIME can be utilized to test more than just the LISA phasemeter and its contribution to the whole metrology chain. In general, all components in the phase sensitive path behind the final beam splitter can be tested. For example, flaws in the utilized photoreceivers were revealed. Nonetheless, additional components can be tested as well if their effect onto the phase performance can be transferred non-commonly into the sensitive path. This is the case for lasers regarding their RIN in the MHz regime and at mHz frequencies. A method to analyze the RIN coupling utilizing the Hexagon will be described in the following.

4.4.1 Method

In order to see an effect of RIN and in particular of RIN at MHz frequencies, it needs to be increased artificially in the current setup. Instead of changing laser models or increasing their amplitude noise behavior, an EOAM is utilized to introduce additional amplitude noise. The earlier used VOAs cannot provide sufficient bandwidth for this task. The EOAM is driven with a white noise generator intrinsic to the signal generator SMF100A (by Rohde&Schwarz). It comes with an adjustable noise bandwidth of up to 10 MHz. A custom-made analog band path filter designed by Gerhard Heinzl provides the possibility of further noise shaping. Two filter branches can be used independently. One features a pass band frequency of 2 MHz together with a notch at 4 MHz, while the other is designed vice versa. The band pass linewidth is given by several kHz.

In the following, three different cases are considered. The first is RIN around the beat note heterodyne frequency in the MHz regime. The associated coupling mechanism was already explained in Section 2.4.1. The second case is RIN at twice the heterodyne frequency. From hereon, the two cases are referred to as f and $2f$, respectively. Finally in the third case RIN at DC is examined, which was probed qualitatively already in the noise projection of Figure 4.46.

To inject f - or $2f$ -RIN non-commonly into the three different Hexagon interferometers, a proper choice of the beat note heterodyne frequencies is essential. For example, band-passed noise introduced at 2 MHz to one laser

will show up at two interferometers and their output beam splitters. One of those interferometers can then be operated with a heterodyne frequency of 2 MHz. The heterodyne frequency of the other two interferometers is determined also by the third laser and can thus be steered away from 2 MHz. However, this scheme cannot be used to isolate DC RIN.

4.4.2 Measurements

In the first measurement block presented here, the tests to investigate f - and $2f$ -coupling are presented. Before the actual coupling was probed, a reference measurement without introduced RIN was performed. It assured that the following tests were limited by the RIN-induced noise and the associated plot can be looked up in Appendix C.11. The tests were carried out in short time segments of ≈ 20 min and in quick succession, which might have led to some additional deterioration of performance towards lower frequencies. Nevertheless, the sensitivity was considered sufficient to measure the RIN coupling.

Prior to the presentation of probing for f -coupling, the model for the latter is derived. To start with, RIN is according to its name a relative quantity. Despite being defined as intensity, it is usually written down in terms of power as

$$\text{RIN} = \frac{\delta P}{\bar{P}} \quad (4.4)$$

where δP describes the power fluctuations and \bar{P} denotes the laser average power. These quantities are further used to describe the full laser power signal:

$$P_{\text{total}} = \bar{P} + \delta P . \quad (4.5)$$

From hereon, the dash will be dropped for consistency with the nomenclature of laser power in this thesis. Furthermore, when substituting numbers in the formula, the fluctuations will be treated as the measured ASD of the power ($\delta P \Rightarrow \tilde{P}$).

To calculate the f -RIN-induced phase error, the model of Section 2.4.1 and in particular Equation (2.27) are picked up. A signal according to Section 2.1 is assumed as well as lasers with identical RIN specifications.

4 Implementing an optical three-signal test

Reducing the power fluctuations to contributions at f_{het} only, it follows:

$$\begin{aligned}\tilde{\varphi} &= \frac{\tilde{k}\sqrt{2}}{k_{\text{het}}} = \frac{\sqrt{2}G_A R \sqrt{\delta P_0^2 + \delta P_1^2}}{2k_{\text{het}}} = \frac{\sqrt{2}G_A R \sqrt{\delta P_0^2 + \delta P_1^2}}{2AC} \\ &= \frac{\sqrt{2}\sqrt{\delta P_0^2 + \delta P_1^2}}{C(P_0 + P_1)} = \text{RIN} \frac{\sqrt{2}\sqrt{P_0^2 + P_1^2}}{C(P_0 + P_1)}.\end{aligned}\quad (4.6)$$

For the case regarded here, δP_1 is set to zero, as δP_0 exhibits significantly higher fluctuations due to the EOAM. Hence it can be written:

$$\tilde{\varphi} = \text{RIN}(f_{\text{het}}) \cdot \frac{\sqrt{2}P_0}{C(P_0 + P_1)}.\quad (4.7)$$

The required power levels were monitored right before the coupling tests were performed. While they were measured as photoreceiver voltages, the form of Equation (4.7) allows direct substitution. Consequently, using the monitored values which can be looked up in Appendix F.1 leads to an expected induced phase noise of

$$\tilde{\varphi} = 1.33 \times 10^{-4} \text{ rad}/\sqrt{\text{Hz}}.\quad (4.8)$$

The associated measurement is shown in Figure 4.50 and is in good agreement with the model. The influence was successfully isolated in one interferometer output, as shown in the π measurements. Additionally, an attenuation of the coupling by balanced detection can be observed. The fact that it does not cancel completely is likely connected to an insufficient balancing: the total noise measured in the noisy π measurement is distributed unevenly into the three-signal measurements which use only one of the two channels each.

For the derivation of the $2f$ -coupling model, a slightly different approach was chosen. While for the f -coupling, δP simply added to the beat note and thus could directly be treated as additive noise, for $2f$ it will be assumed that the frequency-dependent amplitude fluctuations are also involved in the optical mixing process. Thus the fluctuations are written into the heterodyne amplitude. Here the approximation $\delta P_1 = 0$ is adapted in the beginning and the derived expression is generalized afterwards to two RIN sources. This leads to

$$\begin{aligned}v_{\text{AC}} &= G_A R \sqrt{\eta_{\text{h}}(P_0 + \delta P_0)P_1} \cos(2\pi f_{\text{het}}t - \varphi) \\ v_{\text{AC}} &= G_A R \sqrt{\eta_{\text{h}}\sqrt{P_0 P_1 + \delta P_0 P_1}} \cos(2\pi f_{\text{het}}t - \varphi).\end{aligned}\quad (4.9)$$

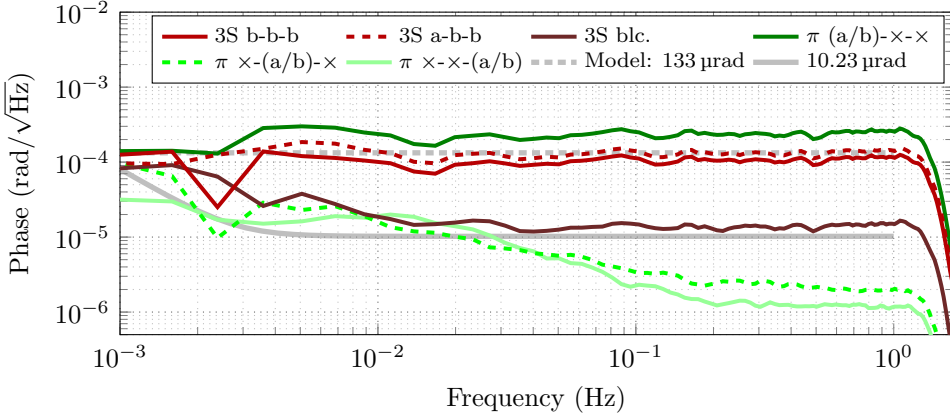


Figure 4.50: Measurement with f -RIN coupling. A limitation in accordance to the model is clearly visible. However, the noise can be attenuated by balanced detection. The latter seems to be not sufficiently balanced, as visible in the difference of the three-signal measurements using the two different channels of the noisy interferometer.

In the next step, a Taylor expansion for $\delta P_0 \ll 1$ to the first order is applied which leads to

$$v_{AC} = G_A R \sqrt{\eta_h} \left(\sqrt{P_0 P_1} + \frac{1}{2} \sqrt{\frac{P_1}{P_0}} \delta P_0 \right) \cos(2\pi f_{\text{het}} t - \varphi)$$

$$v_{AC} = G_A R \sqrt{\eta_h P_0 P_1} \cos(2\pi f_{\text{het}} t - \varphi) + \frac{G_A R}{2} \sqrt{\eta_h \frac{P_1}{P_0}} \delta P_0 \cos(2\pi f_{\text{het}} t - \varphi) .$$
(4.10)

Now the initial expression of the heterodyne signal is visible in the first term and can be separated from the additional error term. At this point it has to be considered that the frequency-dependent δP_0 in the error term mixes with the heterodyne signal itself. Thus the content of its frequency bin at $2f_{\text{het}}$ will be mixed to f_{het} and $3f_{\text{het}}$. While the latter will be discarded, the former acts now directly as additive noise at the beat note frequency in the well-known scheme as described above. In order to be able to apply the same formula, the error term will be rewritten in terms of the heterodyne amplitude, also taking into account a factor 2 from the mixing process (and

4 Implementing an optical three-signal test

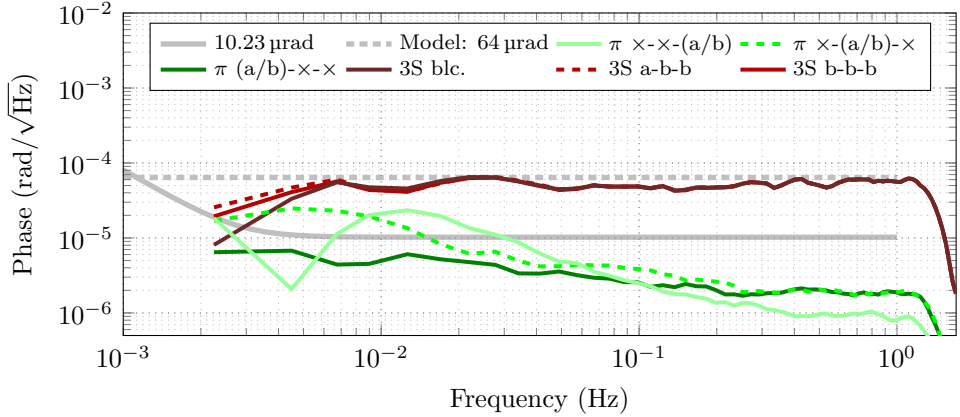


Figure 4.51: Measurement with $2f$ -RIN coupling. A limitation in accordance to the model is visible. However, the excess noise cannot be attenuated by balanced detection.

power fluctuations solely at $2f_{\text{het}}$):

$$\begin{aligned} \frac{G_A R}{4} \sqrt{\eta_h \frac{P_1}{P_0}} \delta P_0 &= G_A R \sqrt{\eta_h P_0 P_1} \frac{1}{4} \sqrt{\frac{1}{P_0^2}} \delta P_0 \\ &= k_{\text{het}} \frac{1}{4} \frac{\delta P_0}{P_0} = k_{\text{het}} \frac{1}{4} \text{RIN} . \end{aligned} \quad (4.11)$$

Now Equation (2.27) can be applied once more:

$$\tilde{\varphi} = \frac{\tilde{k} \sqrt{2}}{k_{\text{het}}} = \frac{\sqrt{2}}{4} \text{RIN}(2f_{\text{het}}) . \quad (4.12)$$

Again, the according power levels were monitored before the measurement and can be looked up in Appendix F.2. Substitution leads to an expected phase noise of

$$\tilde{\varphi} = 6.4 \times 10^{-5} \text{ rad}/\sqrt{\text{Hz}} . \quad (4.13)$$

This value is in good accordance with the measurement shown in Figure 4.51. It can also be observed that the π measurements are not affected by the coupling. Consequently, balanced detection shows no improvement. This difference compared to the f -coupling can be explained by the fact that the $2f_{\text{het}}$ term experiences the same π phase shift as the main signal due to the mixing process with the latter.

Within the frame of the approximation of small RIN, the derivation above can simply be generalized to two RIN sources. Assuming equal noise levels

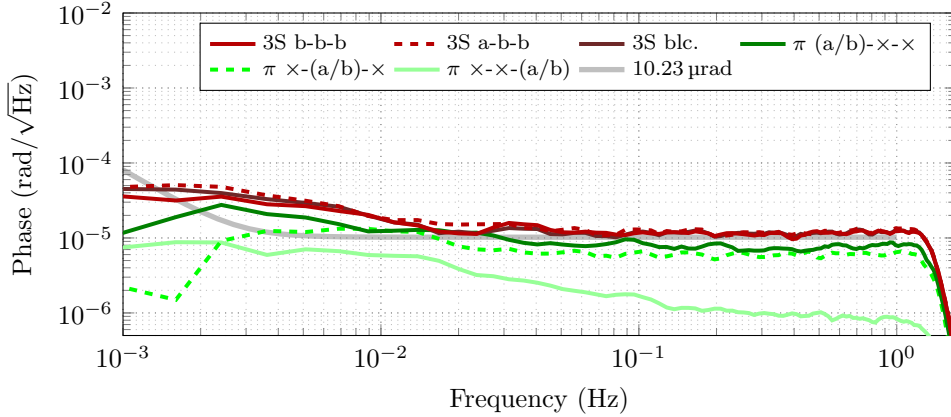


Figure 4.52: Measurement with RIN introduced from DC baseband up to the MHz regime without overlap with the heterodyne frequencies. A coupling in the two involved π measurements is visible while the balanced detection shows no improvement.

for the latter, it leads to a second term identical to the one calculated. Thus Equation (4.12) solely has to be scaled by a factor of $\sqrt{2}$.

Examining Equation (4.10), one could argue that like the $2f_{\text{het}}$ bin also the bin close to DC will be mixed into the heterodyne bin which in turn couples via the additive noise mechanism. A measurement conducted during the preparations of the ones shown above was performed with MHz amplitude noise limited in bandwidth, thus not covering the heterodyne beat note frequencies but the DC baseband. It is shown in Figure 4.52. While the induced noise was generated with similar parameters as in the measurements above, no single beam monitoring data is available for a precise quantification. Nevertheless, a coupling is visible. A significant feature is the coupling into both π measurements provided with light from the EOAM. This makes sense as the DC part of δP cannot be isolated by the choice of the heterodyne frequency. Yet it contradicts the assumption that the mechanism is the same as for $2f$ which showed no coupling into the π measurements. Furthermore, although visible in the latter, no improvement due to balanced detection could be achieved. An alternative explanation is the coupling via testbed noise, for example through thermal effects. Nevertheless, it seems to work differently compared to the harmonic amplitude modulations with the VOA that was used for the noise projection in Figure 4.45. Reasons for the last assumption are differences in the coupling coefficients of the relative heterodyne amplitudes measured with the phasemeter (not shown) into the

4 Implementing an optical three-signal test

phase itself. These differences are in the range of two orders of magnitude.

This discussion concludes the section and the description of the experimental work conducted for this thesis utilizing the Hexagon interferometer.

Outlook

This chapter gives an overview of the plans for the further evolution of the presented experiment. These include improvement of the current phase measurement performance as well as the extension to more advanced testing schemes. The latter will be implemented with the ultimate goal of testing key methods of the LISA metrology chain and their key components.

5.1 Performance and stability improvements

As analyzed in Section 4.3, several approaches for a further mitigation of testbed noise can be pursued. In a first iteration of the setup, the auxiliary optics including the photoreceivers will be reworked. Adjustable lenses in the line of the interferometer outputs will replace the folding mirrors to avoid beam pointing issues. The photoreceivers need to be revised in order to provide sufficient performance also at higher heterodyne frequencies. Furthermore, a switch to a four-channel design with a QPR is pursued. This offers not only additional diagnostic options via balanced DC power detection and DWS but is an actual key component needed to be tested for LISA, see the following Section 5.2.

On the Hexagon bench, an improved concept for the polarization adjustment will be implemented. The currently used square polarizers on their simple mounts will be exchanged with circular ones in rotatable mounts glued to the optical bench. Besides being able to adjust the polarization carefully, it will be essential to analyze it properly as well. For that purpose, a new mechanical photoreceiver mount design for easy and reliable removal and re-insertion is in development. This allows the easy placement of a polarimeter at the exact spot where the polarization matching is important.

Besides the auxiliary optics and polarizers, it will be beneficial to have improved fiber bench optics. This includes mounts with fixed non-zero angle

of incidence for all components. Furthermore, the beam splitter as a single laser power pickup can be put back and will allow a re-activation of the single laser power stabilization. Alternatively, it could be tried to capture a ghost beam emitted from the Hexagon for a power pickup.

For a more stable thermal stability, the passive isolation in the vacuum chamber will be improved by cutting thermal bridges between thermal shield and chamber. Additionally, the overall laboratory temperature stability will be improved by a new air conditioning (AC) control.

Enhancements for the laser preparation bench and the auxiliary phasemeter contain mostly pragmatic changes without expected impact on the performance. These comprise a rework of one laser lock for more reliable long-term locking. Additionally, automated acquisition and re-locking algorithms can be implemented with the auxiliary phasemeter.

While the three-signal testbed actually serves the purpose of testing the LISA phasemeter's phase performance, the noise hunting for testbed noise can get more convenient with less noise contribution from the phasemeter itself. In principal, testbed and phasemeter noise can be improved further in alternating iterations. At least one iteration step for the LISA phasemeter is planned for the near future. This comprises a change of the overall hardware with focus on the development of a new analog front end. The goal is a lower sensitivity to temperature fluctuation together with a better thermal management and control system as well as a reduction of cross-talk. Future investigation could cover the aforementioned amplitude-modulation-to-phase-modulation (AM-PM) coupling.

Furthermore, it is planned to build a second iteration of the Hexagon bench at the AEI. The design is not yet final. However, changes could be the removal of wedged angles in the beam splitters for reduced angular-beam-jitter-to-path-length-coupling and the addition of bonded polarizers and power pickups on the bench. Also the intentional introduction of an angular offset for DWS testing would be desirable for future tests.

5.2 Expansion to more testing schemes

As stated earlier, the long-term goal is the extension of the current setup towards the LIME. The essential step here is the utilization of three independent LISA phasemeters, which will allow testing of the clock tone transfer, ranging and data communication schemes including their key hardware components. This requires also the installation of EOMs which need to be verified for adequate phase fidelity in the modulation signal.

Further iterations comprise the implementation of a controlled power attenuation for the creation of the LISA inter-spacecraft low-power scenario. It is in particular important for the verification of photoreceiver designs in terms of a sufficiently small electronic noise contribution. Additionally, a QPR design must be verified for LISA. A candidate is a receiver developed by Germán Fernández Barranco [13].

As an intermediate testbed for the photoreceivers, an experiment branch will be constructed on the laser preparation bench following the scheme used in Section 4.2.11. An EOAM will modulate a single laser beam which is then detected by several photoreceivers for a differential measurement without interferometric effects. This could cover a stabilization of the EOAM operation point to avoid long-term drifts. An additional beam can be used to be able to switch back to a interferometric signal. Combinations of π measurements and null measurements can be set up for advanced diagnostics as well. Additionally, the same setup can also be used to further test the limitations by RIN.

With all the described improvements and extensions, the LIME setup with the Hexagon at its core provides an important tool on the way to the development and implementation of LISA. Furthermore, it is a unique testbed for heterodyne interferometry in general, a technique which is applied also in other space missions like GRACE-FO. In the associated area of gravimetry and in the climate research based on this gravity monitoring, other interferometry techniques are interesting as well, in particular for future missions which require the tracking of large numbers of degrees of freedoms due to the utilization of multiple TMs. One of these alternative interferometry techniques called DFMI is the topic of the second part of this thesis. In that part, the focus lies on the implementation of the phase readout rather than on the development of an elaborate testing and characterization scheme such as presented here in part one.

Part II

**Development and
implementation of phase
extraction schemes for Deep
Frequency Modulation
Interferometry**

Deep Frequency Modulation Interferometry

This part of the thesis describes the efforts to develop and implement phase extraction schemes for the interferometry technique called DFMI. The experimental work was conducted together with Christoph Vorndamme, whose master's thesis was supervised in the scope of this thesis. Details left out in this part, which is meant as a summary, can be looked up there [55].

The following chapter gives a short introduction to the topic of DFMI, including a description of its key working principles, a comparison to other techniques as well as examples of its application with focus on satellite gravimetry.

6.1 Key principles

In the first part of this section, the key principles of the DFMI technique will be described without pointing out advantages and disadvantages yet. The goal is the tracking of an optical path length change, here in particular due to the movement of a test mirror or test mass. The core of the technique is the application of a deep or strong frequency modulation of a laser source which is used within a self-homodyne interferometry scheme [34]. A sketch of the setup is shown in Figure 6.1, showing also a photoreceiver completing the setup. The interferometer is intentionally set up with unequal arm lengths. While in general this arm length mismatch is strongly limiting, for example in the application of LISA, here it is essential for the working principle. It translates the input laser frequency modulation into an effective phase modulation in one of the interferometer arms. A mathematical description is given for clarification in the following.

The formula of the photocurrent on the associated photoreceiver can be derived similarly as done for heterodyne interferometry in Section 2.1. The

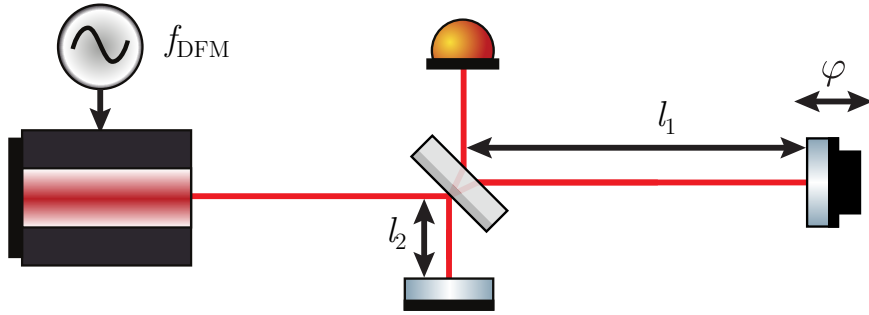


Figure 6.1: Michelson interferometer with unequal arm lengths. The laser source is driven by a strong or deep frequency modulation. A test mirror's movement is tracked.

single electric fields in the two interferometer arms are added up and the square-law detection is applied. Both fields are affected by a frequency modulation f_{DFM} with depth Δf , frequency f_m and phase ψ . In the following, also the angular frequency $\omega_m = 2\pi f_m$ will be used. The modulation signal can be written as

$$f_{DFM} = \Delta f \sin(\omega_m t + \psi) . \quad (6.1)$$

One of the arms experiences a delay τ due to the unequal arm lengths. Additionally, a phase offset ϕ is added. Hence the fields E_1, E_2 with amplitudes a_1, a_2 and optical carrier frequency ω_0 can be written as

$$\begin{aligned} E_1(t) &= a_1 \exp \left[i \left(\omega_0 t + \frac{\Delta f}{f_m} \sin(\omega_m t + \psi) \right) \right] + \text{c.c.} \\ E_2(t) &= a_2 \exp \left[i \left(\omega_0 (t - \tau) + \frac{\Delta f}{f_m} \sin(\omega_m (t - \tau) + \psi) + \phi \right) \right] + \text{c.c.} . \end{aligned} \quad (6.2)$$

It should be noted that the modulation depth is scaled by the modulation frequency. This is due to the fact that the modulation acts on the instantaneous frequency. In the following, the geometric phase shift $\omega_0 \tau$ and the added phase factor ϕ , which describes offsets for example due to the Gouy phase, are summarized and rewritten as $\phi - \omega_0 \tau = \phi_{\text{off}} + \varphi$. While ϕ_{off} is a static phase offset, φ describes small changes due to optical path length fluctuations. The former will be dropped in the following as it is not in the Fourier frequency band of interest for the applications presented later. The latter corresponds to what is later called measurement phase and relates for example to test mirror movement as depicted in Figure 6.1. Together with the common simplification of neglecting the second harmonic of ω_0 due

to detector bandwidth limitations and with the assumption $\omega_m \tau \ll 1$, the photoreceiver voltage signal $V_{\text{PR}}(t)$ can be written as

$$V_{\text{PR}}(t) = A[1 + C \cdot \cos(\underbrace{2\pi\Delta f\tau}_m \cdot \cos(\omega_m t + \psi) + \varphi)] \quad (6.3)$$

with $m = 2\pi\Delta f\tau$ being called the effective modulation depth. Here, the initial beam amplitudes or powers and the receiver response are summarized in A . The coherence of the interferometer is expressed in the contrast C . It is easy to show that the receiver signal is reduced to the one of a simple homodyne interferometer for equal arm lengths. An arm length difference $\Delta l = l_1 - l_2 = 0$ leads to a delay of $\tau = 2\Delta l/c_{\text{eff}} = 0$, where c_{eff} is the effective speed of light.

In order to extract the measurement phase φ , it has to be fetched of the nested trigonometric functions. This is the task of the phasemeter and will be described later in Chapter 7.

6.2 Experimental setup

Next, a measurement setup utilizing DFMI is described for further illustration. Figure 6.2 gives a graphical overview. The setup is divided into four major parts as presented in the following list.

- The utilized laser source needs to be able to handle a strong frequency modulation. For a given desired effective modulation depth m (typically a few π) the applicable modulation depths constrain the minimal value of the arm length mismatch and thus the interferometer's compactness. At the AEI, the model New FocusTM TLB-6821 Vortex PlusTM by Newport is used.
- A reference interferometer is required to independently measure the frequency fluctuations of the laser source within the measurement band. Without mitigation, they couple as undesired side product via the unequal arm length into the phase to be measured. The reference interferometer allows the generation of an error signal for a control loop to actively stabilize the laser source in the measurement band. Feasibility of a stable reference interferometer implementation was shown in [56].
- The measurement interferometer itself is implemented as a so-called optical head (OH). In a development step currently in progress [57],

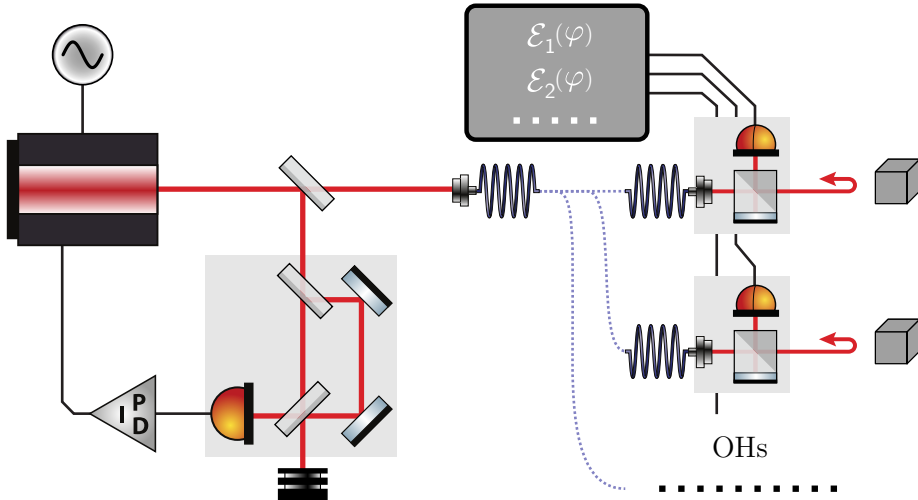


Figure 6.2: Schematic of an experimental setup utilizing DFMI. A reference interferometer serves for the stabilization of undesired laser frequency fluctuations. With the same basic optical components, multiple optical heads (OHs) can be operated. Their photoreceiver signals are captured by a phasemeter to extract the phase.

a prism combines the beam splitting, a reference arm and the beam recombination in a single optical component. It can be glued or bonded onto a compact and stable optical bench together with a FIOS and a photoreceiver. The test mirror or mass to be tracked can then be put into the free-beam measurement arm. The light for the bench is provided via fibers from the laser source. Any phase noise introduced by the fibers is suppressed due to the self-homodyne nature of the OH. Consequently, one laser source with one reference interferometer can easily provide light for multiple OHs at once.

- As mentioned earlier, a phase extraction scheme implemented in a phasemeter is required in order to obtain the measurement phase from the rather complex photoreceiver signal. As it is the main topic of this thesis part, a detailed description is carried out in Chapter 7.

For the discussion of the advantages and disadvantages of DFMI and for a brief overview of its origins, it is put into context with other interferometry techniques.

6.3 Comparison to other interferometry techniques

As already indicated, homodyne interferometry can be expressed as a special case of DFMI. Besides the utilization of an equal arm length interferometer, naturally also skipping the frequency modulation transforms the formula above into the one for homodyne interferometry, which is

$$V_{\text{PR}}(t) = A[1 + C \cdot \cos(\varphi)]. \quad (6.4)$$

While used with unprecedented sensitivity in LIGO [58, 59], it is not optimal for tracking optical path length changes in the range of a wavelength or above. This can be seen in Equation (6.4). If φ adopts all values between 0 and 2π , also the turning points of the trigonometric function are crossed, leading to a loss of sensitivity.

The capability of tracking over multiple wavelengths or interferometer fringes is connected to the attribute dynamic range, which was defined earlier in Section 2.2.7.

In first order, the readout of a DFMI interferometer ignores the issue of sensitivity loss stated above due to its different signal form which can be interpreted as a constantly changing operating point. The same applies to heterodyne interferometry which was introduced in Chapter 2 together with its interferometric signal in Equation (2.7). Additionally, examples for its application in multi-fringe tracking were given. Nevertheless, in particular for the tracking of TMs, it lacks a certain scalability. While LPF serves as an example for unprecedented sensitivity using heterodyne interferometry, it can also show that the readout of an arbitrary amount of degrees of freedom is not straight forward. Staying with the example of LPF, additional readout channels would increase the size and the complexity of the beam paths on its optical bench non-linearly. The usage of multiple benches instead would require a reference interferometer for optical phase length noise on each of those benches. DFMI avoids these issue due to its capability of phase noise suppression by self-homodyning on the single compact OHs.

Additional to the points made above, it should be mentioned that DFMI comes with the capability of absolute ranging. This is based on the fact that the arm length mismatch Δl is woven into the effective modulation depth via $m = 4\pi\Delta f\Delta l/c_{\text{eff}}$. Provided a proper knowledge or control of the modulation depth Δf and the reference arm length, the determination of m yields the absolute length of the measurement arm. This directly translates to the absolute distance between an exemplary TM and the beam splitting point. In the setup described above, an additional calibration interferometer

can serve as reference to estimate Δf . Furthermore, the reference arm of the OH may be implemented compact and stable with a well-known length.

The following points are listed as disadvantages of DFMI. Firstly, the tough requirements on the laser source in terms of frequency modulation should be mentioned. Ideally, it should be capable of enduring strong modulations with depths in the range of GHz and frequencies in the range of kHz without a non-linear response or additional creation of amplitude noise. Secondly, the phase extraction is more complex compared to other techniques. Finally, while proof-of-principle measurements were already conducted in [60], efforts are still ongoing to test the full capability in terms of measurement sensitivities in an optical testbed [57].

To conclude this section, a short overview of the origins and techniques related to DFMI will be given. While its current experimental configuration is based on the concept stated in [34], its close relation to the technique called Deep Phase Modulation Interferometry (DPMI) should be noted here [61, 62, 63]. DPMI basically exhibits the same interferometric signal as DFMI, yet it is directly generated by a phase modulation in one of the interferometer arms, hence the name. Earlier developed techniques with a similar modulation scheme found application in surface profiling [64, 65, 66] and piezo calibration [67]. The same modulation technique as in DFMI, yet with different readout schemes as described in this thesis, was successfully utilized in vibrometry [68, 69].

Besides the manifold of applications for DFMI and similar techniques, its immediate goal is its utilization for the tracking of TMs in particular for gravimetry and climate research satellite missions, which were briefly introduced in Chapter 1.

The next chapter will deal with the challenge of the phase extraction which has been neglected so far.

Phase extraction schemes for DFMI

This chapter focuses on the introduction of two schemes for the extraction of the phase from the interferometric signal of a DFMI interferometer. Besides the phase as the main measurand, both methods also provide the extraction of other signal parameters like for example the effective modulation depth m .

7.1 Spectral analysis and non-linear fit

The first method described in the following is a direct heritage from the DPMI technique, as it exhibits the same interferometric signal. This in turn can be considered as a generalized version of the so-called $J_1 \dots J_4$ method [70]. Thus the extraction scheme has already been described in detail in the context of DPMI [62, 71] as well as in the context of DFMI [55]. Here it will be summarized briefly.

In order to grasp the key idea of the method it is helpful to take a look at the spectral components of Equation (6.3). Using the Jacobi-Anger expression, the formula can be reshaped into a Fourier series. Consequentially, this enables the easy identification of its Fourier components. A generic Fourier series $X(t)$ can be written as

$$X(t) = \sum_{n=-\infty}^{\infty} c'_n e^{in\omega_m t} \quad (7.1)$$

with general complex amplitudes c'_n . For the case at hand, it can be assumed that $X(t) = V_{\text{PR}}(t)$ is a real-valued signal. This means the complex amplitudes are equal to the complex conjugates of their negative counterpart, meaning $c'_n = \overline{c'_{-n}}$. Hence the series can be rewritten and rescaled ($2c'_n = c_n$ for $n > 0$) to

$$V_{\text{PR}}(t) = c_0 + \text{Re} \left[\sum_{n=1}^{\infty} c_n e^{in\omega_m t} \right]. \quad (7.2)$$

As shown in the mentioned references, the complex amplitudes c_n are composed of the interferometric signal parameters as follows:

$$\begin{aligned} c_0 &= A [1 + C \cdot \cos(\varphi) J_0(m)] \\ c_n &= b_n e^{im\psi} \end{aligned} \quad (7.3)$$

where

$$b_n = \begin{cases} k \sin(\varphi) (-1)^{\frac{n+1}{2}} J_n(m) & \text{if } n \text{ is odd,} \\ k \cos(\varphi) (-1)^{\frac{n}{2}} J_n(m) & \text{if } n \text{ is even.} \end{cases} \quad (7.4)$$

Here, J_i denotes the Bessel functions of i -th order while the factor scaling the complex amplitudes' absolute values is rewritten as $k = 2AC$. c_0 is the DC component of the signal.

A closer look at the expression of c_n in Equation (7.3) reveals a system of n equations with four unknown variables. Mathematically a value of $n = 4$ should suffice to be able to determine the four parameters. In the algorithm described here, the value is higher, typically $n = 10$. Furthermore, the search for an analytic solution appears to be rather cumbersome. Hence a non-linear fit algorithm (Levenberg-Marquardt [72]) is applied as a numeric solution. It is based on a sum-of-squares minimization. Assuming knowledge of a set of 10 complex amplitudes c_n , the fit uses the model stated above to compute a set of estimated complex amplitudes C_n from a set of estimated parameters $\mathbf{p} = (k, m, \psi, \varphi)$. A comparison between the two sets of complex amplitudes gives a figure of merit χ^2 for the minimization, written as

$$\chi^2(\mathbf{p}) = \sum_{n=1}^{10} |c_n - C_n(\mathbf{p})|^2 . \quad (7.5)$$

The minimization itself is performed by a hybrid approach comprising the gradient descent method as well as the Gauss-Newton method. Finally, for a sufficiently small χ^2 the set of parameters \mathbf{p} yields a proper estimate of the actual interferometer parameters.

While the non-linear fit is typically implemented in software, the measurement and computation of the complex amplitudes can be carried out in different fashions. This will be discussed in Section 8.1.

For convenience, the just described method will also be referred to as "fit" in the following.

7.2 Kalman filter

Kalman filters [73] are widely used in a manifold of applications, for example in navigation and tracking [74]. In the first part of this section, a general

introduction to the topic will be given. Afterwards, the filter concept will be specified for the application in DFMI.

7.2.1 Basic Kalman filter

Whenever a physical quantity needs to be measured, the quantity itself and the measurement process are in general prone to stochastic uncertainties and noise. Instead of simply using the given measurements to derive an estimation of the physical quantity, the Kalman filter combines the former with predicted values computed by theoretical models of the associated physical system and the measurement system. This works particularly well if the underlying noise probability distributions are Gaussian and the models are linear. The fact can be illustrated by examining an attribute of Gaussian distributions: the fusion or multiplication of two Gaussians with mean values μ_1, μ_2 and variances σ_1, σ_2 lead to another Gaussian with a mean value of

$$\mu_{\text{res}} = \frac{\mu_1 \sigma_2^2 + \mu_2 \sigma_1^2}{\sigma_1^2 + \sigma_2^2}. \quad (7.6)$$

Assuming the two initial Gaussians to be representing measurement data and predicted data from a model, one can recognize an intrinsic weighting process for the resulting contribution. For example, for very high uncertainties and variance σ_2 , the expression converges to μ_1 and vice versa. Within the formalism of the Kalman filter, this weighting is manifested in the so-called Kalman gain K . Furthermore, the simple explanations with one-dimensional Gaussians used here can be extended in a heuristic method to derive the full Kalman filter formalism [75]. Apart from this, it can be shown that for the presented case and assuming completely accurate models, the Kalman filter is the optimal estimator for the measurands.

The formulas presented in the following utilize the notation from [74].

Firstly, a model for the physical system and the measurement process must be set up. For the basic Kalman filter, the framework for the modeling operates on discrete states with steps k and looks like this:

$$\mathbf{x}_k = \mathbf{\Phi}_{k-1} \mathbf{x}_{k-1} + \mathbf{w}_{k-1} \quad \text{with} \quad \mathbf{w}_k \sim \mathcal{N}(0, \mathbf{Q}_k) \quad (7.7)$$

$$\mathbf{z}_k = \mathbf{H}_k \mathbf{x}_k + \mathbf{v}_k \quad \text{with} \quad \mathbf{v}_k \sim \mathcal{N}(0, \mathbf{R}_k). \quad (7.8)$$

The state vector \mathbf{x}_k comprise the system state variables of interest at step k . The state transition matrix $\mathbf{\Phi}$ defines the undisturbed physical model by describing the change of the state variables during one discrete step. Additionally, the process noise is modeled by \mathbf{w} , with values drawn from

Gaussian or normal distributions defined by the covariance matrix \mathbf{Q} and with zero mean. The measurement process is modeled by the observation matrix \mathbf{H} . It translates from the state space to the measurement space with components \mathbf{z} . The measurement noise is added by the vector \mathbf{v} whose components draw values from Gaussian distributions defined by the measurement noise covariance matrix \mathbf{R} and zero mean. Finally, for a specific application, the generic expression of Equation (7.7) must be filled with the proper model description and also the correct numbers in term of noise covariances in order to provide a matching model. The components of the model can then be used in the actual filter as described in the following.

While for the model an ideal description of the state variables \mathbf{x} was assumed, the filter only deals with estimates of the latter. Those are indicated by a hat for example like $\hat{\mathbf{x}}$. Furthermore, the following differentiation will be done: a priori estimates generated by the model prediction are denoted by $(-)$, while a posteriori estimates originating from the fusion of predictions with measurements are denoted with $(+)$. The filter algorithm can be described as a two-step process. Firstly, the model generates prediction values for the state variables $\hat{\mathbf{x}}_{k(-)}$ as well as for their instantaneous estimation uncertainty described by the covariance matrix \mathbf{P}_k . For that purpose it uses initial or previous a posteriori values of the same quantities:

$$\hat{\mathbf{x}}_{k(-)} = \Phi_{k-1} \hat{\mathbf{x}}_{(k-1)(+)} \quad (7.9)$$

$$\mathbf{P}_{k(-)} = \Phi_{k-1} \mathbf{P}_{(k-1)(+)} \Phi_{k-1}^T + \mathbf{Q}_{k-1} . \quad (7.10)$$

Here, Φ^T denotes the transpose of Φ . In the second step, the predictions are fused with the measurement data \mathbf{z} . The earlier defined observation matrix projects the predicted state variables into the measurement space where it is compared to the actual measurement. The result \mathbf{y} is called innovation. Before the actual fusion can take place, the measure of the weighting ratio mentioned above is calculated in terms of the Kalman gain \mathbf{K} . While the measurement noise covariance \mathbf{R} stays the same for every iteration, the covariance of the predictions includes the whole evolution of the estimates including the accumulated process noise in \mathbf{P} . The concrete computations can be written as

$$\mathbf{y}_k = \mathbf{z}_k - \mathbf{H}_k \hat{\mathbf{x}}_{k(-)} \quad (7.11)$$

$$\mathbf{K}_k = \mathbf{P}_{k(-)} \mathbf{H}_k^T (\mathbf{H}_k \mathbf{P}_{k(-)} \mathbf{H}_k^T + \mathbf{R}_k)^{-1} . \quad (7.12)$$

Once \mathbf{K} is calculated, it is applied to perform the weighted fusion. Consequently the a posteriori estimates of the state variables $\hat{\mathbf{x}}_{k(+)}$ and their instantaneous uncertainty $\mathbf{P}_{k(+)}$ are obtained by the formulas

$$\hat{\mathbf{x}}_{k(+)} = \hat{\mathbf{x}}_{k(-)} + \mathbf{K}_k \mathbf{y}_k \quad (7.13)$$

$$\mathbf{P}_{k(+)} = \mathbf{P}_{k(-)} - \mathbf{K}_k \mathbf{H}_k \mathbf{P}_{k(-)} . \quad (7.14)$$

The parameters of $\hat{\mathbf{x}}_{k(+)}$ can be utilized as the filter's output. Yet they are also used as initial values for the next iteration.

This concludes the description of the basic Kalman filter. In its current form, it can only be applied to linear systems whose models can be described with a linear state transition matrix and a linear observation matrix. An approach to be able to use the filter also for non-linear systems is called extended Kalman filter. It begins the modeling with non-linear but differentiable state transition and observation functions $f(\mathbf{x})$ and $h(\mathbf{x})$, respectively. Yet before utilized in the formalism to describe the state transition and observation process, they are linearized at the values of the current state variable estimates by differentiation. While for the non-linear case of DFMI, the concept of the extended Kalman filter will be applied, it should be mentioned that also other deviations of the basic filter offer solutions. One example is the unscented Kalman filter [76].

7.2.2 Adaption for DFMI

Before the concrete adaption is described, it should be noted that while the Kalman filter was introduced above as a method to improve a given measurement system by fusing it with the prediction of a physical model, in DFMI it serves as the readout method itself. Furthermore, while it appeared to be well functioning, it will be shown later that it also profits a lot from the availability of another readout method in order to develop a proper physical model with well-suited parameters. This progress is called empiric state space modeling. The concrete method used for this purpose was developed by Gerhard Heinzl and Reinhard Prix. A description of its deviation can be looked up in [55], here only the main equations will be given. Similar approaches are shown in [77].

To start with, the state variables are defined by the DFMI signal parameters and their first derivatives ($k, m, \psi, \varphi, \dot{k}, \dot{m}, \dot{\psi}, \dot{\varphi}$). When taking a closer look to the time series derived in Equation (6.3), it becomes clear that the four parameters cannot describe the whole expression sufficiently due to the

independent parameter A . Instead of adding another entry to the state vector, the DC part of Equation (6.3) will be removed by a moving average filter prior to the Kalman filter itself. However, it has to be taken into account that the DC component c_0 also includes the term $k \cos(\varphi) J_0(m)$. Accordingly, the measurement model has to be adapted by subtracting this term. Finally, the non-linear, but in the image domain one-dimensional function $h(\mathbf{x})$, can be written then as

$$h(\mathbf{x}) = k \cdot \cos(m \cos(\omega_m t + \psi) + \varphi) - k \cos(\varphi) J_0(m) . \quad (7.15)$$

It can subsequently be linearized to obtain the observation matrix.

$$\mathbf{H} = \left[\begin{array}{cccccc} \left. \frac{\partial h(\mathbf{x})}{\partial k} \right|_{\hat{\mathbf{x}}_{k(-)}} & 0 & \left. \frac{\partial h(\mathbf{x})}{\partial m} \right|_{\hat{\mathbf{x}}_{k(-)}} & 0 & \left. \frac{\partial h(\mathbf{x})}{\partial \psi} \right|_{\hat{\mathbf{x}}_{k(-)}} & 0 & \left. \frac{\partial h(\mathbf{x})}{\partial \varphi} \right|_{\hat{\mathbf{x}}_{k(-)}} & 0 \end{array} \right]^T . \quad (7.16)$$

While the measurement is one-dimensional, the same applies to the measurement noise \mathbf{v} and its covariance matrix \mathbf{R} . In the case of DFMI, its physical model boils down to the quantization noise of the ADCs used to transfer the signal into the digital domain. It can be calculated from (2.31), can be determined experimentally or can be obtained from the device specifications.

In order to obtain the missing state transition matrix and the covariance matrix of the process noise, the following expressions will be introduced. Firstly, it is assumed that the cross power spectral density (CPSD) is computed using a discrete Fourier transform (DFT) with sampling frequency f_s . Then $\text{CPSD}(f_l)$ describes a matrix comprising all cross spectral densities of the state variables for a given frequency bin f_l . Naturally, the diagonal elements yield the spectral densities of the individual state variables for that bin as well. Finally, it can be written:

$$\text{CPSD}(f_l) = \frac{2}{f_s} \mathbf{M}_l \mathbf{Q} \mathbf{M}_l^* \quad (7.17)$$

where

$$\mathbf{M}_l = (\mathbf{I} - z_l \Phi)^{-1} . \quad (7.18)$$

Here, z_l denotes the delay operator for l sampling steps with f_s and \mathbf{M}^* represents the conjugate transpose of \mathbf{M} . \mathbf{I} is the identity matrix. The important point here is the fact that a set of expected state variable spectral densities can be computed from guessed state transition and process covariance matrices. In an iterative approach which tries to minimize the difference between the computed densities on one side and empirically determined densities on the other, the values for a proper physical model can

be derived. The concrete minimization process utilizes an algorithm developed by Gerhard Heinzl. While working with empirical data, some a priori information has to be provided still, as a certain shape of Φ has to be assumed before the aforementioned minimization can happen. This includes for example decisions about the inclusion of higher derivatives or cross correlations. Furthermore, it should be stated that Φ and \mathbf{Q} are assumed to be static here, thus lacking the dependence on k . The same applies to \mathbf{R} .

While a certain parallelism to the fit algorithm stated earlier can be drawn, it should be pointed out that the minimization process described here is not used during the run-time of the extraction method, but ideally directly before the actual measurements.

With the two methods described, the next chapter will present how they were probed in an optical testbed.

Testing phase extraction schemes for DFMI

This chapter will summarize the efforts to implement and test the phase extraction schemes presented in Chapter 7. The first part deals with the hardware used for this purpose while the second shows the application of a testing scheme introduced in Section 3.3.

8.1 Implementation on an SoC

Before the implementation of the two phase extraction schemes is described, a short overview of former implementations in particular in the context of DPMI at the AEI will be given. The first of them was carried out with a data acquisition (DAQ) card connected directly to a PC via PCI interface. It sampled the interferometric signal with 20 kHz. The spectral analysis in terms of an FFT and the calculations of the non-linear fit were performed on the PC [62]. In another iteration, the spectral analysis was outsourced to an FPGA and was implemented as multiple SBFTs with parallel pipelines. This allowed the increment of ADC sampling speed and also of the output frequency of parameters at the back end [71]. Benefits were reduced ADC quantization noise and a higher upper limit for the modulation frequencies. The availability of a faster output additionally enabled potential control loops which utilize the parameter to derive an error signal. The latter point is picked up later in the outlook in Section 8.4.

During the first tests of DFMI [60], also different approaches compared to the ones mentioned so far were utilized. One adapted the idea of the SBFTs to the DAQ setup, effectively replacing the FFT. Another was a time series fit in post-processing.

Here, an extension to the FPGA-based approach is presented. The FPGA was replaced with a system-on-a-chip (SoC). It is a single chip that comprises

two major parts, a processing system (PS) in form of a CPU as well as programmable logic (PL) like in an FPGA. In the application for DFMI, the latter implements the spectral analysis while the first computes the non-linear fit. Thus the whole extraction algorithm can be performed on the single chip. This not only increases the compactness and convenience of the setup, but also increases the bandwidth of the interface between spectral analysis and non-linear fit.

While the digital signal processing (DSP) core of the FPGA-only approach were re-used, effort had to be put into the implementation of the interface between PL and PS as well as the development of the software server running on the latter. Details can be looked up in [55]. While the Kalman filter in fact only requires a CPU, it is implemented here in the same hardware like the fit for better comparability. For this purpose a small DSP part was developed which filters the 80 MHz input signal down to a sampling rate suitable for the PS. While the downscaling rate can be adapted flexibly, it is constrained by the modulation depth and modulation frequency utilized. As the Kalman filter operates on the time series, its sampling rate needs to be at least twice as high as the fastest frequency bin still exhibiting significant power from the modulation. In order not to bloat storage capabilities with the high data rate, it is reduced subsequent to the Kalman filter with a software filter. The spectral analysis in contrast operates directly on the 80 MHz signal and samples it down as part of its functionality. During that progress, the modulation frequency and higher harmonics are mixed to DC. Therefore the fit is free of the constraints described for the Kalman filter. The output rates of both methods are typically chosen to be a couple of Hz.

The hardware assembly of the phasemeter used here is shown in Figure 8.1. It consists of a ZC706 evaluation board by Xilinx featuring a Zynq®-7000 XC7Z045 SoC. An FMC116 ADC card by 4DSP and the DAC card mentioned in Section 4.1.2 handle the signal conversion between digital and analog domain. The DAC card can be used to provide the modulation signal for the laser in an optical setup in order to have readout and signal synthesis synchronized. This allows the removal of clock drifts from the modulation phase ψ .

On a side note, it was tried to derive a Kalman filter design suitable for the PL, with the hope of being able to achieve a higher degree of parallelism. For this purpose, the software tool Vivado HLS by Xilinx was utilized. It converts software code (C, C++, SystemC) into PL compatible code (VHDL, Verilog). The conversion can be customized by certain directives to exert influence on the trade-off between speed and resources. A provisional test on an early version of the Kalman filter showed that even with a switch to 16

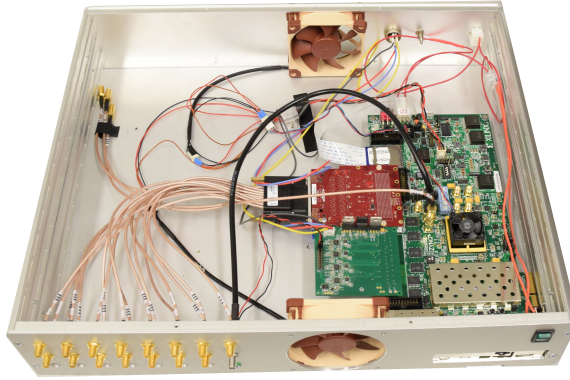


Figure 8.1: Picture of the full phasemeter assembly. On the bottom right an SoC evaluation board serves as the basic platform. An ADC card in red and a DAC card in green are connected. Image credit: C. Vorndamme.

bit fixed point data format, resources are rather limited. In first order, the design is limited by the available dedicated multipliers (DSP48E slices) of the Zynq®-7045's PL. A summary of a single channel design can be looked up in Appendix E.1.

8.2 Performance tests

In this section, measurements conducted with the presented phasemeter and the two different extraction schemes are shown. They were performed in an optical testbed implementing an electrical split measurement with an optical signal. More technically speaking, the DFMI signal of a Mach-Zehnder interferometer was captured with a photoreceiver, was divided by a resistive power splitter and finally was fed to two phasemeter channels. Figure 8.2 shows a sketch of the setup. A mirror in one of the interferometer arms can be moved by a piezo actuator and it can be used to introduce a slow phase signal. The phasemeter provided the modulation signal for the laser. The target frequency band of the measurements was set to the same range as in LISA. For the application in future gravimetry missions, a requirement for the whole interferometric readout precision was developed by Karim Douch. It is located within the LISA frequency band and is plotted as reference in later shown sensitivity plots.

Yet firstly, the capability of the schemes to track an inserted phase signal was tested. Figure 8.3 shows measurements using the spectral analysis and the non-linear fit including a 0.1 Hz signal applied to the piezo mirror.

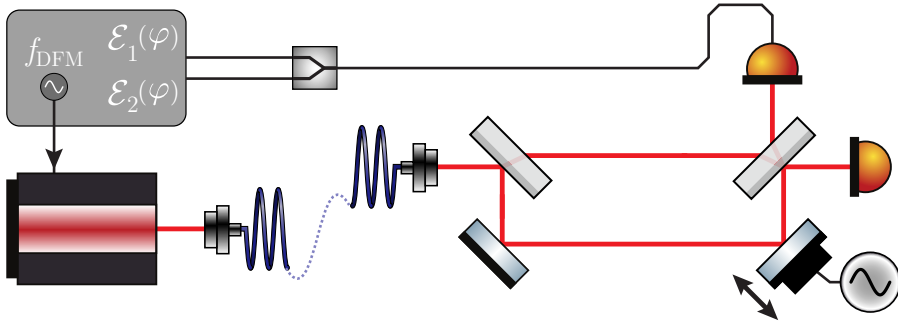


Figure 8.2: Testbed to probe the phasemeter with an electrical split measurement using an optical signal. A piezo mirror introduces a slow phase signal. The laser is driven by the phasemeter’s DAC.

Other parameters were $f_{\text{mod}} = 200.3 \text{ Hz}$ and $m = 6.6$. The single channel raw phase measurement reproduces the phase modulation. Hence the basic functionality of the phasemeter in terms of phase tracking could be shown. The dynamic range at the signal frequency is above four orders of magnitude. However, a non-linear response can be observed. Furthermore, the residuals in the split measurement show higher harmonics as well. Nevertheless, it is assumed that this non-linear response is not due to the principal concept of the readout method, but rather due to a mismatch of the model and the real signal. Such a mismatch can be caused by harmonic distortions of the signal by the ADCs. The caused higher harmonics then create additional tones at the frequency bins of interest. Another example of a harmonic distortion is the non-linear response of the laser to the applied modulation [60].

A similar measurement was carried out using the Kalman filter with $f_s = 10 \text{ kHz}$, $f_{\text{mod}} = 200 \text{ Hz}$ and $m = 2.6$. After several iterations of the design, which led to the concept presented in Section 7.2.2, the capability of tracking a DFMI phase signal with a Kalman filter could be proved for the first time. The associated measurement is shown in Figure 8.4 with the filter utilizing state space models derived by prior fit measurements. Similar to the actual phase test with the fit, non-linearities in the split measurement can be observed while possible higher harmonics in the single raw measurement vanish in the noise floor dominating at that time.

With both methods showing successful proof-of-principle measurements, their performances were probed in split measurements without an injected phase signal. Parameters were $m = 6.0$ in terms of modulation depth while the modulation frequency was set to $f_{\text{mod}} = 200.3 \text{ Hz}$ for the fit and to $f = 200 \text{ Hz}$ for the Kalman filter. The slight difference is based on the ne-

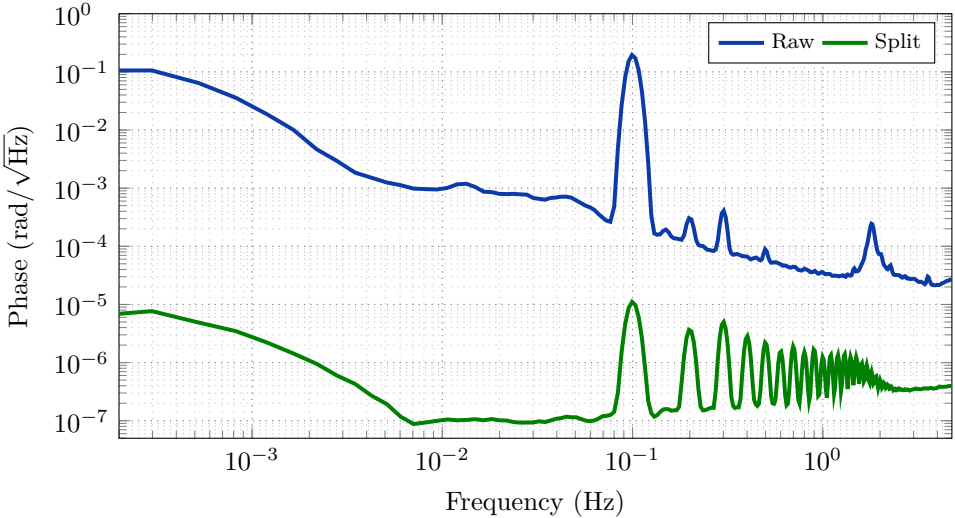


Figure 8.3: Phase extraction by the fit in an optical interferometer with a phase signal injected in one arm. The interferometric signal is divided after the photoreceiver in order to perform the shown split measurement. While tracking of the phase signal is achieved, a non-linear response can be observed.

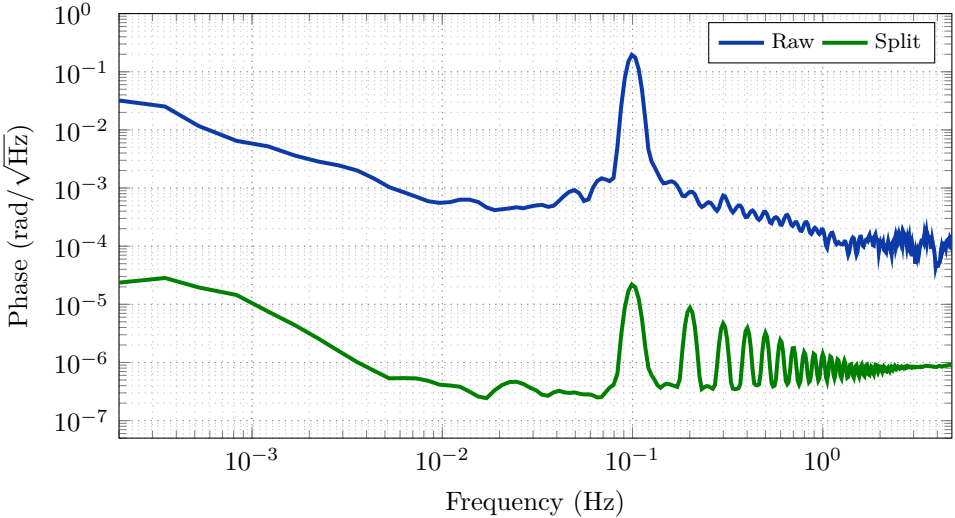


Figure 8.4: Phase extraction by the Kalman filter in an optical interferometer with a phase signal injected in one arm. The interferometric signal is divided after the photoreceiver in order to perform the shown split measurement. While tracking of the phase signal is achieved, a non-linear response can be observed.



8 Testing phase extraction schemes for DFMI

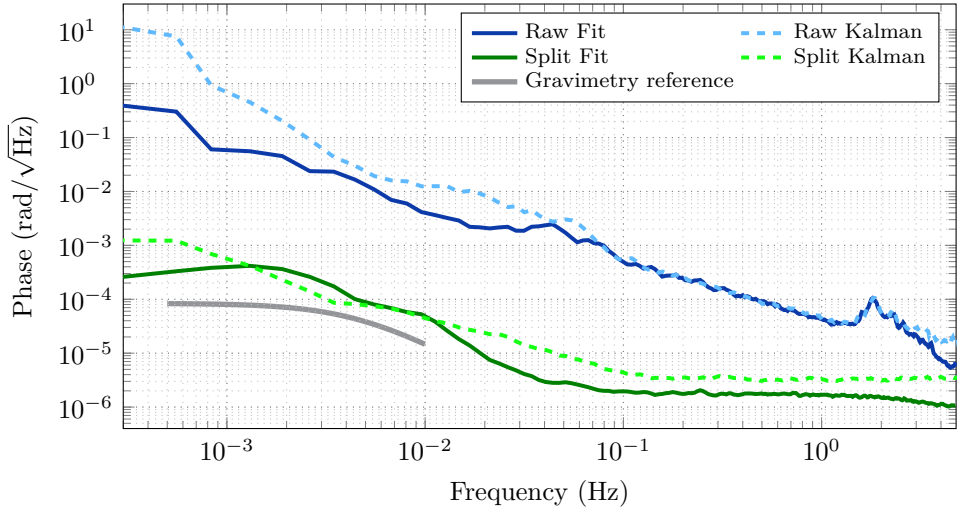


Figure 8.5: Comparison of fit and Kalman filter without phase modulation. The fit shows a slightly better performance at the upper frequencies. The gravimetry reference is not yet reached.

cessity to adapt to the filters in the pipelines used for the spectral analysis [63]. The measurements are shown in Figure 8.5. It should be noted that the measurements were performed at different times and thus with different sampled time series. This explains the difference in the two single raw measurements. For the upper frequency regime of 0.1–1 Hz, both methods show sensitivities below $4 \mu\text{rad}/\sqrt{\text{Hz}}$ with a slightly better performing fit. Both methods show a deterioration in sensitivity towards lower frequencies. This is accounted to strong coupling of thermal fluctuations in the ADC card. As described later in Section 8.4, the currently used card is not optimal for the application in DFMI and will be replaced in the future. The gravimetry reference is not yet reached in these measurements. In order to improve the performance further, the different parameters were varied. A final measurement was performed with a significantly increased modulation frequency of $f_{\text{mod}} = 2.136 \text{ kHz}$ and a modulation depth of $m = 6.9$. It was performed with the fit (the bandwidth of the Kalman filter at the time did not allow the use with the high modulation frequency) and is shown in Figure 8.6 together with the former fit measurement for comparison. The reasons for the improvement are thought to be weaker thermal fluctuations at the higher frequency bins. After the performed measurements with the two extraction methods were presented and described, a brief discussion of

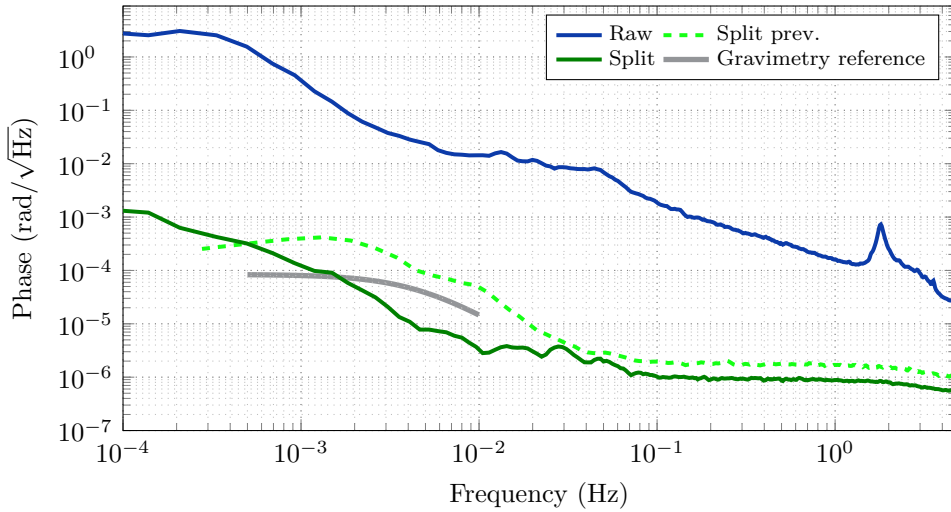


Figure 8.6: Fit measurement with optimized parameters including a high modulation frequency. A former measurement is presented for comparison together with the gravimetry reference which is partially reached.

their advantages and disadvantages will be given in the next section.

8.3 Comparison

A comparison of the two phase extraction schemes and their implementations can be carried out considering different aspects. In terms of performance, dynamic range and phase fidelity, both methods show similar results.

Almost equally important are the considerations of computational effort and required resources. Comparing the single channel designs of the two methods, the Kalman filter appears to be more compact, as only the PS is required. Furthermore, its runtime is deterministic, while the fit exhibits uncertainties due to the variable number of iterations. In total this allows for the application of the Kalman filter also on less complex and cheaper hardware systems, like microcontroller boards or the earlier mentioned DAQ card. For multi-channel applications that were aimed for in this thesis, the considerations become more complex. For example, the modulation frequency directly influences the required processing speed of the Kalman filter but not the fit. For multiple channels, this could quickly lead to an overload of the computational demand for the Kalman filter. However, also the availability of PL for a large number of pipelines for the spectral analysis

is a limiting factor still.

As a principal difference it should further be mentioned that the fit with its prior spectral analysis comes with an intrinsic filter for parasitic signals outside the complex amplitudes' frequency bins, while the Kalman filter operates on the unfiltered AC time series.

It should be stated for completeness here that during the experiments for the development of the optical DFMI setup presented in [57], the earlier mentioned implementation of the multiple SBFT and the fit with a DAQ card on a PC was successfully used. In comparison to the measurements shown here, it achieved a similar performance in the upper frequency band and exhibited close to no deterioration towards the lower end. Besides these advantages, its scalability is rather limited. Additionally, in a direct comparison, the hardware platform presented in this thesis offers the possibility to implement further control logic within one single system, as will be described in Section 8.4. Hopes are that with a new ADC card, similar performances at low frequencies can be reached by the more compact SoC system.

To conclude this chapter, the next section will summarize more possible improvements for the phasemeter and its phase extraction schemes.

8.4 Future developments and outlook

As emphasized before, the next pursued improvement of the setup is the development of a new ADC card which is better suited for the application in DFMI. The FMC116 card utilized so far was a heritage from LISA and GRACE-FO developments and its high sampling frequency is not fully needed. Instead, a new ADC card should rather yield lower harmonic distortions. As mentioned earlier, this is important as those distortions cause interference between the complex amplitudes. Furthermore, a design less sensitive to temperature fluctuations and with higher thermal stability is aimed at.

For the extraction methods themselves, possible improvements include the extension of the state model for the Kalman filter including higher derivatives and also considering cross correlations between the state variables.

Another interesting approach is the combination of the two methods, in best case cherry-picking both their advantages. One option here is to develop a Kalman filter that operates on the complex amplitudes generated by the spectral analysis. Ideally, a filter like this could extract the phase from a few frequency bins only while running with low sampling frequency equal to the output frequency. A working scheme provided, this would reduce the

required resources per channel drastically. Additionally, the hybrid method would benefit from the intrinsic filtering of the spectral analysis.

More pursued enhancements concerning also other parts of the DFMI setup are active stabilizations for the parameters k , ψ and m . Those stabilizations could directly utilize the extracted parameters within the hardware platform of the phasemeter to implement digital servos. Goals are the achievement of a better signal quality in terms of matching to the assumed model. Furthermore, the modulation for the laser generated in the phasemeter could be specifically tailored in order to preventively compensate for the non-linearities of the frequency actuator of the laser.

These considerations conclude the outlook as well as this part of the thesis.

Conclusions

In this thesis, the efforts to develop and characterize the phase extraction schemes and phasemeters for two interferometry techniques, namely heterodyning and DFMI, were presented.

The phase extraction for heterodyne interferometry was investigated in the context of the space-based GW detector LISA. The targeted sensitivity of the latter is broken down into sub-budgets for its different components. One of these is the phasemeter. Efforts were carried out to probe an EBB model of the LISA phasemeter for the three main requirements: phase noise contribution, dynamic range and bandwidth. The first constrains the direct noise contribution to the overall budget in the LISA band (0.1 mHz to above 0.1 Hz), the second is required for a working TDI algorithm and the third is needed to cope with the Doppler shifts occurring between LISA spacecraft. For the purpose of testing, an optical bench called Hexagon was utilized as the core of a testbed that implemented an optical three-signal test. This scheme was chosen to be able to probe the phasemeter for linearity under realistic conditions. An extensive noise hunting procedure was performed that finally led to a three-signal test reaching a performance of $10.23 \mu\text{rad}/\sqrt{\text{Hz}}$ down to 4 mHz. Including deterioration towards lower frequencies, this fulfills the single channel LISA requirement if relaxed with a factor of $\sqrt{3}$ to compensate for the three utilized signals. However, these measurements were conducted with low heterodyne frequencies and low phase dynamics. Separate measurements showed a limitation by the utilized photoreceivers for heterodyne frequencies at the upper LISA beat note bandwidth around 25 MHz. In a combined measurement with input phase dynamics above expected values in LISA ($445 \text{ Hz}/\sqrt{\text{Hz}}$ at 1 Hz) and a linear sweep over all frequencies in the LISA band, a sensitivity could be reached that only exceeded the relaxed requirement in the frequency interval of 0.4–20 mHz.

These measurements present benchmark results for a LISA phasemeter in an optical three-signal test. It should be emphasized that key components

for this were the optical testbed with the Hexagon interferometer and its auxiliary optics. While the LISA phasemeter was successfully tested in electrical split measurements and digital three-signal tests before, the Hexagon's compact design provided the required phase stability in the critical displacements of the optical three-signal test, while the auxiliary optics avoided the coupling of parasitic signals and other distortions. Furthermore, assumptions are that the measured performance is not yet limited by the Hexagon and can be improved further. This not only provides a testbed for the LISA phasemeter and possible revised versions thereof like engineering and flight models, but also for other components like photoreceivers and lasers (RIN). Furthermore, it can be extended to cover more essential parts of the LISA metrology chain like clock tone transfer, ranging and data communication. To put it in a nutshell, the measurements conducted for this thesis show, on the one hand, a benchmark test result of the phasemeter's three-signal performance and, on the other hand, that the utilized testbed may serve as an important corner stone for future technology development and testing for LISA.

The interferometer technique DFMI aims for the tracking of multiple degrees of freedom with high dynamic range and precision down to $\text{pm}/\sqrt{\text{Hz}}$ in a compact optical setup. It uses a deep laser frequency modulation which translates to a phase modulation by intentionally unequal interferometer arms. The self-homodyning properties of the interferometer enable the simultaneous operation of several duplicates of the aforesaid with only one frequency reference interferometer. The technique is primarily developed in the context of future space-based gravimetry and climate research missions which plan for the utilization of several TMs with optical readout. The efforts presented in the associated part of this thesis were focused on the development and implementation of the phase extraction, or phasemeter, rather than the design of an elaborate testbed like in the first part. Two distinct readout techniques were implemented and tested in split measurements with optical signals in an interferometer. The former is based on a spectral analysis with a non-linear fit applied to the analysis output. The second is an extended Kalman filter which was optimized by empiric state space modeling. Both techniques were implemented in an SoC for compactness and comparability. Furthermore, both were able to track the movement of a mirror in the interferometer testbed. A similar sensitivity for both methods was achieved with white noise floors below $4 \mu\text{rad}/\sqrt{\text{Hz}}$ at 0.1–1 Hz. However, deterioration of the performance towards lower frequencies as well as a non-linear response were observed for both. The assumed origin of these effects is the utilized ADC card not being optimally suited for

the application rather than the extraction schemes themselves. Hence the shown tests of the two methods on a single SoC lay the foundation for the future implementation of compact multi-channel DFMI phasemeters. This in turn is a key stone to perform the precise tracking of multiple TMs in multiple degrees of freedom.

Part III

Appendix

A

LIME setup

A LIME setup

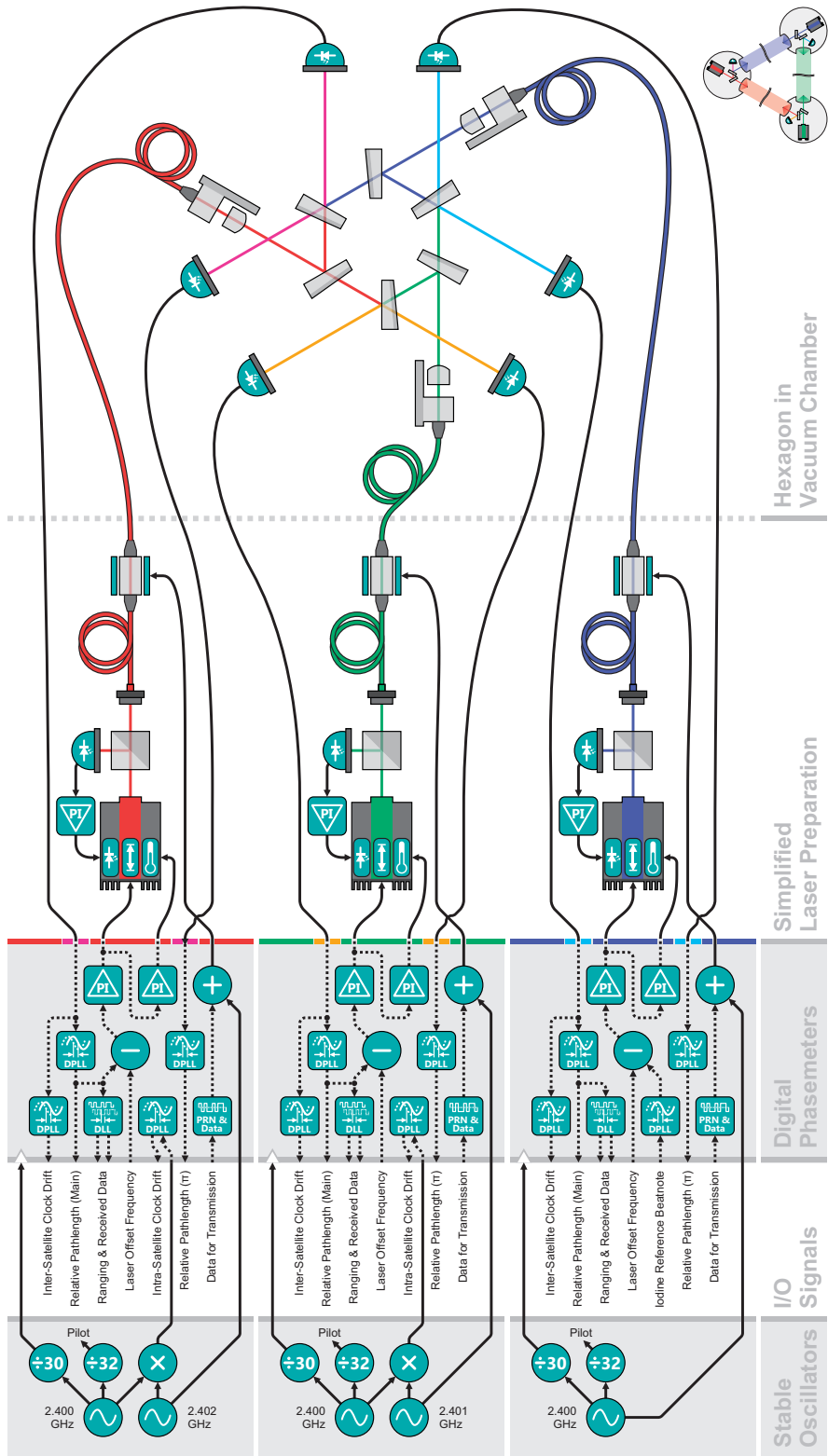


Figure A.1: Sketch of the setup for the planned experiment extension LIME. Image credit: D. Penkert.

B

Heterodyne frequency catalog

B

B Heterodyne frequency catalog

Table B.1: Catalog of heterodyne frequencies (in MHz) used for measurements with one ADC card.

	Channel 1	Channel 2	Channel 3	Channel 4
Fig. 4.3	6	6	6	6
Fig. 4.4	13	8	5	5
Fig. 4.5	13	4	9	9
Fig. 4.6 A	6.5	15	8.5	8.5
Fig. 4.6 B	15	6.5	8.5	8.5
Fig. 4.6 C	15	6.5	8.5	8.5
Fig. 4.6 D	7.75	2.65	5.1	5.1
Fig. 4.7	7.75	2.65	5.1	5.1
Fig. 4.8	7.75	2.65	5.1	5.1
Fig. 4.9			5.1	5.1
Fig. 4.11			5.0	5.0
Fig. 4.12	7.75	2.65	5.1	5.1
Fig. 4.13	7.75	2.65	5.1	5.1
Fig. 4.14	7.75	2.65	5.1	5.1
Fig. 4.15	5.1	5.1	5.1	5.1
Fig. 4.16	7.75	2.65	5.1	5.1
Fig. 4.17	7.75	2.65	5.1	5.1
Fig. 4.18		2.65		
Fig. 4.19	7.75	2.65	5.1	5.1
Fig. 4.22			5.8	5.8
Fig. 4.23			5.8	5.8
Fig. 4.26			5.8	5.8
Fig. 4.27 prev.			5.1	5.1
Fig. 4.27			5.8	5.8
Fig. 4.28			5.8	5.8
Fig. 4.29			5.8	5.8
Fig. 4.31			5.8	5.8
Fig. 4.32			5.8	5.8

Table B.2: Catalog of heterodyne frequencies (in MHz) used for measurements with two ADC cards.

		Channel 1	Channel 2	Channel 3	Channel 4
Fig. 4.34	ADC a			5.8	
	ADC b		5.8	5.8	
Fig. 4.35	ADC a			5.8	
	ADC b		5.8	5.8	
Fig. 4.36	ADC a			5.8	
	ADC b		5.8	5.8	
Fig. 4.37	ADC a			5.8	
	ADC b		5.8	5.8	
Fig. 4.38	ADC a	2.45	6.25	3.8	
	ADC b	2.45	6.25	3.8	
Fig. 4.39	ADC a	2.45	6.25	3.8	
	ADC b	2.45	6.25	3.8	
Fig. 4.40	ADC a	23.9	18.1	5.8	
	ADC b	23.9	18.1	5.8	
Fig. 4.41	ADC a	2.79	3.01	5.8	
	ADC b	2.79	3.01	5.8	
Fig. 4.43 First set	ADC a	2.1	2.1	2.1	
	ADC b			2.1	
Fig. 4.43 Second set	ADC a	2.1	2.1		
	ADC b	2.1	2.1		
Fig. 4.44 First set	ADC a	19.1	19.1	19.1	
	ADC b			19.1	
Fig. 4.44 Second set	ADC a	19.1	19.1		
	ADC b	19.1	19.1		
Fig. 4.45	ADC a	2.79	3.01	5.8	
	ADC b	2.79	3.01	5.8	
Fig. 4.47	ADC a	24.9	6.8	18.1	
	ADC b	24.9	6.8	18.1	
Fig. 4.48	ADC a	24.9	6.8	18.1	
	ADC b	24.9	6.8	18.1	
Fig. 4.49	ADC a	24.9-4.8	6.8-2.32	18.1-2.48	
	ADC b	24.9-4.8	6.8-2.32	18.1-2.48	
Fig. 4.50	ADC a	2	8.9	10.9	
	ADC b	2	8.9	10.9	
Fig. 4.51	ADC a	2	8.9	10.9	
	ADC b	2	8.9	10.9	
Fig. 4.52	ADC a	2.7	6.91	9.61	
	ADC b	2.7	6.91	9.61	

B Heterodyne frequency catalog

Table B.3: Catalog of heterodyne frequencies (in MHz) used for measurements with one ADC cards shown in Appendix C.

	Channel 1	Channel 2	Channel 3	Channel 4
Fig. C.1	7.75	2.65	5.1	5.1
Fig. C.2	7.75	2.65	5.1	5.1

Table B.4: Catalog of heterodyne frequencies (in MHz) used for measurements with two ADC cards shown in Appendix C.

		Channel 1	Channel 2	Channel 3	Channel 4
Fig. C.3	ADC a	5.8	5.8	5.8	5.8
	ADC b	5.8	5.8	5.8	5.8
Fig. C.4	ADC a			5.8	
	ADC b		5.8	5.8	
Fig. C.5	ADC a	2.45	6.25	3.8	6.25
	ADC b	2.45	6.25	3.8	
Fig. C.6	ADC a	23.9	18.1	5.8	
	ADC b	23.9	18.1	5.8	
Fig. C.7 top	ADC a	19.1	19.1	19.1	
	ADC b			19.1	
Fig. C.7 bottom	ADC a	19.1	19.1	19.1	
	ADC b			19.1	
Fig. C.8	ADC a		19.1		
	ADC b		19.1		
Fig. C.9	ADC a	24.9	6.8	18.1	
	ADC b	24.9	6.8	18.1	
Fig. C.10	ADC a	19.1	24.7	5.6	5.6
	ADC b	19.1	24.7	5.6	5.6
Fig. C.11	ADC a	2	8.9	10.9	
	ADC b	2	8.9	10.9	

C

Additional measurements

C

C Additional measurements

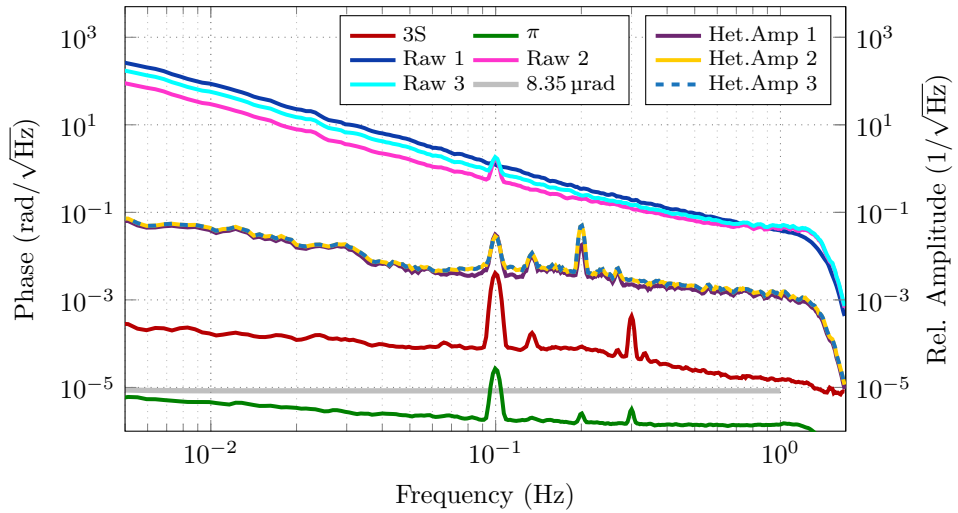


Figure C.1: Coupling of single laser amplitude modulation with high frequency lock gains.

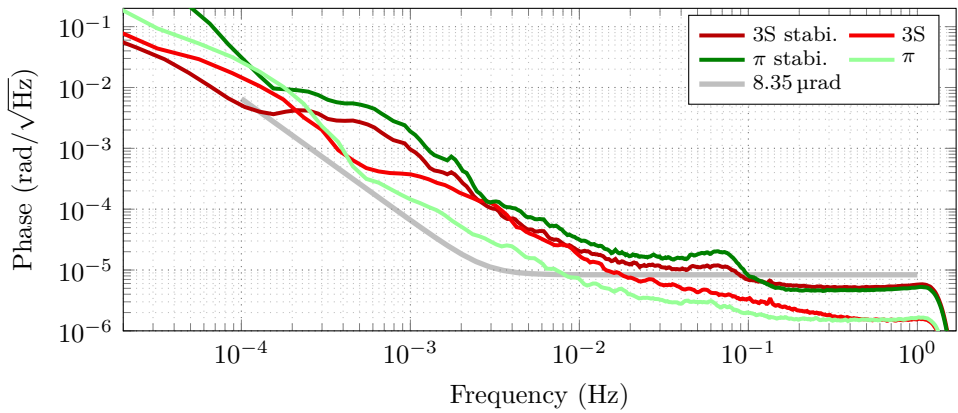


Figure C.2: Measurements with amplitude stabilization.

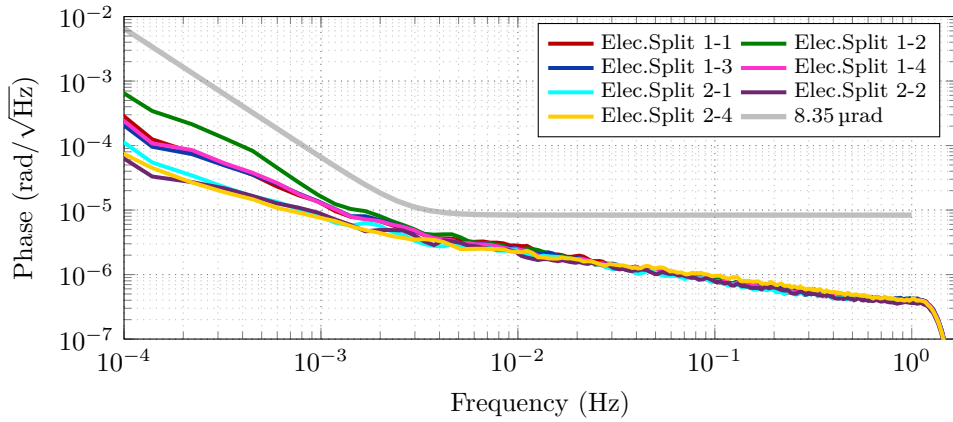


Figure C.3: Split measurement with two ADC cards.

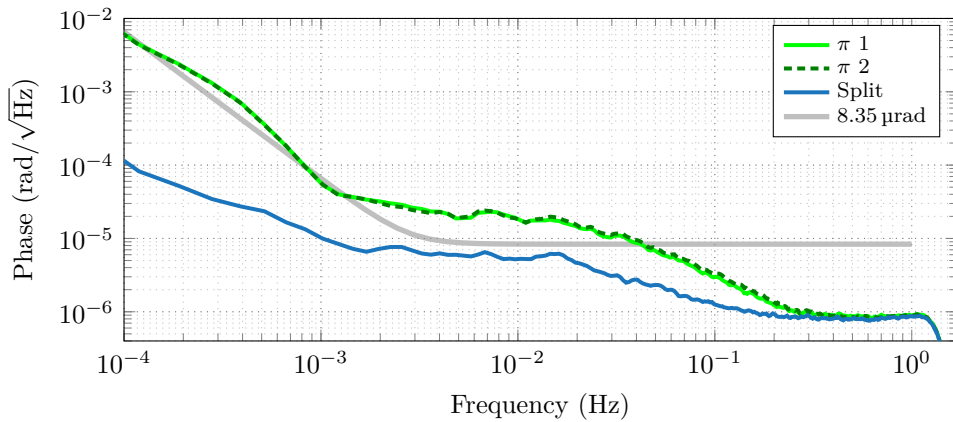


Figure C.4: Measurement with slightly mismatched Glan-Laser polarizers.

C Additional measurements

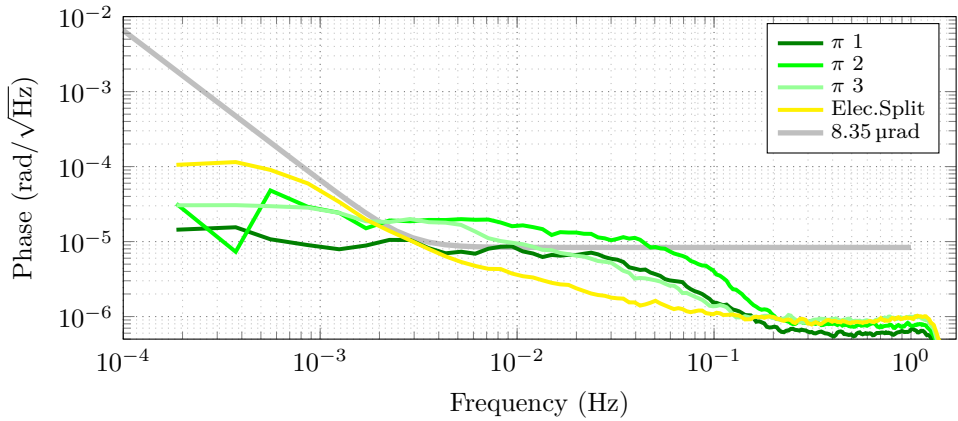


Figure C.5: Electrical split measurement performed with the signal of one π measurement channel.

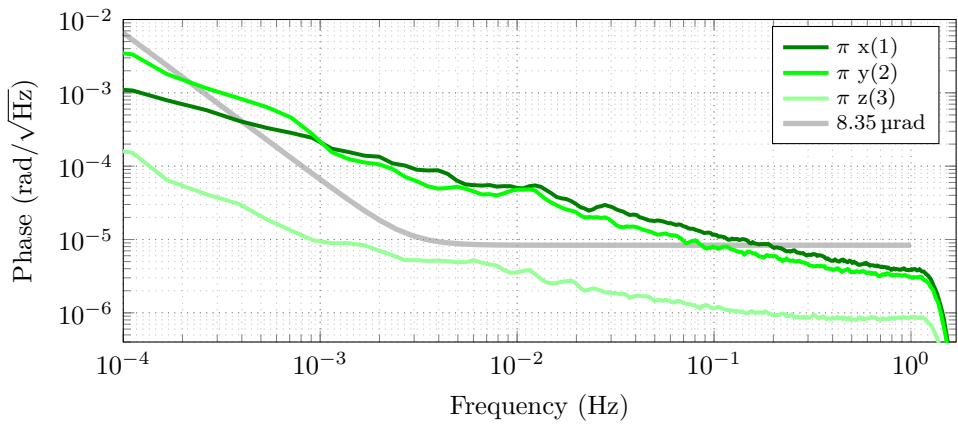


Figure C.6: π measurements with heterodyne frequencies of 23.9 MHz, 18.1 MHz, and 5.8 MHz.

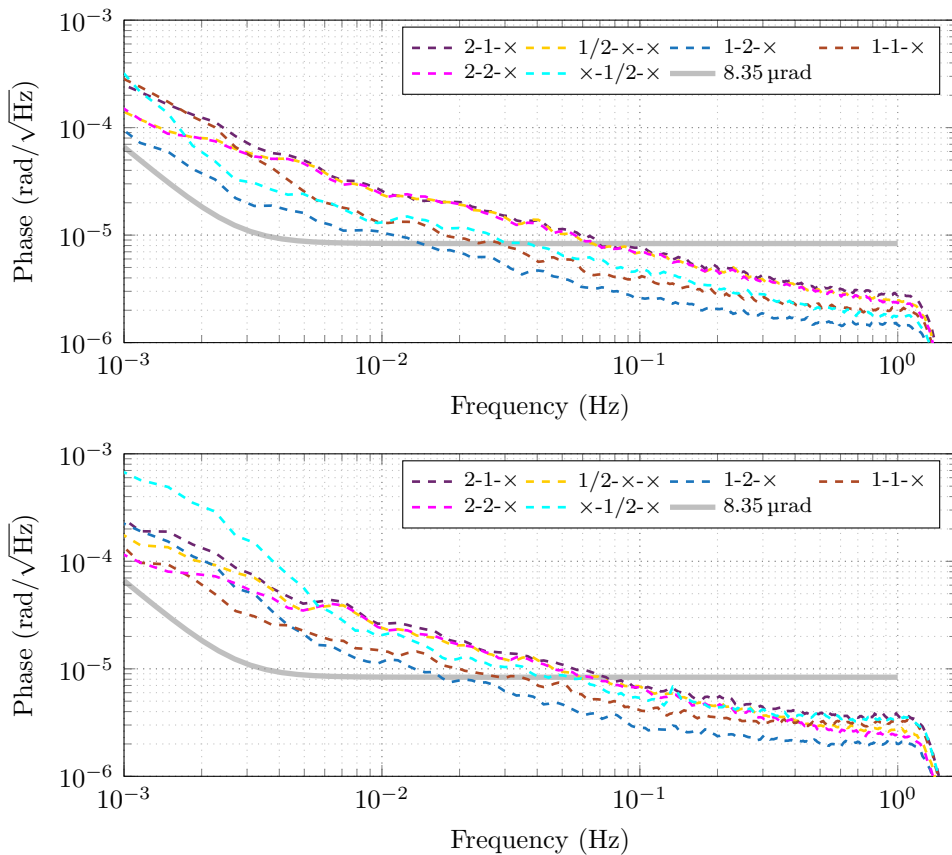


Figure C.7: Photoreceiver tests with amplitude modulated single laser at 19.1 MHz, decreased feedback resistor value and changed OP in one photoreceiver. Differential measurements between pairs of receivers are shown. The nomenclature follows the scheme x-y-z, denoting which of the two complementary receivers 1 or 2 of the three Hexagon outputs x,y and z were used in the full interferometric configuration. ×-1-× denotes the receiver with the decreased resistor value and OP. In the upper plot, only the resistor was replaced while the bottom plot comprises both changes. Some improvement compared to the other receivers 2-×-× and 1-×-× can be observed due to the first step.

C Additional measurements

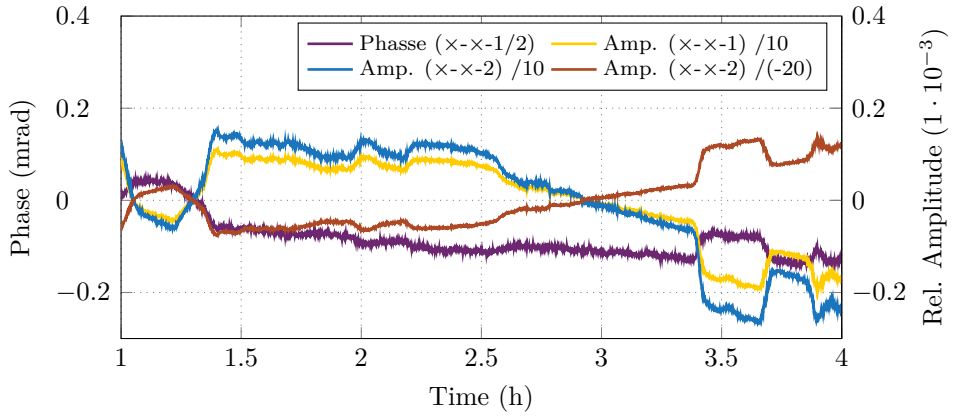


Figure C.8: Comparison of time series of differential phase measurement and associated relative amplitude in photoreceiver tests with amplitude modulated single laser at 19.1 MHz. The relative amplitudes are rescaled. A possible correlation is visible.

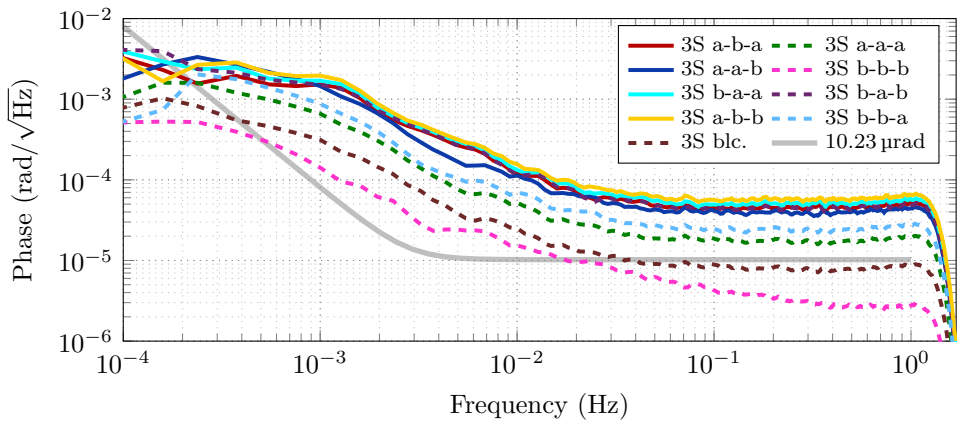


Figure C.9: Rearranged plot of the three-signal measurement in Figure 4.48 (center). Colors match the colors in Figure 4.40 in terms of used photoreceivers.

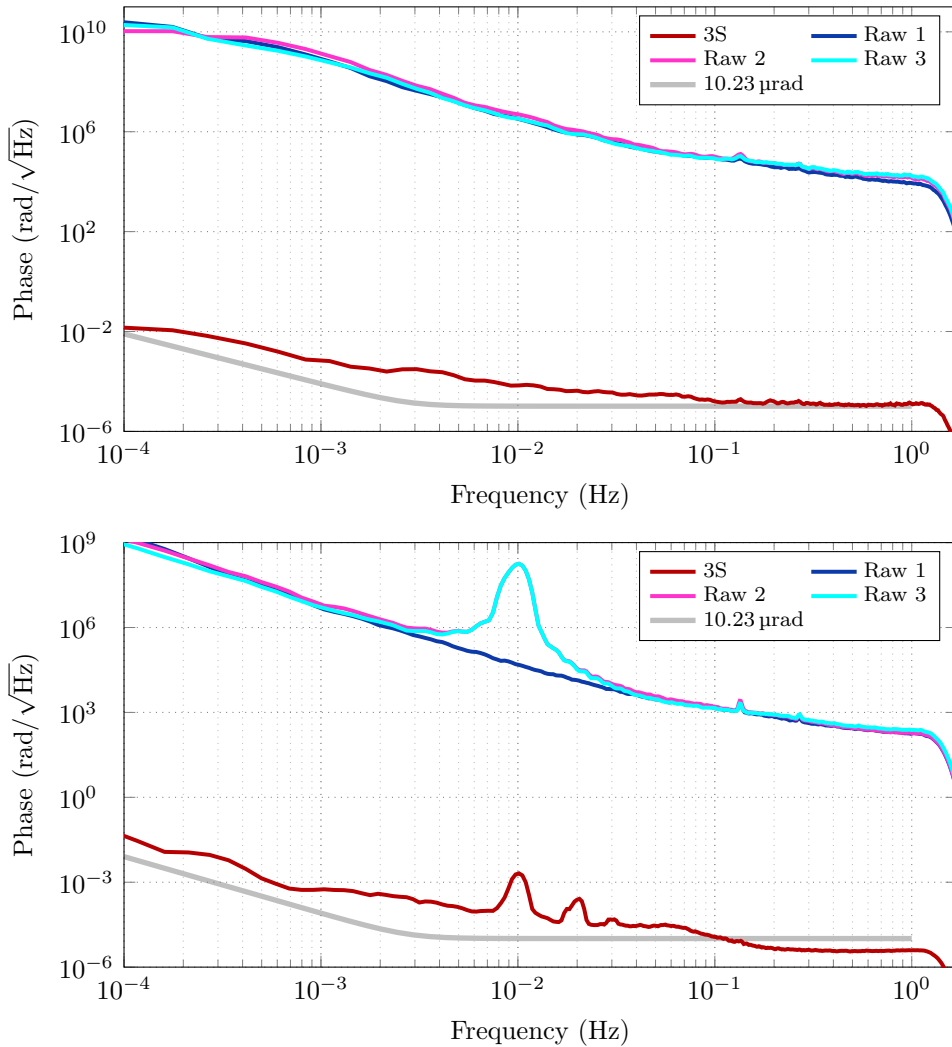


Figure C.10: Probing of dynamic range. The top measurement shows limitation of the three-signal measurements at 1 Hz with a dynamic range of 9 orders of magnitude. It increases to up to 12 orders of magnitude at lower frequencies. The bottom plot shows a measurement with a frequency modulation added at the error point of one of the frequency locks. The coupling shows non-linear components.

C Additional measurements

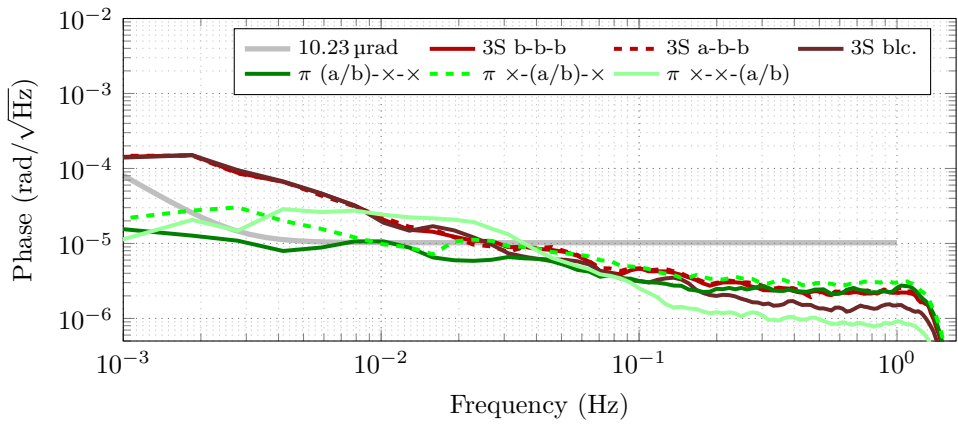


Figure C.11: Reference measurement before the introduction of RIN.

D

Temperature maps of lasers utilized in the experiments

Table D.1: Table of mode-hop-free regions of the three Mephisto NPRO lasers used in the experiments obtained with a SFP. Temperatures are given in °C.

Pump Current [A]	Laser A	Laser B	Laser C
	1.324-1.346	1.225	1.220-1.226
	21.47-23.92	23.97-26.36	21.74-23.68
	24.46-27.19	27.14-33.26	23.68-24.30
	27.73-30.43	34.00-39.66	25.30-30.92
	30.95-33.60	40.36-45.50	31.88-37.10
	34.29-36.84	46.06-49.50	

E

Kalman filter properties in programmable logic derived using a high level synthesis tool (Vivado HLS)

Table E.1: Summary of speed and resources of a single Kalman filter design transformed into PL. The bottom line shows that even for one filter channel, half the amount of available DSP48E blocks are used.

Latency		Interval		Type
min	max	min	max	
556	1556	557	1557	none

Name	BRAM_18K	DSP48E	FF	LUT
DSP	-	-	-	-
Expression	-	-	0	8914
FIFO	-	-	-	-
Instance	13	496	5233	21266
Memory	-	-	-	-
Multiplexer	-	-	-	1392
Register	-	-	8849	-
Total	13	496	14082	31572
Available	1090	900	437200	218600
Utilization (%)	1	55	3	14

F

Monitored powers for RIN coupling measurements

Table F.1: Photoreceiver voltages for coupling measurement of f -RIN. The voltages translate to optical power via photoreceiver gain and responsivity

	DC	$\tilde{v}(f_{\text{het}})$	$\tilde{v}(2f_{\text{het}})$
PR_{dark}	39.4 mV		
Single lasers (other blocked)			
v_0	-18.5 mV	$13.1 \mu\text{V}/\sqrt{\text{Hz}}$	
v_1	-116 mV		
Combined lasers:			
v_{01}	-168 mV	$14.1 \mu\text{V}/\sqrt{\text{Hz}}$	$7.5 \mu\text{V}/\sqrt{\text{Hz}}$
$v_{01\text{min}}$	-33.8 mV		
$v_{01\text{max}}$	-306 mV		

F Monitored powers for RIN coupling measurements

Table F.2: Photoreceiver voltages for coupling measurement of $2f$ -RIN. The voltages translate to optical power via photoreceiver gain and responsivity.

PR_{dark}	DC	$\tilde{v}(f_{\text{het}})$	$\tilde{v}(2f_{\text{het}})$
	39.4 mV		
Single lasers (other blocked)			
v_0	-19.7 mV		$10.7 \mu\text{V}/\sqrt{\text{Hz}}$
v_1	-116 mV		
Combined lasers:			
v_{01}	-168 mV	$7.8 \mu\text{V}/\sqrt{\text{Hz}}$	$10.6 \mu\text{V}/\sqrt{\text{Hz}}$
$v_{01\text{min}}$	-33.8 mV		
$v_{01\text{max}}$	-306 mV		

Bibliography

- [1] B. P. Abbott et al. “Observation of Gravitational Waves from a Binary Black Hole Merger”. In: *Phys. Rev. Lett.* 116 (6 Feb. 2016), p. 061102.
- [2] Peter Bender and the LISA Study Team. *LISA Pre-Phase A Report*. Technical report (1998), available at <https://lisa.nasa.gov/archive2011/documentation.html>.
- [3] Karsten Danzmann, Pau Amaro-Seone, Heather Audley, Stanislav Babak, John Baker, Enrico Barausse, Peter Bender, Emanuele Berti, Pierre Binetruy, and Michael Born. *LISA Laser Interferometer Space Antenna*. Technical report (2017), available as arXiv preprint: arXiv:1702.00786.
- [4] M. Armano et al. “Sub-Femto- g Free Fall for Space-Based Gravitational Wave Observatories: LISA Pathfinder Results”. In: *Phys. Rev. Lett.* 116 (23 June 2016), p. 231101.
- [5] M. Armano et al. “Beyond the Required LISA Free-Fall Performance: New LISA Pathfinder Results down to 20 μHz ”. In: *Phys. Rev. Lett.* 120 (6 Feb. 2018), p. 061101.
- [6] B. P. Abbott et al. “GW170608: Observation of a 19 Solar-mass Binary Black Hole Coalescence”. In: *The Astrophysical Journal Letters* 851.2 (2017), p. L35.
- [7] B. P. Abbott et al. “GW170814: A Three-Detector Observation of Gravitational Waves from a Binary Black Hole Coalescence”. In: *Phys. Rev. Lett.* 119 (14 Oct. 2017), p. 141101.
- [8] B. P. Abbott et al. “GW170817: Observation of Gravitational Waves from a Binary Neutron Star Inspiral”. In: *Phys. Rev. Lett.* 119 (16 Oct. 2017), p. 161101.
- [9] B. P. Abbott et al. “Multi-messenger Observations of a Binary Neutron Star Merger”. In: *The Astrophysical Journal Letters* 848.2 (2017), p. L12.

- [10] Alberto Sesana. “Prospects for Multiband Gravitational-Wave Astronomy after GW150914”. In: *Phys. Rev. Lett.* 116 (23 June 2016), p. 231102.
- [11] Massimo Tinto and J. W. Armstrong. “Cancellation of laser noise in an unequal-arm interferometer detector of gravitational radiation”. In: *Phys. Rev. D* 59 (10 Apr. 1999), p. 102003.
- [12] Markus Otto. “Time-delay interferometry simulations for the laser interferometer space antenna”. PhD thesis. Leibniz Universität Hannover, 2015.
- [13] Germán Fernández Barranco. “Photodetection in intersatellite laser interferometers”. PhD thesis. Leibniz Universität Hannover, 2017.
- [14] Andreas Freise and Kenneth Strain. “Interferometer Techniques for Gravitational-Wave Detection”. In: *Living Reviews in Relativity* 13.1 (Feb. 2010), p. 1. ISSN: 1433-8351.
- [15] Simon Barke. “Inter-Spacecraft Frequency Distribution for Future Gravitational Wave Observatories”. PhD thesis. Leibniz Universität Hannover, 2015.
- [16] Karsten Danzmann and the LISA International Science Team. *LISA assessment study report*. Technical report (2011), available at <http://sci.esa.int/lisa/48364-lisa-assessment-study-report-yellow-book/>.
- [17] K-S Isleif et al. “Suppressing ghost beams: Backlink options for LISA”. In: *Journal of Physics: Conference Series* 840.1 (2017), p. 012016.
- [18] Katharina-Sophie Isleif et al. “Towards the LISA backlink: experiment design for comparing optical phase reference distribution systems”. In: *Classical and Quantum Gravity* 35.8 (2018), p. 085009.
- [19] Christina Brugger, Bernhard Broll, Ewan Fitzsimons, Ulrich Johann, Wouter Jonke, Stefano Lucarelli, Susanne Nikolov, Martijn Voert, Dennis Weise, and Gert Witvoet. “An experiment to test in-field pointing for Elisa”. In: *Proc. SPIE* 10563 (2017), p. 8.
- [20] Massimo Tinto, F. B. Estabrook, and J. W. Armstrong. “Time-delay interferometry for LISA”. In: *Phys. Rev. D* 65 (8 Apr. 2002), p. 082003.
- [21] Massimo Tinto and Sanjeev V. Dhurandhar. “Time-Delay Interferometry”. In: *Living Reviews in Relativity* 17.1 (Aug. 2014), p. 6. ISSN: 1433-8351.

- [22] Michele Vallisneri. “Geometric time delay interferometry”. In: *Phys. Rev. D* 72 (4 Aug. 2005), p. 042003.
- [23] Markus Otto, Gerhard Heinzl, and Karsten Danzmann. “TDI and clock noise removal for the split interferometry configuration of LISA”. In: *Classical and Quantum Gravity* 29.20 (2012), p. 205003.
- [24] Gerhard Heinzl, Juan Jose Esteban Esteban, Simon Barke, Markus Otto, Yan Wang, Antonio F Garcia, and Karsten Danzmann. “Auxiliary functions of the LISA laser link: ranging, clock noise transfer and data communication”. In: *Classical and Quantum Gravity* 28.9 (2011), p. 094008.
- [25] Yan Wang, Gerhard Heinzl, and Karsten Danzmann. “First stage of LISA data processing: Clock synchronization and arm-length determination via a hybrid-extended Kalman filter”. In: *Phys. Rev. D* 90 (6 Sept. 2014), p. 064016.
- [26] Shawn J. Mitryk, Guido Mueller, and Josep Sanjuan. “Hardware-based demonstration of time-delay interferometry and TDI-ranging with spacecraft motion effects”. In: *Phys. Rev. D* 86 (12 Dec. 2012), p. 122006.
- [27] Andrew Sutton, Kirk McKenzie, Brent Ware, and Daniel A. Shaddock. “Laser ranging and communications for LISA”. In: *Opt. Express* 18.20 (Sept. 2010), pp. 20759–20773.
- [28] Simon Barke, Nils Brause, Iouri Bykov, Juan Jose Esteban Delgado, Anders Enggaard, Oliver Gerberding, Gerhard Heinzl, Joachim Kullmann, Søren Møller Pedersen, and Torben Rasmussen. *LISA Metrology System Final Report*. Technical report (2014), available at <http://hdl.handle.net/11858/00-001M-0000-0023-E266-6>.
- [29] Oliver Gerberding. “Phase readout for satellite interferometry”. PhD thesis. Leibniz Universität Hannover, 2014.
- [30] Floyd M. Gardner. *Phaselock Techniques*. 3rd. New Jersey: John Wiley & Sons, Inc., 2005.
- [31] Oliver Gerberding, Benjamin Sheard, Iouri Bykov, Joachim Kullmann, Juan Jose Esteban Delgado, Karsten Danzmann, and Gerhard Heinzl. “Phasemeter core for intersatellite laser heterodyne interferometry: modelling, simulations and experiments”. In: *Classical and Quantum Gravity* 30.23 (2013), p. 235029.

- [32] B. S. Sheard, G. Heinzel, K. Danzmann, D. A. Shaddock, W. M. Klipstein, and W. M. Folkner. “Intersatellite laser ranging instrument for the GRACE follow-on mission”. In: *Journal of Geodesy* 86.12 (Dec. 2012), pp. 1083–1095. ISSN: 1432-1394.
- [33] Juan José Esteban, Antonio F. García, Simon Barke, Antonio M. Peinado, Felipe Guzmán Cervantes, Iouri Bykov, Gerhard Heinzel, and Karsten Danzmann. “Experimental demonstration of weak-light laser ranging and data communication for LISA”. In: *Opt. Express* 19.17 (Aug. 2011), pp. 15937–15946.
- [34] Oliver Gerberding et al. “Readout for intersatellite laser interferometry: Measuring low frequency phase fluctuations of high-frequency signals with microradian precision.” eng. In: *Rev Sci Instrum* 86.7 (July 2015), p. 074501.
- [35] R. Boudot and E. Rubiola. “Phase noise in RF and microwave amplifiers”. In: *IEEE Transactions on Ultrasonics, Ferroelectrics, and Frequency Control* 59.12 (Dec. 2012), pp. 2613–2624. ISSN: 0885-3010.
- [36] G. Heinzel et al. “The LTP interferometer and phasemeter”. In: *Classical and Quantum Gravity* 21.5 (2004), S581.
- [37] Chen Wang. “FPGA-based, 4-channel, High-speed Phasemeter for Heterodyne Interferometry”. MA thesis. University of Rochester, 2013.
- [38] Triantafillos Koukoulas, Stephen Robinson, Srinath Rajagopal, and Bajram Zeqiri. “A comparison between heterodyne and homodyne interferometry to realise the SI unit of acoustic pressure in water”. In: *Metrologia* 53.2 (2016), p. 891.
- [39] O Jennrich, P McNamara, D Robertson, S Rowan, H Ward, and J Hough. “Interferometry developments for LISA and SMART-2”. In: *Classical and Quantum Gravity* 19.7 (2002), p. 1731.
- [40] S. E. Pollack and R. T. Stebbins. “Demonstration of the zero-crossing phasemeter with a LISA test-bed interferometer”. In: *Classical and Quantum Gravity* 23.12 (2006), p. 4189.
- [41] Shawn J Mitryk, Vinzenz Wand, and Guido Mueller. “Verification of time-delay interferometry techniques using the University of Florida LISA interferometry simulator”. In: *Classical and Quantum Gravity* 27.8 (2010), p. 084012.
- [42] D. Shaddock, B. Ware, P. G. Halverson, R. E. Spero, and B. Klipstein. “Overview of the LISA Phasemeter”. In: *AIP Conference Proceedings* 873.1 (2006), pp. 654–660.

- [43] Glenn de Vine, Brent Ware, Kirk McKenzie, Robert E. Spero, William M. Klipstein, and Daniel A. Shaddock. “Experimental Demonstration of Time-Delay Interferometry for the Laser Interferometer Space Antenna”. In: *Phys. Rev. Lett.* 104 (21 May 2010), p. 211103.
- [44] E. J. Elliffe, J. Bogenstahl, A. Deshpande, J. Hough, C. Killow, S. Reid, D. Robertson, S. Rowan, H. Ward, and G. Cagnoli. “Hydroxide-catalysis bonding for stable optical systems for space”. In: *Classical and Quantum Gravity* 22.10 (2005), S257.
- [45] Daniel Penkert. “Hexagon: An Optical Three-Signal Testbed for the LISA Metrology Chain”. Diploma thesis. Leibniz Universität Hannover, 2016.
- [46] Marina Dehne. “Construction and noise behaviour of ultra-stable optical systems for space interferometers”. PhD thesis. Leibniz Universität Hannover, 2012.
- [47] Dennis Schmelzer. “Thermally compensated fiber injectors for the three-backlink and hexagon experiments”. MA thesis. Leibniz Universität Hannover, 2015.
- [48] T. S. Schwarze, G. Fernández Barranco, D. Penkert, O. Gerberding, G. Heinzel, and K. Danzmann. “Optical testbed for the LISA phasemeter”. In: *Journal of Physics: Conference Series* 716.1 (2016), p. 012004.
- [49] G. A. McBean and J. A. Elliott. “Pressure and humidity effects on optical refractive-index fluctuations”. In: *Boundary-Layer Meteorology* 20.1 (Feb. 1981), pp. 101–109. ISSN: 1573-1472.
- [50] G. Heinzel, A. Rüdiger, and R. Schilling. *Spectrum and spectral density estimation by the Discrete Fourier transform (DFT), including a comprehensive list of window functions and some new at-top windows*. Technical report (2002).
- [51] Joachim Kullmann. “Development of a digital phase measuring system with microradian precision for LISA”. PhD thesis. Leibniz Universität Hannover, 2012.
- [52] Michael Troebs. “Laser development and stabilization for the spaceborne interferometric gravitational wave detector LISA”. PhD thesis. Leibniz Universität Hannover, 2005.

- [53] Maurice Lessing, Helen S. Margolis, C. Tom A. Brown, Patrick Gill, and Giuseppe Marra. “Suppression of amplitude-to-phase noise conversion in balanced optical-microwave phase detectors”. In: *Opt. Express* 21.22 (Nov. 2013), pp. 27057–27062.
- [54] R. P. Scott, C. Langrock, and B. H. Kolner. “High-dynamic-range laser amplitude and phase noise measurement techniques”. In: *IEEE Journal of Selected Topics in Quantum Electronics* 7.4 (July 2001), pp. 641–655. ISSN: 1077-260X.
- [55] Christoph Vorndamme. “Development and characterization of a SoC-based phase readout system for deep frequency modulation”. MA thesis. Leibniz Universität Hannover, 2017.
- [56] Oliver Gerberding, Katharina-Sophie Isleif, Moritz Mehmet, Karsten Danzmann, and Gerhard Heinzl. “Laser-Frequency Stabilization via a Quasimonolithic Mach-Zehnder Interferometer with Arms of Unequal Length and Balanced dc Readout”. In: *Phys. Rev. Applied* 7 (2 Feb. 2017), p. 024027.
- [57] Katharina-Sophie Isleif. “Laser interferometry for LISA and satellite geodesy missions”. PhD thesis. Leibniz Universität Hannover, 2018.
- [58] Matthew Pitkin, Stuart Reid, Sheila Rowan, and Jim Hough. “Gravitational Wave Detection by Interferometry (Ground and Space)”. In: *Living Reviews in Relativity* 14.1 (July 2011), p. 5. ISSN: 1433-8351.
- [59] LIGO Scientific Collaboration. *Instrument Science White Paper*. Tech. rep. LIGO, 2017.
- [60] Katharina-Sophie Isleif, Oliver Gerberding, Thomas S. Schwarze, Moritz Mehmet, Gerhard Heinzl, and Felipe Guzmán Cervantes. “Experimental demonstration of deep frequency modulation interferometry”. In: *Opt. Express* 24.2 (Jan. 2016), pp. 1676–1684.
- [61] Gerhard Heinzl, Felipe Guzmán Cervantes, Antonio F. García Marin, Joachim Kullmann, Wang Feng, and Karsten Danzmann. “Deep phase modulation interferometry”. In: *Opt. Express* 18.18 (Aug. 2010), pp. 19076–19086.
- [62] Felipe Guzmán Cervantes. “Gravitational wave observation from space: optical measurement techniques for LISA and LISA pathfinder”. PhD thesis. Leibniz Universität Hannover, 2009.

- [63] Thomas S. Schwarze, Oliver Gerberding, Felipe Guzmán Cervantes, Gerhard Heinzl, and Karsten Danzmann. “Advanced phasemeter for deep phase modulation interferometry”. In: *Opt. Express* 22.15 (July 2014), pp. 18214–18223.
- [64] Osami Sasaki and Kazuhide Takahashi. “Sinusoidal phase modulating interferometer using optical fibers for displacement measurement”. In: *Appl. Opt.* 27.19 (Oct. 1988), pp. 4139–4142.
- [65] Osami Sasaki, Hirokazu Okazaki, and Makoto Sakai. “Sinusoidal phase modulating interferometer using the integrating-bucket method”. In: *Appl. Opt.* 26.6 (Mar. 1987), pp. 1089–1093.
- [66] Osami Sasaki and Hirokazu Okazaki. “Sinusoidal phase modulating interferometry for surface profile measurement”. In: *Appl. Opt.* 25.18 (Sept. 1986), pp. 3137–3140.
- [67] José Henrique Galeti, Paula Lalucci Berton, Cláudio Kitano, Ricardo Tokio Higuti, Ronny Calixto Carbonari, and Emílio Carlos Nelli Silva. “Wide dynamic range homodyne interferometry method and its application for piezoactuator displacement measurements”. In: *Appl. Opt.* 52.28 (Oct. 2013), pp. 6919–6930.
- [68] Thomas Kissinger, Thomas O.H. Charrett, and Ralph P. Tatam. “Range-resolved interferometric signal processing using sinusoidal optical frequency modulation”. In: *Opt. Express* 23.7 (Apr. 2015), pp. 9415–9431.
- [69] Thomas Kissinger, Thomas O. H. Charrett, Stephen W. James, Alvin Adams, Andrew Twin, and Ralph P. Tatam. “Simultaneous laser vibrometry on multiple surfaces with a single beam system using range-resolved interferometry”. In: *Proc. SPIE* 9525 (2015).
- [70] V.S. Sudarshanam and Richard O. Claus. “Generic J1...J4”. In: *Journal of Modern Optics* 40:3 (1993), pp. 483–492.
- [71] Thomas S. Schwarze. “FPGA-based modulation signal synthesis and measurement system for high precision laser interferometry”. MA thesis. Leibniz Universität Hannover, 2013.
- [72] William H. Press, Brian P. Flannery, Saul A. Teukolsky, and William T. Vetterling. *Numerical recipes in C*. 1st ed. Cambridge University Press, 1988.
- [73] Rudolf Kalman. “A New Approach to Linear Filtering and Prediction Problems”. In: *Journal of Basic Engineering* 82 (Jan. 1960), pp. 35–45.

- [74] Mohinder S. Grewal and Angus P. Andrews. *Kalman filtering. Theory and practice using MATLAB®*. eng. Hoboken, New Jersey: John Wiley & Sons, 2015.
- [75] R. Faragher. “Understanding the Basis of the Kalman Filter Via a Simple and Intuitive Derivation [Lecture Notes]”. In: *IEEE Signal Processing Magazine* 29.5 (Sept. 2012), pp. 128–132. ISSN: 1053-5888.
- [76] Simon J. Julier and Jeffrey K. Uhlmann. “New extension of the Kalman filter to nonlinear systems”. In: *Proc. SPIE* 3068 (1997), p. 59.
- [77] Bruce P. Gibbs. *Advanced Kalman filtering, least-squares and modeling. A practical handbook*. eng. Hoboken, New Jersey: John Wiley & Sons, 2011.

Acknowledgments

At this point, I would like to thank all the people that made this thesis possible. First of all, thanks to Prof. Dr. Karsten Danzmann, for making the AEI what it is now and for giving me the opportunity to take part in its fantastic story!

The same applies to Gerhard Heinzl, without whom I couldn't imagine the Space Interferometry group to be where it is today. His commitment to this group is admirable and his knowledge and curiosity an inspiration. Thank you, Gerhard, for giving me the chance to work in this exciting environment!

A special "thanks" to my colleague, supervisor and last but not least friend, Oliver Gerberding, who always managed to keep me motivated even when frustration reigned the lab or the keyboard.

To my office mates Germán and Daniel, I couldn't imagine a better place to spend my working hours. I fear the day that one of us will walk out of the office door for good.

To all my colleagues at the AEI, despite all the amazing science that is going on here, without you guys it would only be half the fun! In particular I would like to thank "Team Mensa" for providing a climax for every weekday thanks to lots of laughter!

Many people were bugged by me to proof-read this thesis. So, Oliver, Sweta, GeFeBa, Daniel, Lea, Christoph, Vaishali and Mandarina.... thanks a lot!

A special "thanks" also to my colleague Katharina for introducing me to the art of pgfplots used in this thesis. For the sketches, the ComponentLibrary (<http://www.gwoptics.org/ComponentLibrary/>) by A. Franzen was used. Furthermore, Daniel and Katharina kindly provided more components.

Apparently there is also a life outside the AEI, thus on this way I would also like to say thanks to Simon S. and Felix W., friends that I wouldn't want to miss!

Last but not least, I have nothing but gratitude for my family! I am happy that once again I get the chance to say "thank you!" for your unconditional support!

Curriculum Vitae

1996 - 2005	High School Diploma (Abitur), Gymnasium Petershagen
2005 - 2006	Civilian service, Weserlandklinik Bad Hopfenberg
2006 - 2009	Bachelor of Science in Physics, Leibniz Universität Hannover
2009 - 2013	Master of Science in Engineering Physics, Leibniz Universität Hannover, Holder of Scholarship Niedersachsenstipendium 2010/2011
01/2011 - 07/2011	Erasmus Exchange Program, Uppsala University, Sweden
01/2013 - 07/2013	Erasmus Internship Program, Axcon Aps., Denmark
2013 - 2018	Doctoral Studies, Institut für Gravitationsphysik, Leibniz Universität Hannover & Max-Planck-Institut für Gravitationsphysik (Albert-Einstein-Institut)
12/2013	Research visit at NASA Goddard Space Flight Center, Washington D.C.

Publications

Refereed journal articles

- **Schwarze, T. S.**, Gerberding, O., Cervantes, F. G., Heinzl, G., & Danzmann, K. (2014). “Advanced phasemeter for deep phase modulation interferometry.” *Optics express*, 22(15), 18214-18223.
- Gerberding, O., Diekmann, C., Kullmann, J., Tröbs, M., Bykov, I., Barke, S., ... **Schwarze, T. S.**, ... & Danzmann, K. (2015). “Readout for intersatellite laser interferometry: Measuring low frequency phase fluctuations of high-frequency signals with microradian precision.” *Review of Scientific Instruments*, 86(7), 074501.
- Isleif, K. S., Gerberding, O., **Schwarze, T. S.**, Mehmet, M., Heinzl, G., & Cervantes, F. G. (2016). “Experimental demonstration of deep frequency modulation interferometry.” *Optics express*, 24(2), 1676-1684.
- Chwalla, M., Danzmann, K., Barranco, G. F., Fitzsimons, E., Gerberding, O., Heinzl, G., ... **Schwarze, T. S.**, ... & Schuster, S. (2016). “Design and construction of an optical test bed for LISA imaging systems and tilt-to-length coupling.” *Classical and Quantum Gravity*, 33(24), 245015.
- Barranco, G. F., Gerberding, O., **Schwarze, T. S.**, Sheard, B. S., Dahl, C., Zender, B., & Heinzl, G. (2017). “Phase stability of photoreceivers in intersatellite laser interferometers.” *Optics Express*, 25(7), 7999-8010.
- Isleif, K. S., Bischof, L., Ast, S., Penkert, D., **Schwarze, T. S.**, Barranco, G. F., ... & Reiche, J. (2018). “Towards the LISA Backlink: Experiment design for comparing optical phase reference distribution systems.” *Classical and Quantum Gravity*, 35(8), 085009.
- Tröbs, M., Schuster, S., Lieser, M., Zwetz, M., Chwalla, M., Danzmann, K., ... **Schwarze, T. S.**, ... & Ward, H. “Reducing tilt-to-

length coupling for the LISA test mass interferometer.” *Classical and Quantum Gravity* (accepted)

Proceedings

- Teran, M., Martín, V., Gesa, L., Mateos, I., Gibert, F., Karnesis, N., ... **Schwarze, T. S.**, ... & Guzmán, F. (2015). “Towards a FPGA-controlled deep phase modulation interferometer.” In *Journal of Physics: Conference Series* (Vol. 610, No. 1, p. 012042). IOP Publishing.
- **Schwarze, T. S.**, Barranco, G. F., Penkert, D., Gerberding, O., Heinzl, G., & Danzmann, K. (2016, May). “Optical testbed for the LISA phasemeter.” In *Journal of Physics: Conference Series* (Vol. 716, No. 1, p. 012004). IOP Publishing.
- Isleif, K. S., Gerberding, O., Mehmet, M., **Schwarze, T. S.**, Heinzl, G., & Danzmann, K. (2016, May). “Comparing interferometry techniques for multi-degree of freedom test mass readout.” In *Journal of Physics: Conference Series* (Vol. 716, No. 1, p. 012008). IOP Publishing.
- Tröbs, M., Chwalla, M., Danzmann, K., Barranco, G. F., Fitzsimons, E., Gerberding, O., ... **Schwarze, T. S.**, ... & Robertson, D. I. (2017, September). “Experimental demonstration of reduced tilt-to-length coupling by using imaging systems in precision interferometers.” *International Conference on Space Optics-ICSO 2016* (Vol. 10562, p. 1056245). International Society for Optics and Photonics.